MECHANICAL AND TRIBOLOGICAL PROPERTIES OF POWDER FORGED Fe-P ALLOYS

Ph.D. THESIS

by

SHAILESH KUMAR CHAURASIA

DEPARTMENT OF METALLURGICAL AND MATERIALS ENGINEERING
INDIAN INSTITUTE OF TECHNOLOGY ROORKEE
ROORKEE-247667 (INDIA)
September, 2018

MECHANICAL AND TRIBOLOGICAL PROPERTIES OF POWDER FORGED Fe-P ALLOYS

A THESIS

Submitted in partial fulfilment of the requirement for the award of the degree

of

DOCTOR OF PHILOSOPHY

in

METALLURGICAL AND MATERIALS ENGINEERING

by

SHAILESH KUMAR CHAURASIA

DEPARTMENT OF METALLURGICAL AND MATERIALS ENGINEERING
INDIAN INSTITUTE OF TECHNOLOGY ROORKEE
ROORKEE-247667 (INDIA)
September, 2018

INDIAN INSTITUTE OF TECHNOLOGY ROORKEE
ROORKEE

CANDIDATE'S DECLARATION

I hereby certify that the work which is being presented in the thesis entitled "**MECHANICAL AND TRIBOLOGICAL PROPERTIES OF POWDER FORGED Fe-P ALLOYS**" in partial fulfilment of the requirements for the award of the Degree of Doctor of Philosophy and submitted in the Department of Metallurgical and Materials Engineering of the Indian Institute of Technology Roorkee, Roorkee is an authentic record of my own work carried out during a period from July, 2013 to September, 2018 under the supervision of Dr. Ujjwal Prakash, Professor and Dr. Vikram V. Dabhade, Associate Professor, Department of Metallurgical and Materials Engineering, Indian Institute of Technology Roorkee, Roorkee.

The matter presented in this thesis has not been submitted by me for the award of any other degree of this or any other Institution.

(SHAILESH KUMAR CHAURASIA)

This is to certify that the above statement made by the candidate is correct to the best of our knowledge.

(Ujjwal Prakash)
Supervisor

(Vikram V. Dabhade)
Supervisor

The Ph.D. Viva-Voce Examination of Mr. **Shailesh Kumar Chaurasia**, Research Scholar, has been held on 5th February, 2019.

Chairman, SRC **Signature of External Examiner**

This is to certify that the student has made all the corrections in the thesis.

Signature of Supervisor(s) **Head of the Department**

Date: February, 2019

This thesis is dedicated to my departed parents and family
for their love, endless support
and encouragement.

ABSTRACT

Phosphorus (P) is an undesirable element in steels. During cold working, phosphorus induces cold shortness or brittleness due to which its content in modern steels is limited to < 0.04 wt. %. It has been seen that the embrittlement of phosphoric iron is due to segregation of phosphorus along the grain boundaries. The inter-granular failure occurs due to decohesion of the grain boundary. The resistance to brittle fracture is reduced by addition of phosphorus in the steel. On the other hand, phosphorus addition has been reported to improve magnetic permeability, lower coefficient of friction and improve wear resistance and corrosion resistance. Phosphorus provides solid solution strengthening to the ferrite matrix. The Iron-Phosphorus alloys are two-phase materials, which have the potential to be used as wear resistant materials. Their microstructure consists of hard phosphide phase in the ductile matrix of the ferrite. The presence of phosphide phase in these alloys also leads to an increase in hardness. Despite these advantages, it is rarely used because of the low ductility associated with phosphorus-containing alloys.

Fe-P alloys may be prepared by melting and casting route. Here, the last liquid to solidify is rich in phosphorus and this can lead to embrittlement. Fe-P Powder metallurgy alloys developed by conventional pressing and sintering route of metal powders takes a long time to complete the powder metallurgy process. To expedite this process, liquid phase sintering (LPS) has been used. Most powder metallurgy (P/M) approaches for Fe-P alloys use liquid phase sintering by using the eutectic reaction where liquid decomposes into Fe (α) and Fe_3P. In LPS the liquid at the particle boundaries is enriched in phosphorus; therefore, both cast as well as conventional powder metallurgy (P/M) routes, have limitations.

In the present work, the Fe-P alloys have been developed by hot powder forging process to overcome the problem of segregation at the grain boundary and heavy volume shrinkage. In this process, phosphorus was admixed with water-atomized iron powder by a chemical route. Further, the powder was heated below the melting point (liquid phase) of the alloy (upto1050 ^oC) in the presence of hydrogen gas (H_2 gas) prior to forging. The surface oxides were reduced during heating by the continuous flow of H_2 gas. This facilitates proper bonding between the powder particles. Care was taken that no liquid phase formation took place during the processing. Powder forging ensures a higher density and may lead to improved properties. In the present work, the powder forged alloys with phosphorus contents

~1wt. % or less exhibited significant ductility. Possible reasons for this are discussed. The solid-state processing used may lead to the development of ductile phosphorus containing alloys with attractive properties. Iron-phosphorus alloys were developed by hot powder forging route to avoid the problem of segregation and shrinkage as well as to control the dimensional stability. The process produced forgings with negligible porosity. In the investigation, hot powder forging was carried out in such a manner that the formation of the liquid phase is avoided during forging.

In the present study, six binary Fe-P alloys such as Fe-0wt.%P, Fe-0.35wt.%P, Fe-0.65wt.%P, Fe-1.3wt.%P, 2wt.% and 3wt.%P have been developed by hot powder forging technique. In P/M alloys prepared by conventional pressing and sintering route, small additions of carbon (<0.05wt.%C) to the Fe-P alloys may also reduce brittleness. A ternary alloy with carbon i.e., Fe-0.65wt.%P-0.20wt.%C was developed by the same route. The samples were cut off from the forged slabs after the removal of end caps and mild steel skin for the characterization.

Mechanical properties were improved by the addition of P in the iron. Strength was observed to increase from 302MPa to 495MPa with the addition of phosphorus in the iron by scarifying the ductility. The Fe-0.65wt.%P showed the best combination of mechanical properties (UTS 365MPa and elongation 12%) among the six binary alloys. The significant amount of ductility accompanied with high density is one of the important achievements of the present investigation. Significant increase in strength and hardness of Fe-0.65wt.%P alloy occurred with the addition of 0.20wt. %C. The strength and hardness were improved from 365MPa to 552MPa and 111HV to 200HV respectively by addition of 0.20wt.%C in Fe-0.65wt.%P.

The influence of P addition (0 to 3wt.%) on the dry sliding behavior of Fe-based alloys developed by hot powder forging has also been investigated in the present work. The effect of normal load on the wear behavior of Fe-P alloys is also studied. The wear mechanisms are oxidative, abrasive and delaminations depending on the amount of P addition. The Fe-3wt.%P alloy shows the minimum wear loss and lower coefficient of friction among all the binary alloys developed in the present investigation during dry sliding condition. Without P content alloy exhibited a higher wear rate which indicates that the ferrite matrix did not support wear in this alloy. Also, the tribological investigation was carried out on Fe-0.65wt.%P-0.20wt.%C alloy. The wear rate, Archard wear coefficient and the average coefficient of friction observed for Fe-0.65wt.%P-0.20wt.%C are less than for Fe-0.65wt.%P alloy. For alloy Fe-0.65wt.%P-

0.20wt.%C these values are 0.07 x $10^{-5}$$mm^3$/m, 0.05 x 10^{-7} and 0.44 to 0.40 for three loads respectively and for Fe-0.65wt.%P the values are 0.46 x $10^{-5}$$mm^3$/m, 1.4 x 10^{-7} and 0.54 to 0.48 for three loads respectively. This is attributed to the higher hardness of steel containing pearlite apart from phosphide. The results show that wear rate decreased by the addition of C in the Fe-P alloy which indicates that the pearlite resists the wear of material. The corresponding coefficient of friction was lower which indicated the real contact area decreased by the formation of oxides. Among all the developed alloys in the present work, the carbon containing alloy was found to undergo minimum wear loss and lower coefficient of friction during the dry sliding test. The mechanism of wear was observed to be mainly oxidative in the behavior.

ACKNOWLEDGEMENT

It gives me immense pleasure to express my deepest sense of gratitude and sincere thanks to my revered research supervisors **Dr. Ujjwal Praksh,** *Professor & Chairman, DRC* and **Dr. Vikram V. Dabhade**, *Associate Professor,* Department of Metallurgical and Materials Engineering**,** Indian Institute of Technology Roorkee, for their guidance, constant encouragement and wholehearted assistance. His intelligent coordination and thought-provoking discussions made my work highly successful. He has also made an inestimable contribution to my future career by putting an end to those dull moments at the beginning of this study.

I am grateful to **Dr. A. K. Chaturvedi**, Professor & Director, Indian Institute of Technology Roorkee, who have been a constant source of inspiration for me. I am equally grateful to **Dr. Anjan Sil**, Professor & Head, and **Dr. S. K. Nath**, Professor & former Head, Department of Metallurgical and Materials Engineering**,** Indian Institute of Technology Roorkee, for providing me all the infrastructural facilities to carry out this work in the department.

I wish to express my sincere thanks to **Dr. Devendra Singh**, *Associate Professor (Internal Expert of SRC),* Department of Metallurgical and Materials Engineering**,** Indian Institute of Technology Roorkee, and **Dr. B. K. Mishra**, Professor *(External Expert of SRC),* Department of Mechanical and Industrial Engineering**,** Indian Institute of Technology Roorkee, and **Dr. S. K. Nath**, *Professor & Chairman, SRC,* Department of Metallurgical and Materials Engineering**,** Indian Institute of Technology Roorkee, for giving their valuable time and suggestions in successful completion of this work.

I also express my sincere thanks to all the faculty members of the department for their constant support and encouragement during my research work.

I am great thankful to **Dr. Shri Chand**, Professor and former Head, Department of Chemical Engineering, Indian Institute of Technology Roorkee, for giving his valuable time for the corrections of my thesis, especially to the grammatical corrections in the entire thesis.

I am also thankful to the technical and non-technical staff member of the Metallurgical and Materials Engineering Department, specially to Mr. Narendra Kumar, Mr. Dinesh Kumar, Mr. Raj Kumar Sharma, Mr. Rajendra Sharma, Mr. S. M. Giri, Mr. H. K. Ahuja, Mr. Dhan

Prakash, Mr. Ashish Kumar of this for necessary help during experimental work in their respective laboratories.

Eagerness and vitality to continue interest in research has been provided by my seniors and friends through frequent discussions. The support received specially from Dr. K. K. Yogesh, Dr. Amit Joshi, Dr. Lokedra Thakur, Mr. Ravi Raj, Mr. Sandeep Kumar, Mr. Suresh Sonkar, Mr. Ratnagar Singh, Dr. Deepak Kumar, Mr. Atul Kumar, Mr. Amit Kumar Chaurasia, Mr. Vineet Kumar Rathore, Mr. Ravinder Kamboj, Mr. Rahul Gupta, Mr. Mumtaj Shah, Mr.Shubham Sharma, Mr.Reddipalli Bhargav is gratefully acknowledged.

I am also thankful to Quality Improvement Programme(QIP) centre, IIT Roorkee for providing me entire support during my research work.

I am great thankful to **Dr. A. K. Gupta**, Professor and Dean, Institute of Engineering and Technology, M.J.P. Rohilkhand University Bareilly (U.P.) for giving me an opportunity to do my research work at Indian Institute of Technology Roorkee, Roorkee (U.K).

Expression of gratitude would be definitely incomplete if I do not mention my wife **Smt. NISHA CHAURASIA** who held the key to my success and her continuous encouragement, especially at difficult times and the perseverance shown by her to bear the extra responsibilities of the family due to grass negligence on my part. My daughters **KRITIKA (KHOOSHI)** and **KAMYA (KAVYA)** had also to face similar neglect during my involvement in this work. Most affectionate gratitude and appreciation are due to all of them.

Finally, I must express my very profound gratitude to my departed parents for providing me with unfailing support and continuous encouragement throughout my year of study and this research endeavor. Thank you for the selfless love, care, pain and sacrifice you did to shape my life. Although you hardly understood what I researched on, but you were willing to support any decision I made.

I would like to express my sincere gratitude from the core of my heart to **God Almighty** for giving me courage, strength, sound health, and patience to carry out my research.

Last but not the least, I wish to place on record my deep sense of gratitude to my departed parents and family members whose blessings I would not have been able to join this prestigious department for research (Ph.D.) to enrich myself with the latest knowledge. I dedicate this work and thesis to fond memories of my departed mother and father.

(SHAILESH KUMAR CHAURASIA)

CONTENTS

ABSTRACT **i**

ACKNOWLEDGEMENT **v**

CONTENTS **vii**

LIST OF FIGURES **xi**

LIST OF TABLES **xix**

RESEARCH PUBLICATIONS **xxi**

CHAPTER 1 INTRODUCTION **1**

CHAPTER 2 LITERATURE REVIEW **5**

2.1 Fe-P alloy system 5

2.2 Fe-P alloys 6

2.3 Manufacturing of Fe-P alloys 8

2.3.1 Melting and casting route 9

2.3.2 Powder metallurgy route 9

2.3.3 Powder Forging Process 22

2.4. Mechanical properties 27

2.5 Friction behaviour of metals and alloys 33

2.5.1 Friction theories 33

2.5.2 Factor affecting the friction behaviour of steels 34

2.6. Types of wear 36

2.7. Dry sliding wear of steels 37

2.7.1 Microstructure and dry sliding wear 37

2.7.2 Oxidative and metallic wear 40

2.8 Tribological properties 42

2.9 Corrosion properties 44

2.10 Magnetic properties 48

2.11 Fe-P-C system 51

2.11.1 Fe-P-C phase diagram 51

2.11.2 Grain boundary segregation of phosphorus 54

2.12 Fe-P-C alloys and their properties 55

2.12.1 Mechanical properties 59

2.12.2 Tribological properties 63

CHAPTER 3 FORMULATION OF PROBLEM 65

CHAPTER 4 EXPERIMENTAL WORK 67

4.1 Powder characterization 67

4.2 Preparation of master alloy (Fe-P) powders 67

4.3 Preparation of binary alloy (Fe-P) powder mixtures 68

4.4 Preparation of ternary alloy (Fe-P-C) powder mixtures 69

4.5 Preparation of mild steel (M.S) capsule and encapsulation of powders 69

4.6 Heating of encapsulated powder 69

4.7 Hot forging of heated capsule powder 70

4.8 Homogenization 73

4.9 Sample preparation from the forged slab 73

4.10 Stress relieving and annealing treatments 74

4.11 Measurement of density 74

4.12 Metallography examination 74

4.12.1 Optical examination 75

4.12.2 Field emission scanning electron microscope (FESEM) examination 75

4.13 Grain size measurement 75

4.14 X-ray diffraction (XRD) 75

4.15 Hardness measurement 76

4.15.1 Bulk hardness measurement 76

4.15.2 Microhardness measurement 76

4.16 Tensile test 77

4.17 Charpy impact test 77

4.18 Dry sliding wear test 78

4.18.1 Wear sample preparation 78

4.18.2 Wear test 78

CHAPTER 5 RESULT AND DISCUSSIONS 81

5.1 Powder characterization, processing of forged alloys and density measurement 81

5.1.1 Powder characterization 81

5.1.2 Processing and density measurement of forged alloys 83

5.2 Effect of phosphorus on microstructure and mechanical properties of iron-based alloys 86

5.2.1 Microstructure 86

5.2.2 Hardness 88

5.2.3 Yield strength and tensile strength 91

5.2.4 Ductility 92

5.2.5 Fractographs 94

5.3 Effect of phosphorus on tribological properties of iron-based alloys 96

5.3.1 Dry sliding wear and friction behaviour at 2.2 m/s 96

5.3.1.1 Wear characteristics 96

5.3.1.2 Dry sliding friction 103

5.3.1.3 Worn surface analysis and wear mechanism 105

5.3.2 Dry sliding wear and friction behaviour at 3m/s 107

5.3.2.1 Wear characteristics 107

5.3.2.2 Dry sliding friction 112

5.3.2.3 Worn surface analysis and wear mechanism 115

5.3.2.4 Wear debris analysis 116

5.4 Effect of carbon on microstructure and mechanical properties of fe-0.65wt. %p alloy 118

5.4.1 Microstructure 118

5.4.2 Mechanical properties 119

5.5 Effect of carbon on tribological properties of fe-0.65 wt.% p alloy 122

5.5.1 Wear characteristics 122

5.5.2 Dry sliding friction 126

CHAPTER 6 CONCLUSIONS 131

CHAPTER 7 SUGGESTIONS FOR FUTURE WORK 135

REFERENCES 137

LIST OF FIGURES

FIGURE. NO.	DESCRIPTION	PAGE NO.
Figure 2.1	(a) Iron-phosphorus phase diagram, (b) High-temperature γ region (Kubaschewski 2013).	6
Figure 2.2	Microstructure of the ancient iron. The dark regions show phosphorus (Kumar and Balasubramaniam 2002).	7
Figure 2.3	SEM micrograph showing the irregular shape of the slag phase along grain boundaries. A few such boundaries are indicated by GB (Kumar and Balasubramaniam 2002).	8
Figure 2.4	Optical micrograph of polished P/M steel with porosity (left) and full dense (right) (Sundaram and Maheswaran 2017).	9
Figure 2.5	Mechanical properties vs. the relative density of P/M steels with different processes (Höganäs Höganäs Handbook for Sintered Components-3).	10
Figure 2.6	Process route of powder metallurgy (Weblink 1).	11
Figure 2.7	SEM micrographs showing typical powder morphology of (a) water and (b) gas atomized powder (Weblink 1).	12
Figure 2.8	Sintering sequence on a microscopic scale (Höganäs Handbook 2).	14
Figure 2.9	Relative costs for various die compaction processes (Whittaker 2007).	17
Figure 2.10	P/M part industries in the various segments (Weblink 2)	19
Figure 2.11	Automotive P/M components (Loberto et al. 2010; Ramakrishnan 2013).	20
Figure 2.12	Forging mode and stress conditions on pores for (a) repressing (b) upsetting (James 1994).	22
Figure 2.13	Comparison of tensile and yield strength of FLN2-4405 over a range of densities. All samples processed in the sintering furnace cooled condition (Marucci and Rawlings 2004).	25
Figure 2.14	Comparison of maximum elongation and apparent hardness of FLN2-4405 over a range of densities. All samples processed in the sintering furnace cooled condition (Marucci and Arthur 2004).	25
Figure 2.15	Effect of phosphorus on impact energy of gray cast iron (Abbasi et al.	

	2007).	28
Figure 2.16	Effect of phosphorus on steadite of gray cast iron (Abbasi et al. 2007).	29
Figure 2.17	Cooling curve of gray cast irons containing P (Abbasi et al. 2007).	29
Figure 2.18	Effect of phosphorus on the eutectic temperature of gray cast iron (Abbasi et al. 2007).	30
Figure 2.19	Influence of alloying elements on the hardness of ferrite (Engstrom et al. 1992).	30
Figure 2.20	Tensile properties and dimensional as functions of the phosphorus content (Lindskog 1973).	31
Figure 2.21	Yield strength variation as a function of elongation on parts sintered to different densities for Fe–P powder mixtures (Narasimhan 2001).	31
Figure 2.22	Impact energy of Fe–P powder mixtures sintered to different densities (Narasimhan 2001).	31
Figure 2.23	A force, F, is needed to overcome friction and cause motion by (a) rolling (b) sliding (Hutchings 2017).	33
Figure 2.24	The variation of coefficient of friction with a normal load for steels sliding against themselves in the air, unlubricated (Hutchings 2017).	35
Figure 2.25	Three basic wear curves (Eyre and Walker 1976).	44
Figure 2.26	Effect of phosphorus on wear characteristics of sintered iron (Eyre and Walker 1976).	44
Figure 2.27	Delhi iron pillar at Delhi (Weblink 3).	45
Figure 2.28	The effect of atmospheric humidity on the corrosion of iron.	46
Figure 2.29	Schematic of rusted structure formed on mild steel, weathering steel and DIP (Balasubramaniam 2005).	47
Figure 2.30	Coercive force of iron-phosphorus alloys (Hanejko et al. 1992).	48
Figure 2.31	Maximum Permeability of Iron-Phosphorus alloys (Hanejko et al. 1992).	49
Figure 2.32	Saturation induction versus density for several alloys (Hanejko et al. 1992).	49
Figure 2.33	Electrical resistivity of Fe-P alloys with increment of P in iron (Chaurasia et al. 2012).	50
Figure 2.34	C-Fe-P computed liquidus projection (Raghavan 2004). C-Fe-P	52
Figure 2.35	computed isothermal sections at (a) 1100 °C and (b) 1000 °C (Raghavan 2004).	52

Figure 2.36	C-Fe-P computed isothermal sections at (a) 900 °C and (b) 800 °C (Raghavan 2004).	53
Figure 2.37	C-Fe-P computed vertical section at P =0.1 wt. % (Raghavan 2004).	53
Figure 2.38	Schematic diagram of sintering mechanisms of Fe-P-C alloy (Molinari et al. 1992). (a) Phosphide and graphite particles are in contact with the iron particles, (b) Diffusion of carbon into the matrix starts, (c) Diffusion couple of phosphide and matrix particles, and (d) Two different transformations of particles (Molinari et al. 1992).	56
Figure 2.39	True stress-strain graphs of dual phase steels with varies volume fraction of martensite (V_m) of fixed carbon content (C_m= 0.35%). It shows the different stages of strain hardening. Arrows indicate transition strains. (●) 1C, 16.5 %;(▲) 2C, 32.2 %;(▼) 3C, 47.8% (Mediratta et al. 1990).	58
Figure 2.40	Stage I strain hardening exponent (n) vs. the volume percent martensite for different values of $C_{m.}$ (●) 0.65%; (▲), 0.54%; (▼), 0.35 % (Mediratta et al. 1990).	58
Figure 2.41	Effect of carbon additions upon the properties of sintered iron phosphorus alloys (Höganäs Handbook for Sintered Components-3 2004).	60
Figure 2.42	(a) Microstructure of Fe-0.45%P alloy and (b) Microstructure of Fe-0.45%P-0.5% C alloy (Höganäs Handbook for Sintered Components-3).	61
Figure 2.43	Effect of phosphorus additions upon density of sintered iron (Höganäs Handbook for Sintered Components-3).	61
Figure 2.44	Effect of phosphorus on carbon alloys containing (a) 0.25% C (b) 0.50%C (Straffelini et al. 1993).	62
Figure 2.45	The deformation mechanism of P/M containing powder metallurgy ferrous alloys (Straffelini et al. 1993).	62
Figure 4.1	Schematic diagram showing the preparation of iron-phosphate.	68
Figure 4.2	Hollow mild steel capsule.	69
Figure 4.3	Heating of encapsulated powder.	70
Figure 4.4	A Channel die of dimension 220(l) × 75(w) × 25(h) mm^3.	70
Figure 4.5	Friction screw driven forge press.	71

Figure 4.6	Die and punch placed in Friction screw driven forge press.	71
Figure 4.7	Schematic diagram of a process for development of Fe-P alloys.	72
Figure 4.8	Forged slab after removing both gas flow pipes.	72
Figure 4.9	Forged slab after reforging. (a) The thickness of the slab (b) Width of the slab.	73
Figure 4.10	Microhardness testing equipment.	76
Figure 4.11	Schematic diagram of round tensile specimen.	77
Figure 4.12	Schematic diagram of the Charpy impact test specimen.	77
Figure 4.13	Conventional impact testing machine.	75
Figure 4.14	Representative initial surface roughness of disc.	79
Figure 4.15	Pin on disc wear testing apparatus.	79
Figure 5.1	The SEM micrographs of powders (a) Fe (b) Fe-0.35wt.%P (c) Fe-0.65wt.%P (d) Fe-1.3wt.%P (e) Fe-2wt.%P (f) Fe-3wt.%P.	82
Figure 5.2	Elemental mapping of powder mixture alloy for (a) iron and (b) phosphorus.	83
Figure 5.3	Line scan in scanning electron microscope of Fe–0.65wt.%P showing phosphorus distribution within the grains as well as along grain boundaries in the forged alloys. The blue line is for P, and the red one is for Fe variation. The major peaks indicate the presence of phosphide phase.	83
Figure 5.4	Unetched optical micrograph of Fe-2wt.% P alloy under final forged condition. It shows the iron phosphide (black region) distributed over the ferrite matrix (bright region).	84
Figure 5.5	XRD pattern of Fe-2wt.% P forged alloy showing ferrite and iron phosphide peaks.	85
Figure 5.6	Optical micrographs of powder-forged specimens of (a, d) Fe–0.65 wt.%P, (b, e) Fe–2 wt.%P, and (c, f) Fe–3 wt.%P alloy.	87
Figure 5.7	Volume fraction of phosphide at different phosphorus contents in Fe-P alloys.	88
Figure 5.8	(a) Secondary electron scanning electron microscope micrograph of Fe–2 wt.%P alloy. Elemental analysis of matrix (c) and precipitates (d) of Fe–2 wt.%P alloy using energy dispersive analysis of x-rays.	89
Figure 5.9	Showing the hardness based on the rule of mixture and experimental	

	hardness of Fe-P alloys.	90
Figure 5.10	Effect of phosphorus on Charpy impact energy of Fe-P P/M alloys.	92
Figure 5.11	Variation of percentage elongation with P content in iron.	93
Figure 5.12	Scanning electron microscope micrographs of tensile fracture surfaces of powder-forged specimens (a) Fe–0.65wt.%P, (b) Fe–2wt.%P, and (c) Fe–3 wt.%P alloys. (b) shows ductile dimple failure, while cleavage failure is observed in (c) with Fe–2wt.%P alloy showing mixed mode failure.	94
Figure 5.13	Scanning electron microscope micrographs of impact fracture surfaces of powder-forged specimens (a) Fe–0.65 wt.%P, (b) Fe–2 wt.%P, and (c) Fe–3 wt.%P alloys. The alloys with <1%P exhibit ductile dimple failure. For the alloys with >1 wt.%P, the fracture mode is a mix of ductile and cleavage.	95
Figure 5.14	Variation of cumulative wear volume loss as a function of sliding distance at different loads for pure iron at 2.2 m/s.	97
Figure 5.15	Variation of cumulative wear volume loss as a function of sliding distance at different loads for Fe-0.35wt.%P at 2.2 m/s.	98
Figure 5.16	Variation of cumulative wear volume loss as a function of sliding distance at different loads for Fe-0.65wt.%P at 2.2 m/s.	98
Figure 5.17	Variation of cumulative wear volume loss as a function of sliding distance at different loads for Fe-1.3wt.%P at 2.2 m/s.Variation of	99
Figure 5.18	cumulative wear volume loss as a function of sliding distance at different loads for Fe-2wt.%P at 2.2 m/s.	99
Figure 5.19	Variation of cumulative wear volume loss against sliding distance at different loads in Fe-3wt.%P at 2.2 m/s.	100
Figure 5.20	Variation of wear rate with a normal load in pure iron, Fe-0.35wt. %P, Fe-0.65wt. %P, Fe-1.3wt. %P, Fe-2wt. %P and Fe-3wt. %P containing 0, 7, 10, 21, 25 and 34 % phosphide respectively at 2.2 m/s.	101
Figure 5.21	Variation of wear rate against phosphide volume fraction at the normal loads of 19.6, 29.4 and 39.2N at 2.2 m/s.	102
Figure 5.22	Variation of average coefficient of friction as a function of normal load for pure iron, Fe-0.35wt.%P, Fe-0.65wt.%P, Fe-1.3wt.%P, Fe-2wt.%P and Fe-3wt.%P containing 0, 7, 10, 21, 25 and 34 % phosphide	

	respectively at 2.2 m/s.	103
Figure 5.23	Variation of average coefficient of friction as a function of phosphide volume fraction at the normal loads of 19.6, 29.4 and 39.2N at 2.2 m/s.	104
Figure 5.24	SEM images of worn surfaces of (a) pure iron (Fe), (b) Fe-0.35wt. %P, (c) Fe-0.65wt.%P, (d) Fe-1.3wt. %P, (e) Fe-2wt. %P and (f) Fe-3wt. %P alloys at 29.4 N after sliding for 30 min at a sliding speed of 2.2 m/s.	105
Figure 5.25	(a) SEM micrograph of worn surfaces of Fe (b) SEM micrograph of worn surfaces of Fe-0.35wt. %P. (c) Elemental analysis of Fe (d) Elemental analysis of Fe-0.35wt. %P.	106
Figure 5.26	Variation of cumulative wear volume loss as a function of sliding distance at different loads for pure iron at 3 m/s.	107
Figure 5.27	Variation of cumulative wear volume loss as a function of sliding distance at different loads for Fe-0.35wt.% P at 3 m/s.	108
Figure 5.28	Variation of cumulative wear volume loss as a function of sliding distance at different loads for Fe-0.65wt.% P at 3 m/s.	108
Figure 5.29	Variation of cumulative wear volume loss as a function of sliding distance at different loads for Fe-1.3wt.% P at 3 m/s.	109
Figure 5.30	Variation of cumulative wear volume loss as a function of sliding distance at different loads for Fe-2wt.% P at 3 m/s.	109
Figure 5.31	Variation of cumulative wear volume loss as a function of sliding distance at different loads for Fe-3wt.%P at 3 m/s.	110
Figure 5.32	Variation of wear rate with a normal load for pure iron, Fe-0.35wt. %P, Fe-0.65wt. %P, Fe-1.3wt. %P, Fe-2wt. %P and Fe-3wt. %P containing 0, 7, 10, 21, 25 and 34 % phosphide respectively at 3 m/s.	111
Figure 5.33	Variation of wear rate as a function of phosphide volume fraction at the normal loads of 19.6, 29.4 and 39.2N at 3 m/s.	112
Figure 5.34	Variation of average coefficient of friction as a function of normal load for pure iron, Fe-0.35wt.%P, Fe-0.65wt.%P, Fe-1.3wt.%P, Fe-2wt.%P and Fe-3wt. %P containing 0, 7, 10, 21, 25 and 34 % phosphide respectively at 3 m/s.	113
Figure 5.35	Variation of average coefficient of friction as a function of phosphide volume fraction at the normal loads of 19.6, 29.4 and 39.2N at 3 m/s.	113
Figure 5.36	(a) Worn surface of Fe-3wt. %P under SEM (b) Elemental analysis of	

	worn surface using energy dispersive analysis of X-rays. It shows the compacted layer of Phosphorus at the worn surface.	114
Figure 5.37	SEM of worn surfaces of (a) pure iron (Fe), (b) Fe-0.35wt.%P, (c) Fe-0.65wt.%P, (d) Fe-1.3wt.%P, (e) Fe-2wt.%P and (f) Fe-3wt.%P alloys at 39.2 N after sliding for 30 min at a sliding speed of 3 m/s.	115
Figure 5.38	SEM images of debris collected after sliding at 29.4 N from (a) pure iron (Fe), (b) Fe-0.35wt. %P, (c) Fe-0.65wt.%P, (d) Fe-1.3wt.%P, (e) Fe-2wt.%P and (f) Fe-3wt.%P alloys. Insets in (a), (c) and (d) are EDS of debris collected from the worn surfaces.	117
Figure 5.39	(a) and (b): Optical microstructure for Fe-0.65 wt.%P and Fe-0.65 wt.%P-0.20wt. % C, respectively; (c) and (d): SEM microstructure for Fe-0.65 wt.%P and Fe-0.65 wt. %P-0.20wt. % C, respectively.	118
Figure 5.40	SEM and EDS analysis from the matrix, iron phosphide and pearlitic region of Fe-0.65wt.%P-0.20wt.%C alloy showing the presence of phosphorus.	119
Figure 5.41	Tensile fracture surfaces of powder forged specimens by SEM of (a) Fe-0.65 wt. %P and (b) Fe-0.65 wt. %P-0.20wt. %C showing ductile dimple failure.	121
Figure 5.42	SEM images of Charpy fracture surfaces of powder forged specimens (a) Fe-0.65 wt. %P, (b) Fe-0.65wt. %P-0.20wt.%C. The alloys exhibit ductile dimple failure.	121
Figure 5.43	Cumulative wear volume loss vs sliding distance at different normal loads for Fe-0.65wt.% P-0.20wt.% C at 2.2 m/s.	123
Figure 5.44	Variation of wear rate vs normal load for Fe-0.65wt.% P and Fe-0.65wt.% P-0.20wt.% C containing 10 % phosphide and 23 % pearlite at 2.2 m/s.	124
Figure 5.45	(a) and (c): Optical microstructure for Fe-0.65 wt.%P and Fe-0.65 wt.%P-0.20wt. % C, respectively; (b) and (d): Red color indicates the presence of phosphide and pearlite phase for Fe-0.65 wt. %P and Fe-0.65 wt. %P-0.20wt. % C, respectively.	124
Figure 5.46	Variation of cumulative wear volume loss vs sliding distance at different loads for Fe-0.65wt.%P-0.20wt.%C.	125
Figure 5.47	Variation of wear rate vs normal load for Fe-0.65wt.%P and Fe-0.65wt.%P-0.20wt.%C containing 10 % phosphide and 23 % pearlite	

	at 3 m/s.	126
Figure 5.48	Variation of average coefficient of friction vs normal load in Fe-0.65wt.%P and Fe-0.65wt.%P-0.20wt.%C containing 10 % phosphide and 23 % pearlite at 2.2 m/s.	127
Figure 5.49	Variation of average coefficient of friction with normal load for Fe-0.65wt.% P and Fe-0.65wt.%P-0.20wt.%C containing 10 % phosphide and 23 %. pearlite.	128
Figure 5.50	SEM images showing the worn surface of (a) Fe-0.65wt.%P and (b) Fe-0.65wt.%P-0.20wt.%C after sliding for 30 min at a sliding speed of 2.2 m/s.	128

LIST OF TABLES

TABLE NO.	DESCRIPTION	PAGE NO.
Table 2.1	Comparison of P/M and other manufacturing process (Randall 1998).	10
Table 2.2	Segments of the market in P/M Industry (PM94 World Congress).	21
Table 2.3	Market trends in Western European P/M Industry (PM94 World Congress).	21
Table 2.4	Comparison of powder forging with competing technologies (Huppmann and Hirschvogel 1978).	25
Table 2.5	Physical and mechanical properties(Eyre and Walker 1976).	32
Table 2.6	Atmospheric corrosion of steel and Zinc (Hudson 1953).	45
Table 2.7	Meteorological observation at New Delhi (1951) (Hudson 1953)	46
Table 2.8	DIP iron's composition.	47
Table 2.9	Magnetic Properties of Fe-P alloys (Das et al. 2008).	50
Table 2.10	Magnetic properties of alloys under d.c. mode (Chaurasia et al. 2012).	51
Table 2.11	Values for strain hardening coefficient n and strength coefficient K at room temperature (Dieter 1986).	57
Table 2.12	Table 2.12: Strain hardening exponent (n) at different stages of work hardening (Mediratta et al. 1990).	59
Table 4.1	Fe-P alloy powders.	68
Table 4.2	Fe-P-C alloy powder	69
Table 5.1	Microhardness of Fe-P alloys.	90
Table 5.2	Grain size and mechanical properties of Fe–P alloys.	91
Table 5.3	Wear rate and Wear coefficient for F-P alloys for sliding velocity of 2.2m/s.	102
Table 5.4	Wear rate and Wear coefficient of Fe-P alloys for sliding velocity of 3m/s	112
Table 5.5	Mechanical properties of alloys.	120

RESEARCH PUBLICATIONS

Papers Published in International journals:

1. **S.K.Chaurasia**, U. Prakash, V.V. Dabhade, "Effect of Phosphorus on Microstructure and Mechanical Properties of Iron-Based Alloys Processed through Powder Forging," Metallography, Microstructure and Analysis, Vol.6 (2017) pp.561-568.
2. **S.K. Chaurasia**, U. Prakash, V.V. Dabhade and S.K. Nath, "Effect of phosphorus addition on the dry sliding behavior of Fe-P alloys prepared by powder forging," Metallography, Microstructure and Analysis, Vol.6 (2018) pp.1-9.
3. **S.K. Chaurasia**, U. Prakash, V.V. Dabhade and S.K.Nath, "Dry sliding wear of Fe based powder Processed through Hot Powder forging technique," Materials Today: Proceedings, Vol.5 (2018) pp.17170-17179.
4. **S.K. Chaurasia**, U. Prakash and V.V. Dabhade, "Tribological properties of Fe-P powder metallurgy alloys," Trans. of PMAI, Vol.41 (2015) pp.45-50.
5. **S.K. Chaurasia**, U. Prakash, V.V. Dabhade and S.K.Nath, "Effect of carbon addition on mechanical properties and dry sliding behavior of Fe-0.65wt. %P alloy processed by powder forging," (Ready to be communicated)

Papers Presented in International Conference/ Symposium:

1. **S.K. Chaurasia**, U. Prakash and V.V. Dabhade, "Tribological properties of Fe-P powder metallurgy alloys," presented in PM15 International conference organized by PMAI, India at Mumbai during January 19-21, 2015.
2. **S.K. Chaurasia**, U. Prakash and V.V.Dabhade, "Microstructure and Mechanical properties of Iron-phosphorus powder metallurgy alloys," presented at PM16 International conference organized by PMAI, India at Pune during February 18-20, 2016.
3. **S.K. Chaurasia**, K.K. Yogesha, U. Prakash, V.V. Dabhade, "Influence of Phosphorus Addition on Strength and Ductile Behavior of Fe based Alloy Processed through Powder Metallurgy (P/M) Route," ISAMEA-2017 International Symposium organized by NIE at Mysuru, India during March 24-25, 2017.
4. **S.K. Chaurasia**, K.K. Yogesha, U. Prakash, V.V. Dabhade and S.K.Nath, "Influence of phosphide microstructure on the tribological properties of iron-based alloys through hot powder forging route," ISMA-2017 International Symposium organized by JSS IT campus at Mysuru, India on December 27, 2017.

CHAPTER 1

INTRODUCTION

Iron-phosphorus may be prepared by casting route in which the last liquid to solidify is rich in phosphorus which may lead to embrittlement. In the conventional powder metallurgy (pressing and sintering) route Fe-P alloys experience heavy volume shrinkage. It also takes a long time to complete this process. Use of liquid phase sintering to develop Fe-P alloys where liquid decomposes into Fe (α) and Fe_3P (eutectic reaction) expedites this process. But phosphorus is enriched at the particle boundaries during LPS. Thus, cast as well as conventional P/M have limitations.

Iron-phosphorus (Fe-P) P/M alloys show better mechanical properties in terms of high hardness and high strength. It shows low friction, excellent wear resistance, and improved corrosion resistance. It also exhibits improved magnetic properties. Phosphorus provides solid solution strengthening to the ferrite matrix. Phosphorus addition may lead to an increase in the density of P/M iron-based alloys.

In spite of these advantages, phosphorus (P) is rarely used in the steels. During cold working, phosphorus induces cold shortness or brittleness. Therefore, the content of P in steels is limited to < 0.05 wt.%. It is observed that the embrittlement occurs in the phosphoric iron due to the segregation of phosphorus along the boundaries of grain. The inter-granular failure occurs due to decohesion of the grain boundary. The resistance to brittle fracture behavior reduces with the addition of phosphorus in the steel.

The Iron-Phosphorus alloys are two-phase materials, which have the potential to be used as wear resistant materials. It has a unique structure consisting of hard phosphide phase in the ductile matrix of the ferrite. These alloys posses some special properties i.e., the absence of yield point phenomena, high rate of work hardening, high total and uniform elongation, excellent forming characteristics and reasonably fracture toughness. The mechanical properties can be altered by changing the amount of phosphide in the structure. The amount of phosphide can be varied by P addition in the iron powder. The manufacturers are always trying to reduce the cost of the product without the loss of quality. Thus, to produce quality products at low-cost novel technichnological approaches should be explored. Further, the obtained mechanical properties can be enhanced by the alloy design and processing parameters. Powder metallurgy (P/M) is a technique that has advantages over material utilization, to produce a component in

near net shape. Moreover, higher amount of phosphorus can be added as an alloying element in the system if desired which is not possible through melting and casting route. Thus, P/M technique gives flexibility to material and product designer. The presence of a relatively high amount of phosphorus (P) in ancient Indian iron results in several interesting effects (Stewart et al. 2000; Tylecote and Gilmour 1986; Piaskowski 1964).

Wear leads to an unwanted loss of material, which may only be reduced but cannot altogether be completely mitigated. Wear encountered in the industry has been classified as the following different types and their estimated relative values are Abrasive 45%; Adhesive 20%; Erosive 10%; Fretting 10%. In steel and other Metallurgical Industries in Germany, the loss due to unlubricated wear was estimated as 53% of the total loss. Hence, in view of the huge loss of material due to wear it becomes challenging for an engineer to design and develop newer wear resistant and cost-effective materials for the tribological applications.

Wear and friction behaviour of steels depends on the mechanical properties of the constituent phases like hardness and strength. The material should be soft in order to bear the contour of the shaft so that conditions for elastohydrodynamic lubrication could be established. At the same instance, the material has to be hard enough to bear the load under a given condition. It is not possible to meet these properties in single phase materials limiting their use in wear resistant applications. Some of the two-phase materials like Cu-Sn, Cu-Ti alloys, Fe-TiC composites, Fe based alloys, aluminium based alloys, magnesium-based alloys etc have been widely employed in bearing and other wear resistant applications. The underlying aim here is to utilize the mutual advantages of both the phases when the less desirable features of these phases are mitigated by the presence of the second phase. The morphology i.e., shape, size, distribution and volume fractions of the second phase critically control the mechanical properties of the two-phase system which in turn influence its tribological behavior.

Most of the tribological studies are on P/M alloys prepared by conventional pressing and sintering. As an alloying element, P is used in iron for particular applications in P/M alloys such as brake shoes due to its high resistance to wear and absence of sparking. The wear behavior of iron-phosphorus hot powder forging alloys has not yet been studied extensively.

The proposed thesis consists of the seven different chapters. **Chapter one** consists of an introduction to the topic and gives a brief background of ferrous powder metallurgy along with some introductory significance of powder forging. Alloying of Fe with phosphorus (P) is discussed. Powder metallurgy processes used in the literature for fabricating Fe-P alloys are compared with powder forging.

The literature review is given in **chapter two** and presented in different segments: a history of Fe-P and Fe-P-C alloys, various powder metallurgy processes, the mechanical and tribological behavior of Fe-P and Fe-P-C alloys. The importance of powder forging route over wrought and cast alloys and various P/M methods are presented. The role of phosphorus in removing the porosity which leads to near full density is discussed. The mechanism of densification during powder forging, mechanism of wear and friction behavior of Fe-P/Fe-P-C P/M alloys has been highlighted. The effect of microstructure, mechanical properties, normal load and sliding velocity on the friction and wear characteristic of the steels have also been reviewed.

In view of the certain gap in the literature review, the problems have been formulated in **chapter three.**

The details of the experimentation performed right from the development of process up to the development of impurity-free high-performance alloys and their characterization is given in **chapter four**. The chapter describes different characterization techniques used for the investigation of microstructure, mechanical and tribological properties of forged alloys.

In **Chapter five** the microstructural, mechanical and tribological behavior of Iron-phosphorus powder metallurgy alloys has been discussed. This chapter has been divided into five sections. Section **5.1** describes the powder characterization, processing of powder forged alloys and density measurement. The effect of phosphorus addition on microstructure and mechanical properties of Fe-P alloys (different composition of P in wt.%) are discussed in section **5.2.** The section **5.3** deals with the tribological properties of alloys. In this section, the role of phosphorus, normal load and sliding speed on the wear and friction characteristics of these alloys having different microstructures are presented and discussed. Section **5.4** describes the effect of carbon (C) addition on the microstructure and mechanical properties of a typical Fe-0.65wt.%P alloy, such as, hardness, strength, ductility, and toughness. The effects of carbon addition on wear and friction behaviour of Fe-0.65wt.%P have been discussed in section **5.5**.

Chapter six presents the major conclusions of the present study on microstructure, mechanical properties and tribological behavior of the alloys. Suggestions for the future work have been given in **Chapter seven**.

CHAPTER 2

LITERATURE REVIEW

This chapter presents critical review of the existing literature on the iron-phosphorus and iron-phosphorus-carbon alloys, their manufacturing processes, microstructure, and the mechanical properties. A review of the surface characteristics and the effect of surface interaction on the friction and wear processes are also included in this chapter. It is followed by a review of different types of wear mechanisms and friction and wear behavior of steels. The effects of microstructure, mechanical properties, normal load, sliding speed and the outer environment on the friction and wear behaviour of steels have also been given.

2.1 Fe-P ALLOY SYSTEM

The phase diagram of the Fe-P system is shown in Figure 2.1 (a and b). The solid line indicates the equilibrium phase diagram and a dotted line indicate the metastable phase diagram. The solid solubility of phosphorus in α-Fe is about less than 1% at ambient temperature while the solubility at 1050 ^{o}C is 2.6%. A eutectic reaction occurs at 1050 ^{o}C. The low phosphorus region in Fe-P phase diagram has been of interest, in historical context. While in modern steel making processes, the phosphorus content is usually controlled to less than 0.04% (Balasubramaniam 2003), archeological bloomer iron artifacts contain relatively higher phosphorus contents (0.05–0.5%) (Kumar and Balasubramaniam 2002). For example, the Indian iron samples from several archeological excavations indicate relatively high phosphorus content (Balasubramaniam 2000). Similarly, ancient European iron posses relatively high phosphorus content (Gerry 1989). This may be related to a more uniform distribution of P in these alloys. Phosphorus causes non-uniformity in the modern steels, mainly in the cast iron. This non-uniformity of phosphorus in steel leads to deterioration in mechanical properties.

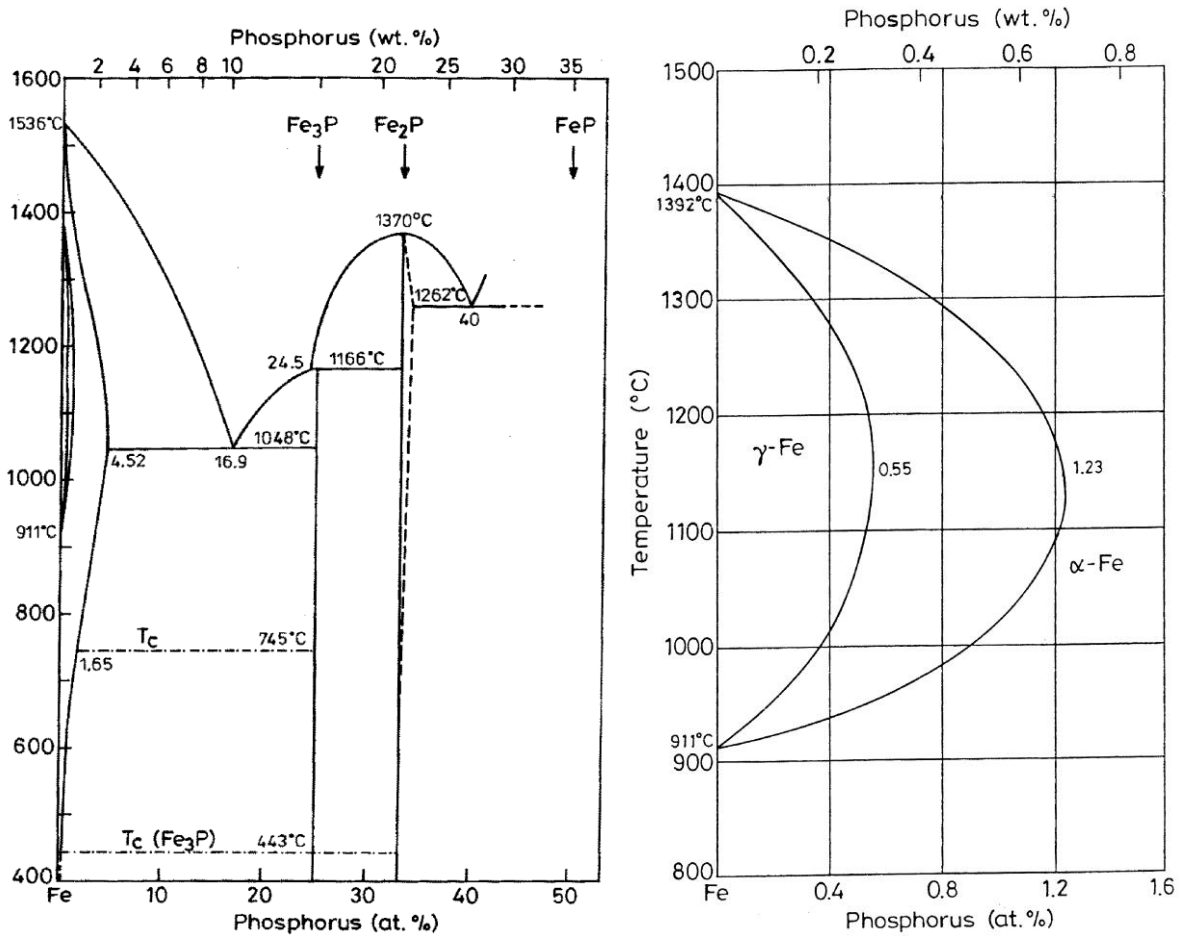

Figure 2.1: (a) Iron-phosphorus phase diagram, (b) High-temperature γ region (Kubaschewski 2013).

The high-temperature region of the Fe-P phase diagram for low phosphorus Fe-P alloys has been established by Vogel 1929. This is shown in Figure 2.1(b). The phase diagram shows a gamma loop. The (α+γ) region exists between austenite and ferrite phase fields in the temperature range 910 to 1400 ^{o}C. The phase boundaries are shown by the solid line in Figure 2.1(b). The phase diagram indicates that the phosphorus is an alpha phase stabilizer. Kubaschewski 2013 has proposed the Fe-P phase diagram as shown in Figure 2.1(a).

2.2 Fe-P ALLOYS

The presence of phosphorus has been found in the ancient Indian iron (Balasubramaniam 2000, Goodway and Fisher 1988). Its high content in ancient Indian iron shows the superior atmospheric corrosion resistance. An example of high P content in wrought iron is Delhi iron pillar which has attracted researchers (Kumar and Balasubramaniam 2002). Balasubramaniam 2000 has reported the content of phosphorus ranges from 0.05 to 0.50 wt. % in the ancient irons. The thermodynamic analysis has been carried out to detect the origin of high P contents in the archeological Indian steels (Kumar and Balasubramaniam 2002).

Since, the phosphorus is normally considered an undesirable impurity in steels (Lindskog 1973, Ehrenreich 1986). It causes cold shortness and hot shortness in ferrous alloys (Liu and Rana 2014; Balasubramaniam 2000). It may also lead to grain boundary failure due to segregation of phosphorus (Balasubramaniam 2000; Lindskog 1973; Liu and Rana 2014). For these reasons, the amount of phosphorus is limited to 0.04% in the majority of steels (Balasubramaniam 2000). Also, Liu and Rana 2014 have reported that the upper limit of phosphorus is restricted to 0.01% or even 0.005%. Lindskog 1973 has investigated that the less amount of phosphorus content in iron showed the improved properties in conventional powder metallurgy processes.

In spite of that Gerry 1989; Kumar and Balasubramaniam 2002 have found the very low carbon content in the most of ancient steels. The low carbon contents were detected in ancient steels because the iron was not kept for sufficient time during its extraction in the bloomer furnace (Tholander 1989), while higher phosphorus contents were obtained due to the absence of limestone in the charge of the ancient bloomery furnaces (Kumar and Balasubramaniam 2002).

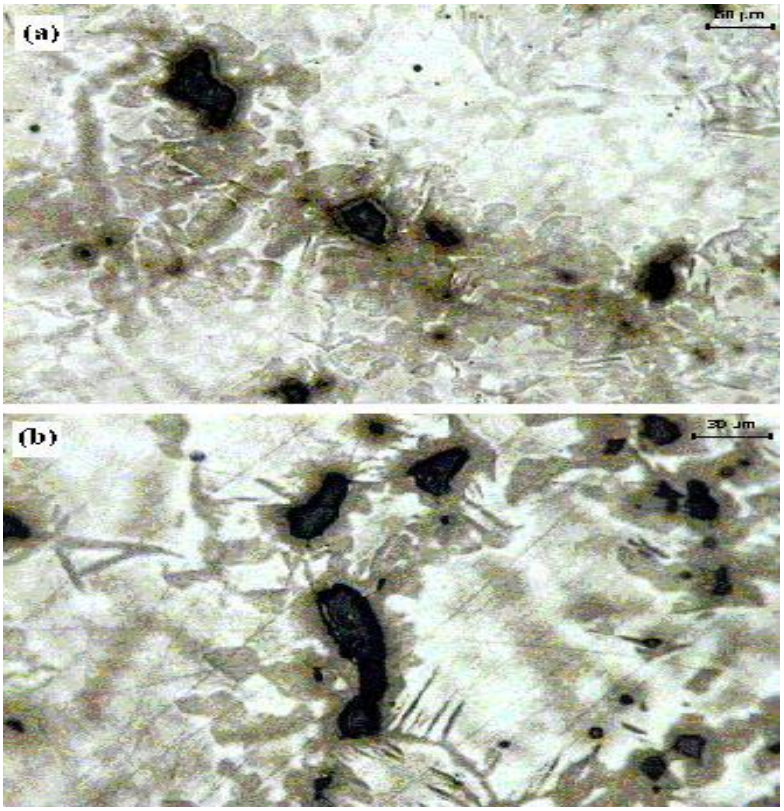

Figure 2.2: Microstructure of the ancient iron. The dark regions show phosphorus (Kumar and Balasubramaniam 2002).

In addition, few volume percentage of entrapped slag inclusions have been observed in the ancient irons as shown in Figure 2.2. Also, the segregation of P has been observed in ancient irons as shown in Figure 2.3 at microscopic (as opposed to macrosegregation observed during solidification) level in nature. This is due to solid state processing of the ore using bloomery furnace.

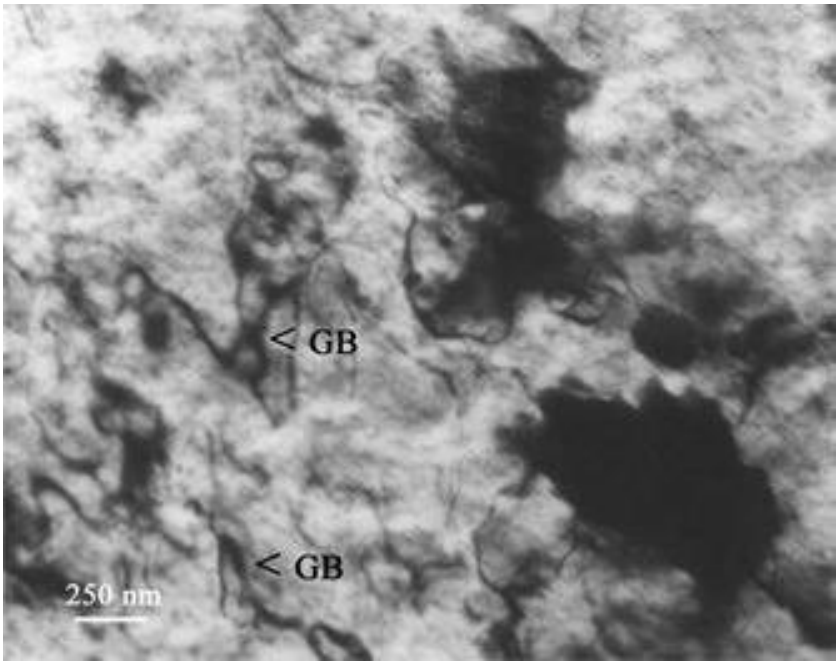

Figure 2.3: SEM micrograph showing the irregular shape of the slag phase along grain boundaries. A few such boundaries are indicated by GB (Kumar and Balasubramaniam 2002).

In bloomery furnace, the iron ore is extracted without melting. The micro segregation of phosphorus occurred in the ancient iron due to local dephosphorization (Kumar and Balasubramaniam 2002, Gordon 1988).

2.3 MANUFACTURING OF Fe-P ALLOYS

Phosphorus is known to be an undesirable element in the steel. In melting and casting, the last molten alloy liquid to enrich with phosphorus during the solidification leads to grain boundary decohesion. Therefore, it is a very difficult task to design and develop the iron-phosphorus alloys for the engineering applications. As per the literature available, there are various methods by which these alloys can be developed. However, mainly two processes are used for the same as below:

1. Melting and casting route
2. Powder metallurgy route

2.3.1 Melting and Casting Route

P exhibits strong segregation along the grain boundaries during solidification in the cast steels which lead to failure due to embrittlement. Due to this, the content of P is limited to the maximum up to 0.05% in the majority of steels. Therefore, this process may not be suitable for the development of high P content alloys.

2.3.2 Powder Metallurgy Route

The uniqueness of P/M is its ability to form complex shape components in a single pressing and single sintering step with high production volumes and low material waste. Also, the segregation like in the melting and casting route does not take place in PM process. Application of P/M is growing due to its cost competitiveness against other processes. Ferrous structural parts constitute almost 70% of the total P/M parts produced globally. When it comes to the P/M steels, about 80% of the raw material for the powder production is coming from the scrap recycle. This makes it even more resource efficient and overall a sustainable manufacturing process (Sundaram et al. 2017). Nagesh et al. 2014 have used the powder metallurgy technique for manufacturing of friction material (Brake pad).

For P/M manufacturing processes to remain competitive and have an advantage over other manufacturing processes such as casting, it is necessary to improve the process continuously in order to increase the current density levels and improve the properties, while maintaining the advantage of P/M as net-shaping or near-net-shaping technology. For high-performance applications, this can be done by a number of ways as shown in Figure 2.4.

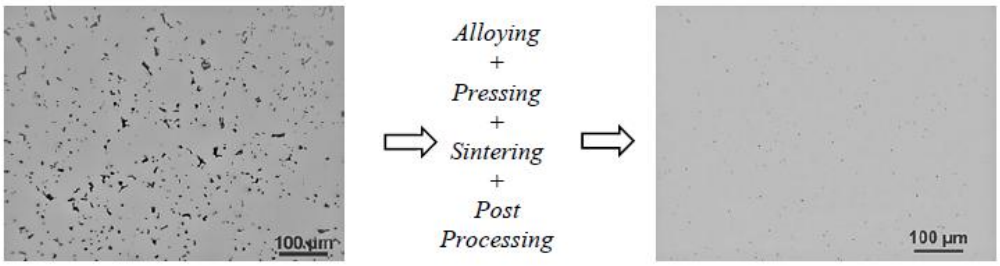

Figure 2.4: Optical micrograph of polished P/M steel with porosity (left) and full dense (right) (Sundaram and Maheswaran 2017).

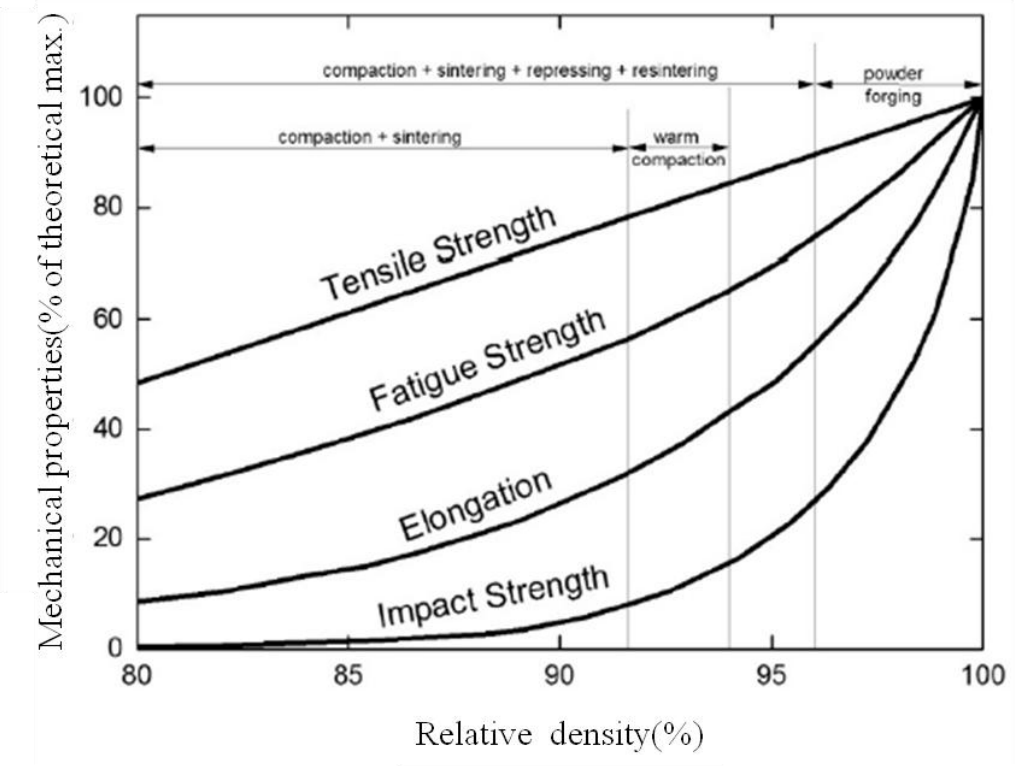

Figure 2.5: Mechanical properties vs. the relative density of P/M steels with different processes (Höganäs Höganäs Handbook for Sintered Components-3).

Table 2.1: Comparison of P/M and other manufacturing process (Randall 1998)

Manufacturing process	Advantages	Disadvantages
Casting	The widely used technique, a variety of part size, low setup and tooling cost	Not useful for many materials, flashing, pores, chemical segregation, parting line.
Cold Forging	Faster production, higher strength, good surface finish	Lower precision, shorter tool life, limited materials.
Extrusion	Long size parts, good surface finish, rapid production	Consumption of high energy, low precision, simple shapes, short life of the tool.
Hot Forging	Better mechanical properties, complex parts, high production rate.	Material waste, difficult to dimensional control, tool wear higher.
Machining	Used in industry, high precision, short lead time, production volumes less.	Waste, productivity low, non-uniform properties, high-cost labor cost.

There has always been some competition between metalworking technologies. Each production route is entrusted with improving and pushing capabilities to secure better quality, performance. A summarized comparison of powder metallurgy with other production technologies is given in Table 2.1. With the given features in Table 2.1, powder metallurgy has come out as a continually and rapidly evolving technology which embraces most metallic elements and it is now a highly developed method for making ferrous and nonferrous parts with good reliability. Figure 2.5 shows the variation in mechanical properties for different powder metallurgy processes. Figure 2.6 shows the process route of powder metallurgy. However, one of the principal limitations of classical powder metallurgy route (compaction and sintering) is their inherent porosity which affects the mechanical properties significantly. The existence of pores in parts developed by powder metallurgy degrades its mechanical properties and performance (Chawla et al. 2005). It is unsuitable for heavy duty applications.

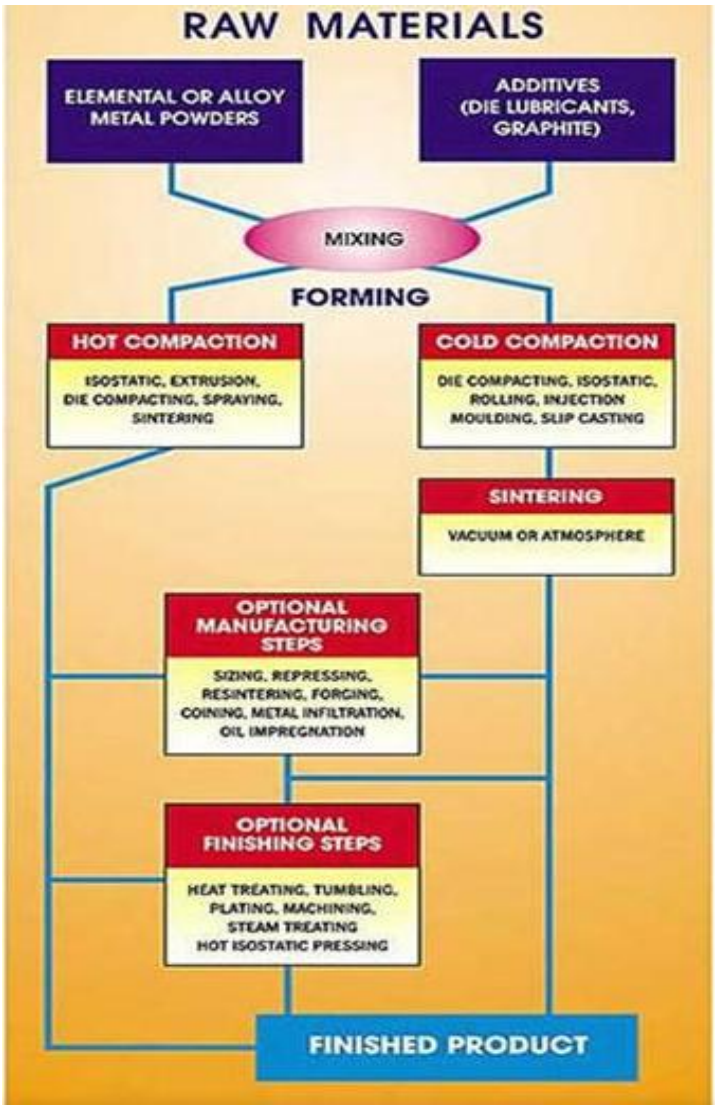

Figure 2.6: Process route of powder metallurgy (Weblink 1).

Advantages of P/M technique are as below (Weblink 1):

- It may be applied to all types of materials.
- Requires low processing temperature.
- Uniform and highly homogeneous structures may be obtained.
- Components with precision can be developed.
- High production rate.
- The machining and grinding operations are not required.
- There is no scrap.

(1) Iron powders

Iron powder is made by sponge iron process, atomization processes, and electrolysis. The size of particles varies in the range 20-200 μm. Their properties depend on the production method. The iron powders are classified as: atomized powder, reduced iron powder, and electrolyte iron powder. The physical appearance of reduced iron powder is different from atomized iron powder.

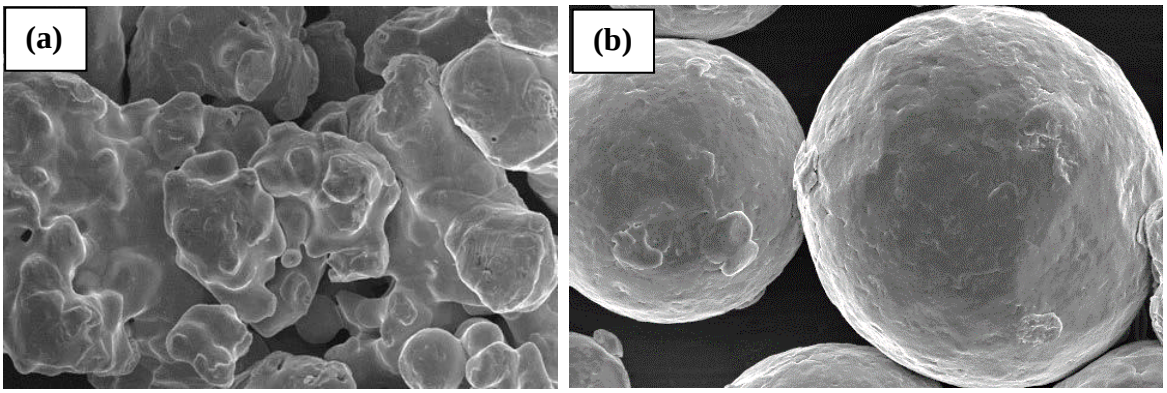

Figure 2.7: SEM micrographs showing typical powder morphology of (a) water and (b) gas atomized powder (Weblink 1).

The powder morphology varies with the production method, which produce irregular and spherical shaped powder particles when water and gas are used, respectively. The powder morphology of water atomized powders is irregular in shape (Figure 2.7 a) which is suitable for compaction since their shape helps in the better interlocking of the particles after pressing, which contributes to the green strength of the product.

In the atomization process, the molten metal or alloy is injected through a small orifice and the emerging liquid stream is broken into fine droplets by a jet of air, steam or inert gas. The fine droplets, when cooled form fine particles of varied shapes. The particle size formed

depends on the size of the orifice, temperature of the metal, pressure or velocity of the atomizing gas stream etc. Atomization produces finer powders with a spherical shape and smooth surface

Gas atomized iron powders typically have spherical morphology as shown in Figure 2.7(b) and exhibit good flow ability, but are difficult to be uniaxially compact. Water atomized powder is covered by thicker oxide layer depending on alloy composition and hence it may be subsequently annealed in reducing atmosphere to remove oxides and to achieve good compressibility. After the annealing, the powder surface is covered by a thin oxide layer of the base metal with the presence of the low amount of oxide particles. The thin oxide layer is basically a result of the contact of the powder with air after annealing. Depending on the alloying elements present, the surface features will be enriched accordingly. In case of gas-atomized powder, additional annealing procedure is not required as powder possesses high purity after atomization.

(2) Compaction

Uniaxial compaction is the most common method of densification in P/M steels. Water atomized powder admixed with lubricant and graphite is filled in the die cavity and pressed by the axial movement of the punches (Höganäs Handbook 2). The compaction pressure generally ranges between 400 to 1000 MPa. During the powder pressing, the metal particles will rearrange with the pressure exerted by the punches and interlocking between them occurs due to their irregular shape. Sometimes even cold welding of the particles can take place at high pressures. This gives the compact sufficient green strength for further handling. There will be a density gradient after pressing due to the difference in pressure distribution because of the moving punches and solid die. This density gradient is especially created in the surface region along the compaction direction owing to the frictional resistance at die wall, while it is much less pronounced inside the compact. The compaction presses are either mechanical or hydraulic with multilevel punch movements. For the multilevel components (e.g. synchronizer hubs, oil pump gears, etc.), in order to have the uniform densification and to avoid variation in density among different sections, the punches move relative to one another according to the density requirements of different sections in the component (Höganäs Handbook 2). The final properties of the P/M component obtained heavily depend on this stage of the process (Sundaram 2017).

The mechanism of densification depends on the material and structural characteristics of powder particles. Mostly, the less compacting pressure is needed for coarse powders in

comparison to fine powders. It has also been found that less compacting pressure is required for smooth powders of spherical shapes than irregular shape powders. Regarding compressibility, more compacting pressures are needed for hard powders with respect to soft powder and to obtain equal densities in the product (Sundaram 2017).

(3) Sintering

Sintering imparts necessary strength to the component by creating bonding between the metal particles. Figure 2.8 shows the sintering sequence on a microscopic scale. Sintering is usually performed below the melting point at roughly 75-80% of the melting temperature. Through the mass transport between the adjoining metal particles, the inter-particle necks are developed.

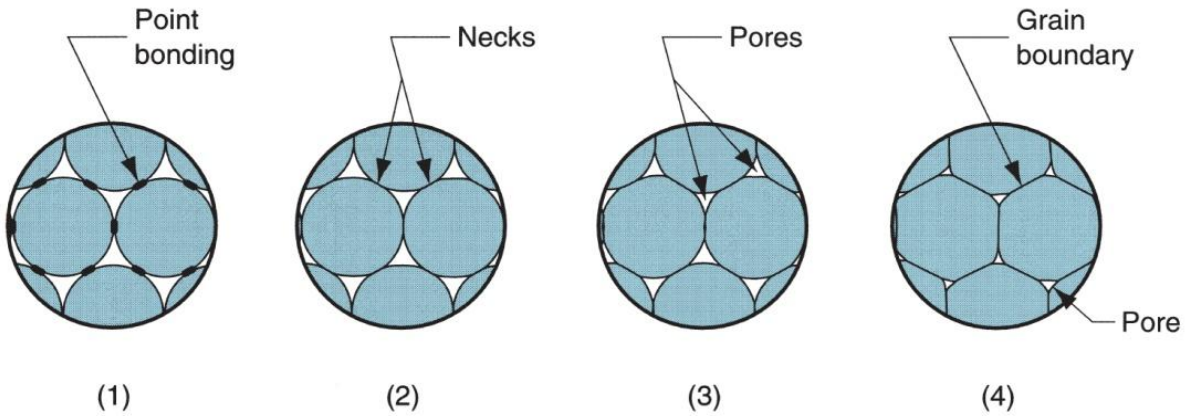

Figure 2.8: Sintering sequence on a microscopic scale (Höganäs Handbook 2)

The degree of sintering is determined by the number and strength of the established sinter necks. Formation and growth of inter-particle necks are enabled by early and efficient reduction of the surface oxides covering the powder. Sintering in reducing atmospheres removes the surface oxides. Admixed graphite also plays an extremely vital part during deoxidation by reducing the oxides through direct and indirect carbothermal reduction mechanisms. In P/M steels, endo-gas is the most commonly used sintering atmosphere. When it comes to Cr-alloyed P/M steels, N_2-10%H_2 is used as a processing atmosphere for reducing oxides. During cooling, endo-gases provide carbon restoration but not with Cr-alloyed P/M steels. Hence, carbon control during sintering is vital in order to reach the required properties. Studies on lean sintering atmospheres containing carbon monoxide have shown that the CO acts as both reducing-oxidizing and carburizing-decarburizing agent (Sundaram and Vattur 2017). This implies that proper control of the atmosphere during sintering is extremely critical for robust P/M steel processing and also for tailoring the sintered properties. Apart from solid state sintering, which mainly contributes to the strengthening of P/M steel, liquid phase

sintering can be applied to improve densification. This can be applied to improve densification during sintering without changing conditions on the compacting stage.

(4) Densification processes

For the continuous progress of P/M industry, the trend towards reaching higher relative density levels should be emphasized. There has been an increasing trend in the usage of high-density P/M steels over the last decades (Narasimhan 2001). Through improvements and innovation in alloy design, machine development (compaction techniques) and liquid phase sintering, a significant increase in the density and overall material properties has been demonstrated (Narsimhan 2001). To sustain the future development of P/M and competitiveness with the other manufacturing processes, reaching full or near-full density is a key factor. There are various processes within the P/M field that can be used alone or in combination to achieve increased density levels (Rutz and Hanejko 1994; Hanejko 2010). These processes can be classified into compaction-based, sintering-based and hybrid approaches. Some of the important methods are given below.

- Warm die compaction process
- Cold isostatic pressing process
- Hot isostatic pressing process
- Powder forging process
- High-temperature sintering process
- Liquid phase sintering process
- Additive manufacturing process

Warm Compaction

In this process, both die and powder are preheated to a temperature of 130-140 °C at which compaction is performed. Here, densities of up to 7.3 g/cm^3 for ferrous material can be achieved.

Warm die compaction process

Unlike warm compaction, only the die is now heated and the powder remains at room temperature. This procedure allows for an increase in productivity and decrease in process cost. However, lower density levels are achieved in comparison to the warm compaction.

Cold isostatic pressing process

In this process, the pressure is applied uniformly at room temperature through pressurizing medium like liquid or air. The process can be either the wet bag process or dry bag process, depending on how the moulds are used. In the wet bag process, a flexible rubber mould is filled with powder which is then sealed and evacuated. The mould with powder inside is further placed directly in the cold isostatic pressing (CIP) chamber and exposed to the pressurizing liquid. In the dry bag process, the flexible mould is fixed within the chamber and is filled with powder before each compaction cycle. The CIP is highly advantageous with regard to the component size, cheaper mould price (in comparison with HIP) and the ability to achieve homogeneous density distribution without the need for lubricants. These features make CIP an attractive consolidation process (Yamamoto et al. 2010). Due to the isostatic pressing, the density variation inside the component being small reduces the distortions during sintering (ASM Handbook Vol 07, German 1998).

Hot isostatic pressing

Hot isostatic pressing (HIP) involves simultaneous application of pressure and temperature onto a metallic container encapsulating the powder or components containing porosity in order to reach full densification. This process is used to eliminate pores, defects and also for heat treatment of cast parts, powder consolidation, densifying ceramic and metal parts, material joining, infiltration and densification of powder-based components (Richter et al. 1985). The consolidation in the HIP is usually done by having powder filled into a capsule of the required dimensions made of similar material. The capsule is further evacuated, sealed and placed in the HIP. Upon HIP, the powder is densified into a single part with the help of high pressure and temperatures. The densification is governed by yield, creep and final diffusion process. The main advantage of the HIP is the very large components with high length to diameter ratio that can be HIP-processed, otherwise difficult/impossible to realise by means other alternative techniques as e.g. die pressing (Richter et al. 1985).

The sequence of stages involved before the HIP consists of the preparation of the capsule, filling with powder, welding, evacuation, and sealing. After the HIP process, the capsule has to be removed. Hence, this process is more time consuming and not economical for mass production. However, the recent development of the HIP furnace systems with the combination of rapid cooling and quenching not only reduces the HIP processing time but also means that the heat-treatment and hardening processes can integrate into the HIP run.

Powder forging process

In this process, the compact either in green, pre-sintered or sintered state is hot forged into a final fully-dense component (ASM Handbook Vol 07). A Relative cost for various die compaction processes is shown in Figure 2.9. Almost all the automotive connecting rods, produced nowadays, are processed through powder forging. Since powder forging is principally applied as consolidation technique (Adkins and Tsakiropoulos 1991) for the powders in the present study, the details about this process are given in the coming section.

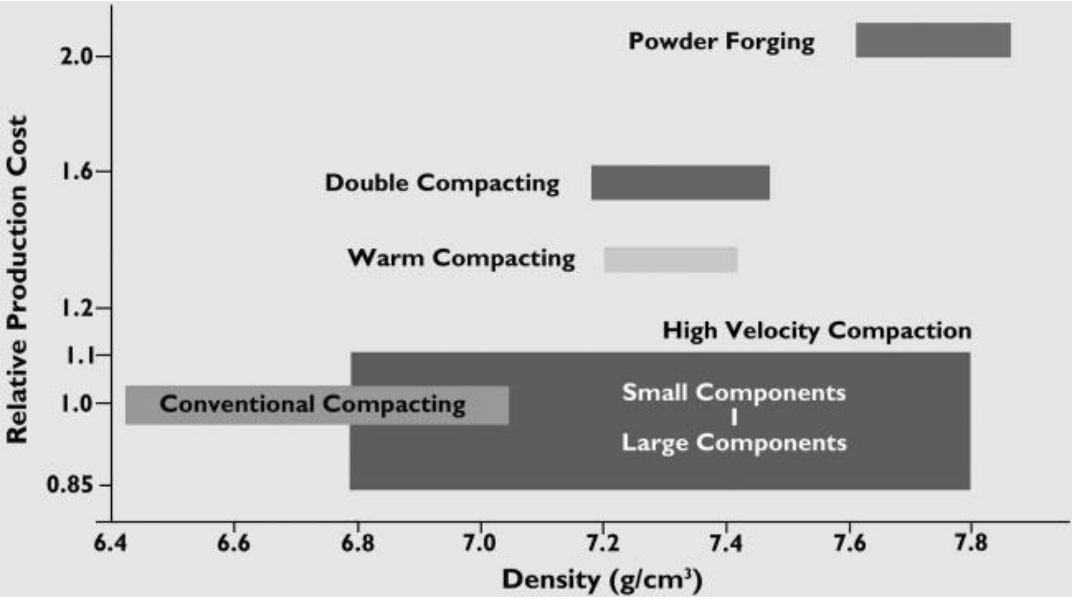

Figure 2.9: Relative costs for various die compaction processes (Whittaker 2007).

High-temperature sintering process

Sintering at around 1120 °C is a standard industrial practice for the majority of P/M components, the reasons being that industrial belt furnaces are limited in use to around such a temperature, while there is also a concern not to apply too high temperature to maintain proper tolerance control of sintered parts. Sintering at higher temperature is, however, beneficial for more efficient oxide reduction since the equilibrium for oxide reduction is shifted with increasing temperature. This fact is of particular importance in the case of P/M steels containing alloying elements like Cr, Mn, and Si all prone to form stable oxides. At higher temperatures, lattice diffusion becomes also significantly improved and this fact plays a major role in alloy homogenization, which is important in particular for the case of admixed and diffusion alloyed P/M steels. Another important effect of the high-temperature sintering is the rounding of the pores and strengthening of the inter-particle necks owing to e.g., improved oxide reduction, which results in a significant improvement in the strength, especially fatigue

properties of P/M components (Dlapka 2010). The drawback with high-temperature sintering may be that there is some more marginal shrinkage during sintering and hence dimensional control could be worse.

Liquid phase sintering process

Liquid Phase sintered components account for ~70% of all the sintered goods which includes low alloyed steels, tool steels and especially hard metals (Tandon and Johnson 1998). Liquid phase sintering (LPS) is a well-known method to achieve densification through the addition of low melting alloys or elemental powder that melts below the sintering temperature. The densification is hence assisted by liquid phase formation. The LPS is employed mainly in the case of high-speed steels, tool steels, and hard metal, where the necessity for LPS is realized to its full potential. With respect to low alloyed ferrous P/M steel components, LPS is not a dominant process. For ferrous P/M, the liquid phase formers are added either in the form of elemental mix or as a master alloy.

Introducing elements through master alloy addition in order to obtain a liquid phase at a temperature well below the sintering temperature is the principle objective of this approach. There exist two phenomena: shrinkage or expansion which occurs depending on the solubility of the base material in the liquid or the liquid in the base material. Hence, the selection of the activator or the liquid phase forming additives should be such that it does not extensively dissolve in the base material for shrinkage to occur.

The amount of liquid phase can be estimated from the corresponding phase diagram based on the amounts of alloying elements present. The initial powder size has a significant effect on the particles rearrangement during sintering. The master alloy system which has a melting point much below the sintering temperature will start to melt and spread around the base metal particles due to capillary force, as well as along the grain boundaries, which aids in particle rearrangement. For irregular particles during initial rearrangement, there will be rapid shrinkage as the contact between the particles is not perfect and the liquid starts to fill the pores (Exner and Clemens Mueller 2009). The final stage of sintering pertains to pore elimination, grain coarsening and strengthening on inter-particle necks. One critical consideration during sintering is the preservation of the dimensional stability of the component.

Master alloy additions to P/M steels were studied by Zapf et al. 1975 at the beginning of the 70's using Mn-Cr-Mo additions. They found better mechanical strength considering the least addition of each alloying element. Master alloy in ferrous P/M steel has been widely studied before using different alloying additions, especially based on phosphorus and boron

compounds, which form eutectic at low temperatures. Boron addition is of special interest and is addressed in this work.

Additive manufacturing process

Additive manufacturing (AM) involves adding the material layer by layer required for building a component. The AM offers flexibility in manufacturing, as components with complicated features and shape can be manufactured. It contributes to lower material waste. Powder bed process with the utilization of the focused energy source as electron or laser beam is commonly used for layer by layer fabrication of structural components to its final dimensions. The powder is locally melted using an electron beam or laser beam when it moves along and fuses the powder after every layer of spreading.

(5) Scope of Powder metallurgy components

The enormous growth has been successfully bringing about using ferrous powder metallurgy (P/M) component in various areas. The segments of the market in P/M industry and market trends in Western European P/M industry are given in Table 2.2 and 2.3 respectively. This technology is ensuring itself as a minimum cost alternative process rather than to machining, casting, stamping and other similar metalworking technologies. The advancement in technology through powder production, alloy development, lubricants, and parts production has enhanced the growth of P/M market in the world as shown in the Figure 2.10.

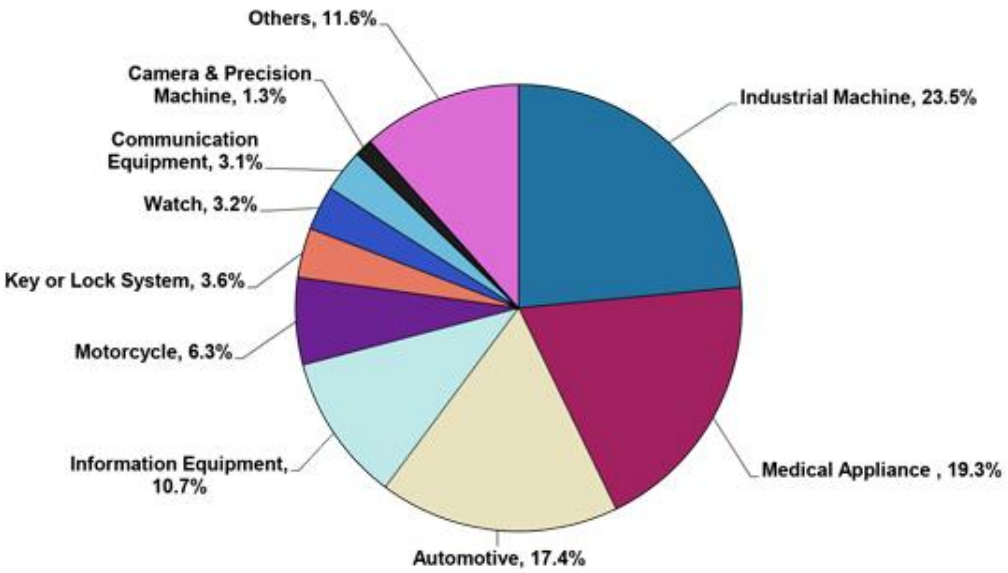

Figure 2.10. P/M part industries in the various segments (Weblink 2)

The huge scope of P/M components are in the industrial machine and in medical appliances. Next major demand of P/M components are in automotive components like cam-followers, connecting rods, camshaft lobes and components for the variable camshaft. Synchronizer hubs and rings, shift forks and clutch hubs for transmissions break shoe, gears, fuel injectors, oil pump gears etc. as shown in the Figure 2.11. Other applications of ferrous P/M components are being used in the different field such as information devices, keys, locks, watches etc.

Figure 2.11. Automotive P/M components (Loberto et al. 2010; Ramakrishnan 2013).

Table 2.2: Segments of the market in P/M Industry (PM94 World Congress).

Segment	Production 2000 (tonne)	Annual growth 1985-1990 (%)	Estimated growth 1991-2000 (%)
P/M components, bearings and friction materials (85% ferrous, 15% non-ferrous, ~55 manufacturers)	>135000	3-5	4-7
Hard metals (32% cutting tools, 12% rock drills, 56% wear parts, ~80 manufacturers)	6250	0--.5	0.5-2
P/M semi products (HSS, tool steels, superalloys, light metals, metal matrix composites)	6250	0--.5	0.5-2

Table 2.3: Market trends in Western European P/M Industry (P/M94 World Congress)

Application	P/M parts per car, kg		Total P/M parts production, tone	
	Actual	Theoretical	1993	Theoretical
Automotive engine				
Oil pump	0.5	0.5	6000	6000
Pulleys	1.2	1.2	14400	14400
Camshaft	0	0.4	0	4800
Valve guides	0.1	0.4	1200	4800
Valve seats	0.1	0.4	1200	4800
Cylinder linings	0.1	0.3	1200	3600
Connecting rods	0	2.0	0	24000
Starter/ generator	0.05	2.0	600	24000
Main bearing caps	0.1	1.5	1200	18000
Total	0.05	0.5	600	6000
Transmission	2.2	9.2	26400	110400
Synchronising parts				
Gears	1.2	1.5	14400	18000
Power steering, ABS	0	1.5	0	18000
Locks and seat belts	0.3	0.6	3600	7200
Shock absorbers	0.2	0.3	2400	3600
Total automotive	0.8	0.8	9600	9600
Appliances and power tools	4.7	13.9	56400	166800
Agricultural machines	…	…	9000	23000
Office machines	…	…	4000	16000
Small electric motors	…	…	2000	5000
Other applications	…	…	400	5000
All applications	…	…	2200	4200
	…	…	74000	220000

2.3.3 Powder Forging Process

Powder forging is an economical method (if large numbers of parts are produced) of producing components directly from metal powders. Therefore, it is currently of arousing interest in many parts of the world. Forging is the working of metal into a useful shape by hammering or pressing. The two broad categories of forging processes are open-die forging and closed-die forging. Open-die forging is performed between flat dies of simple shape where as the workpiece is deformed between two die halves in closed-die forging (Dieter 1986). Forging denotes a family of processes by which plastic deformation of the workpiece is carried out by compressive forces. There are two basic forms of powder forging (Serope and Schmid 2003):

- Hot upsetting
- Hot repressing

Powder forging (P/F) is applied to develop components without internal porosity. The conventional P/F process consists of four steps. Among four steps first two are the similar to normal P/M processing. In the first step, a preform is pressed as a conventional P/M compact. The preform is sintered in the second step with attention paid to the reduction of non-metallic inclusions. The sintered preform is then reheated and placed in the die of the forging press. In the fourth step heated preform is forged to get full density. The other modes of the powder forging processes are hot upsetting and repressing powder forging.

In hot upsetting, the perform experiences a significant amount of lateral material flow while in the re-pressing material flow during densification is mainly in the direction of pressing. These two deformation modes and the stress conditions are shown in Figure 2.12.

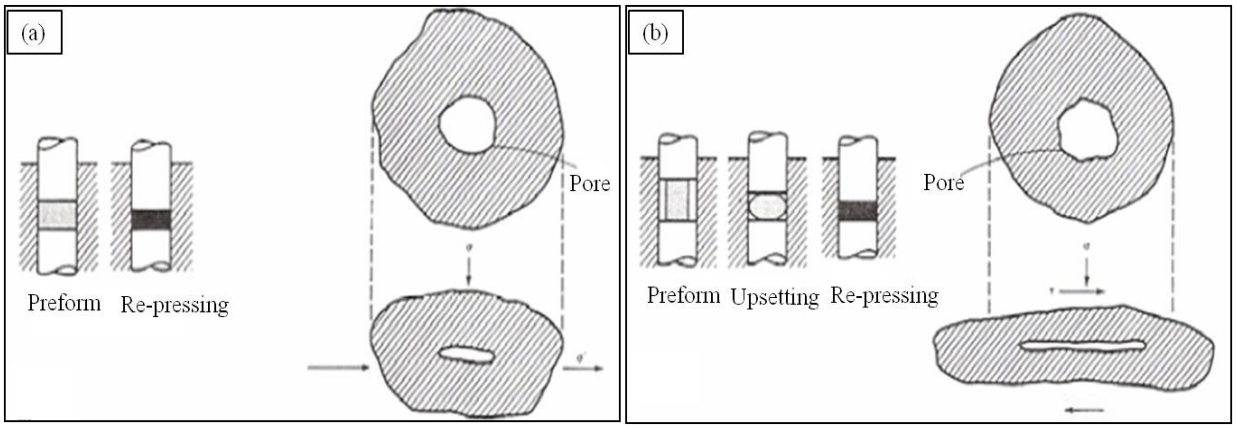

Figure 2.12: Forging mode and stress conditions on pores for (a) repressing (b) upsetting (James 1994).

In the first mode of powder forging, the pores are surrounded by the combination of normal and shear stresses due to the excessive unconstrained lateral flow of material. As a result, a spherical pore becomes flattened and elongated in the direction of the lateral flow. The sliding motion due to shear stress breakes up any residual inter-particle oxide films which may lead to strong metallurgical bonding across collapsed pore interfaces.

The second mode of powder forging consists of a small difference between vertical and horizontal stresses. It minimizes material movement in the horizontal direction and limits in the lateral flow. As densification proceeds, the stress condition approaches a pure hydrostatic condition. The pore is typically flattened, and the opposite sides of the pore are brought together under pressure. The second mode of powder forging requires higher forging pressures than the first mode of powder forging for comparable densification. The movement of interparticle in the second mode decreases compared to the first mode of densification which may reduce the tendency to break up any residual interparticle oxide films and as a result in lower ductility and toughness (James 1994; James 1968). There are three principal parameters of powder forging which include performing density, forging temperature and the applied force.

The conventional powder forging process consists of four steps:

1. Mixing of the powder
2. Compacting
3. Sintering
4. Forging

The determination of optimal parameters on the powder forging process is very important (Park et al. 2002; Hirschhorn 1976).

Densification mechanism in powder forging

Heating of powder prior to forging causes cleaning of the powder surface and improves the workability of the porous preform. During forging considerable shear deformation is involved since the preform is in a different shape from the forging. Pore closure takes place in the powder forging mainly due to the plastic collapse of pores and material flow into the pores. Diffusional flow, particle sliding, rotation, revolution, and dislocation motion also contribute to densification.

Advantages of powder forging process

The following advantages can result from the use of the powder forging processes:

- Simplified forging route
- Improved detail and surface finish
- Material saving
- Machining saving
- Weight control
- Superior in respects of directionality
- Homogeneity greater
- Refinement of microstructure
- Absence of internal discontinuities (Balasubramaniam 1995)
- Dimensional consistency may be achieved
- Reduction of a number of steps for producing components(Raghavan 2000)
- Reduction of scrap due to the elimination of flash and secondary machining operation.
- Reasonably high density can be obtained and the mechanical properties of P/M parts are comparable to the wrought product (Raghavan 2000)

Disadvantages and limitations of powder forging process

- Component size is currently limited
- Production costs are higher than conventional

Mechanical properties

Comparing the density data with P/M for FLN2-4405(Fe-0.85Mo-2.0Ni-0.6C) shows a strong linear relationship between mechanical properties and density. The yield and tensile strength increase with density when processed under similar cooling conditions as shown in Figure 2.13. The properties are independent of the processing route (Marucci and Rawlings 2004).

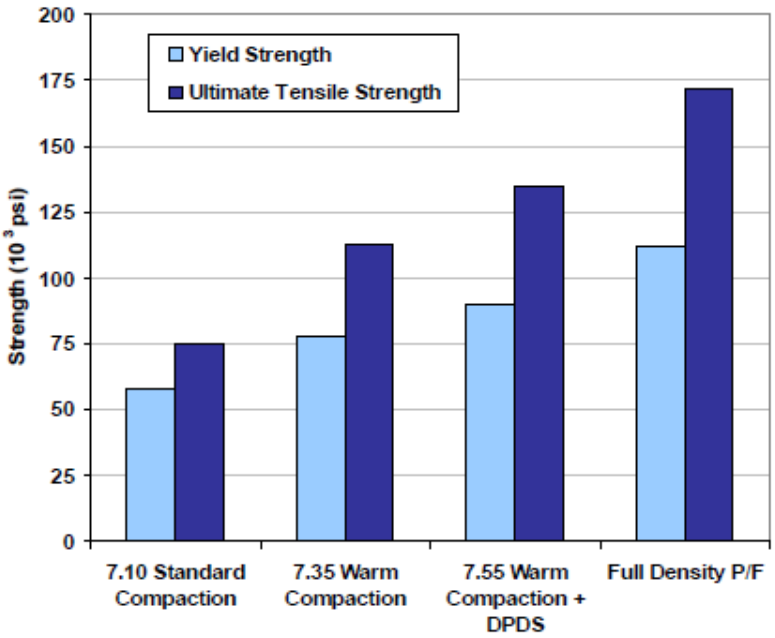

Figure 2.13: Comparison of tensile and yield strength of FLN2-4405 over a range of densities (7.10, 7.35 and 7.55 g/cm^3). All samples processed in the sintering furnace cooled condition (Marucci and Rawlings 2004). DPDS refers to double press and double sintering process.

Figure 2.14 shows a similar trend for the elongation, however, the increase in elongation from a density of 7.55 g/cm^3 to full density departs from linearity and increases substantially (Marucci and Rawlings 2004).

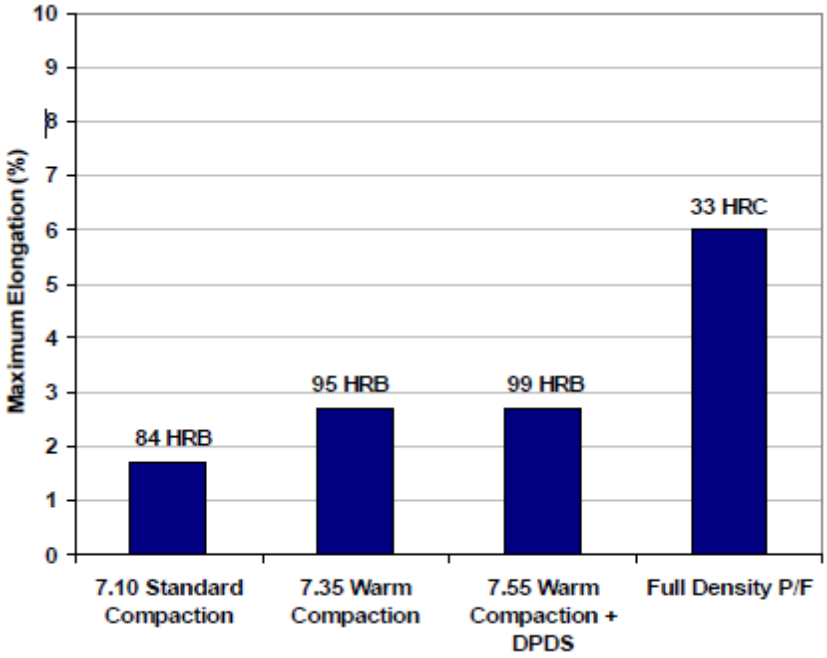

Figure 2.14: Comparison of maximum elongation and apparent hardness of FLN2-4405 over a range of densities. All samples processed in the sintering furnace cooled condition (Marucci and Arthur 2004)

An accurate comparison between powder preform forging and other densification technique can be made only on the basis of a selected part and its service requirements. Huppmann and Hirschvogel 1978 have made an attempt to list all potential competitive processes, (Table 2.4) and compared them with powder preform forging. They have concluded that the powder preform forging is well defined among all the densification processes as listed in Table 2.4.

Table 2.4: Comparison of powder forging with competing technologies (Huppmann and Hirschvogel 1978).

Process	Powder preform forging	Sintering	Die forging	Cold forging	Precision casting
Part weight, kg	0.1-5	0.01-1	0.05-1000	0.01-35	0.1-10
Height/ dia.	≤1	≤1	Not Limited	Not limited	Not limited
Shape	No large variation in crossection, openings limited	No large variation in crossection, openings limited	Any, openings limited	Mostly of rotational symmetry	Any, any openings possible
Material utilization,%	100	100	50-70	95-100	70-90
Tolerances	IT 8-10	IT6-8	IT13-15	IT 7-9	IT 8-10
Surface roughness,µm	5-30	1-30	30-100	1-10	10-30
Production begins to become economical at number of parts (for 0.5 kg/part)	20000	5000	1000	5000	2000
Main goal	High strength no machining	Moderate strength, porous materials, no machining	High strength, machining to final shape	High strength, minimal machining	Intermedia te strength, minimal machining
Cost of one production unit (sintering =100%)	250	100	150	150	100
Possibilities for automation	Good	Good	Limited	Very good	Limited
Price, $DMkg^{-1}$	4-5	3-4	3	4	6

2.4. MECHANICAL PROPERTIES

It has been found that the addition of phosphorus to pure iron increases the tensile strength, at the expense of ductility. The grain refining effects and increase in tensile strength due to additions of P were found to be very significant (Islam et al. 2011). Kang et al. 2016 has made an investigation on grain boundary strengthening in steel and reported that yield strength is increased by reducing the grain size. Phosphorus improves the strength and hardness by sacrificing the elongation and area at the failure. Very high phosphorus contents promote brittle behavior. Phosphorus causes solid solution strengthening (Rana et al. 2006), similar to carbon and nitrogen (Stewart et al. 2000). Norman and Tsakiropoulos 1992 studied the strengthening mechanism in powder metallurgy alloy. They have suggested that among various strengthening mechanism, solid solution strengthening is a major contributor towards strengthening the alloy. Cold working also results in marked work hardening in iron (Tylecote 1986). In the ancient time, tools were developed using phosphoric steels successfully.

If low alloy steel containing phosphorus is heated in the temperature range of 350 to 600 ^{o}C, there is a loss in toughness (Stewart et al. 2000). This is noted in tests conducted at room temperature. This is referred to as temper embrittlement. Low alloy steel is used in the petroleum and power generation industries which exhibit premature intergranular cracking following exposure in the temperature range of 450-600 ^{o}C. If Fe-P alloys or phosphorus containing low alloy steels are not cooled very slowly or not exposed to low temperatures in the range of 250-600 ^{o}C for long times, they would not display brittle behavior.

Impurity atoms, such as P, As, Sb or Sn, lead to temper embrittlement (Krahe and Guttman 1973; Capus 1968). These impurities segregate to grain boundaries and decrease cohesive energy. Molybdenum, Vanadium, and tungsten cause embrittlement in steel when added above a certain concentration. The embrittlement of P manifests itself by a change in the brittle fracture mode from cleavage to intergranular mode, decrease in the impact fracture energy (Dumoulin et al. 1980; Guillou et al. 1981). For every 0.01% addition of phosphorus, ductile to brittle transition temperature increases by 70 ^{o}C (Correa et al. 2009; Correa et al. 2008). Therefore, during cold working of steel (below 500 ^{o}C), the steel will be brittle if the ductile to brittle transition temperature falls below the cold working temperature. The increase in temperature from ductile to brittle transition has been observed with both carbon and phosphorus. The addition of Mn increases strength as well as lowers transition temperature. This counteracts the effect due to the presence of carbon. The manganese to carbon(C) ratio in

mild steel should be at least 3:1 for satisfactory notch toughness (Correa et al. 2009; Correa et al. 2008).

According to Abbasi et al. 2007, the brittle and intergranular, steadite (10.2% of phosphorus and 89.8% of Iron) has deleterious effects on mechanical properties of cast iron as shown in Fig. 2.15. The impact strength decreases from 4.3 to 2.7 J with the addition of phosphorus from 0.45 to 2.58 wt% in gray cast iron. The last liquid to solidify produced steadite which constitutes the inclusion of prone grain boundaries. This leads to nucleation of cracks which decreases the tensile strength and impact energy in the presence of steadite (Abbasi et al. 2007; Slynko 1993).

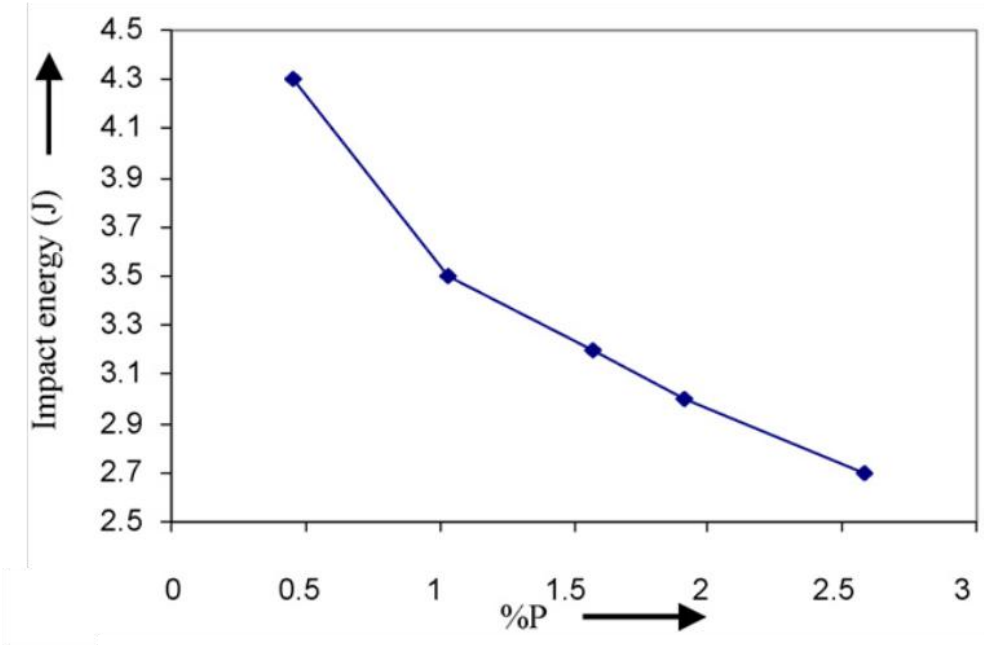

Figure 2.15: Effect of phosphorus on the impact energy of gray cast iron (Abbasi et al. 2007).

Abbasi et al. 2007 have also investigated and shown that with an increase of phosphorus content in gray cast iron from 0.45 to 2.58 wt% increases the phosphide eutectic (amount of steadite) from 4.7 to 17.81% as shown in Figure 2.16, because last liquid to solidify is rich with phosphorus. Figure 2.17 shows the cooling curve of gray cast irons containing P. The steadite areas are often displayed as cellular patterns and grains that are surrounded by this intergranular structure. Abbasi et al. 2007; Slynko et al. 1993 have shown the effect of phosphorus addition on cooling rate of gray cast iron. The phosphide eutectic point is also noticeable other than the ordinary points (liquidus, eutectic and eutectoid).

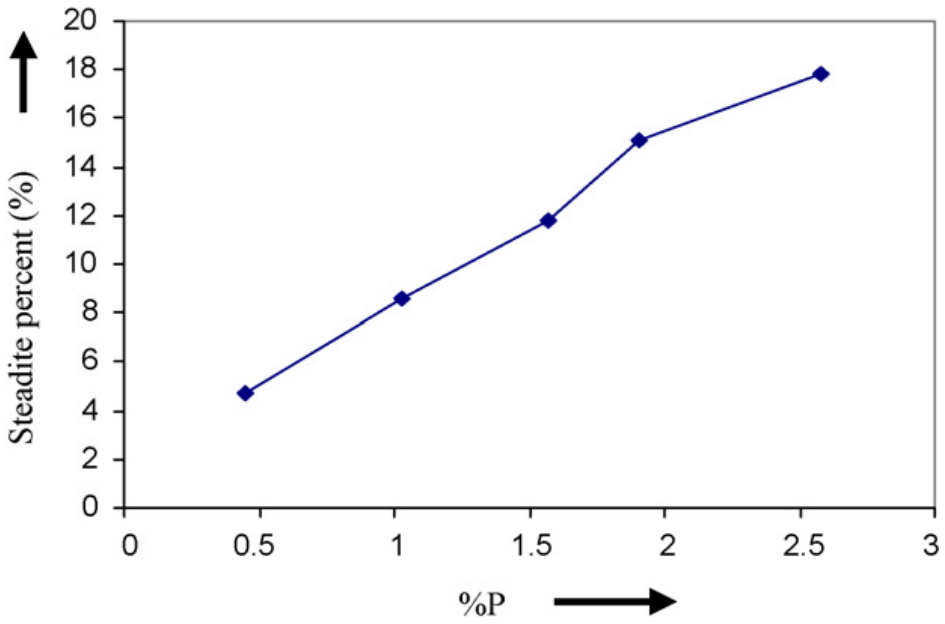

Figure 2.16. Effect of phosphorus on steadite of gray cast iron (Abbasi et al. 2007).

The phosphide eutectic is seized when the phosphorus addition is greater than 0.45% as shown in the cooling curve. The eutectic temperature of ledeburite is about 1121 ^{o}C which is higher than the temperature (935 ºC) required for the steadite formation in 1.57%P. This shows that the last liquid to solidify is steadite.

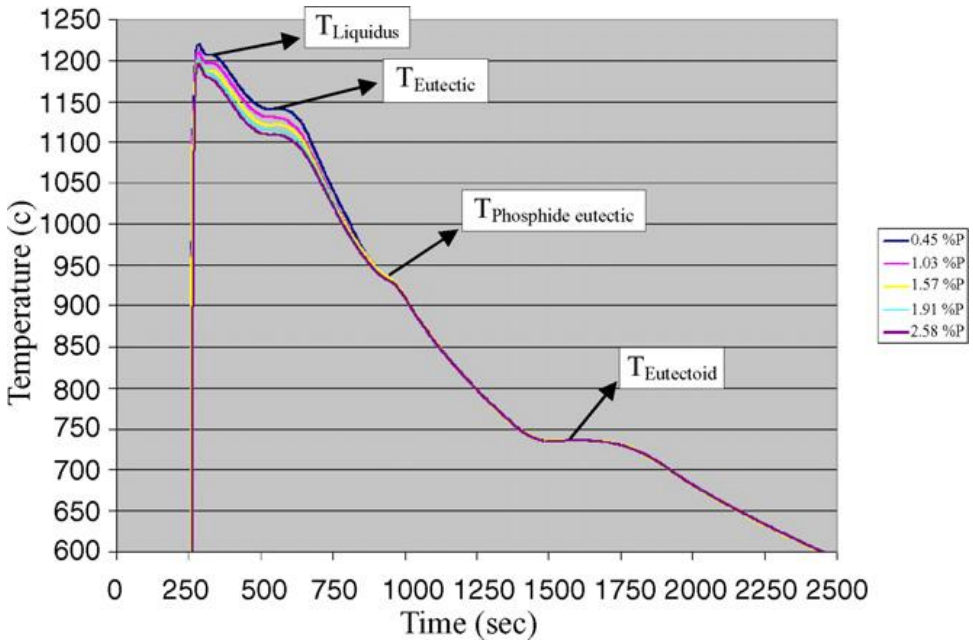

Figure 2.17: Cooling curve of gray cast irons containing P (Abbasi et al. 2007).

The eutectic temperature ledeburite decreased by increasing the amount of phosphorus in the alloy as shown in Figure 2.18. This decrease is useful in increasing fluidity (Abbasi et.al 2007; Slynko et al. 1993).

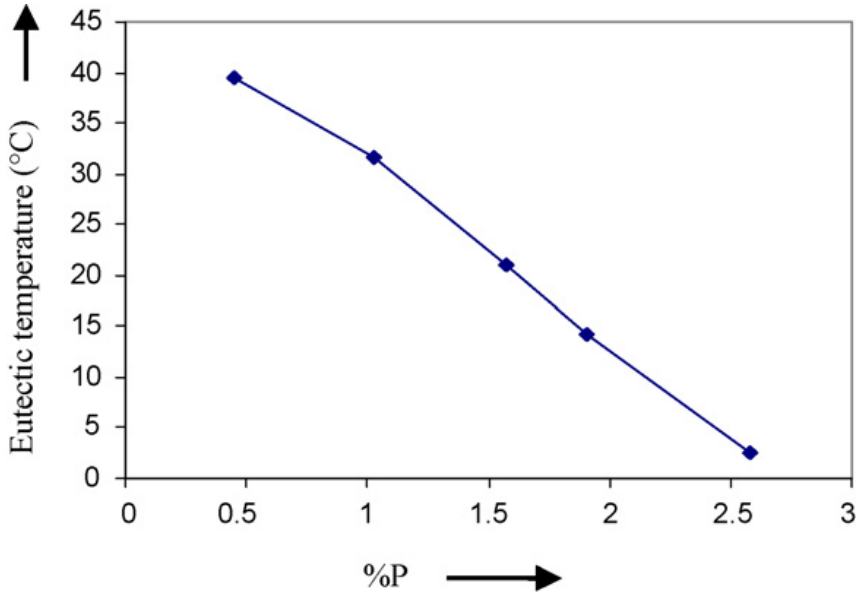

Figure 2.18: Effect of phosphorus on the eutectic temperature of gray cast iron (Abbasi et al. 2007.

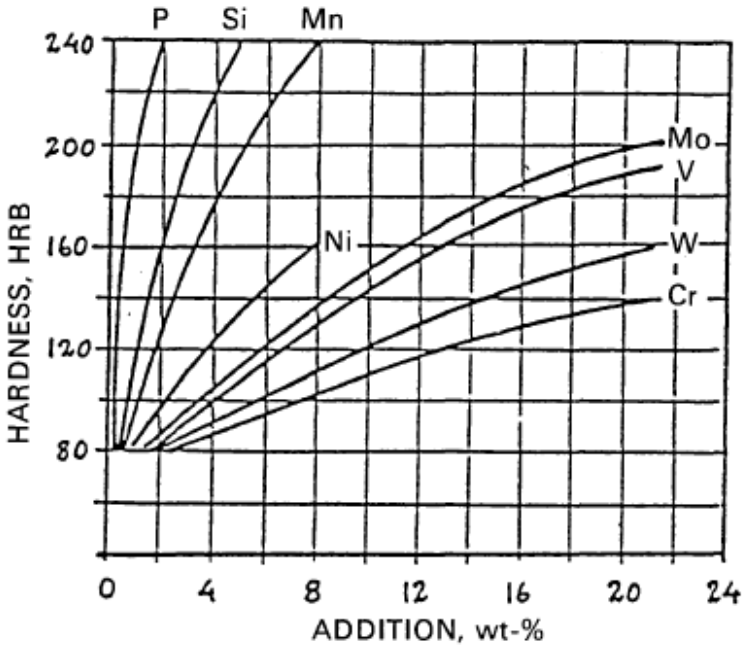

Figure 2.19: Influence of alloying elements on the hardness of ferrite (Engstrom et al. 1992).

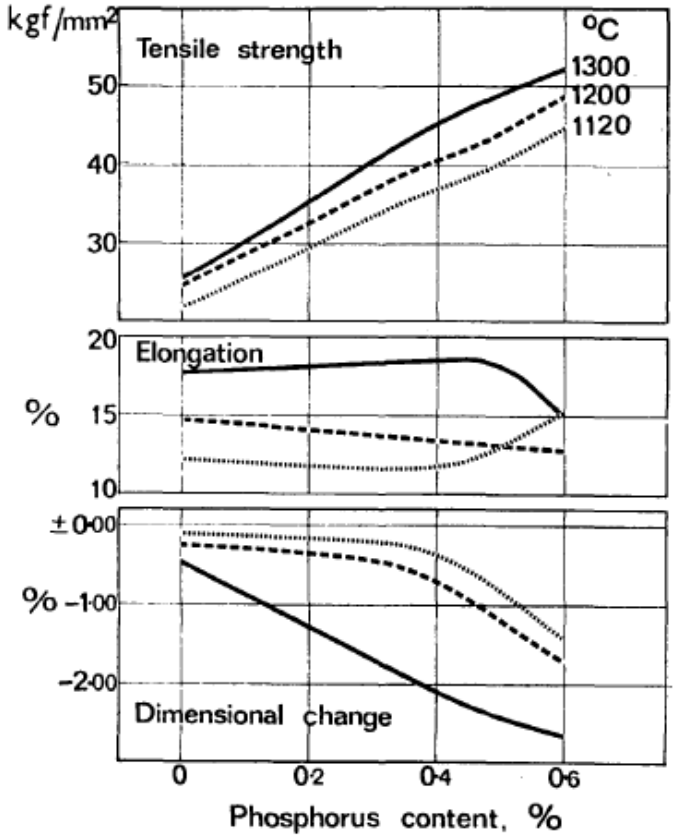

Figure 2.20: Tensile properties and dimensional as functions of the phosphorus content (Lindskog 1973).

The influence of P on the hardness of the ferrite matrix is much higher than comparable amounts of other metallic alloying elements as shown in Figure 2.19 (Engstrom et al. 1992). When P is present in the solid solution of ferrite, it distorts the lattice because the atomic radius of P is 1.1 Å and that of iron is 1.24 Å. It results in an increase in strength and decrease in percentage elongation and reduction in area. The solid solution strengthening the effect of P in ferrite matrix is much higher than comparable amounts of metallic alloying elements (Hopkins and Tipler 1958; Goodway and Fisher 1988).

Figure 2.20 shows the effect of phosphorus and sintering temperature on mechanical properties and dimensional change in Fe-P P/M alloys. Phosphorus can be added up to 0.45% at a sintering temperature of 1120 °C without causing the shrinkage (Lindskog 1973). Figure 2.21 and 2.22 show the yield strength variation as a function of elongation on parts sintered and impact energy of Fe–P powder mixtures sintered to different densities for Fe-P powder mixtures respectively.

Eyre and Walker 1976 have made an investigation on the sintered iron phosphorus alloys under various conditions as shown in Table 2.5. They have observed that level of

porosity increased by increasing the phosphorus content in the alloy consequently decreases the mechanical properties. The reported results are shown in Table 2.5.

Table 2.5: Physical and mechanical properties (Eyre and Walker 1976)

Materials	Sinter Temp.,^{0}C	UTS kg/mm^2	Transverse rupture, (kg/mm^2)	Density, gm/cm^3	Porosity, %	Elongation % from tensile	Hardness, HV10
Pure Fe	1050	13.6	20.6	6.60	16.0	~4.5	56
	1150	14.2	22.0	6.66	15.2	~5.0	57
1%P mix	1100	18.8	30.9 to 32.8	6.37	18.9	~0.5	99
3%P mix	1000	17.1	25.2 to 27.4	6.28	20.1	~0.2	103
5%P mix	1000	12.8	20.0 to 22.3	6.12	22.1	<0.1	160

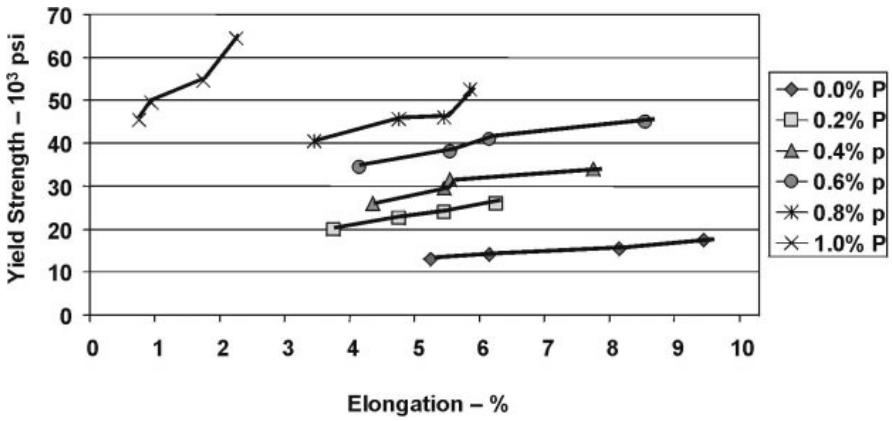

Figure 2.21: Yield strength variation as a function of elongation on parts sintered to different densities for Fe-P powder mixtures (Narasimhan 2001).

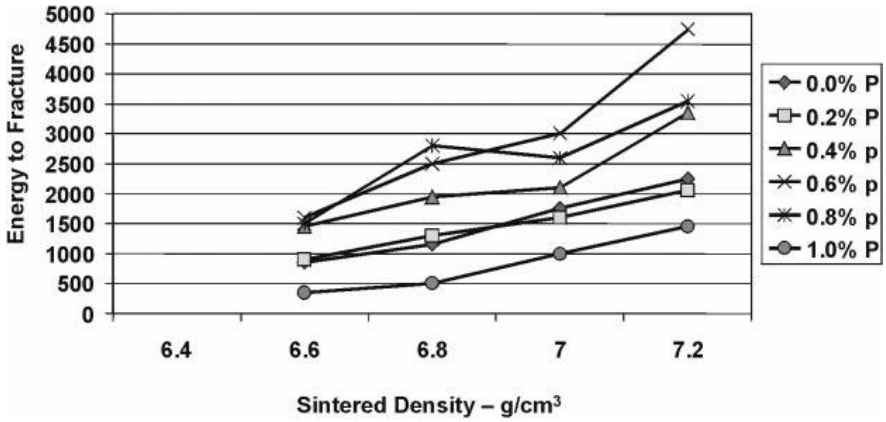

Figure 2.22: Impact energy of Fe–P powder mixtures sintered to different densities (Narasimhan 2001).

2.5 FRICTION BEHAVIOUR OF METALS AND ALLOYS

Friction is defined as the resistance encountered by one solid body when it moves or tries to move over the other body. The frictional force arises due to the interactions between the opposing asperities of the two mating surfaces. Each asperity interaction contributes to the friction force thus; the total friction force at any time is the sum of the forces at the individual asperity contacts. Bowden and Tabor 1954 has reported the basic laws of friction which are given as below:

- The frictional force is directly proportional to the load
- The frictional force is independent of the apparent area of contact
- The friction is independent of the sliding velocity

A drop in coefficient of friction is observed as the sliding velocity increases, which may be due to the thermal softening at the interface (Rabinowicz 1965).

2.5.1 Friction Theories

Bowden and Tabor 1950 proposed the adhesion theory of friction which states that, when a relative motion is imported to the interface by applying a tangential force, each pair of contacting asperities weld together and shear to accommodate the relative motion. According to this theory, the force needed to shear the junctions is a major force of friction between the two bodies at the real area of contact. This force of friction is given by,

$$F = \tau A_r \qquad \text{----------} \qquad 2.1$$

Where, τ is the shear strength of these junctions, which is a function of the materials of the bodies. The coefficient of friction μ is then given by the following equation,

$$\mu = \frac{F}{L} = \frac{\tau \, \mathrm{Ar}}{H \, \mathrm{Ar}} = \frac{\tau}{H} \qquad \text{----------} \qquad 2.2$$

Thus, friction coefficient can be taken as the ratio of two quantities τ and H, representing respectively, the resistance to plastic flow of the weaker of the contacting materials in shear and in compression.

Hutchings 2017 has established that a force, F, is needed to overcome friction and cause motion by (a) rolling (b) sliding (Fig.2.23). Suh and Sin 1981 have established that there are three basic mechanisms responsible for the origin of friction. These are as below:

- Asperity deformation,

- Plowing,
- Adhesion

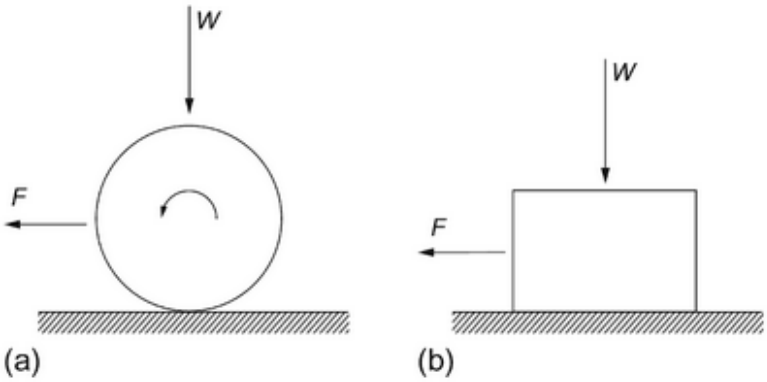

Figure 2.23: A force, F, is needed to overcome friction and cause motion by (a) rolling (b) sliding (Hutchings 2017).

Liu et al. 1992 have indicated that friction force arises due to the interaction between the asperities as (a) contacting point adhesion and (b) either elastic or plastic deformation of the asperities under load. The coefficient of friction μ is, therefore, represented as,

$$\mu=\frac{Fa+Fd}{L}=\mu a+\mu d \qquad \text{2.3}$$

Where L is the applied normal load on the contacting surface, μ_a and μ_d are the friction coefficients due to adhesion and deformation, respectively. F_a is the force required to shear the adhesion bond whereas, F_d is the force required to deform elastically or plastically the asperities.

2.5.2 Factor Affecting the Friction Behaviour of Steels

The coefficient of friction is not a given material property but it also depends on the mechanical properties of the opposing surfaces and the environmental conditions. The frictional behavior is affected by the following factors:

- Sliding velocity
- Applied load
- Sliding distance
- Environmental conditions
- Surface topography
- Mechanical properties of the two mating materials.

Friction between two rubbing objects is not independent of the velocity as suggested by (Coulomb 1785). Rabinowicz 1965 and other researchers have shown that friction is a function of sliding velocity and not dependent on the load alone. Rabinowicz 1965 has represented that a drop in friction is universally observed as sliding speeds are raised to high values due to thermal softening of the interface, resulting in the lower shear strength of the interfacial layer while maintaining the substrate at almost the same level of hardness. Li et al 1991 have also observed a decrease in the coefficient of friction with increasing sliding velocity in eutectoid steels and have attributed this decrease to the thermal softening of the outermost layer and simultaneous hardening of the subsurface layers. Friction has also been shown to decrease with increasing normal load. Bowden and Tabor 1964 have shown that in carbon steels the coefficient of friction decreases with increasing normal load as shown in Figure 2.24.

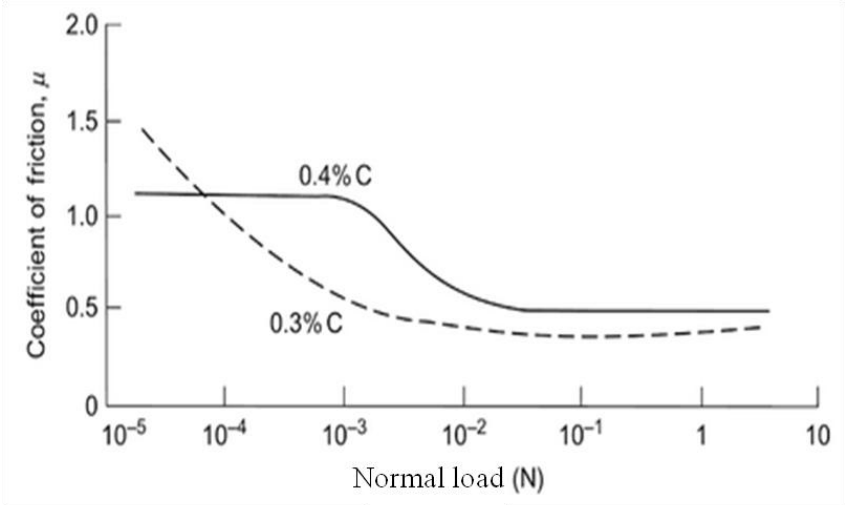

Figure 2.24: The variation of coefficient of friction with a normal load for steels sliding against themselves in the air, unlubricated (Hutchings 2017).

It has been suggested that this is the result of the presence of oxides on the surface of steel (Hutchings 1992). Li et al. 1991 have also observed similar results for the dry sliding friction of the eutectoid steels and have attributed it to the thermal softening of the surface layers due to frictional heating.

The frictional behavior of steels is dependent on the history of sliding. Suh and Sin 1981; Blau 1981 have reported that during sliding the friction may advance into three stages: (i) the first stage depends on the surface finish and the nature of oxide films, (ii) a second stage consists of plastic deformation and work hardening and (iii) a third stage evolve uniform microstructure or equilibrium of sliding processes which results from temperature stability and equilibrium of oxide formation and breakdown.

Madakson 1983 has investigated that the friction at the initial stage rises and then settles to an almost steady state. It was further represented that the friction coefficient is heavily influenced by the oxidation characteristics of the materials in rubbing contact at a given loading condition and sliding velocity. According to Rigney and Hirth (1979), the steady-state friction is due to the attainment of a steady state microstructure. Vingsbo et al. 1981 have also reported that the coefficient of friction depends on the microstructure of steels but no reasonable clarification has been readdressing by them.

2.6 TYPES OF WEAR

The progressive loss of substance from the operating surface of a body occurring as a consequence of the interfacial rubbing process is called wear (Ramesh et al. 1991). Wear may be classified on the basis of the appearance of the worn parts or mechanisms and conditions, which prevail during material removal. According to the wear mechanisms and conditions, types of wear are classified as (i) Adhesive wear (ii) Abrasive wear (iii) Erosive wear (iv) Impact wear (v) Fatigue wear and (vi) Corrosive wear

Adhesive Wear

It is associated with low sliding velocity, small load, and smooth surfaces. This is a universal type of wear that can occur on every machine and is very difficult to eliminate but can only be reduced.

Abrasive Wear

It occurs when two surfaces, one of which is harder and rougher than the other, are in sliding contact. It is the removal or the displacement of material from one surface by the harder asperities of another surface or by softer, loose particles. This type of wear is more dangerous because it can occur suddenly with the introduction of a contaminant and may lead to higher wear rates and extensive damage to the surfaces. Stack and Mathew 2003 have conducted a series of test to study the effect of sliding distance and load on the micro-abrasion of the metallic materials. They have investigated that micro-abrasion mechanism maps have as a function of sliding distance and applied load showing significant differences between locations of three-body and two-body abrasion regimes for pure metals and steels.

Erosive Wear

It is a combined process of repeated deformation and cutting. When a solid surface is gradually worn away by the action of fluids and particles, it is called erosion. Erosion of materials can take place under four various conditions: (i) Impingement of solid particles against a solid surface, (ii) Impingement of liquid droplets against a solid surface, (iii) Flow of

hot gases over a solid surface and (iv) Cavitation at a solid surface in liquid media. The most important form of erosion is that caused by solid particle impingement.

Impact Wear

It arises from the repetitive impact of two surfaces, which differs from the impact of solid particles on a surface causing erosive wear.

Fatigue Wear

It arises from the repeated cyclic stresses on the surface of a part which induces a small degree of mechanical damage in the surface and subsurface regions. The damage accumulated on the surface leads to failure by deformation at the surface.

Corrosive Wear

It arises from the chemical reaction at the surface with the mechanical wear mechanisms. In a corrosive environment sliding surface experience corrosive wear. However, in some cases, the reaction layer may protect the surface or even act as a lubricant.

2.7 DRY SLIDING WEAR OF STEELS

Wear of metals in the air at room temperature in the absence of any lubricant is termed as dry sliding wear. Dry sliding wear of steels has long been the object of research. The various researchers (Arora et al. 2013; Roy 1992; Mohan 2002 and Pathak 2002) have also performed wear behavior of alloy using a pin-on-disc wear test apparatus. Also, Gurumoorthy et al. 2007 have developed the dry sliding wear testing machine (pin-on-disc) for evaluation of sliding behavior at high stress. They have investigated the different aspects of dry sliding wear behavior of steels under different conditions like load, sliding velocity, initial surface roughness, microstructure, mechanical properties, environment etc., and at the same time to detect the mechanisms of wear operating under these conditions.

2.7.1 Microstructure and Dry Sliding Wear

A lot of work has been carried out to correlate the microstructure with the observed behavior of metals, in general, and of steels, in particular, but the study has not been carried out on Fe-P alloys. Wang et al. 1999 have studied the wear behavior of 52100 and 1080 steels with different microstructures under dry sliding. It has been reported that there is no change in the wear volumes of different microstructures. However, considerable differences in the wear volumes are observed in the regime of severe wear. Khorsand et al. 2002 have investigated the dry sliding wear of powder metallurgy low alloy steel with 0.60wt.% carbon developed by

compaction and sintering, using a pin on disc wear testing machine. They have investigated that in low alloy steel with 0.6%C, the resistance to wear is increased by increasing the density of the steel. Tomlinson et al.1987 have reported the influence of phosphorus on the sliding wear of a grey cast iron by an increment of 0.2wt% using steel-pin-ring equipment at a speed of 1.5m/s and load with an increment of 0.5Kg. They have observed a uniform pattern of wear behavior in this case. Severe wear was observed in the 0.2 wt. % P iron at all loads. Wear rate reduces continuously at all loads with the increase in phosphorus content from 0.4 to 1wt%. In another study, Tomlinson et al. 1989 have also investigated the dry sliding wear of grey iron under stresses of 0.5 and 2.0 MPa at a sliding speed of 1.5 m/s. The grey iron consisted continuous network of phosphide embedded in the matrices of ferrite, pearlite, and martensite. They have investigated that the wear rate of pearlite iron reduced due to the presence of phosphide in the iron. Further, the network of phosphide stiffened in the weaker matrices (pearlite, ferrite, and martensite). During the dry sliding, the matrix is fractured and formed a particulate composite of phosphide at the deformed surface which resisted the further wear out of the surface.

Eyre T.S. et al.1976 have studied the effect of phosphorus on wear rate under various conditions, a material developed by compaction and sintering, using a pin on disc technique to describe the wear mechanisms with it. They have studied that increase in pressing pressure and sintering temperature improved the wear resistance. Further, the phosphorus addition in the alloy which forms a eutectic hard phosphide phase leads to wear resistance. P is used as an alloying element in the iron for special applications in P/M alloys such as brake shoes due to its high resistance to wear and absence of sparking (Pavlygo et al. 2000).

Tekeli et al. 2007 have investigated the wear characteristic of low carbon (0.3wt. %) dual phase P/M steels using a pin on disc sliding wear machine under a constant load of 25N and a sliding speed of 2.08m/s for a sliding distance of 3000m. They have observed that the sintered specimen show high wear rate because of low microhardness. In the intercritically annealed sample the hard phases locked in the matrix like martensite which shows resistance to wear.

Zhang et al. 2002 have reported that the wear condition, phosphorus addition and morphology of graphite are the most important factors which influence the wear properties of the steels. They have investigated that the coefficient of friction decreases with an increase in the sliding velocity and contacting pressure. Also, the wear mass loss increase with an increase in the sliding velocity and contacting pressure. They have also shown that the wear mass loss

decreases with increasing of P content in cast iron. They have observed that the content of phosphorus in the surface layer is much higher than the actual phosphorus added. This has been suggested that during the sliding process, the some parts of worn out phosphorus eutectic wear away and the other portions of worn out deposited on the surface which diffuses into the layer. Thus, the hardness of the layer shows higher hardness than that of the base metal. Its value varies from point to point on the layer because P content in the layer is not uniformly distributed. The outer side of the layer shows maximum value and gradually decreases as the depth increases. The phosphorus content on the surface increases as the sliding velocity and contacting pressure increased which raises the hardness values in the surface layer. Some researchers (Coyle and Tsang 1983; Terheci et al. 1995) have observed the tribological characteristics of different graphite morphologies. Among the three types of graphite morphologies, the heat transfer ability is higher in the cast iron with F.C morphology while the iron with nodular graphite morphology has the lowest value. The nodular graphite iron has the highest surface temperature and largest temperature gradient. Therefore, during sliding nodular graphite iron shows the highest deformation.

Terheci et al. 1995 and Kubota et al. 2000 have studied friction and wear on a comprehensive model of SAE G3500 which is used in cylinder liners of diesel engines. The various wear mechanism such as adhesion, delaminations, and ploughing were taken into the account. They have investigated that the coefficient of friction is insensitive to load.

Roy et al. 1999 studied the influence of the applied load on the abrasive wear rate of mild steel. They have shown that the wear rate increases with increase in applied load for all the materials.

Rigney 1988 has shown that the wear rate of materials is a function of subsurface deformation, crack propagation and crack nucleation, which is dependent on the microstructure of the materials. Similar findings have also been reported by (Argon 1978), who concluded that the microstructure of a material has a bearing on its wear behavior. He also examined the effect of the second phase particles on the wear rate of two-phase alloys and stated that it is not only the hardness but mean free path as well, which controls the wear rate. The wear rate also depends on the size of the particle and coherency because these parameters affect the crack nucleation rate.

Suh 1986 has indicated that the hardness and the toughness are the two most important properties in the context of wear of materials and these properties are affected by the microstructure. Hence, a change in microstructure changes these properties, consequently

changing the wear behavior of a material. It has been further reported that the toughness of a material is closely related to the crack propagation rate, which also affects the wear. Clayton 1980 has investigated different types of pearlitic steels having 0.30 to 0.79 wt.% carbon and a pearlitic volume fraction ranging from 40 to 100 % in order to make the correlation between the wear nature and material properties. The volume fraction of pearlite phase improves the wear behavior.

Clayton 1980 has emphasized that the alloying contents influence the microstructure of the steels and consequently the resistance to wear of the pearlitic steels. Carbon is the most influential alloying element because it controls the amount of the cementite. Gladman 1970 has observed two distinct effects of manganese addition on the morphology of pearlite. Firstly, it produces the eutectoid reaction to give a fine pearlite with reduced interlamellar spacing. Secondly, it decreases the carbon required to make the full pearlitic steel as a result increase in the volume fraction of pearlite in a hypereutectoid steel for a given carbon content.

2.7.2 Oxidative and Metallic Wear

Oxidative wear

In the mild wear mechanism, the real contact area is protected by the oxide film during the sliding. It is also termed as “mild wear”. Mild wear results due to the oxidative reaction of the surface in the atmosphere (Quinn 1983).The initial stage is that of severe wear when two sliding surfaces come into contact, in which the mating surfaces attain a measure of conformity. After this initial stage, the large areas of both surfaces come into contact during sliding. This area then expands thermally in the direction perpendicular to the plain of contact between the specimen in a similar fashion as proposed by Baber 1969, so that there will be a plateau of contact. If the load and sliding speed are such that there is sufficient heating, the contacting plateau will be oxidized preferentially to the other plateaux. This oxidation mainly occurs during contact between opposing surfaces at a temperature, T_c at the real area of contact, well in excess of the general surface temperature T_s. Due to the presence of plateaux on the surface, the wear track observed extremely smooth and parallel to the direction of sliding (Suh 1977). The surface cracks are seen perpendicular to the direction of sliding at this plateau. The surfaces surrounding each plateaux are rough and packed with wear debris and wear tracks are not observed. It seems that these wear debris are fragments of the plateau. It became unstable when reached to the critical height.

In oxidative wear, the area of these plateaux (A) has been found by assuming that the entire load is borne by only one of these plateaux at a time and is given by:

$$A = \frac{L}{H} \quad \text{----------} \quad 2.4$$

Where L is the normal load and H is the hardness of the bulk metal of the softer of the two contacting surfaces.

The plateau-plateau interaction does not take place along the entire surface area of a plateau but there are several sub-area of contact on each plateau and these are the regions of actual contact at which oxidation occurs. The oxide film builds up until it reaches a critical thickness, ξ, when it is assumed that the film becomes unstable and is removed. When all the sub-areas of contact get removed from the plateau, then another plateau elsewhere on the surface becomes operative. The virgin surface can only get oxidized at the general surface temperature (T_s). Without external heating, the amount of oxidation at a typical value of T_s (say, 80 ^oC), is very less compared to that taking place at a typical value of T_c around 400 ^oC. Hence, the original plateau or its subsurface region when goes out of contact, will not oxidize significantly.

The oxide film prevents direct metal-metal contact between the two mating surfaces and thus mitigates the severe adhesive wear. Stott and woods 1978 have also reported that the formation of oxide on the sliding surfaces is instrumental in reducing the wear rates in metal and alloys. Glascott et al. 1985 have also indicated that in dry sliding, the oxides are developed by oxidation of metal surface while in contact and the extent of oxidation depends on the temperature developed at the asperity contacts, the duration of contacts and the oxidation characteristics of the metal. These oxides may remove completely during subsequent sliding, exposing fresh metallic surface for further oxidation. The resulting wear debris may be swept aside which also provides protection against wear.

Jiang et al. 1998 have also reported that during dry sliding the compact layers are formed. Due to the oxide-to-oxide contact between two surfaces, the real contact areas are reduced compared to the metal-to-metal contact. Therefore, wear is reduced when the compacted layers are formed. These layers are more wear-resistant than the metallic surface areas towards the edges of the wear track (Kato 2008).

Metallic wear

The metallic wear takes place when there is metal to metal contact between the two sliding surfaces under relative motion. This can happen under two conditions: (i) at low load and speed when frictional heating is negligible and the oxide film does not form over the surface, thereby, allowing direct metal-metal contact and (ii) at high loads and low sliding

velocities when the contact pressure is enough to penetrate through the thin layer of oxide and direct metal-metal contact takes place (Lim et al. 1987; Lim et al. 1987).

Archard and Hirst 1956; Archard and Hirst 1957 have shown that at low sliding velocities below 0.1m/s heating effect is negligible and the metal surface is deformed by the frictional force, shearing it in direction of sliding. The shearing causes the removal of slivers of metal from one or both the surfaces by the plastic failure. When one surface is softer than the other metal may be transferred from the softer to the harder surface. If both the surfaces are equally hard, particles of metallic debris form due to wear. It has also been reported by them that in severe wear the subsurface is heavily deformed and the crystal structure becomes highly distorted.

Welsh 1965 has reported that there is a critical load at each sliding speed, at which the wear changes from mild (oxidative) to severe (metallic) type. The wear rate in severe wear is around 100 times higher than those observed in the case of mild oxidative wear. Above T_1, the wear debris consists of large metallic particles visible to the unaided eye and the surfaces are severely form and damaged (Welsh 1965).

Bhattacharyya 1980 has evaluated the mild and severe regimes of wear in pearlitic and spheroidized steels. A test was conducted at a constant sliding speed of 0.698 m/s in the load range from 1.11 to 267 N using a pin on cylinder wear testing machine. A sharp transition from the mild to severe wear has been observed which indicates the severe wear regime.

Eyre et al. 1976 have observed that characteristics of grey cast iron having phosphorus using a pin on ring machine. In the observation, at low sliding speed, the iron-containing 0.15%P showed a mild wear. It is controlled by the oxidation at the interface whereas severe wear occurs due to the breakdown of the protective oxide film formed during mild wear. Phosphorus modifies the wear behavior of grey iron under dry sliding conditions, by providing a hard phase. This hard phosphide phase reduced the real contact area between surfaces during sliding. It also withstands the applied load.

2.8 TRIBOLOGICAL PROPERTIES

Phosphoric iron shows high wear resistance. Presence of phosphide in the iron favours an increase in the hardness and wear resistance of the alloy (Krecar et al. 2004). Eyre and Williams 1973 have suggested some points with respect to phosphorus as follows. (i) The phosphide may carry the applied load, (ii) The phosphide increases the strength of the iron which resists to the plastic flow, (iii) A layer of phosphide may spread over the surface.

Iron phosphide (Fe_3P) is formed when the addition of P is beyond the limit of solubility under the certain cooling condition (Shyrokov et al. 2004; Shirokov et al. 2003). In the case of a somewhat higher P content in irons, there arise fusible hard inclusions of (ferrite + phosphide) or triple phosphide eutectic (PE) of steadite (phosphide + cementite + ferrite) which are disoriented separately (Shyrokov et al 2004). The reorientation of inclusions reduces the mass losses and coefficient of friction.

Eyre and Walker 1976 have conducted experiments on Fe-P alloys using a pin-on-disc wear testing machine. They have observed three type of wear as shown in Figure 2.25 at a sliding velocity constant at 300 cm/s over a load range up to 36 kg. The relevant features are:

Type 1: At low load, an oxide was produced on both wearing surfaces quickly.

Type 2: At higher load wear behavior was more complicated.

Debris were produced and adhered to the disc which increased the wear rate. After a relatively short sliding distance, the disc was covered by oxides that built up in patches as a result of which wear diminished to zero.

Type 3 The metallic wear occurres at a higher load.

Phosphorus in grey cast iron has a pronounced effect on transition load (Eyre and Williams 1973; Tomlinson and Vandrill 1987). A small addition of phosphorus has been made to sintered iron (Lindskog 1973; Lindskog and Svensson 1974). Eyre and Walker 1976 have produced alloys containing phosphorus in a range up to 5% P. The mild-severe transition load has been observed by addition of small amount of P which lies within the solid solution range. Beyond this limit, the hard iron phosphide in the form of a eutectic structure improved the wear resistance as shown in Figure 2.26(a). A little observation has been made with higher P content. Figure 2.26(b) shows that there is little advantage in increasing phosphorus above 3%. The smoother surfaces were observed free from adhered metal particles on the surface (Eyre and Walker 1976). The pressing pressure was kept constant during the test. However, the resistance to wear was improved and these observations lead to emphasize the absence of correlation of wear with other mechanical properties (Eyre and Walker 1976).

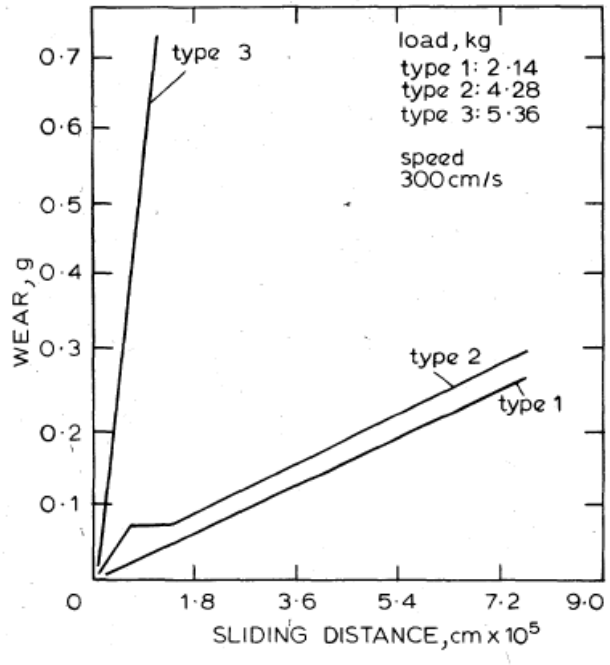

Figure 2.25: Three basic wear curves (Eyre and Walker 1976))

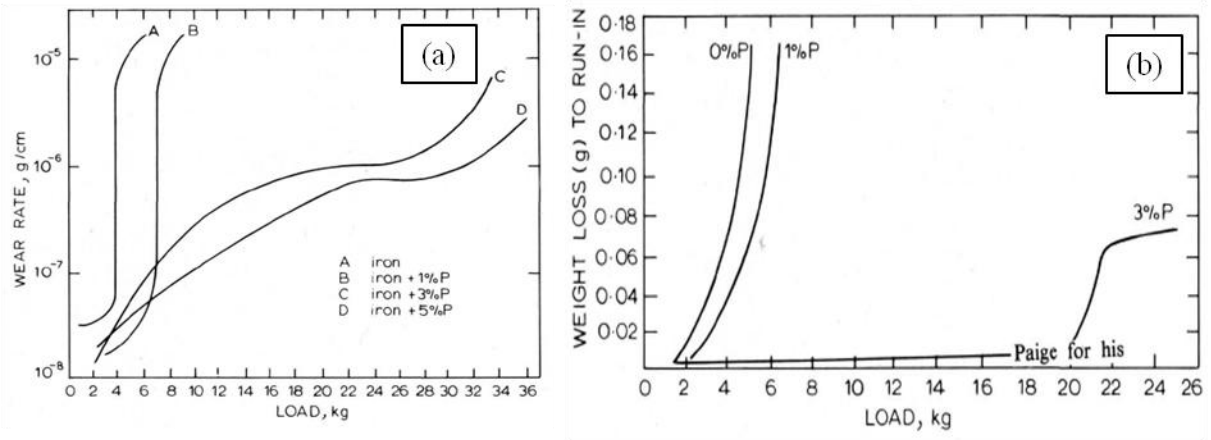

Figure 2.26: Effect of phosphorus on wear characteristics of sintered iron (Eyre and Walker 1976).

2.9 CORROSION PROPERTIES

The Delhi Iron Pillar (DIP) has already attracted the attention of metallurgists and corrosion technologists. Because of its resistance to corrosion for the last 1600 years. In this regard, theories have been proposed to explain its superior corrosion resistance. The theories may broadly classify such as the environmental (Hudson 1953; Wranglen 1970; Ghosh 1963) effect, and material (Balasubramaniam 1995; Balasubramaniam 1998; Wranglen 1970). Deacon et al. 2009 has evaluated the corrosion resistance of Fe-Al-Cr alloys in the NO_x environments. He has investigated that the thin layer of oxides at the surface acts as a corrosion

protection layer. Similarly, phosphoric iron forms a protective layer on the surface as observed in the DIP (Fig.2.27).

Figure 2.27: Delhi iron pillar at Delhi (Weblink 3).

The immunity of iron from rusting over such a long period is a striking phenomenon and it may, therefore, be of interest to report the results of some experiments. Hudson 1953 has conducted an experiment on specimens of iron and zinc for one year and results of that reported here in Table 2.6 and 2.7. After the experiment, he has found that the corrosive condition in Delhi is very mild. The opinion of (Hudson 1953) is the lack of serious rusting of the pillar is to be attributed to the mildness of local climate rather than any intrinsic superiority in the corrosion resistance in the iron itself.

Table 2.6: Atmospheric corrosion of steel and zinc (Hudson 1953).

Exposure station		Corrosion rate. Mils (0.001 in.) per year	
		Steel	Zinc
Delhi	1950-1951	0.23	-
	1951-1952	0.17	0.006
Godalming	1951-1952	1.7	0.042
Sheffield	1951-1952	4.2	0.51
Khartoum	Average, 9 yr.	0.1	0.02
Basrah	” 8 ”	0.6	0.04
Singapore	” 10 ”	0.6	0.04

Table 2.7: Meteorological observation at New Delhi (1951) (Hudson 1953)

	Jan.	Feb.	Mar.	Apr.	May	June	July	Aug.	Sept.	Oct.	Nov.	Dec.
Relative humidity, per cent, 0830h.	74	52	53	42	35	41	63	74	63	50	50	69
Relative humidity, per cent, 1730h.	46	24	33	21	21	26	48	60	52	37	42	47
Rainfall(in.)	0.9	0.0	2.1	0.9	0.1	0.5	4.8	3.1	4.1	0.3	0.6	Nil

British investigators have suggested that the climatic conditions are the main reason for the freedom from corrosion of the DIP whereas metallurgists and archaeologists from Indian have emphasized on the composition alloy for corrosion resistance as shown in Figure 2.28.

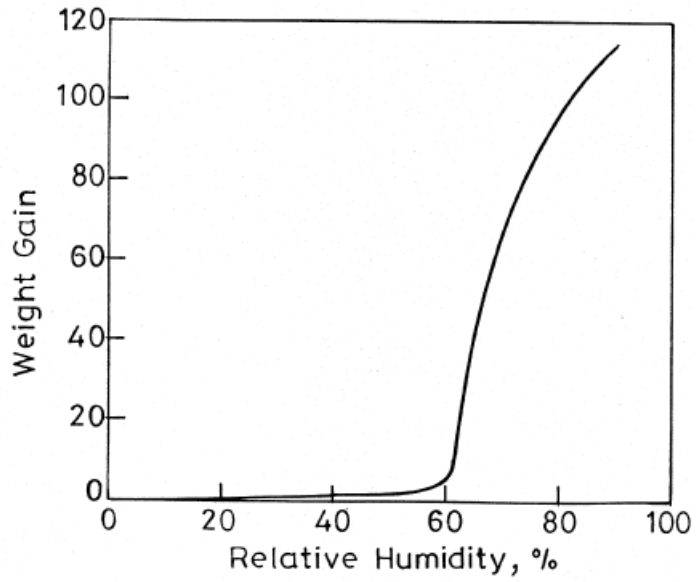

Figure 2.28: The effect of atmospheric humidity on the corrosion of iron.

The DIP iron shows a wide variation in a structure which is the characteristic feature of ancient Indian iron. The several investigators have made a chemical analysis of the DIP that is reported in Table 2.8. The results show the variation in magnitude which may due to the non-uniform structure.

Table 2.8: Composition of Delhi iron Pillar

	Hadfield(1912)	Ghosh(1963)		Lahiri et al.(1963)	Lal(1945)
		Above	Under		
C	0.08	0.23	0.03	0.26	0.90
Si	0.046	0.026	0.004	0.056	0.048
S	0.006	Trace	0.008	0.003	0.007
P	0.114	0.280	0.436-0.48	0.155	0.174
Mn	Nil	Nil	Nil	Nil	Nil
N	-	0.0065			
Fe	99.720	Diff			99.67
Others	0.246				0.011
Specific gravity	7.81	7.672-7.747		7.5	

The chemical analysis of the phosphorus content in DIP iron has revealed that phosphorus in the DIP is in the form of solid solution in iron (Balasubramaniam 2005). The researchers have found a large amount of pearlite near the slag inclusions which indicates the depletion of P in these regions. SEM analysis of Eran iron and Dhar pillar iron shows the presence of P in the entrapped slags (Balasubramaniam 1999).

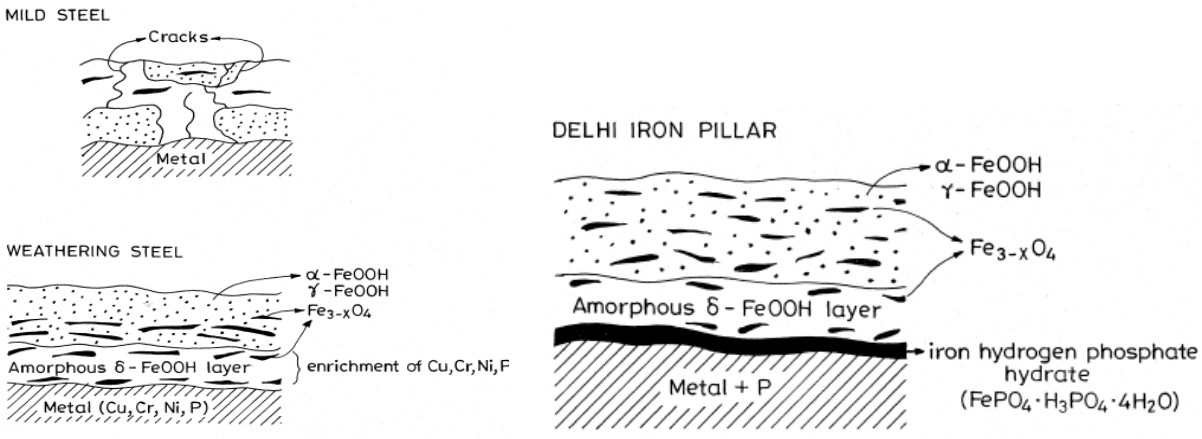

Figure 2.29: Schematic of rusted structure formed on mild steel, weathering steel and DIP (Balasubramaniam 2005).

The structure of the passive film has been given on the DIP as shown in Figure 2.29 for comparison with other steels (mild and weathering). The corrosion behavior of welds has been studied by Rao et al. 2004. They have reported that scandium addition did not alter the pitting

corrosion resistance of the weld metals. Anne et al.2017 have investigated the corrosion behavior of the multilayered composite using electrochemical polarization test. They have reported that among severe plastic deformation (SPD) techniques, accumulative roll bonding process (ARB) is one of the most suitable methods for practical applications to develop multilayered composite sheets with excellent mechanical properties such as high strength and toughness along with good corrosion resistance. They have concluded that multilayered composites showed better corrosion resistance.

2.10 MAGNETIC PROPERTIES

Shokrollahi and Janghorban 2007 have reported the application of various types of magnetic materials, such as iron and its alloys, Fe-Ni, Fe-Ni-P, Fe-Nd-B and Fe-Si and soft and hard ferrites. In soft magnetic materials, the hysteresis losses must be kept down to a minimum. When the induction is large for a small applied field, the loop area is small and hysteresis loss is reduced. Soft magnetic materials should be free from the impurities and inclusions. The eddy current loss is also low in soft magnets (Raghavan 2000). The variation in coercive force and maximum permeability are shown in Figure 2.30 and 2.31 respectively.

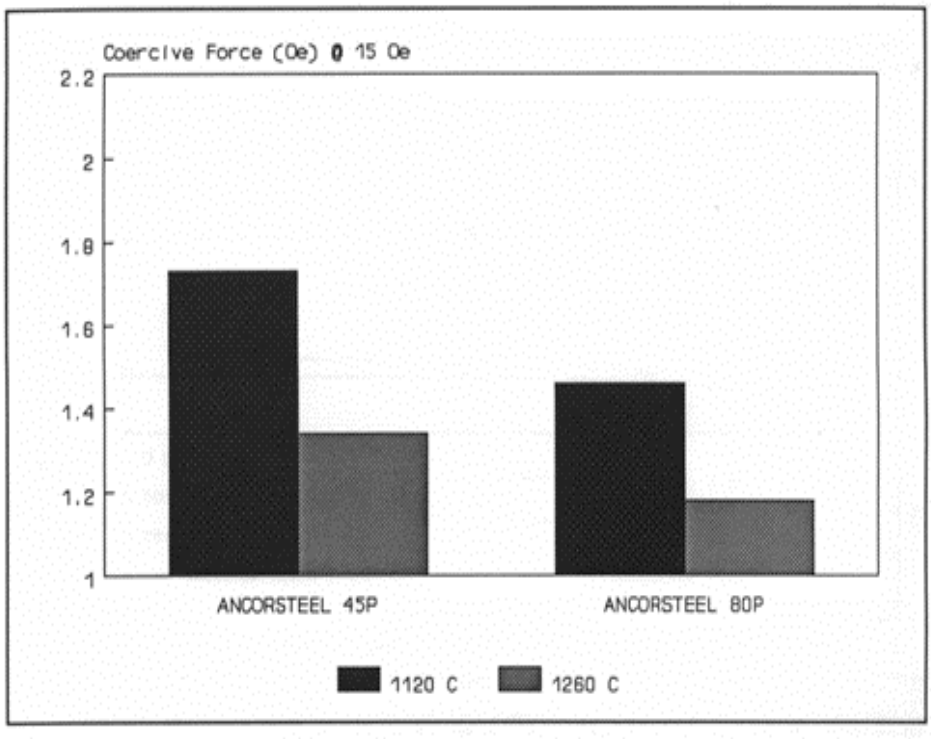

Figure 2.30: Coercive force of iron-phosphorus alloys (Hanejko et al. 1992).

Shokrollahi and Janghorban 2007 have suggested that the preparation and processing of the parts influence the properties of components. Also, the purity of material, shape, and size of

particles influence the overall magnetic response. Figures 2.30-2.32 show the improved magnetic performance of 0.45% P/Fe and 0.80% P/Fe alloys sintered at 1120 °C and 1260 °C (Hanejko et al. 1992). Figure 2.32 shows the saturation induction versus density for several alloys.

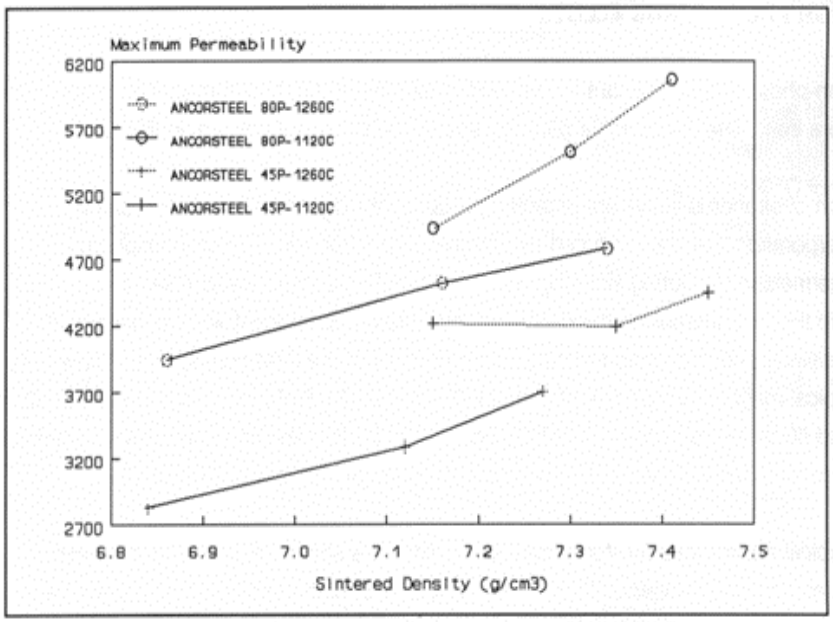

Figure 2.31: Maximum permeability of iron-phosphorus alloys (Hanejko et al. 1992).

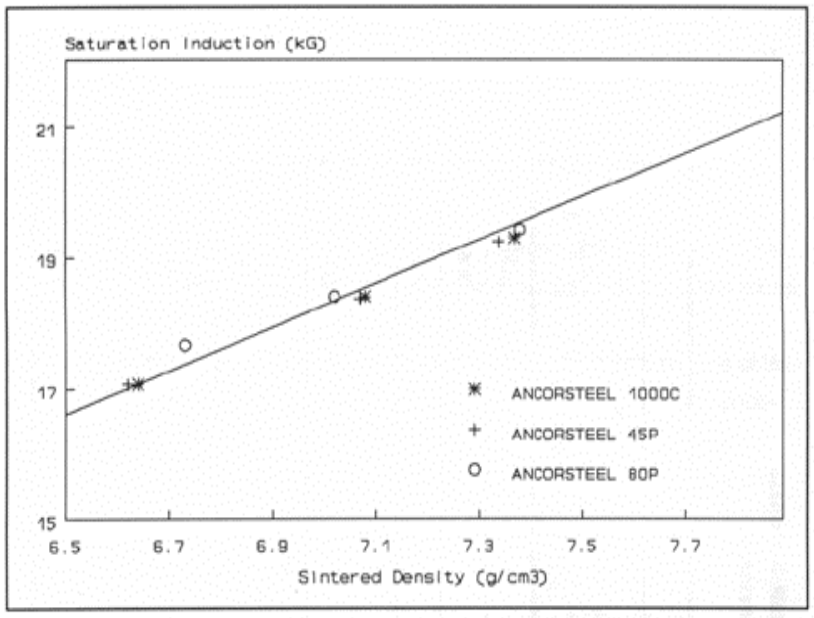

Figure 2.32: Saturation induction versus density for several alloys (Hanejko et al. 1992).

Das et al. 2008 have investigated the soft magnetic properties of Fe-P based alloys. The results are reported in Table 2.9.

Table 2.9: Magnetic Properties of Fe-P alloys (Das et al. 2008)

Material	Coercivity(O_e)	Max. flux density (G)	Retentivity(G)
Fe-0.35P-0.35Cr	1.50	874.0	510.0
Fe-0.7P-0.7Cr	1.40	787.0	520.5
Fe-0.35P-0.35Cr-1Si	1.10	905.8	338.0
Fe-0.7P-0.7Cr-1Si	1.00	977.5	565.0
Fe-0.35P	2.20	998.0	608.0
Fe-0.7P	1.50	980.0	597.0
Fe-1Si	1.67		
Fe-2Si	1.27		
Fe-3Si	1.10		
Fe-6.5Si	0.30		
Fe-3Si-0.45P	0.98		

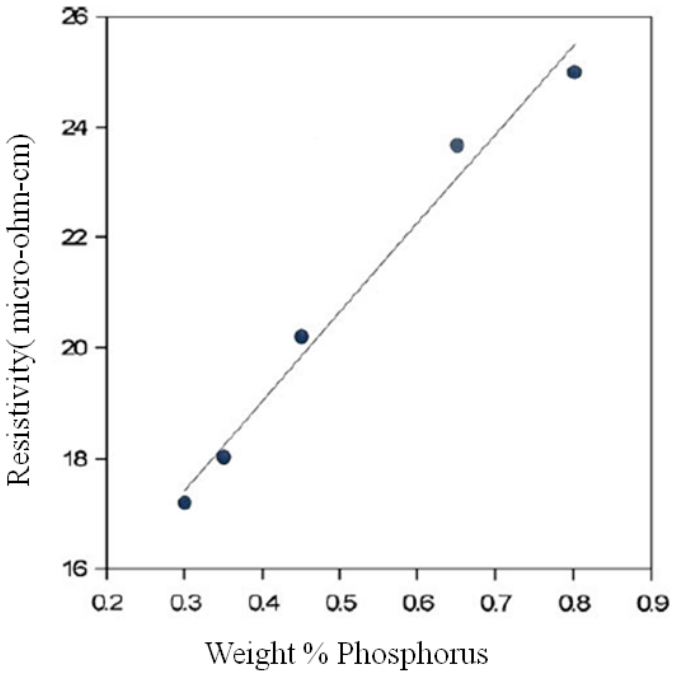

Figure 2.33: Electrical resistivity of Fe-P alloys with increment of P in iron (Chaurasia et al. 20-12).

Chaurasia et al. 2012 have investigated that with increment of phosphorus in iron the linear variation in the electrical resistivity has been observed as shown in the Figure 2.33. This

investigation is supported by the results of work reported by (Lindskog et al. 1977; Panasyuk et al. 1973 and Rana Radhakanta et al. 2007). They have also conducted experiments on toroid samples to measure the magnetic properties using hysteresis loop tracer at 50 Hz.

The obtained results are here reported in Table 2.10 at the maximum applied field of about 60 Oe. At a given magnetizing force the saturation magnetization increases with the increase of P content in iron up to 0.45 wt.%.

Table 2.10: Magnetic properties of alloys under D.C mode (Chaurasia et al. 2012).

Alloy	Coercivity(Oe)	Sat.magnetization(G)	Retentivity(G)	Permeability(μ)
Fe-0.30P	1.241	10716	8121	185
Fe-0.35P	1.206	15599	8354	270
Fe-0.45P	0.384	17499	10836	294
Fe-0.65P	0.353	16666	8229	288
Fe-0.80P	0.375	14145	6402	241

The improved properties of the phosphorous containing materials may be attributed to their higher density achieved (Lindskog et al. 1977). Lindskog et al. 1977 have reported that the saturation magnetization varies from 14,700 gauss to 15,200 gauss in Fe-P alloys. The maximum value is corresponding to 0.6% P whereas the saturation magnetization varied from 14,145 gauss to 17,499 gauss with a maximum at 0.45% P (Chaurasia et al. 2012). The obtained value of coercivity in the range of 0.35–1.24 Oe with a minimum obtained corresponding to 0.65% P (Chaurasia et al. 2012) which is lower than that achieved by conventional route of powder metallurgy as reported here coercivity varies from 1.22 Oe to 1.42 Oe with a minimum at 0·70% P (Lindskog et al. 1977). The lower coercivity may be due to the presence of lower porosity in the alloy (and hence higher density).

2.11 Fe-P-C SYSTEM

2.11.1 Fe-P-C Phase Diagram

The partial Fe-P-C phase diagram (Fig.2.34) describes three intermediate phases such as Fe_3P (Tetragonal), Fe_2P (Hexagonal), and FeP (orthorhombic) (Raghavan 2004). The two-sublattice model has been used for the FCC and BCC solid solutions. Fe and P substitute for each other on the substitutional sites whereas Vacancies (Va) and C reside in the interstitial sublattice. The liquidus projection and four isothermal sections at 1100, 1000, 900 and 800 °C

have been computed for the metastable equilibrium with Fe_3P. The liquidus projection is represented in Fig.2.34.

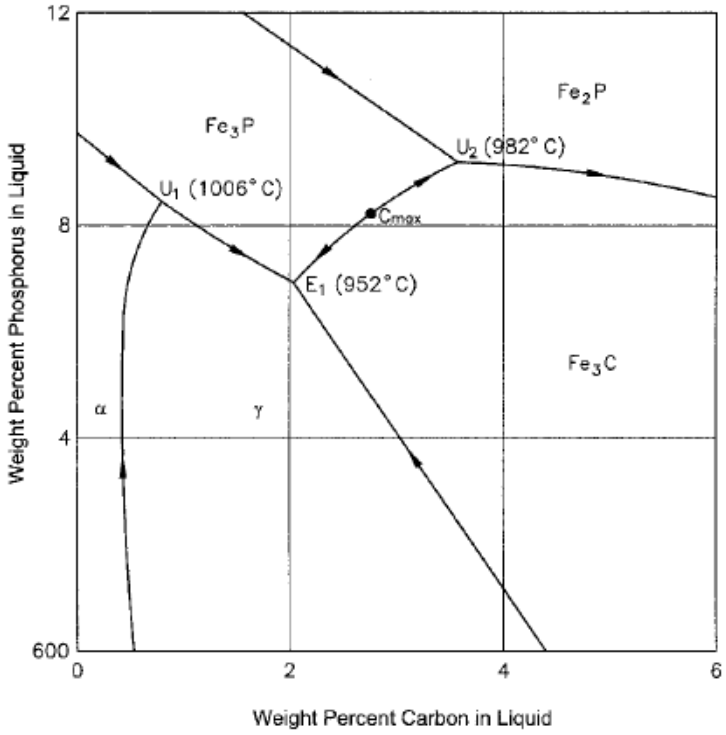

Figure 2.34: C-Fe-P computed liquidus projection (Raghavan 2004).

At the junction of Fe_3P-Fe_3C, the liquidus shows that an additional transition reaction U2 is present in the computed projection as shown in Fig.2.34. The computed isothermal sections at 1100, 1000, 900, and 800 °C are depicted in Fig. 2.35 and 2.36.

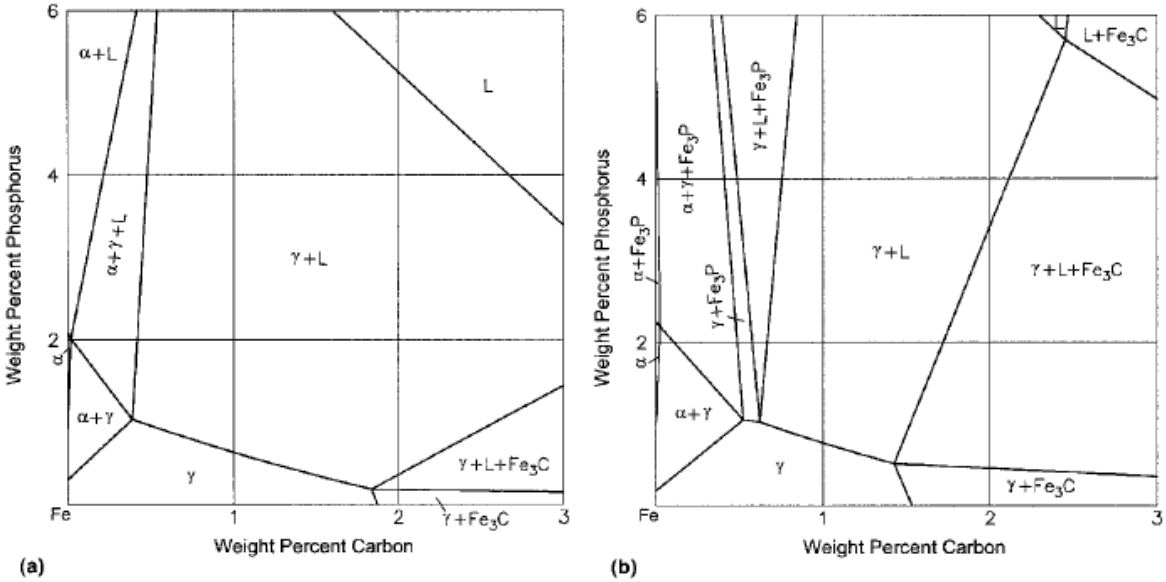

Figure 2.35: C-Fe-P computed isothermal sections at (a) 1100 °C and (b) 1000 °C (Raghavan 2004).

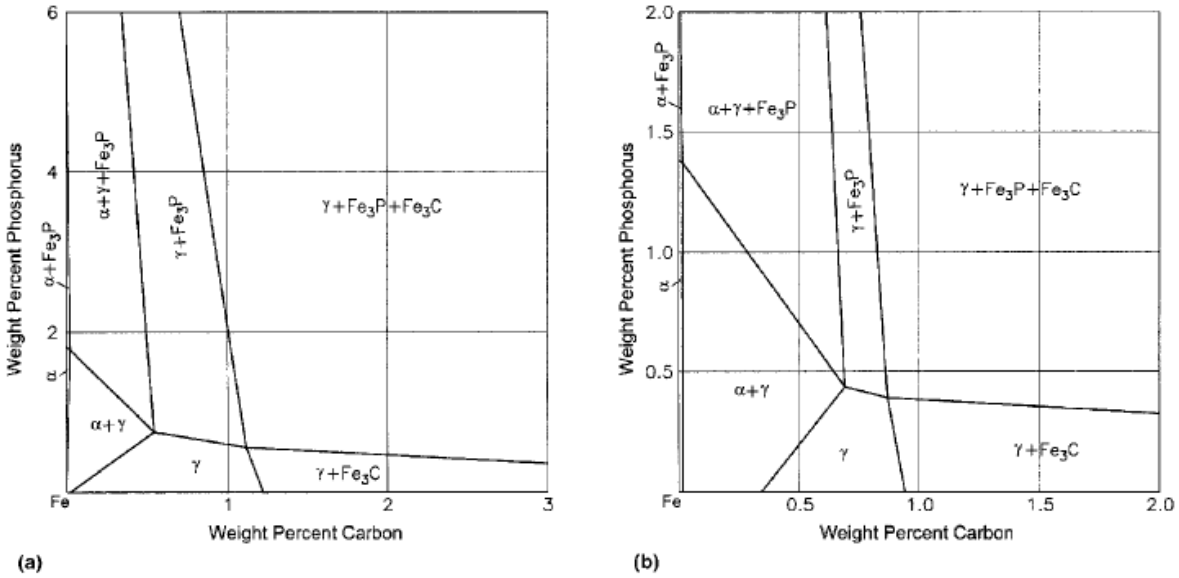

Figure 2.36: C-Fe-P computed isothermal sections at (a) 900 °C and (b) 800 °C (Raghavan 2004).

The vertical section at 0.1 wt. %P is represented in Fig. 2.37. The invariant reaction observed at 952 °C is the ternary eutectic reaction:

$$L \leftrightarrow \gamma + Fe_3C + Fe_3P \quad \text{----------} \quad 2.5$$

The horizontal at 766 °C corresponds to the transition reaction as below placed at ~750 °C by [Rag. 1988].:

$$\gamma + Fe3P \leftrightarrow \alpha + Fe3C \quad \text{----------} \quad 2.6$$

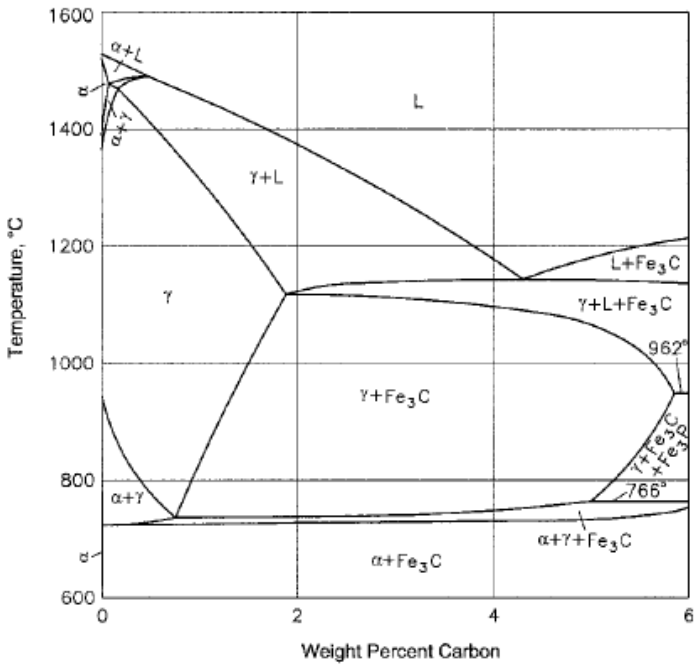

Figure 2.37: C-Fe-P computed vertical section at P =0.1 wt. % (Raghavan 2004).

2.11.2 Grain Boundary Segregation of Phosphorus

There is a severe problem of segregation of alloying element in steels such as phosphorus (P), sulfur (S), arsenic (As). This is due to the fact that inter-granular failure occurs because of decohesion of the grain boundary. Phosphorus induces brittleness in the steels which deteriorates the mechanical properties (Islam 2011). Phosphorous is found to have a pronounced effect in weakening the grain boundaries of iron. When iron phosphate is added to iron in the hydrogen furnace, complete reduction occurred with substantially no loss of phosphorous.

Drawback:

- It has been observed that the brittle fracture increased with the increasing the phosphorous content. The iron containing 0.3% P does not show the brittle fracture which starts over the 0.45% P.
- The use of Fe-P parts is that owing to the liquid phase sintering that occurs, dimensional control is more difficult.

The problem of brittleness has been reduced by small addition of carbon (generally between 0.1 and 0.4%) to the system. A maximum is obtained at about 0.02-0.03% carbon (Hansel and Grabke 1986). It is also allowed to go with the high phosphorus addition up to 1.2%, without a problem.

In another study, Fe-P-0.05%C alloys did not show any indications of grain boundary failure (Hopkins and Tipler 1958). Abiko et al. 1982; Suzuki et al. 1985 found that optimum concentration of carbon for containing ductile failure was about 0.01%. The intergranular failure displayed below 0.01%C while they showed transgranular failure above of that. The strength is observed high in the transgranular mode. Raghavan 2004; Tengzelius 1993; Hanse et al. 1969 have reported that the displacement of phosphorus by carbon as the following reaction:

C (dissolved) + P (segregated) = C (segregated) + P (dissolved) ---------- 2.6

Tengzelius 1993 has reported that the precipitation of Fe_3P at a given phosphorus content starts at a lower temperature (~950 ^{o}C) by addition of small amount of carbon in the alloy than in the absence of carbon. In order to improve the understanding of brittleness, this study is more helpful for technically understanding the alloys. Stewart et al. 2000 have investigated that the solubility of phosphorus in austenite is low. This decreases the grain

boundary segregation of phosphorus. The solubility of carbon in austenite is high correspondingly and carbon is located in the grain boundary area.

2.12 Fe-P-C ALLOYS AND THEIR PROPERTIES

Researchers have studied archaeometallurgical structures widely (Balasubramaniam 2002; Balasubramaniam 2003). They have found the presence of higher amount of phosphorus in early iron usage than those found in the modern steels. The microstructures of archeological irons are similar to those produced by the ferrite-austenite transformation or diffusion of phosphorus.

Since the phosphorus in steels shows the deterioration in the mechanical properties with an increase in the phosphorus content in the iron. Presence of P also induces brittle behavior (cold shortness) during cold working. That is why the content of the phosphorus in the modern steels is limited to <0.04wt.% while the archaeological phosphoric iron generally contained 0.05-0.50wt. % (Balasubramaniam 2002). The level of the phosphorus up to 1% has been detected in some artifacts. Therefore modern steel plants control the level of phosphorus in the alloy to maintain better mechanical properties. However, the manufacturing phosphoric iron by forging does not show hot shortness or brittle at higher temperatures in the artifacts. The effect of phosphorus has also been observed during cold working. It produces the work hardening in the iron. Phosphorus has shown the solid solution strengthening effect in ferrite which is same in the order of as shown by the interstitial elements, carbon, and nitrogen. After the study, Stewart et al. 2000 have found an improvement in strength due to the addition of phosphorus in iron. The brittle failure occurs at the point of reduction in area. The presence of carbon reduces the brittle nature of these alloys.

Lindskog et al. 1977 have investigated that the deterioration in mechanical properties of phosphorus containing alloys can be minimized by the addition of small amount of carbon in the alloy. It has also been found that alloys with carbon contents of about 0.01wt.% show ductile failure during impact test at lower temperatures than alloys with either higher or lower carbon contents. Beyond this limit of the carbon addition, the steel showed the brittle behavior during impact testing which is the formation of the carbides that acts as initiation sites for the fracture (Suzuki et al. 1985).

Molinari et al. 1992 have analyzed the sintering behavior of Fe-P-C alloys. They have described the mechanism of sintering of the phosphide and graphite particles as shown in Figure 2.38. The rate of diffusion of carbon into the matrix is higher than phosphorus due to the

different characteristics of the sites. Since carbon is an interstitial solid solution whereas phosphorus is a substitutional solid solution.

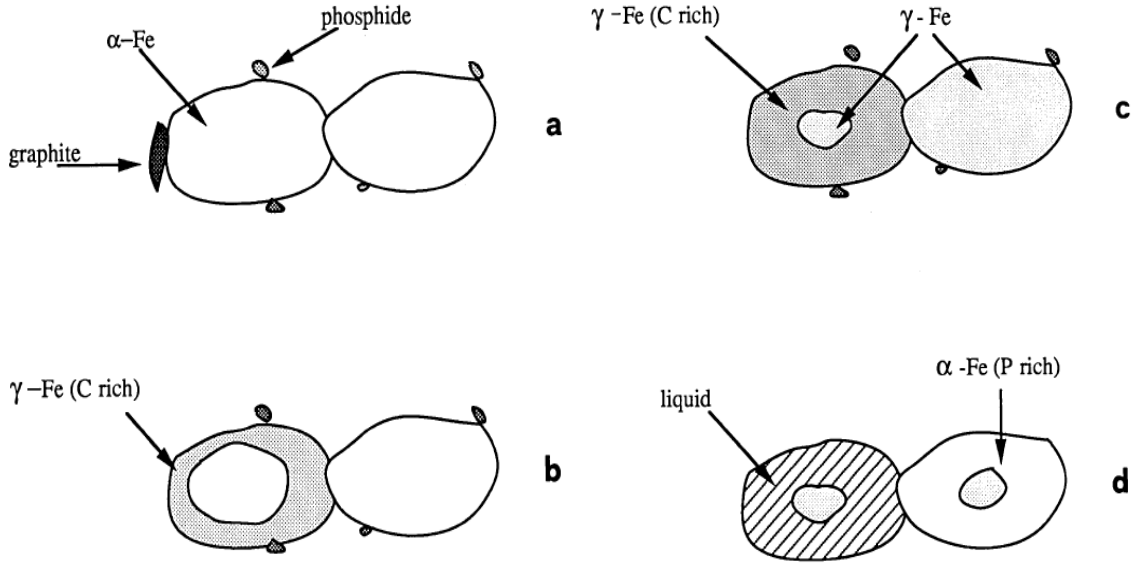

Figure 2.38: Schematic diagram of sintering mechanisms of Fe-P-C alloy (Molinari et al. 1992). (a) Phosphide and graphite particles are in contact with the iron particles, (b) Diffusion of carbon into the matrix starts, (c) Diffusion couple of phosphide and matrix particles, and (d) Two different transformations of particles.

The final state of the elemental particles is characterized by two types of austenite as shown in Figure 2.38 (c). The phosphide and matrix particles form a diffusion couple which may lead to two different transformations. The transformations depend on the austenite type with which phosphide particles are in contact (Figure 2.38(d)) as below:

γ (C poor) + phosphide $\rightarrow \gamma$(P rich)$\rightarrow \alpha$ (P rich) ---------- 2.7

γ (P rich) + phosphide $\rightarrow$ liquid (steadite) ---------- 2.8

Hopkins and Tipler 1958 have also shown in their investigation that mechanical properties (strength and hardness) improved by the addition of phosphorus in iron. Dieter 1986 has restated the values of strain hardening exponent measured for several steels given in Table 2.11. The strain hardening exponent tends to decrease as the carbon (Bleck 2004) content is increased but changes in the microstructure. Hu 1989 has investigated in all cases that the strain hardening exponents are less than those for the phosphoric irons. In order to better understanding the stress-strain relationship of a metal during plastic deformation may be determined by the following power curve relation:

$\sigma = K \varepsilon^n$ ---------- 2.9

Where σ is the true stress, ε is the true strain, K is the strength coefficient and n is the strain hardening exponent.

According to Dieter 1986, it can be shown that the maximum reduction in area r_{max} is one pass that can theoretically be achieved for a ductile material as per the following relationship:

$r_{max} = 1- \exp(-\eta[n + 1])$ ---------- 3.0

Where, η is the efficiency of the process (i.e. the proportion of work used in producing a useful shape change, and n is the strain hardening component.

Table 2.11: Values for strain hardening coefficient n and strength coefficient K at room temperature (Dieter 1986).

Steel	Condition	Strain hardening exponent(n)	Strength coefficient K, MPa
Fe-0.05C	Annealed	0.26	530
SAE 4340 (0.38-0.43wt.%C)	Annealed	0.15	640
Fe-0.6C	Quenched and tempered 540 ^{0}C	0.10	1570
Fe-0.6C	Quenched and tempered 705 ^{0}C	0.19	1230

Some work has displayed that the true stress-strain curve often shows several distinct stages (Figure 2.39). Each stage described by its own value of strain hardening exponent (Mediratta et al. 1990). Table 2.12 shows the strain hardening exponent (n) at different stages of work hardening. Therefore, it has been supposed that the phosphoric alloys would display better cold drawing properties than any of the steels quoted. According to Mediratta et al. 1990, in the early stages of plastic flow, the strain hardening exponent is influenced by the behavior of the matrix (Bleck 2004) and is not sensitive to the presence of the second phase. All the dual phase steels display three-stage strain hardening except steel 3wt. %C. The dual phase steel having 3wt. %C shows four-stage strain hardening behavior due to the highest volume percentage of martensite (47.8%) in the alloy.

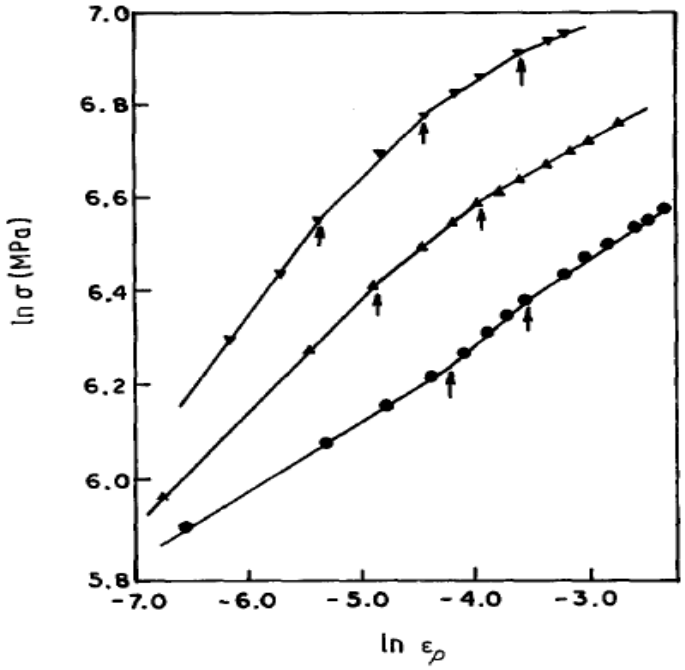

Figure 2.39: True stress-strain graphs of dual phase steels with varies volume fraction of martensite (V_m) of fixed carbon content (C_m= 0.35%). It shows the different stages of strain hardening. Arrows indicate transition strains. (●) 1C, 16.5 %;(▲) 2C, 32.2 %;(▼) 3C, 47.8% (Mediratta et al. 1990).

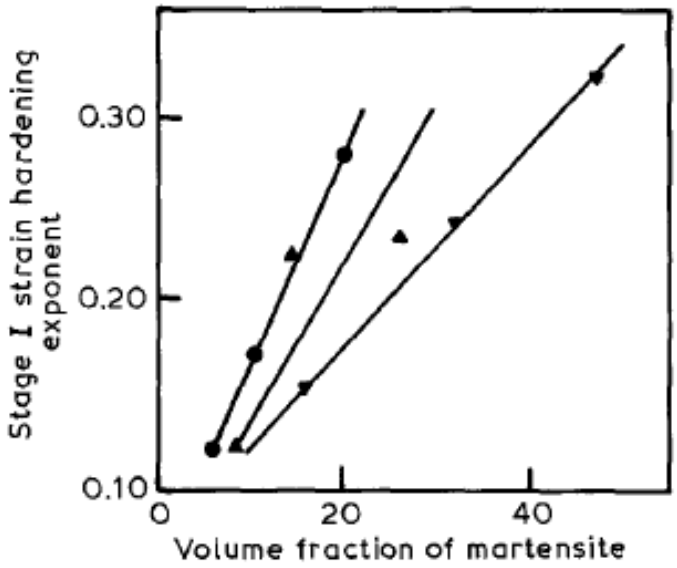

Figure 2.40: Stage I strain hardening exponent (n) vs. the volume percent martensite for different values of $C_{m.}$ (●) 0.65%; (▲), 0.54%; (▼), 0.35% (Mediratta et al. 1990).

In stage I, the martensite particles are distributed uniformly in the ferrite matrix which is surrounded to the mobile dislocations/ residual stresses (Figure 2.40). Thus, in this stage, homogeneous deformation takes place in the ferrite matrix. In the transition stage from I to II,

inhomogeneous deformation of the ferrite occurs due to deformation of the ferrite matrix (Byun 1993). Since in stage II the higher dislocation in a single phase material brings due to the deformation regime of ferrite which increases a significantly higher dislocation density. As a result of a cross slip and dynamic recovery in stage II associated with cellular dislocation array (Sherwood and Hamilton 1991). The plastic strain (about 10%) has been observed in polycrystalline iron in the transition stage from II to III, at 4 to 6% strain in spherodized carbon steels (Atkinson 1984). Also, dual phase steels experienced 4 to 6% plastic strain which was independent of the amount of martensite. Mediratta et al. 1990 have observed the plastic strains of 1 to 8% in this transition which depends upon the vol. % of martensite. Higher vol. % of martensite (V_m) leads to transition at lower strains. This difference in transition strain is due to the quality of ferrite (Mediratta 1990; Paruz 1989). The higher values of V_m are related with the higher level of mobile dislocation density. Ferrite quickly becomes work hardened with the increase in V_m in the third stage, which leads to lowering of the n value. The lower values of the strain hardening exponent in the third and fourth stage are partially responsible for the deformation of martensite.

Table 2.12: Strain hardening exponent (n) at different stages of work hardening (Mediratta et al. 1990).

Steel	C_m (%)	V_m (%)	Stage I (n_1)	Stage II (n_2)	Stage III (n_3)	Stage IV (n_4)
1A		6.5	0.120	0.196	0.162	---
2A	0.65	10.8	0.173	0.201	0.154	---
3A		20.1	0.293	0.230	0.130	---
1B		8.6	0.119	0.183	0.156	---
2B	0.54	14.8	0.226	0.201	0.145	---
3B		26.5	0.237	0.227	0.138	---
1C		16.5	0.153	0.198	0.160	---
2C	0.35	32.2	0.245	0.199	0.132	---
3C		47.8	0.329	0.240	0.132	0.10

2.12.1 Mechanical Properties

The influence of carbon upon the mechanical properties of Fe-P alloys has been shown in Figure 2.41 (Höganäs Handbook for Sintered Components-3 2004). Lindskog et al.1977 have also studied the behavior of Fe-P-C powder metallurgy alloys with different amount of phosphorus (0.3-1.2%) and carbon content in the range of 0 to 0.49%. They have reported that the high phosphorus contents than 0.6% shown very large shrinkage during the sintering which

makes it impossible to keep close tolerances. They have established that a minute carbon addition brings about a remarkable stabilization of the dimensional change. They have also investigated that tensile strength and elongation improved by the addition of a minute carbon in Fe-P alloys. Liu and Rana 2014 have also investigated that the addition of carbon between 0.15 to 0.25% in the steel is used to increase the strength. However, if the amount of carbon increases beyond this limit, the amounts of cementite will be increased which would contribute to an increase in strength, but greatly decrease ductility of steel .

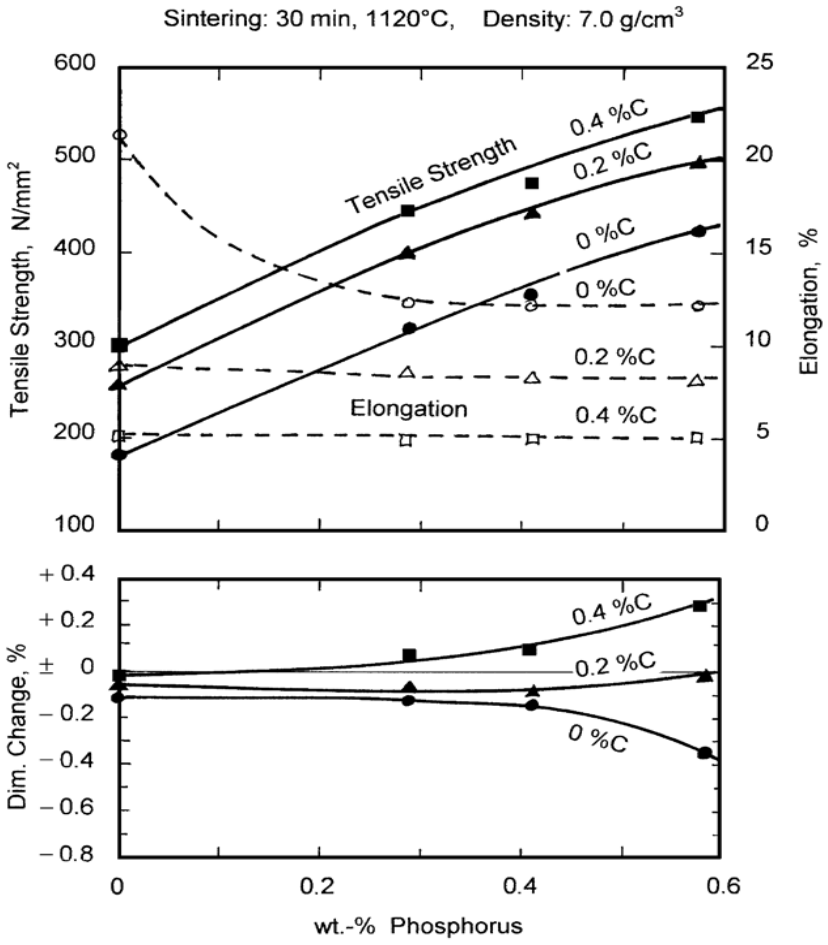

Figure 2.41: Effect of carbon additions upon the properties of sintered iron phosphorus alloys. (Höganäs Handbook for Sintered Components-3 2004).

The microstructure of carbon containing Fe-0.45%P alloy is shown in the Figure 2.42(b) whereas Figure 2.42(a) shows the microstructure of Fe-0.45%P. These alloys have been developed by compaction and sintering process at a sintering temperature of 1120 ^{o}C for 30 minutes. Figure 2.43 shows the effect of phosphorus additions upon the density of sintered iron.

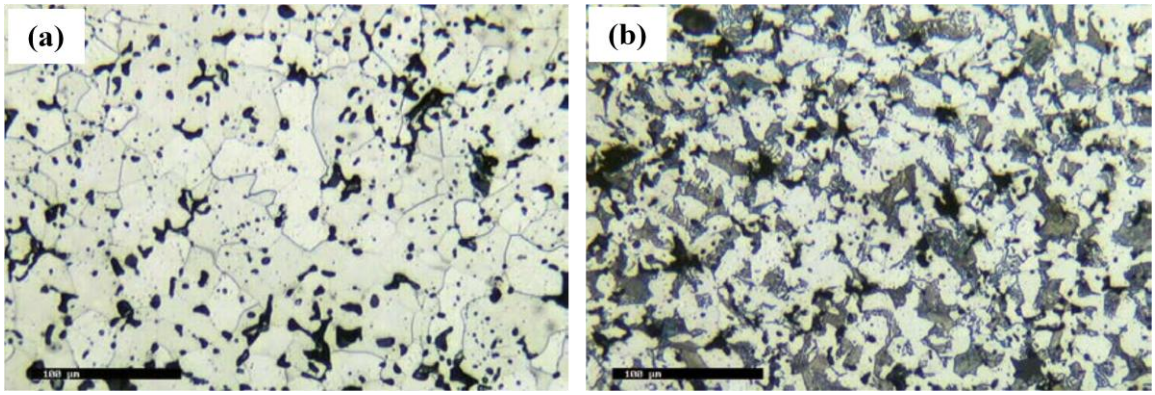

Figure 2.42: (a) Microstructure of Fe-0.45%P alloy and (b) Microstructure of Fe-0.45%P-0.5% C alloy (Höganäs Handbook for Sintered Components-3).

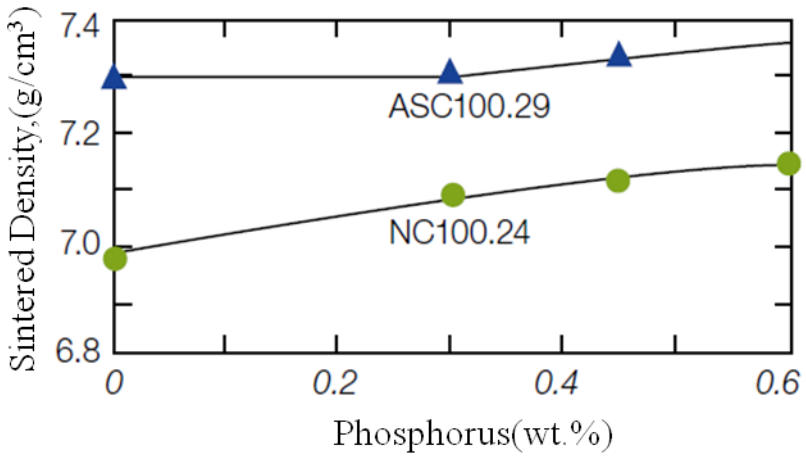

Figure 2.43: Effect of phosphorus additions upon the density of sintered iron (Höganäs Handbook for Sintered Components-3 2004).

Addition of 0.01%C in Fe-P alloys is beneficial in displacing phosphorus away from grain boundary region by site competition effect and obtaining good ductility in the phosphoric iron. In addition to this, P forms a solid solution strengthening and work hardening effect of phosphorus which increases the strength of the alloy.

Molinari et al.1992 have studied the effects of the P and C on the dimensional behavior of iron. They have observed that all the samples display favorable dimensional behavior with the presence of carbon.

The alloys containing a small quantity of alloying elements, 0.25%C-0.45%P and 0.50%C-0.45%P, show the lowest values of σ_{UTS} (Figure 2.44). This is the prevalence of ferrite microstructure and a ductile fracture surface (Straffelini et al. 1993). Straffelini et al. 1993 have interpreted that the low strength as a consequence of insufficient process (a low increase of the

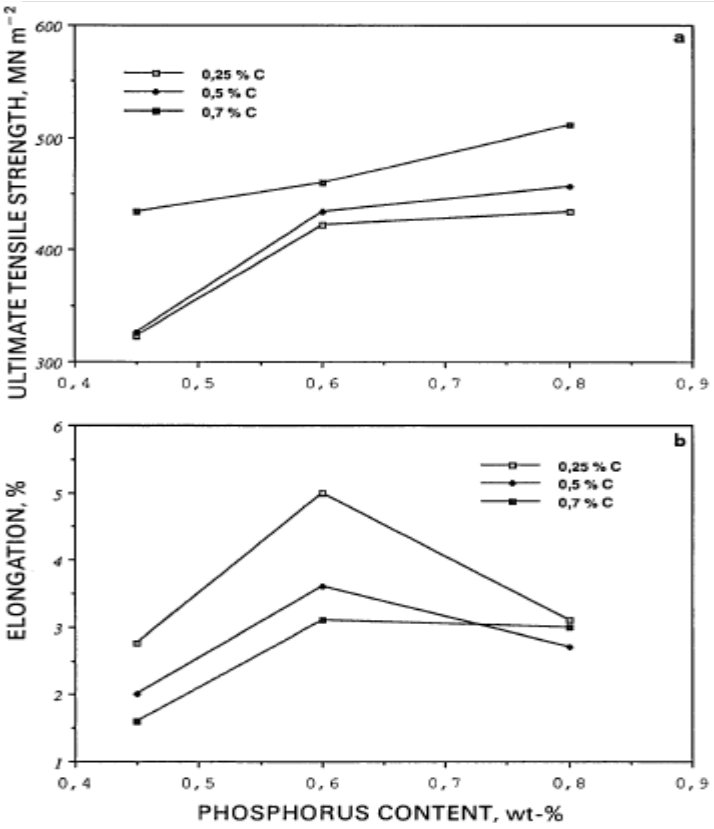

Figure 2.44: Effect of phosphorus on carbon alloys containing (a) 0.25% C (b) 0.50%C (Straffelini et al. 1993).

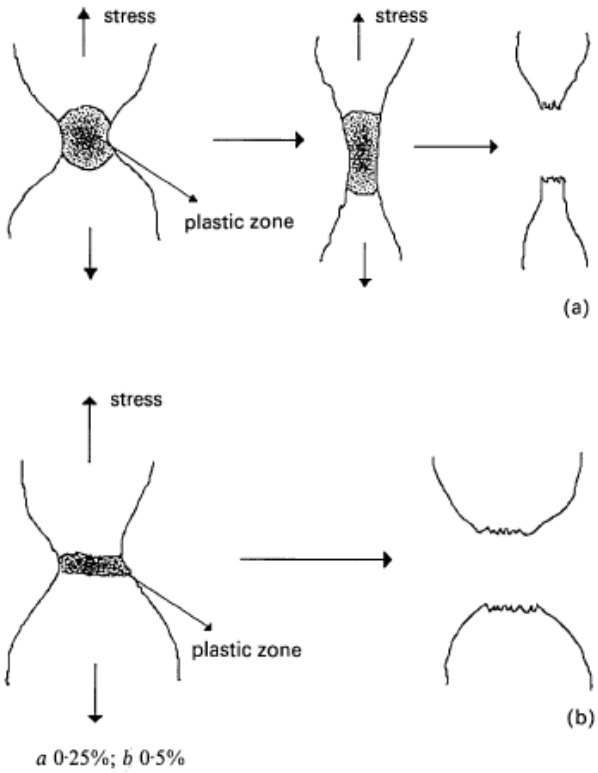

Figure 2.45: The deformation mechanism of P/M containing powder metallurgy ferrous alloys (Straffelini et al. 1993).

neck size ratio) and of limited strengthening of the ferrite. This is due to the fact that the phosphorus remains localized in a few ferrite areas. The alloy (0.50%C-0.45%P) shows lower percentage elongation than that of alloy (0.25%C-0.45%P) (Figure 2.44b) while the former shows a higher percentage of ductile fracture area.

The behavior (σ_{UTS} and A) of alloy (0.70wt.%C-0.45wt.%P) is entirely different from the other two alloys with the same P content. This is due to the presence of a large amount of pearlite in a phosphorus-rich ferrite matrix. These phases show a high yield point and triaxial stress field. The alloys containing 0.60wt.%P are characterized by an increase in strength and ductility. At the low level of carbon maximum ductility was observed in the alloy. The alloy with composition 0.25wt.%C-0.60wt.%P shown high deformability and zones characterized by high hardness (pearlite and phosphorus-rich ferrite) (Straffelini et al. 1993). Figure 2.45 shows the deformation mechanism of P/M containing powder metallurgy ferrous alloys.

2.12.2 Tribological Properties

Welsh 1964 studied broad trends of wear rate when steel containing carbon (0.026 to 0.985%C) rub together without lubrication using pin and ring apparatus. He has observed that first mild wear regime occurs in the range of load up to 100g. Between 100 and 200g, the wear rate increases by two orders of magnitude and remain at this high level over the load range up to 5 Kg.

Abouei et al. 2007 have investigated the tribological properties of dual phase steel containing 0.2 wt.%C using a pin on disc apparatus under the different loads of 21.3, 28.5, 35.7 and 42.6N and at a constant sliding speed of 1.20 m/s. They have analyzed the worn surfaces and wear debris of the specimens. Gutsfeld and Thummler 1990 have studied the wear behavior of sintered steels containing 0.6wt.%P and 0.90wt.%C using a pin on ring. In their study they have investigated that hard phase affect the wear behavior of material by decreasing the area of contact. As for as sliding wear applications are concerned, the alloy containing 0.6%P has proven highly efficient in this area. The general advantage of this class of material reflected the superior wear properties (Rosskamp et al.1996).

Tanase et al. 1990 have investigated the wear properties of an alloy having a high volume fraction of carbides using a block on ring test. As volume fraction of carbide increases, the area fraction of the metallic matrix decreased. As a result, improves the wear properties.

CHAPTER 3

FORMULATION OF PROBLEM

From the extensive review of the available literature the plan of the present work was determined:

1. Most of the studies of P addition in Fe-based alloys have been carried out using ferrophosphorus as a source of P. A chemical route has been employed for addition of P in the iron to develop impurity free master alloy (iron phosphate) powder.
2. As per the literature, most of the Fe-P alloys have been developed with a limited amount of P addition by conventional powder metallurgy route (compaction and sintering) which showed the problem of shrinkage or dimensional instability of the component. In the present investigation, these problems have been circumvented by the use of hot powder forging.
3. Use of powder forging to achieve uniform distribution of phosphorus in ferrite matrix leads to high density alloy components. This is important as almost all mechanical properties and tribological properties of these alloys are influenced by the presence of porosity.
4. Development of Fe-P alloys with improved ductility has been achieved by avoiding liquid phase sintering on account of solid-state processing during hot powder forging.
5. Most of the studies conducted in the past have been restricted to the correlation between the microstructure and the mechanical properties of the Fe-P alloys. There are very few investigations carried out to understand the tribological properties of the Fe-P alloys. However, the wear behavior of Fe-P P/M alloys had hardly been paid any attention.
6. There are limited studies on the influence of carbon in Fe-P alloys. These are limited to the correlation between microstructure and mechanical properties in the press and sinter conditions. However, in the present investigation relation between microstructure and mechanical properties including tribological properties has been investigated in the hot powder forged conditions.

CHAPTER 4

EXPERIMENTAL WORK

This chapter deals with the experimental details carried out in the present work in respect of the development of iron-phosphorus/iron-phosphorus-carbon alloys and characterization of the different alloys developed.

4.1 CHARACTERISATION OF IRON POWDER

The average particle size and size distribution of water atomized iron powder (M/S HOGANAS AB, Sweden) were measured on computerized laser particle size analyser equipment (ANKERSMID CIS 100). The physical properties of the atomized iron powder are as below:

Grade No	: AHC100.29
Supplied by	: M/S HOGANAS AB, Sweden
Particle size	: 0.17mm
Apparent density	: 2.59 gm/cm^3
Flow	: 25-28 second per 50 gm.
Compressibility	: 6.65-6.68 gm/cm^3
Hydrogen loss (%)	: 0.1-0.2(i.e. reducible oxygen content)
Carbon content	: 0.01-0.02

A given quantity (0.5mg) iron powder sample was required for the measurement. The morphology of powder was examined under SEM (Zeiss EVO18 Special Edition).

4.2 PREPARATION OF MASTER ALLOY (Fe-P) POWDERS

For the preparation of 1 kg master alloy containing 5wt.% phosphorous (P), 950 gm of atomized elemental iron powder was mixed with 100 ml ortho-phosphoric acid (H_3PO_4). The elemental iron powder (kept in a tray) was mixed with diluted orthophosphoric acid. The orthophosphoric acid was diluted with distilled water (approximately 800 ml) in order to completely dip the iron powder. The iron powder dipped in diluted orthophosphoric acid was left in the open air to dry. The orthophosphoric acid reacts with the surfaces of iron particles and forms $Fe_3 (PO_4)_2$ on the iron particle surface by the reaction:

$$3Fe + 2H_3PO_4 \rightarrow Fe_3 (PO4)_2 + 3H_2 \quad \text{----------} \quad 4.1$$

The composite (i.e. coated) powder so produced was decanted and allowed to dry as described. The situation is schematically illustrated in Figure.4.1

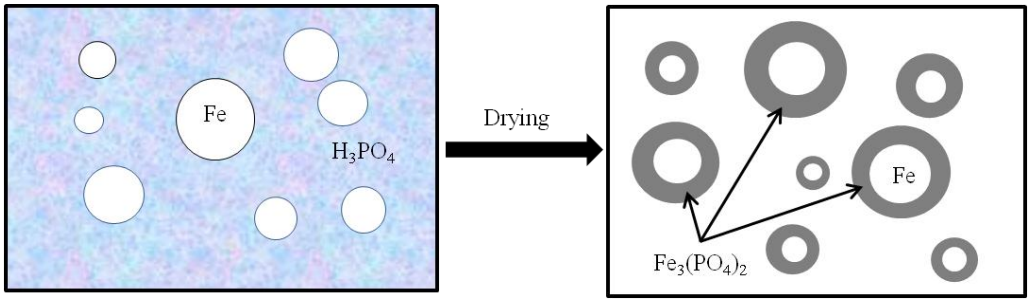

Figure 4.1: Schematic diagram showing the preparation of iron-phosphate.

The physical properties of the orthophosphoric acid, which was used in the present investigation, is as follows:

Purity : 83-98%

Contains in 1cc : 1.75 gm H_3PO_4

4.3 PREPARATION OF Fe-P ALLOY POWDER

As per the planned compositions, an equivalent amount of master alloy powder ($Fe_3(PO_4)_2$) was thoroughly mixed with water atomized iron powder for the preparation of six different compositions of the alloy as shown in Table 4.1. Mixing of one kilogram powder was carried out in a laboratory jar mill for 2 hrs at 80 rpm using steel balls with 1:5 ball to charge ratio. The steel balls of bearing grade of the 10mm diameter were used. These compositions were made to investigate the effect of varying P content (0-3wt. %) in the alloy.

Table 4.1: Fe-P alloy powders.

Sr.No.	P (wt. %)	Fe (wt. %)	Alloy Composition
1	0.00	Bal.	Fe
2	0.35	Bal.	Fe-0.35wt.%P
3	0.65	Bal.	Fe-0.65wt.%P
4	1.00	Bal.	Fe-1wt.%P
5	1.30	Bal.	Fe-1.3wt.%P
6	2.00	Bal.	Fe-2wt.%P
7	3.00	Bal.	Fe-3wt.%P

4.4 PREPARATION OF Fe-P-C ALLOY POWDER

The equivalent amount of Fe-P master alloy powder (iron phosphate) was mechanically mixed with a required amount of natural crystalline graphite powder (as a source of carbon supplied by Graphite India Ltd. Kolkata, India) and iron powder for the preparation of ternary alloy as shown in Table 4.2. The process adopted was similar to the one stated for binary alloy powder.

Table 4.2: Fe-P-C alloy powder

P(wt.%)	**C (wt.%)**	**Fe (wt.%)**	**Alloy composition**
0.65	0.20	Bal.	Fe-0.65wt.%P-0.20wt.%C

4.5 PREPARATION OF MILD STEEL (M.S) CAPSULE AND ENCAPSULATION OF POWDERS

This mild steel (MS) capsule (Figure 4.2) is a hollow tube of 61.5 mm outer diameter (OD), 2 mm wall thickness and 80 mm length fabricated with hemispherical end caps at both sides by joining with the help of electric arc welding.

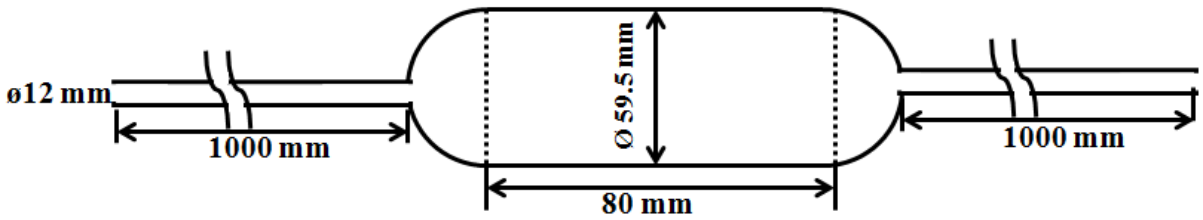

Figure 4.2: Hollow mild steel capsule.

A hole of 10mm was provided at the center of end caps. The end caps were joined by electric arc welding with the hollow can as well as with 12mm diameter hollow pipe of length 1000 mm for the passing of hydrogen gas during heating.

4.6 HEATING OF ENCAPSULATED POWDER

The encapsulated mixed powder was kept in a tubular furnace. The ceramic tube is surrounded by heating elements circumferentially for the heating of the capsule as shown in Figure 4.3.

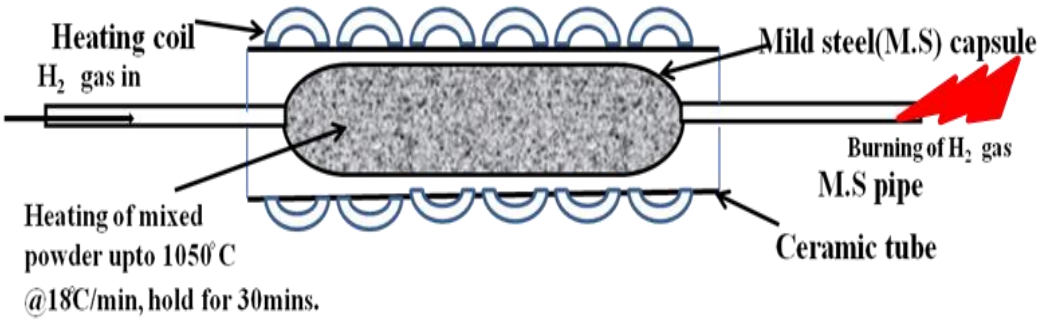

Figure 4.3: Heating of encapsulated powder.

The heating of the encapsulated powders was carried out at a rate of 18 °C/min and held for 30 minutes at 1050 °C in the tube furnace in the presence of a continuous supply of dry hydrogen. During heating iron powder coated with iron-phosphate converted into iron-phosphide prior to the hot forging. The hydrogen gas was used to remove the oxide layer from the surfaces of the powders during heating at a high temperature. The cleaning of the powder during heating provides good bonding between the particles which help in getting nearly full density. The following reaction takes place during the heating of encapsulated powder:

$$3Fe + Fe_3(PO_4)_2 + 8H_2 \rightarrow 2Fe_3P + 8H_2O \quad \text{----------} \quad 4.2$$

4.7 HOT FORGING OF HEATED CAPSULE POWDER

The hot capsule after holding for 30 min. was taken out from the furnace and placed in the channel die (Figure 4.4) of dimension (220 × 75 × 25 mm^3) fitted over a semi-automatic 100 metric ton capacity friction screw driven forge press (make BIRSON™ Ludhiana, India) (Figure 4.5 & 4.6) to obtain the forged slabs (of approximate thickness 15mm). The schematic of the forging process is shown in Figure 4.7.

Figure 4.4: A channel die of dimension 220(l) × 75(w) × 25(h) mm^3.

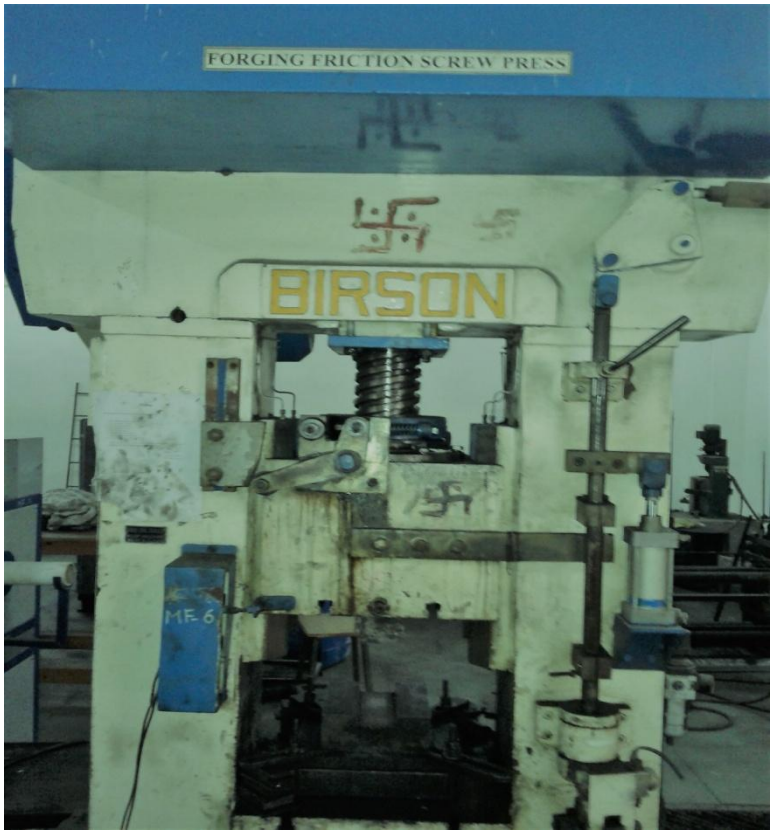

Figure 4.5: Friction screw driven forge press.

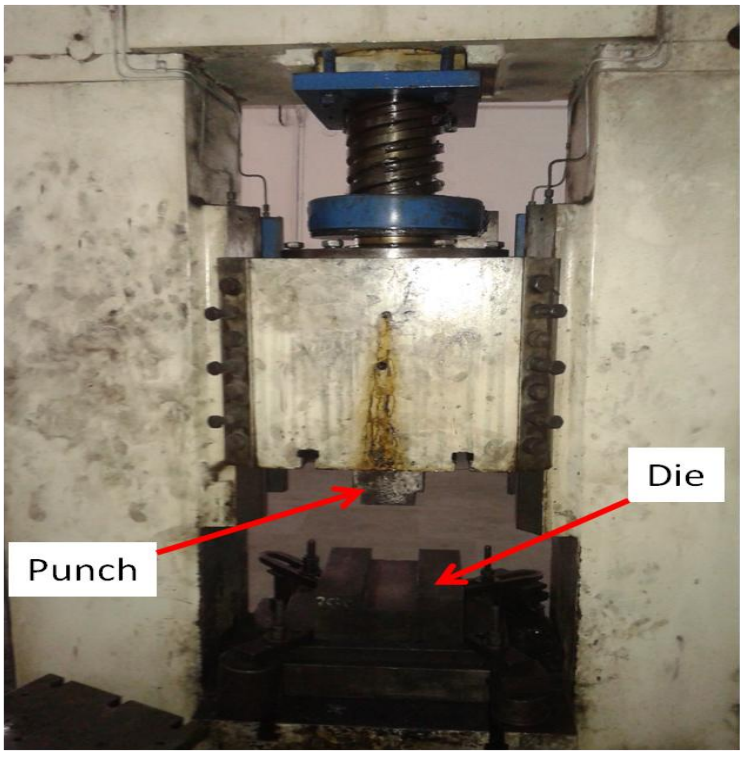

Figure 4.6: Die and punch placed in Friction screw driven forge press.

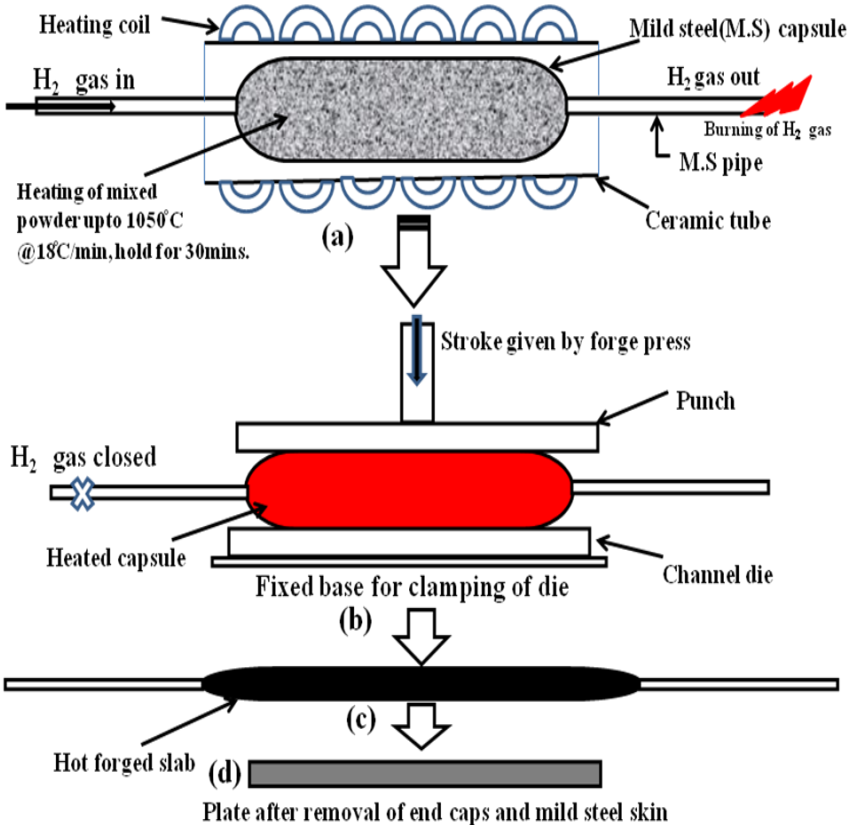

Figure 4.7: Schematic diagram of a process for development of Fe-P alloys.

The forged slabs were left in the open atmosphere to cool down. The end pipes of 12 mm diameter and 1000mm length were removed using handsaw. The forged slabs were obtained as shown in Figure 4.8.

Figure 4.8: Forged slab after removing both gas flow pipes.

After cooling of forged slabs in the open atmosphere, the forged slabs were again put in the muffle furnace for heating up to the forging temperature. The heated slabs were taken out

from the muffle furnace and placed on the channel die for re-forging. This was repeated two times to obtain nearly full density. After removal of the end caps rectangular slabs of approximate dimension length 110mm, width 70mm, and thickness 15mm were obtained as shown in Figure 4.9.

Figure 4.9: Forged slab after reforging. (a) The thickness of the slab (b) Width of the slab.

4.8 HOMOGENIZATION

The forged slabs were then homogenized at 1100 ºC for 2 h in a muffle furnace whose temperature was controlled to ±10̊ C. This was followed by air cooling to ensure uniform distribution of alloying elements throughout the cross-section of the forged component. The additional purpose of homogenization is to eliminate brittle non-equilibrium phases present along grain boundaries. After homogenization, the end hemispherical caps of mild steel capsule were cut off and the mild steel cover was also removed by machining. A forged plate measuring $120 \times 73 \times 10$ mm was thus obtained (Figure 4.7d).

4.9 SAMPLE PREPARATION FROM THE FORGED SLAB

Samples were sectioned from the forged slabs of different composition by precision cutting saw for metallographic studies, hardness measurement, density measurement, SEM examination, X-ray diffraction (XRD), tensile test, Charpy test and Wear test.

4.10 STRESS RELIEVING TREATMENTS

The sectioned specimens were stress relieved by keeping them in a muffle furnace at 600 ºC for 1h to relieve the residual stresses and then cooling in the furnace. The oxide layers were removed from the surface of the specimens using emery paper.

4.11 MEASUREMENT OF DENSITY

The densities of forged alloys were estimated by measuring the volume of a given piece of the alloy by water displacement method (Archimedes principle) and its weight in air using an electronic balance. Samples were weighed in the air (M_a) and distilled water (M_w) by placing on a stainless steel pan. The pan along with the sample was freely suspended by an attachment provided at the bottom of the weighing machine in a glass beaker filled with distilled water. The level of water in the beaker and depth of immersion of the compact holding pan were maintained constant. Measurements were repeated on the same sample for 2-3 times and average weights were used to report densities. The density was calculated by using the following formula:

$$\rho = \frac{Ma}{Ma - Mw} \qquad \text{----------} \qquad 4.3$$

The measured density of the alloys approached the full density range from 7.74-7.87g/cc on account of increase in the content of P in iron. The maximum value obtained corresponding to 2wt. %P.

4.12 METALLOGRAPHIC EXAMINATION

The metallographic examination was carried out to study the distribution of phosphorus in the Fe-based alloy and microstructure of phases using optical microscopy as well as SEM. Microstructural specimens (having about 10 x 10 mm surface area) were cut from the forged and annealed slab. These samples were mounted in 20mm diameter cold setting phenolic resin based quick hardening compound. Conventional polishing methods are used for the preparation of the sample, such as grinding on the belt as well as on emery paper up to 4/0 grade. The paper polished samples were cleaned with distilled water before cloth polishing. The cloth polishing was performed manually. The cloth was mounted on 8'' diameter aluminium disc which rotated at 200-230 rpm. During cloth polishing, the polishing cloth (3-6 µm grade) with fine grains and an abrasive slurry of 1 to 0.1micron alumina powder were used. Samples were finally cleaned with acetone after cloth polishing.

4.12.1 Optical Examination

Microstructural examination of mirror finished polished samples were carried out in etched condition after etching with a prepared etchant, 2% nital solution (2ml nitric acid and 98ml methanol) for 8-10 second. Sometimes, repeated polishing and etching was applied in order to reveal grain boundaries clearly. The microstructures were examined on DMI5000M^{TM} (Leica, Switzerland) metallurgical microscope having 1000X maximum compound magnifications interface with a computer to capture the images.

4.12.2 Scanning Electron Microscope (SEM) Examination

The samples were prepared in the similar fashion to metallographic examination. Scanning electron microscopy (SEM) studies were carried out using Carl Zeiss ultra plus FE-SEM and Zeiss EVO 18 special edition SEM equipped with EDAX detector. The Zeiss EVO18® LaB6 filament SEM is capable of delivering excellent resolution, high contrast topographic and compositional images of metallic and non-metallic surfaces. It is equipped with energy dispersive spectroscopy (EDS) system for elemental analysis.

4.13 GRAIN SIZE MEASUREMENT

The average grain size of the alloys was measured by grain intercept method. This test method of determination of average grain size in metallic materials is primarily measuring procedures and, because of their purely geometric basis, is independent of the metal or alloy concerned. The intercept method involves an actual count of the number of grains intercepted by a test line or the number of grain boundary intersections with a test line, per unit length of the test line, used to calculate the mean linear intercept length. The precision of the method is a function of the number of intercepts or intersections counted. A precision of better than ±0.25 grain size units can be attained with a reasonable amount of effort. Results are free of bias; repeatability and reproducibility are less than ±0.5 grain size units. Because an accurate count can be made without need of marking off intercepts or intersections.

4.14 X-RAY DIFFRACTION (XRD)

For X-ray diffraction analysis of the phases present in the alloys, small specimens of dimension 5mm x 5mm x 1mm were sectioned from forged and homogenized plate. The sectioned specimens were placed in the muffle furnace for stress relieving. The specimens were prepared similarly as described for the optical examination to minimize the distortion in the X-ray diffraction pattern. The specimens were subjected to X-ray diffraction using Rigaku Smart

Lab X-ray diffractometer fitted with a goniometer with Cu-Kα radiation (λCu=0.154nm). The goniometer angle ranged from 0º- 90º (2θ). The detector moved around the sample and measured the intensity and position of peaks which satisfy the Bragg's law. An Expert High Score Plus™ software was used to index the peaks of phases present in the pattern of iron phosphorus alloy.

4.15 HARDNESS MEASUREMENT

4.15.1 Bulk Hardness Measurement

The hardness of the alloys was measured on Vicker's hardness testing equipment (RTA) using a 5-kg load. The load was applied for 30 seconds on the test surface. Standard hardness test block was used to calibrate the equipment prior to testing of samples. The test samples were prepared using machining operation to make the flat surface and surface polished to 4/0 emery grade polishing papers followed by cloth polish. The indentations were taken 4-5 times at the different location of each sample surface. The average hardness value is reported to minimize the error possibility during the measurement of the hardness.

4.15.2 Microhardness Measurement

Microhardness measurement was carried out on polished samples to measure the hardness of matrix and precipitates using UHL-VHMT™ Germany microhardness testing equipment as shown in Figure 4.10 with indentation speed 50µm/s. The load applied was 50gf with 20 second dwell time. Ten indentations were taken out to measure the average microhardness.

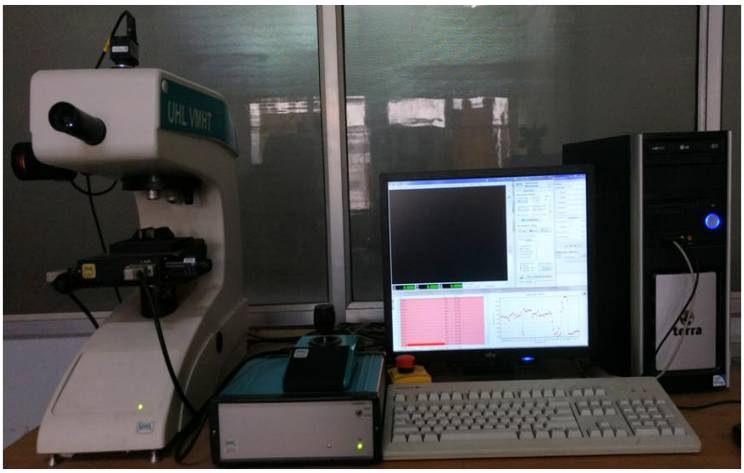

Figure 4.10: Microhardness testing equipment.

4.16 TENSILE TEST

Tensile test specimens with a gauge length 25mm and diameter 5mm were machined from the forged slabs as per the ASTM standard (E8M) as shown in Figure 4.11. Tensile tests were performed for all compositions on a computer controlled Hounsfield test equipment (H25K-S) Universal testing machine of 25 kN capacity at strain rate 1mm/min. All specimens were polished to remove any tool markings due to machining of oxide layers formed during stress relieving. At least two specimens were tested for each composition.

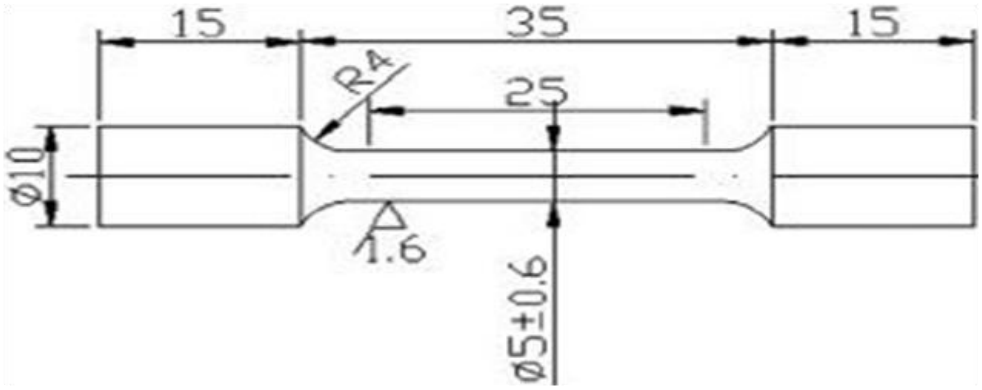

Figure 4.11: Schematic diagram of the round tensile specimen.

4.17 CHARPY IMPACT TEST

Charpy impact tests were performed on samples (10mm x 10mm x 55mm) prepared according to ASTM E23 standard as shown in a schematic Figure 4.12. Charpy tests were performed for all compositions on a manually operated conventional impact testing machine as shown in Figure 4.13.

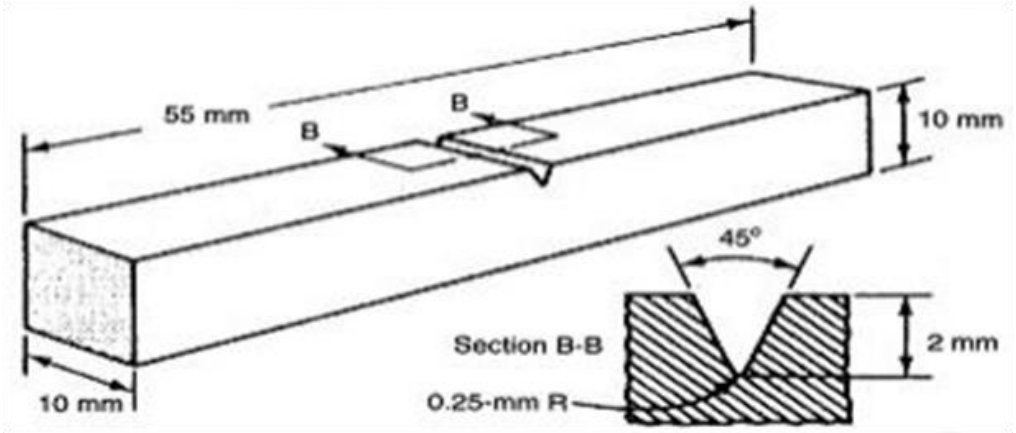

Figure 4.12: Schematic diagram of Charpy impact test specimen.

All specimens were polished to remove any tool markings due to machining of oxide layers formed during annealing. At least two specimens were tested for each composition. The

fracture surfaces were analyzed on a Zeiss EVO18 Special Edition (scanning electron microscope).

Figure 4.13: Conventional impact testing machine.

4.18 DRY SLIDING WEAR TEST

4.18.1 Wear Sample Preparation

Wear test samples (cylindrical pin) dimensions 40mm x 6mmø were prepared by machining operation from forged and homogenized slabs. The test samples were kept in the muffle furnace for relieving of the residual stresses. All pin samples were prepared with a flat surface at one end and corners rounded using emery paper polished up to 4/0 grade (~38µm). Before the test, the surface of pin sample was cleaned with acetone to eliminate unwanted particles.

4.18.2 Wear Test

Dry sliding wear tests were carried out with the counter face of a hardened and polished disc made up of EN-31 steel at atmospheric temperature. A representative initial surface roughness measured by profilometer as shown in Figure 4.14. A pin-on-disc wear testing apparatus (Figure 4.15), made by Magnum Engineers, Bangalore, was used to carry out the

wear tests. Weight losses of pin samples were measured at different time intervals. Volume loss was calculated using the weight loss and density of alloy (7760 kg/m^3).

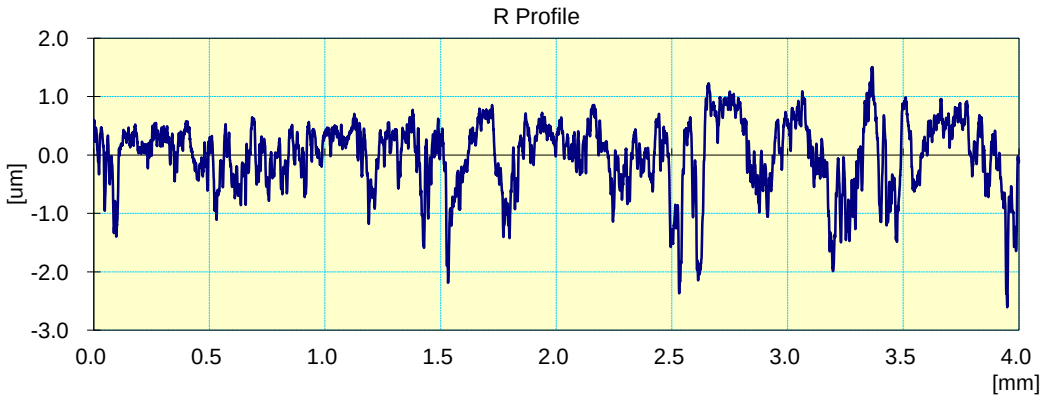

Figure 4.14: Representative initial surface roughness of the disc.

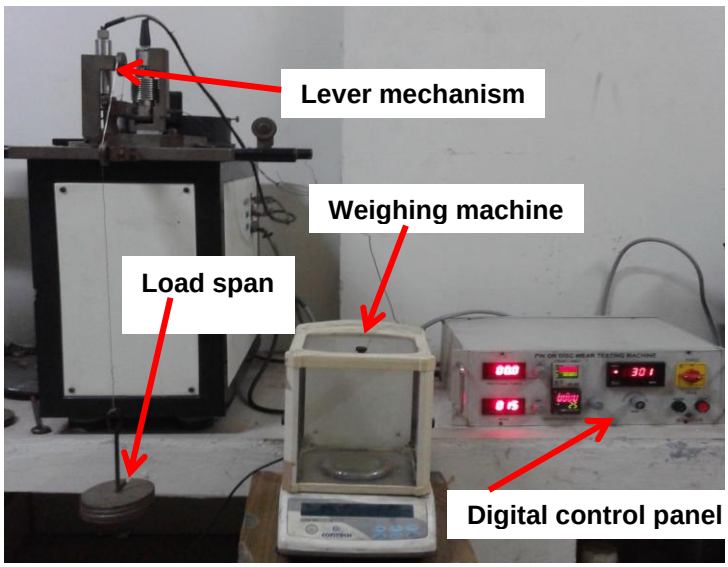

Figure 4.15: Pin on disc wear testing apparatus

Each test was repeated three times at a given load and sliding velocity. The average value was taken to calculate the volume loss after each interval of time. All samples were tested at stresses of 0.17, 0.26 and 0.35MPa and at sliding speeds of 2.2 m/s and 3 m/s respectively. The variation in frictional force was continuously displayed by a digital electronic sensor installed in the equipment to calculate the average coefficient of friction (COF). The worn surfaces of the pin were cleaned by ultrasonic cleaning. The worn surfaces, as well as the sub-surfaces of the pin samples, were analyzed under scanning electron microscope with energy dispersive X-ray spectroscopy (SEM-EDS) (ULTRA plus, Carl Zeiss, Germany) to identify the various mechanisms of wear.

CHAPTER 5

RESULTS AND DISCUSSION

In the present investigation total of seven (Fe-P and Fe-P-C) formulations were prepared based on iron as a main constituent to study the mechanical and tribological behavior of the resulting alloys. Among seven compositions one is a ternary alloy. The phosphorus content varied from 0 to 3wt.% while that of graphite was fixed at 0.20wt.%.

This chapter has been divided into five sections.

- The subsection 5.1 describes the powder characterization, density measurement, and processing of alloys developed.
- The subsection 5.2 explains results of mechanical properties viz hardness, tensile strength, Charpy impact strength etc. of alloys with different content of phosphorus in iron as a function of their microstructure.
- The effect of phosphorus on the dry sliding behavior of iron-based P/M alloys were determined on pin-on-disc wear testing machine and discussed in the subsection 5.3.
- The effect of carbon addition on microstructure and mechanical properties has been presented in subsection 5.4.
- The effect of carbon addition on wear and friction behavior has been described in chapter 5.5.

5.1 POWDER CHARACTERIZATION, PROCESSING OF FORGED ALLOYS AND DENSITY MEASUREMENT:

This section deals with the characterization of powders by various techniques, density measurements and study of processing of the alloys prepared in the present work. Homogenization of element P in the ferrite matrix has also been discussed.

5.1.1 Powder Characterization

SEM was used to determine the powder morphology. The SEM images of iron and Fe-P alloy powders are shown in Figures 5.1(a-f).

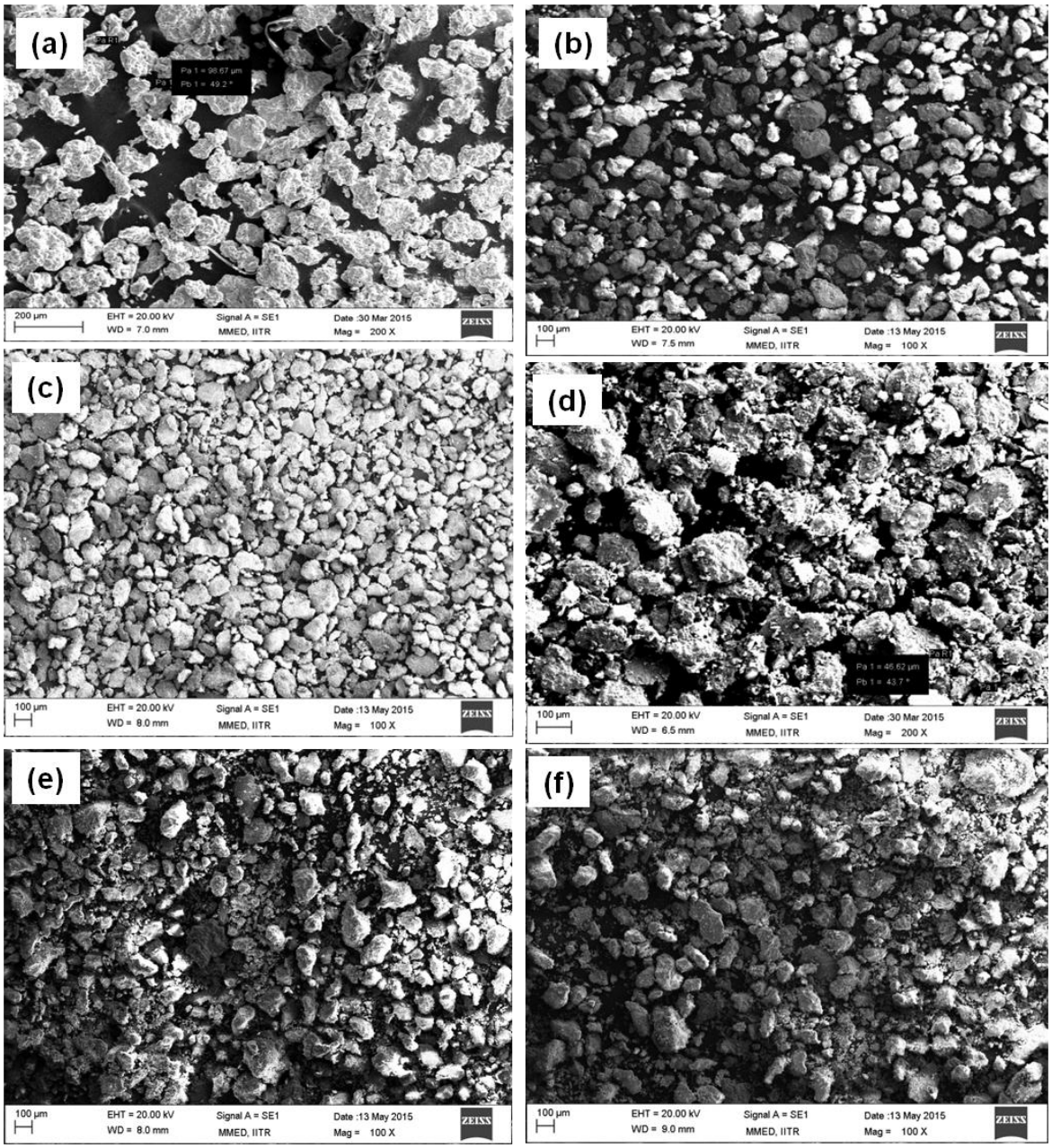

Figure 5.1:The SEM micrographs of powders (a) Fe (b) Fe-0.35wt.%P (c) Fe-0.65wt.%P (d) Fe-1.3wt.%P (e) Fe-2wt.%P (f) Fe-3wt.%P.

The SEM images exhibited irregular morphology of iron powder and regular with mostly rounded morphology for Fe-P alloy powders. The size of mixed powders is finer (~125µm) than iron (unmixed) powder. This is due to the milling action. In high content P alloy, agglomeration of powders was observed. The particle size was measured by laser scattering method which indicated the average particle size ~170 microns of iron powder. The distribution of P in a typical Fe-P powder mixture is shown in Figure 5.2.

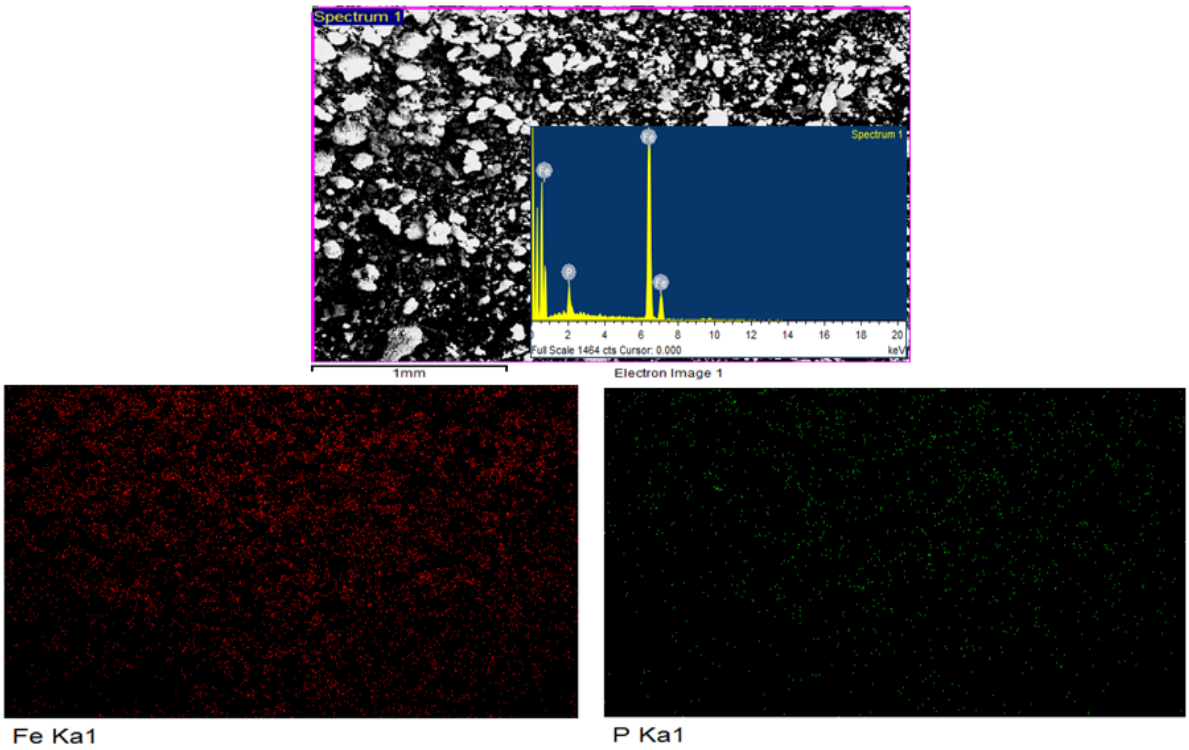

Figure 5.2: Elemental mapping of powder mixture alloy for (a) iron and (b) phosphorus

5.1.2 Processing and Density Measurement of Forged Alloys

Forged slabs were kept in the muffle furnace for the homogenization treatment to ensure the uniform and homogeneous distribution of alloying elements.

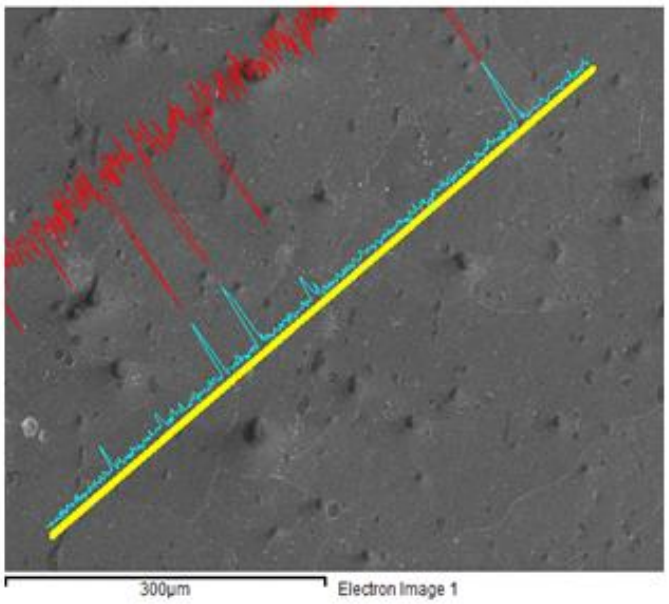

Figure 5.3: Line scan in scanning electron microscope of Fe–0.65wt.%P showing phosphorus distribution within the grains as well as along grain boundaries in the forged alloys. The blue line is for P, and the red one is for Fe variations. The major peaks indicate the presence of phosphide phase.

Homogenization study was initially carried out on a forged product with 0.65wt.% P alloy. Homogenization was carried out at 1100 ºC for the duration 1hr. The distribution of phosphorus has been analyzed by optical microstructure as well as with EDS elemental map. Line scan in scanning electron microscope of Fe-0.65wt.% P showing phosphorus distribution within the grains as well as along grain boundaries in the forged alloys is shown in Figure 5.3. The blue line is for P, and the red one is for Fe variation. The major peaks indicate the presence of phosphide phase. The scan crosses several grains, but no significant phosphorus build up near the grain boundaries could be detected. The EDS result along with the corresponding SEM image is shown in Figure 5.3. The status after 1hr homogenization is depicted in SEM-EDS which indicates that after 1hr uniformity has been achieved in the dissolution of P.

Measurement of porosity of forged specimen (from the center of the forged slab) was done using image analyzer software in the final forged sample. Unetched optical micrographs of Fe-P alloy is shown in Figure 5.4. The microstructure of forged Fe-2wt.% P revealed that the pores are mostly eliminated and a porosity level of 1.09% is observed which corresponds to above 99% relative density.

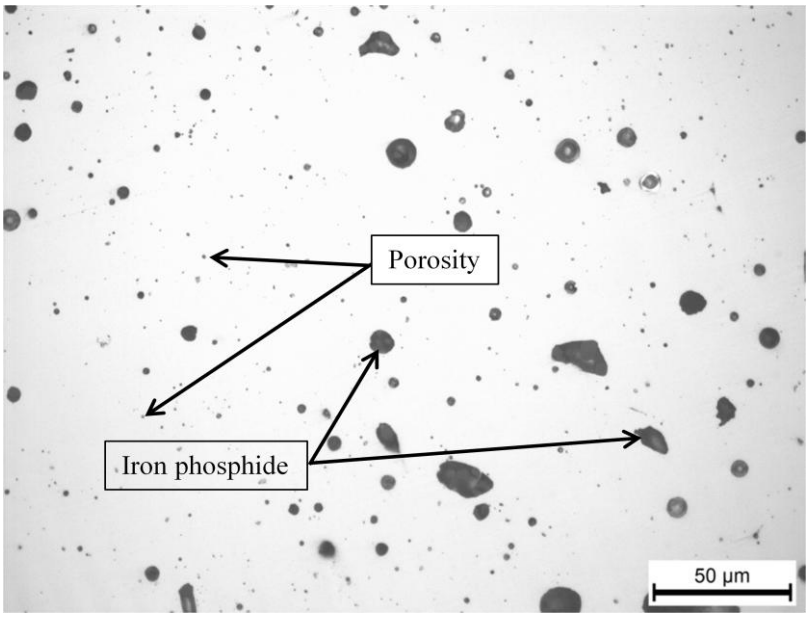

Figure 5.4: Unetched optical micrograph of Fe-2wt.% P alloy under final forged condition. It shows the iron phosphide (black region) distributed over the ferrite matrix (bright region).

The density of Fe alloy, which was developed by hot powder forging of encapsulated water-atomized iron powder, is 7.73 gm/cm^3 whereas the density of wrought iron is 7.87 gm/cm^3 (Moyer 1998). The results indicate that ~99% densification has been achieved by powder forging of water atomized powder. Further, the density increased with addition of

phosphorus in the iron as shown in Table 5.1. The density of Fe-2wt.%P alloy produced by the hot powder forging is 7.87gm/cm^3. Thus the phosphorus addition in atomized iron powder helps in increasing the near full density when hot forging technique is employed for the consolidation of iron-based P/M alloys. Even the addition of P in an amount more than 0.35wt.% P has been found to improve the density of the alloys in the present investigation. Further, powder forging followed by solid-state heating, i.e. heating at a temperature lower than conventional sintering temperatures, has brought about densification of greater magnitude. The forged alloys consisting of ferrite and iron phosphide as shown in Figure 5.4 has been confirmed by the XRD analysis of Fe-2wt. %P alloy, which indicates the peaks of both the phases (Figure 5.5).

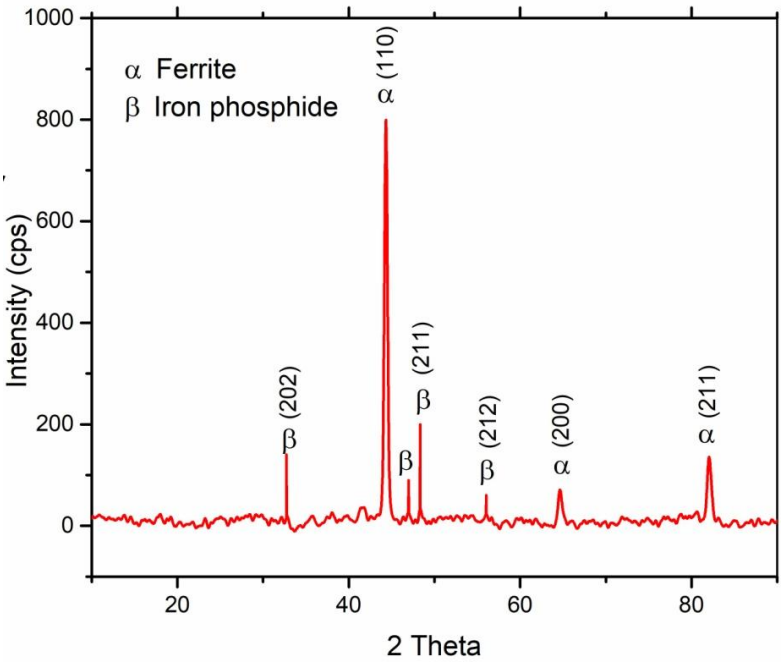

Figure 5.5: XRD pattern of Fe-2wt.% P forged alloy showing ferrite and iron phosphide peaks.

Addition of small amount of graphite in the Fe-P P/M alloys leads to increase in density because it drives phosphorus into ferrite matrix by segregating to the grain boundaries as the following reaction:

C (dissolved) + P (segregated) = C (segregated) + P (dissolved)

The phosphorus is rearranged and strengthened to the iron particle. Also, it improves the pore morphology, as a result, the density is improved of carbon containing Fe-P alloys. The measured density of Fe-0.65wt.%P-0.20wt.%C is 7900 kg/m^3 which is higher than density achieved for Fe-0.60wt.%P-0.25wt.%C alloy by conventional route of powder metallurgy (Straffelini et al. 1993).

Summary

1. With the use of hot powder forging technique, near full density alloys with varying P content were successfully developed through powder metallurgy route.
2. The forged alloys exhibited a uniform distribution of P within and along grain boundaries.

5.2 EFFECT OF PHOSPHORUS ON MICROSTRUCTURE AND MECHANICAL PROPERTIES OF IRON-BASED ALLOYS

This section describes the mechanical properties such as bulk hardness, microhardness, strength, ductility and toughness of all alloy compositions investigated in the present work. The alloys have been characterized on the basis of their microstructure and grain size. All above mechanical properties were also correlated with the microstructure.

5.2.1 Microstructure

Representative optical micrographs of forged alloy (Fe-0.65wt.%P, Fe-2wt.%P and Fe-3wt.%P) samples in stress relieved condition (at 600 ºC for 1hr and cooled in the furnace) are shown in Figure 5.6. The forged alloys exhibit iron phosphide (Fe_3P) precipitates in a ferrite matrix (Figure 5.6). The microstructure has dark etching phosphide phases in the bright region of ferrite. As P wt.% increased, the phosphide volume fraction increased (Figure 5.6(a-c). Phosphorus gets precipitated out in the form of phosphide at and within grain boundary since the solubility of P in the ferrite is less at room temperature. The volume fraction of phosphide is increased with increasing the content of P in the iron as shown in Figure 5.7. The volume percentage of phosphide was measured from polished samples in the optical microscope using a phase analyzer software. Figure 5.8 shows a secondary electron SEM micrograph of Fe–2 wt.%P alloy, elemental analysis of matrix and precipitates of Fe–2 wt.%P alloy using energy dispersive analysis of x-rays.

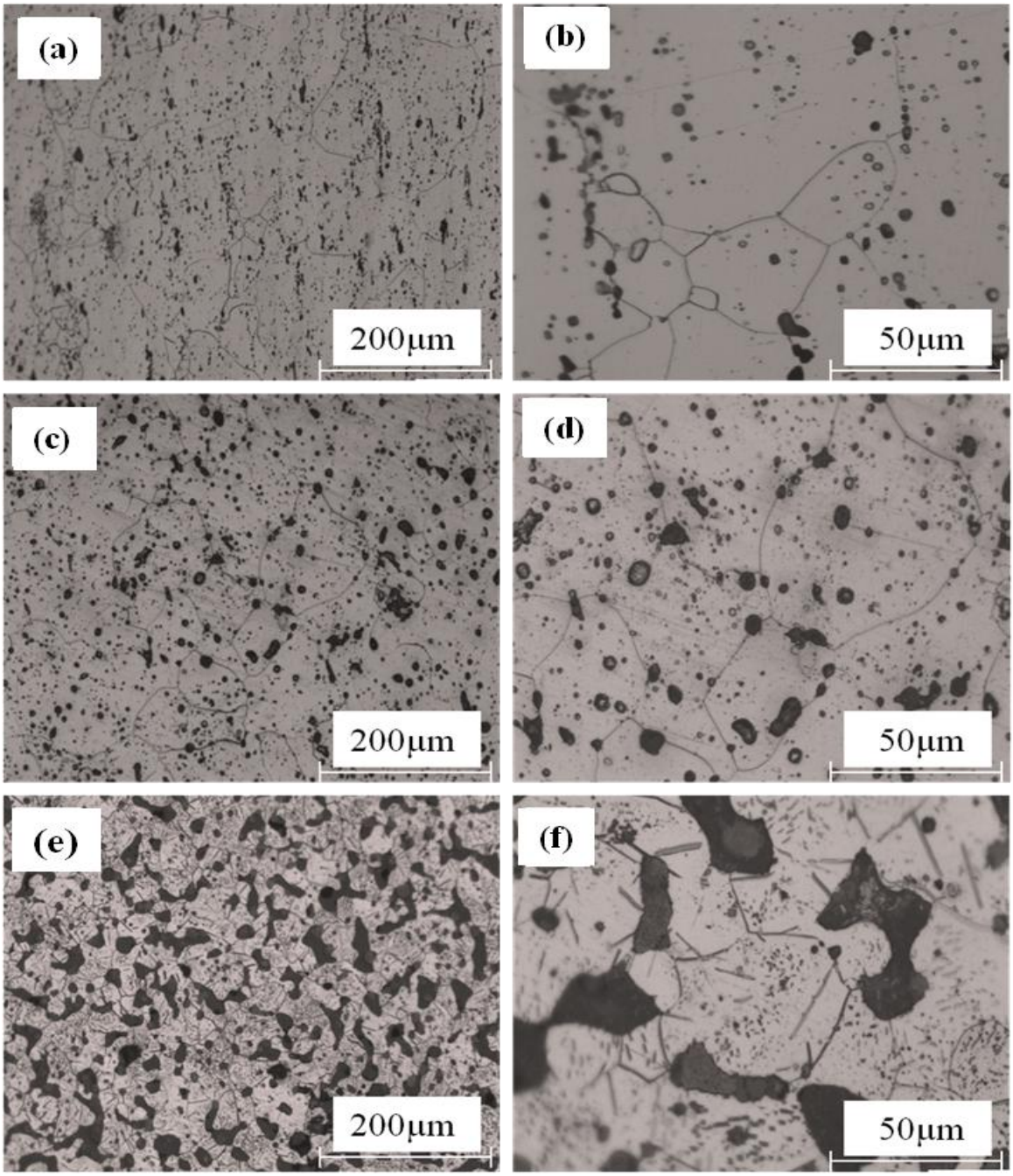

Figure 5.6: Optical micrographs of powder-forged specimens of (a, b) Fe–0.65 wt.%P, (c, d) Fe–2 wt.%P, and (e, f) Fe–3 wt.%P alloy.

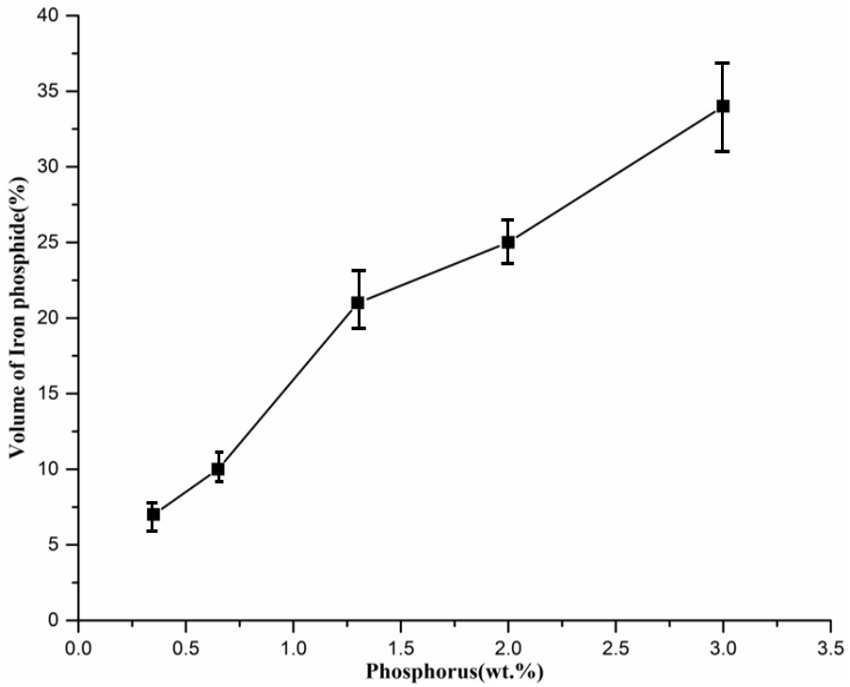

Figure 5.7: Volume fraction of phosphide at different phosphorus contents in Fe-P alloys.

It has been observed that the phosphide volume fraction increases from 7 to 34% in the ferrite matrix corresponding to P contents of 0.35 to 3wt.%. Equiaxed grains were observed in all the alloys. Addition of phosphorus results in a decrease in grain size (Table 5.2). This is mainly due to the solid state processing of the alloys. Other important factors which may disperse nucleating particles (phosphide) well are sufficient in number and efficient for grain refinement (web link 4). A theoretical approach has already been derived in the web link 4 to assess the potency of a nucleating particle. A similar decrease in grain size on phosphorus addition has been reported earlier in cast alloys (Hopkins and Tipler 1958; Kirchheim 2002). Phosphorus partitions were observed between the ferrite matrix and the Fe_3P precipitates (Figure 5.6).

5.2.2 Hardness

The hardness of Fe-P alloys is reported in Table 5.2. With increasing the phosphorus content in the iron, hardness values increase (Figure 5.9). The hardness has been observed to vary from 78HV for pure iron to 243HV for 2wt.% P alloy. In Fe-2%wt.P alloy phosphides are uniformly distributed and are spherical phosphides leading to an improved hardness (Klar et al.1989; Lindskog et al. 1977). Klar et al.1989 and Lindskog et al. 1977 have also observed spherical in shape which leads to enhancement in hardness and strength.

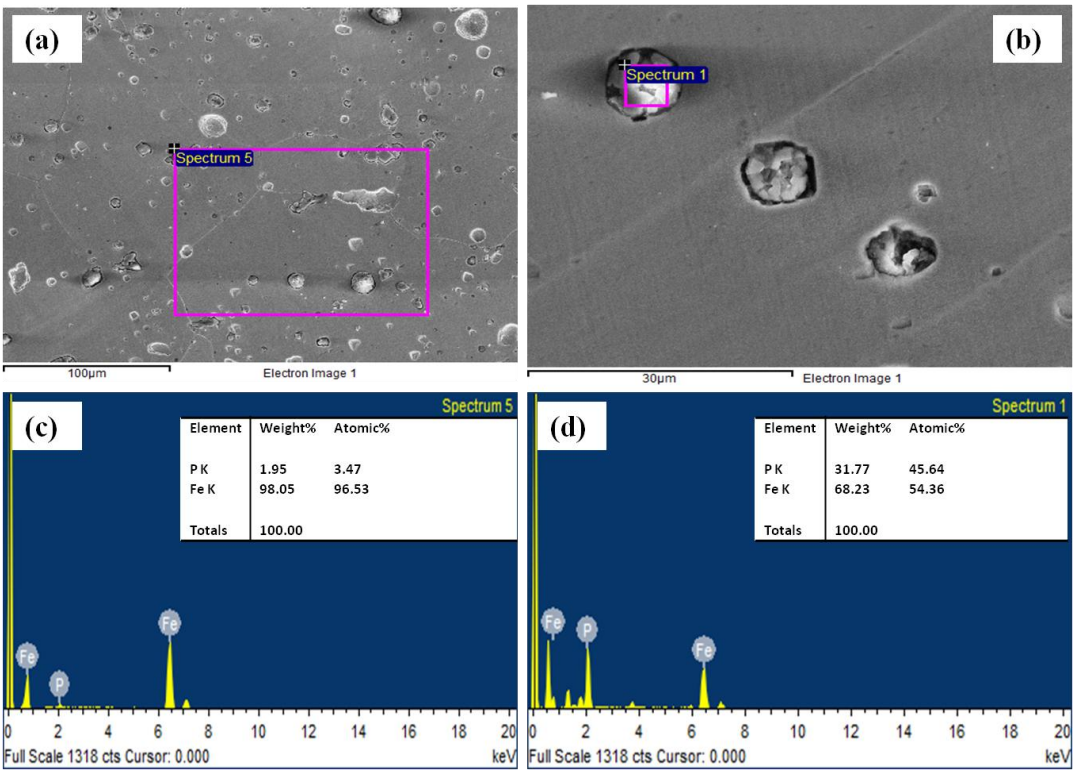

Figure 5.8: (a) Secondary electron SEM micrograph of Fe–2 wt.%P alloy. Elemental analysis of matrix (c) and precipitates (d) of Fe–2 wt.%P alloy using energy dispersive analysis of x-rays.

The alloy with 3 wt.% P has a very high volume fraction (34 vol.%) of phosphide. These coarse phosphide particles may not be fully dense. Panetoa et al. 2015 have also shown a similar fall in the hardness and strength. The hardness values obtained are better than those reported in the literature (Jandeska 1982; Eyre and Walker 1976; Batienkov et al. 2011) for alloys with <1% P. No data have been reported for higher P contents. The hardness of these alloys was calculated by the following rule of mixtures:

$$H_T = f \times H_f + (1 - f)H_m \qquad \text{----------} \qquad 5.1$$

Where H_T = Theoretical hardness, H_f = Hardness of phosphide, H_m= Hardness of matrix and f = Volume fraction of phosphide. Figure 5.9 shows that the theoretical hardness values are greater than the experimental hardness values for all the composition of alloys. The experimental bulk hardness values are probably more reliable as these cover a larger area than microhardness measurements. Microhardness of the ferrite and phosphide regions in Fe-P alloys is given in Table 5.1.

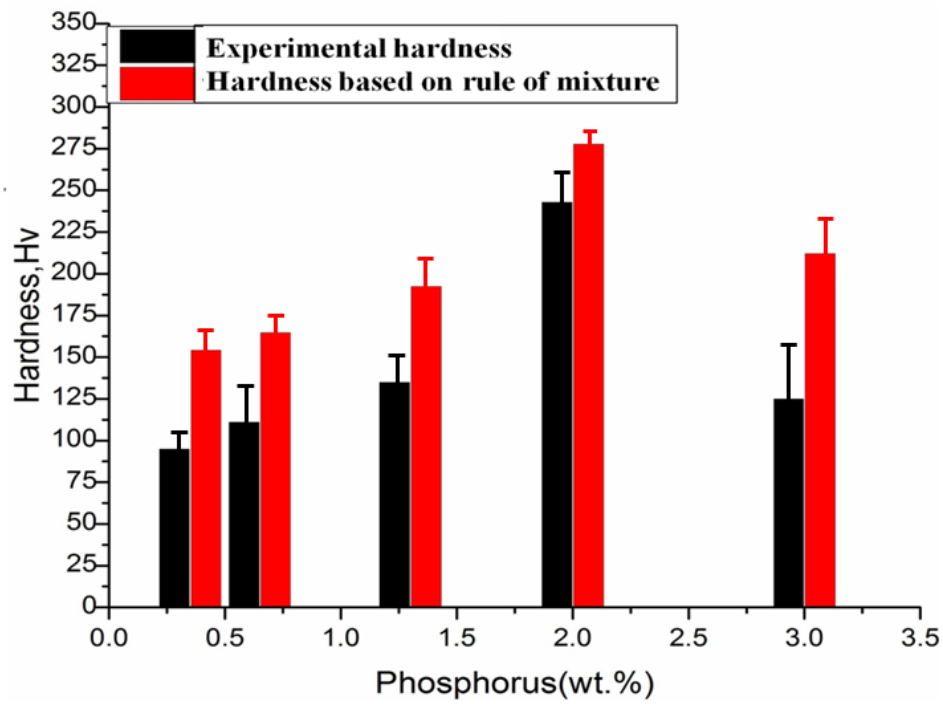

Figure 5.9: Showing the hardness based on rule of mixture and experimental hardness of Fe-P alloys.

Table 5.1: Microhardness of Fe-P alloys.

Alloy	Density (g/cc)	Regions	Phases identified	Av. Microhardness (HV) (Standard Deviation)
Fe-0.35wt.%P	7.75(±0.10)	Bright Dark	Ferrite Iron-phosphide	198 (±9) 465 (±7)
Fe-0.65wt.%P	7.78(±0.12)	Bright Dark	Ferrite Iron-phosphide	211 (±7) 470 (±6)
Fe-1.3wt.%P	7.84(±0.11)	Bright Dark	Ferrite Iron-phosphide	218 (±7) 480 (±10)
Fe-2wt.%P	7.87(±0.10)	Bright Dark	Ferrite Iron-phosphide	254 (±8) 487 (±9)
Fe-3wt.%P	7.76(±0.14)	Bright Dark	Ferrite Iron-phosphide	263 (±7) 475 (±10)

The volume fractions of phosphide in Fe-0.35wt. %P, Fe-0.65wt. %P, Fe-1.3wt. %P, Fe-2wt. %P and Fe-3wt. %P alloys, as determined by Radical Meta Check 5.0 phase analyzer software from polished samples in the optical microscope, are approximately 7, 10, 21, 25 and 34 vol. % respectively.

5.2.3 Yield strength and Tensile Strength

The yield and tensile strength values for Fe-P alloys are shown in Table 5.2. The yield strength (YS) and ultimate tensile strength (UTS) of the Fe based alloys increases with the addition of P. The ferrite matrix is strengthened by the solid solution of phosphorus in iron (Islam et al. 2011). Also, the small precipitates can further strengthen the ferrite matrix or other phases and by this, the strength level of steel is increased (Bleck and Phiu-on 2005).

Table 5.2: Grain size and mechanical properties of Fe–P alloys

S.No.	Alloys/ Compositions	YS (MPa)	UTS (MPa)	% Elongation	Hardness (H V 5)	Average grain size(μm)
1.	Fe	212±7	302±9	20±0.50	78±4	165
2.	Fe-0.35P	224±8	325±7	17±0.60	95±6	155
3.	Fe-0.65P	260±6	365±6	12±0.50	111±7	102
4.	Fe-1.3P	281±9	408±8	6±0.40	135±8	98
5.	Fe-2P	351±6	495±7	3±0.20	243±6	96
6.	Fe-3P	155±8	255±4	2±0.70	125±5	92

Tensile properties are significantly influenced by the addition of phosphorus in iron. Among the six alloys, strength was the highest of 2wt.%P content alloy. In Fe–2wt.%P alloy phosphides are uniformly distributed and are spherical in shape leading to an improvement in yield and ultimate tensile strength (Klar et al. 1989). The obtained strength values are better than those reported in the literature (Jandeska 1982; Eyre and Walker 1976; Batienkov et al. 2011) for alloys with ~1% P processed by pressing and sintering. The strength values increased gradually with P addition and its values ranged from 302MPa in 0 %P (Pure iron) to 495MPa in 2wt. %P content alloys.

Charpy impact results are shown in the Figure 5.10. The impact energy decreases with an increase in phosphorus content. Though adding P reduces the grain size, it also increases the phosphide volume fraction (which is more pronounced) leading to a loss of impact strength values.

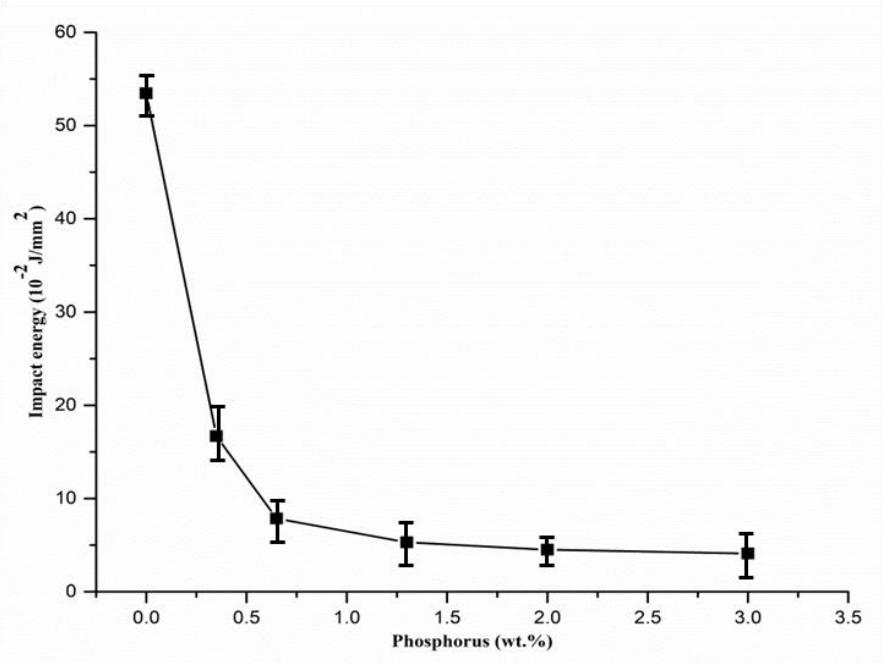

Figure 5.10: Effect of phosphorus on Charpy impact energy of Fe-P P/M alloys.

The sudden drop beyond 0.35wt.%P is observed which may be likely due to the following reasons:

1. Upto 0.35 or 0.50wt.%P is in α-solid solution beyond which it is also in the form of Fe_3P phosphide which is a brittle phase.
2. The weak interface between α and Fe_3P phosphide may decrease the toughness values.

5.2.4 Ductility

The percentage elongation for iron is found to be highest having values of 20 % whereas it is found to be lowest for 3wt.% P with a value of only 2 %. The variation of percentage elongation with phosphorus is shown in the Figure 5.11. The corresponding fracture surfaces are also shown in Figure 5.11.

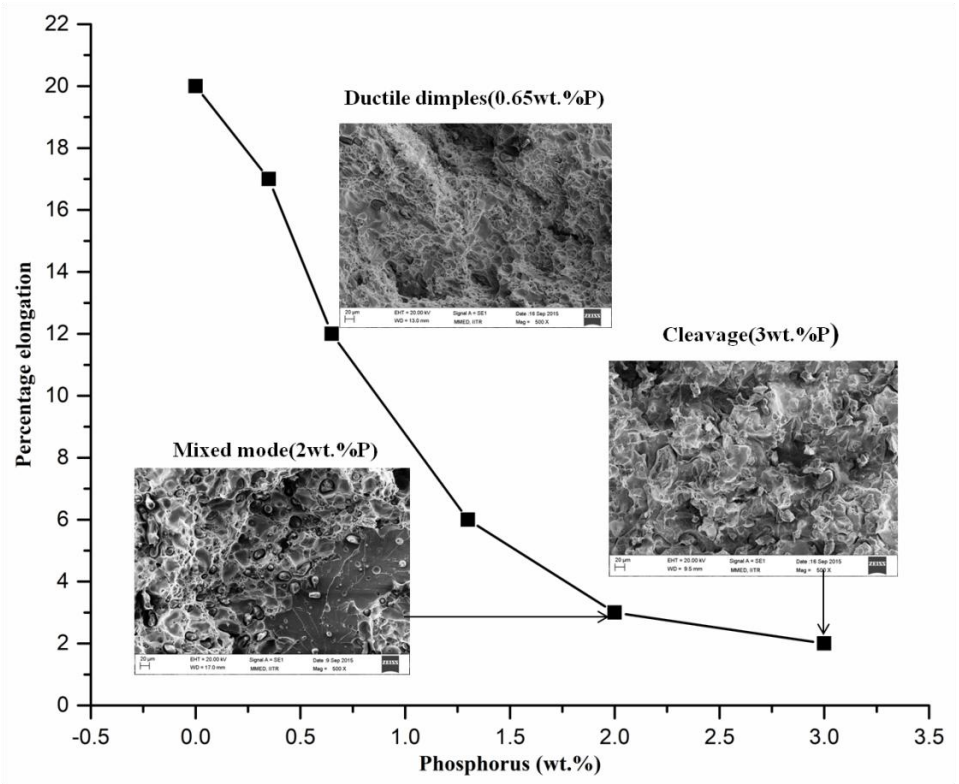

Figure 5.11: Variation of percentage elongation with P content in iron.

The ductility observed is very low in compositions with more than 1% P. This may be because phosphorus addition increases the amount of phosphide in the alloys, thus reducing ductility at high P levels. The volume fraction of phosphide decides the ductility. Ductility decreases with increasing phosphide volume fraction. The ductility values obtained are better than those reported in the literature (Jandeska 1982; Eyre and Walker 1976; Batienkov et al. 2011) for alloys with <1% P processed by conventional route of powder metallurgy.

Among P/M processes, powder forging leads to high density and this may explain better ductility observed in the present research work. Further, chemical and structural homogeneity may also be improved by powder forging (James and McDermott 1998). In the casting route, the last liquid to solidify is enriched with phosphorus which is segregated at grain boundaries (Muchnik 1984; Lejcek 2010). This may lead to the deterioration of mechanical properties with high phosphorus due to the weakening of grain boundaries (Wettlaufer and Kaspar 2000; Song et al. 2010). Similarly, P/M routes rely on liquid-phase sintering due to the eutectic reaction where liquid decomposes into Fe (α) and Fe_3P. This also leads to the formation of phosphorus-rich liquid at inter-particle interfaces and consequent phosphorus enrichment at the grain boundaries. Lindskog 1973; Lindskog et al. 1977 reported that liquid-phase sintering may be used in P/M Fe–P alloys with phosphorus content up to 0.60% prepared by pressing and sintering route at sintering temperatures above 1100 ºC. At 1100 ºC, a Fe-Fe_3P eutectic results

in the formation of a liquid phase which helps to distribute phosphorus in iron by capillary action (Moyer 1998). This too may lead to phosphorus enrichment at grain boundaries. These problems in the casting or conventional P/M routes can be overcome by powder forging. While investigating the effect of phosphorus on the magnetic properties of iron it was realized that the Fe–P alloys did not show any cracking during working (Chaurasia et al. 2012). Alloys used in the present work have very high phosphorus contents. There is a gradual loss of ductility with phosphorus content as opposed to embrittlement due to even small amounts of phosphorus (0.05%) reported in the literature (Muchnik 1984). In the present investigation, the ductility (absence of embrittlement) may be attributed to the absence of a liquid phase during processing. It is proposed that the presence of phosphorus-enriched liquid layer at the grain boundaries is the main cause of embrittlement in conventional steels.

5.2.5 Fractograph

The fracture surfaces of tensile and Charpy impact test specimens of iron-based alloys with increasing the volume fraction of phosphide from 0 to 34% have been observed under scanning electron microscope (SEM). Figure 5.12 shows the micrograph of the tensile fractured surface of Fe-0.65wt.%P, Fe-2wt.%P and Fe-3wt.%P as observed under SEM.

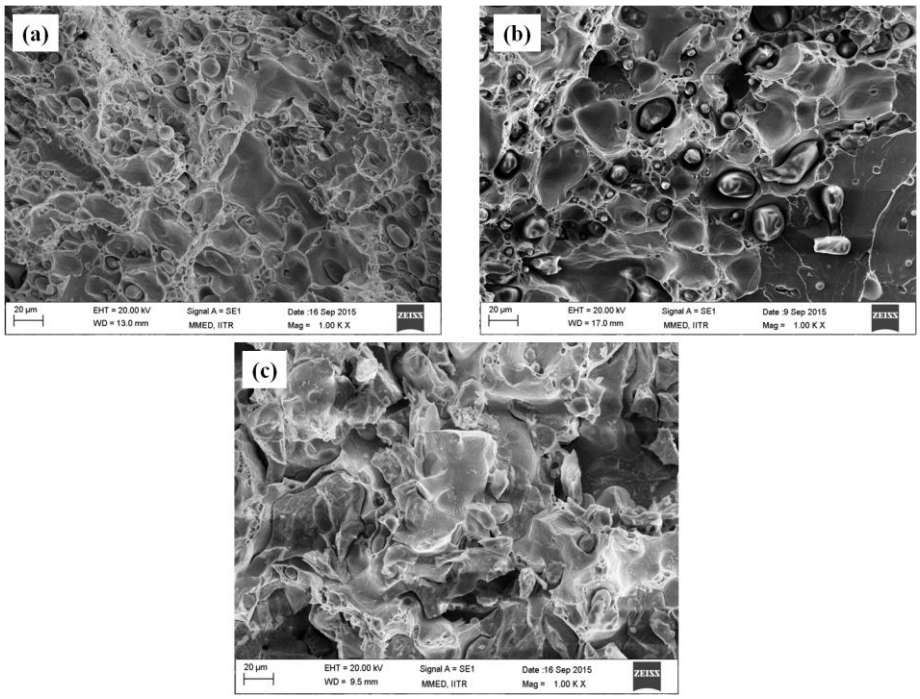

Figure 5.12: Scanning electron micrographs of tensile fracture surfaces of powder-forged specimens (a) Fe–0.65wt.%P, (b) Fe–2wt.%P, and (c) Fe–3 wt.%P alloys. (a) shows ductile dimple failure, while cleavage failure is observed in (c), with Fe–2wt.%P alloy showing mixed mode failure (b).

Ductile dimple fracture is observed in the low phosphorus (Fe-0.65wt.%P) alloy, while cleavage failure occurs in the Fe–3wt.%P alloy. Also, a mixed fracture mode may be seen in 2 wt.% P alloy.

The Charpy impact energy of Fe-P alloys decreased with an increase in the phosphorus content in the iron (Figure 5.10). The Charpy impact fracture surfaces of alloys with<1%P exhibit ductile dimple failure (Figure 5.13). This suggests a greater cohesion, less porosity, and more efficient bonding than that reported (Muchnik 1984) during sintering. The use of hydrogen atmosphere during heating of powders may reduce surface oxides and improve interparticle bonding and cleanliness of the P/M part. Further, the coated iron particle surface, i.e., $Fe_3(PO_4)_2$, has been transformed into iron phosphide (Fe_3P), during heating. For the alloys with higher phosphorus content (2 wt.% and 3 wt.%), the fracture mode is a mix of ductile and cleavage. This may be due to the increased volume fraction of the hard and brittle phosphide phase in these alloys.

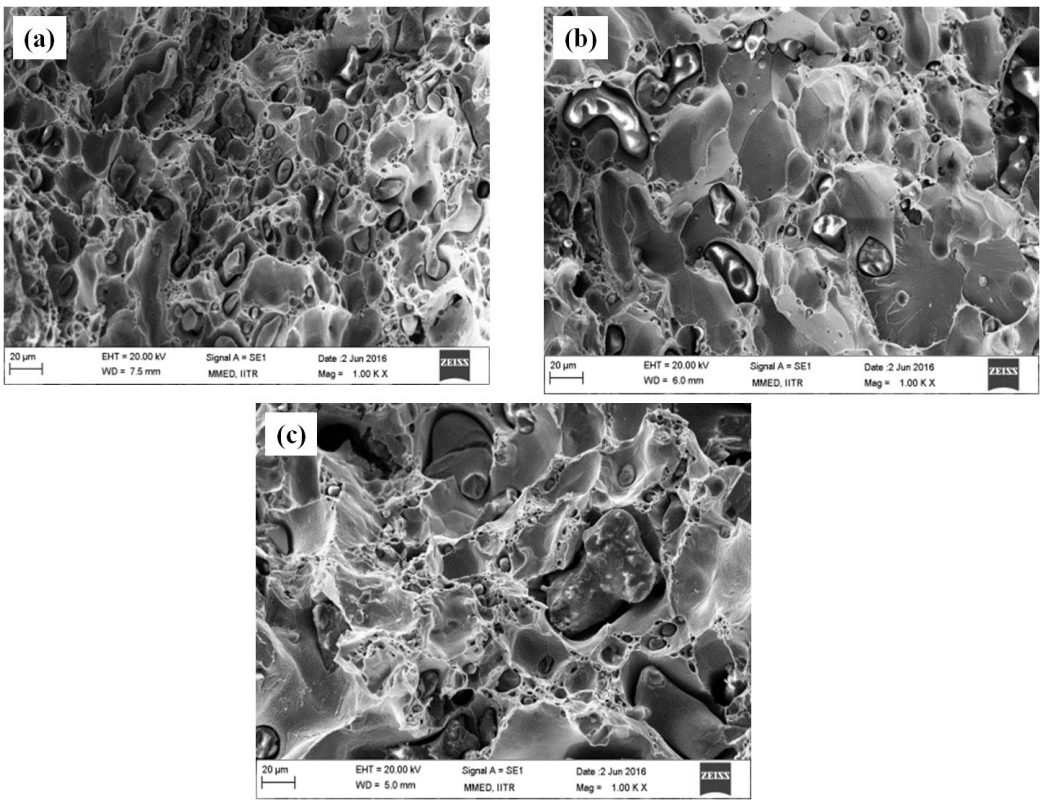

Figure 5.13: Scanning electron micrographs of impact fracture surfaces of powder-forged specimens (a) Fe-0.65 wt.%P, (b) Fe-2 wt.%P, and (c) Fe-3 wt.%P alloys. The alloys with 0.65 wt.%P exhibit ductile dimple failure. For the alloys with 2wt.%P and 3wt.%P, the fracture mode is a mix of ductile and cleavage.

Summary

1. Among all the alloys investigated, lowest hardness (78 HV) was observed in pure iron while the highest hardness (243HV) in Fe-2wt. %P. Hardness was found to increase with the addition of P in the iron.
2. Strength was found to increase with increasing P in the iron. Highest strength (495MPa) was exhibited by Fe-2wt.% P. The lowest strength (255 MPa) was exhibited in the Fe-3wt.% P alloy. This is due to the high volume fraction of phosphides in the alloy which inhibit densification leading to a loss in ductility, strength, and hardness.
3. Phosphorus addition had a considerable impact on the ductility i.e. drop in ductility. However, high strength with good ductility (except for 3wt.%P) shows the positive effect of powder forging which leads to an improvement in density and ductility. Ductility of powder forged followed by stress relieved samples were improved by 9-13% when compared to alloys processed by pressing and sintering.
4. Fractographs of tensile and impact specimens show the ductile dimple failure in alloys with < 1wt. % P, while cleavage failure is observed in Fe-3wt. % P whereas Fe–2wt.%P alloy shows mixed mode failure.

5.3 EFFECT OF PHOSPHORUS ON TRIBOLOGICAL PROPERTIES OF IRON-BASED ALLOYS

The tribological behavior of pure iron and Fe-P alloys has been investigated in terms of friction and dry sliding wear against the counterface of steel disc. The primary focus of this study is to understand the role of phosphorus, normal load and sliding speed on the wear and friction characteristics of these alloys. Their tribological characteristics have been correlated with microstructure and mechanical properties.

5.3.1 Dry Sliding Wear and Friction Behaviour at 2.2m/s Sliding Velocity

5.3.1.1 Wear characteristics

The cumulative wear volume varied with a sliding distance under different normal load at a sliding speed of 2.2 m/s is shown in Figures. 5.14 to 5.19. The cumulative wear volume loss with a sliding distance under different normal loads of 19.6, 29.4 and 39.2N has been plotted. It is observed that the cumulative wear volume loss increases with increasing sliding distance. It is further noted that for a given sliding distance cumulative wear volume loss increases with increasing load. These two observations are in line with Archard Wear Equation 5.2. According to the Archard Wear Equation (Bhushan 2013):

$$\text{Wear Volume}(v) = \frac{KWS}{H} \quad \text{----------} \quad 5.2$$

or

$$\text{Wear rate } \left(\frac{V}{S}\right) = \frac{K\,W}{H} \quad \text{----------} \quad 5.3$$

Where, v is the cumulative volume loss, W normal load, S sliding distance, and H is the hardness of softer material (Pin). K is the Archard wear coefficient which is dimensionless. It is also noted that cumulative wear volume loss decreases with increasing phosphorus content for a given sliding distance and load. The wear rate is given by the line slope. This procedure is followed in all the cumulative wear volume *vs.* sliding distance variations for all the alloys used in the present study.

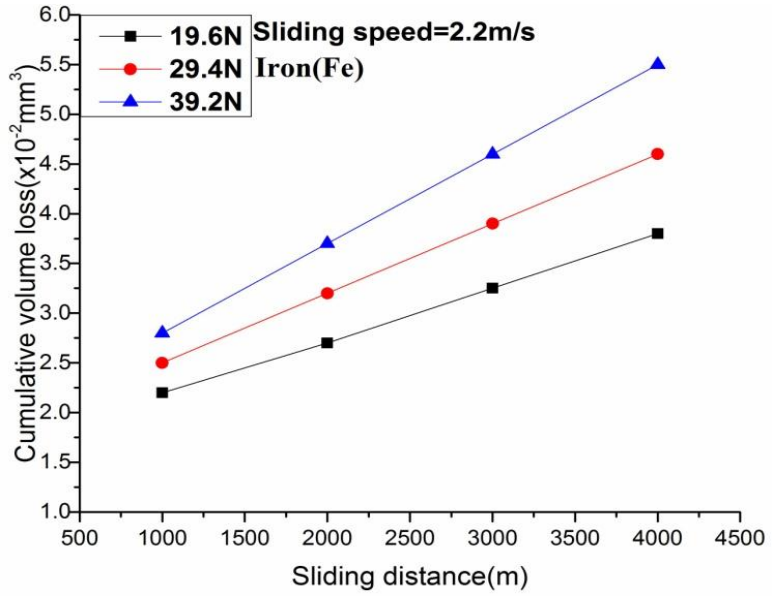

Figure 5.14: Variation of cumulative wear volume loss as a function of sliding distance at different loads for pure iron at 2.2 m/s.

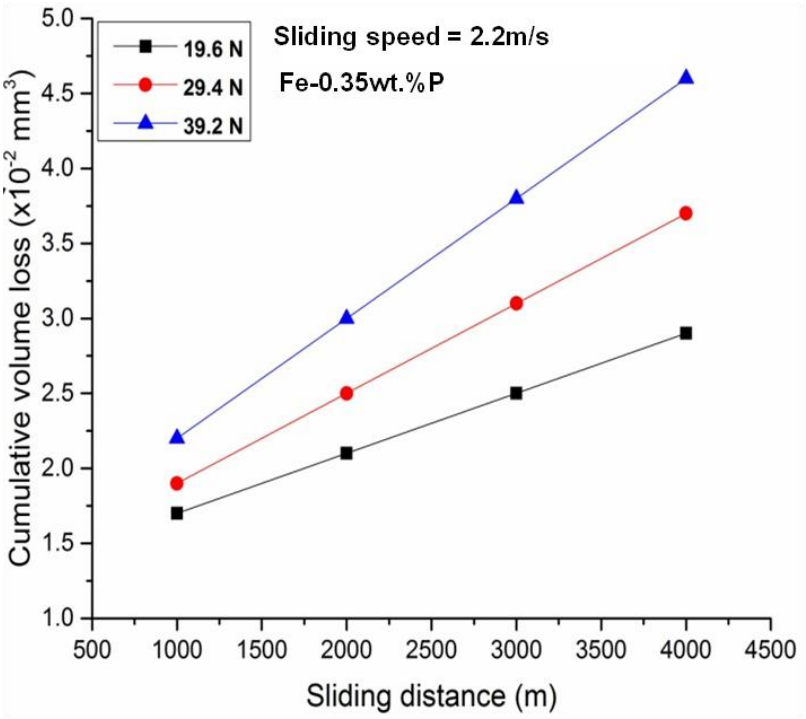

Figure 5.15: Variation of cumulative wear volume loss as a function of sliding distance at different loads for Fe-0.35wt.%P at 2.2 m/s.

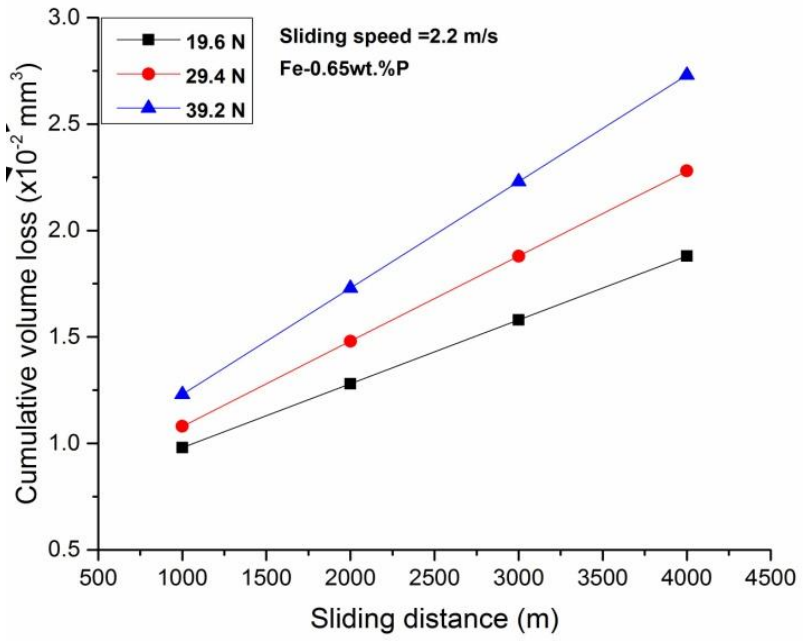

Figure 5.16: Variation of cumulative wear volume loss as a function of sliding distance at different loads for Fe-0.65wt.%P at 2.2 m/s.

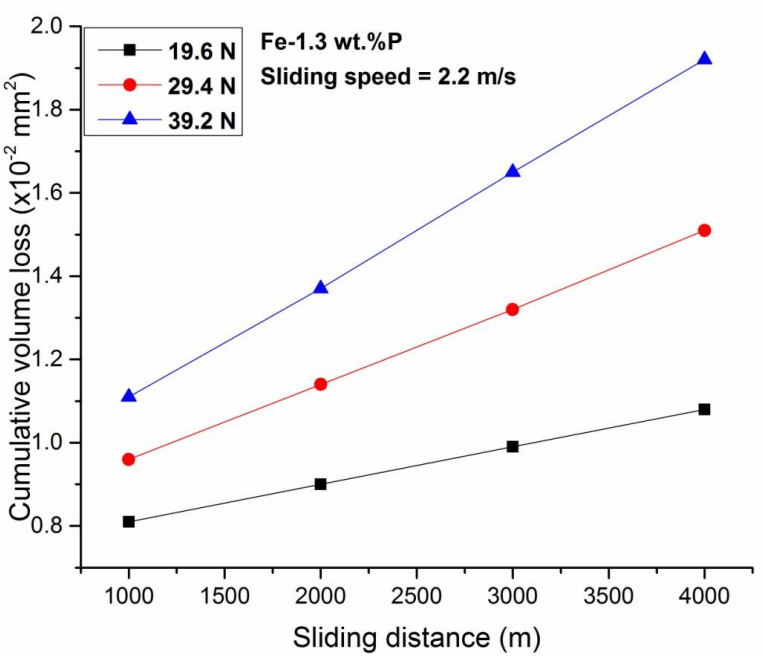

Figure 5.17: Variation of cumulative wear volume loss as a function of sliding distance at different loads for Fe-1.3wt.%P at 2.2 m/s.

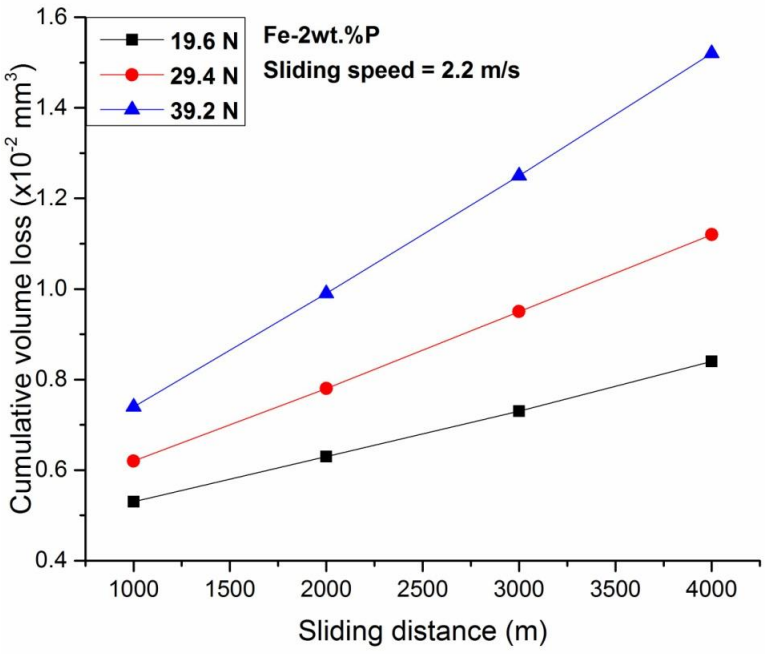

Figure 5.18: Variation of cumulative wear volume loss as a function of sliding distance at different loads for Fe-2wt.%P at 2.2 m/s.

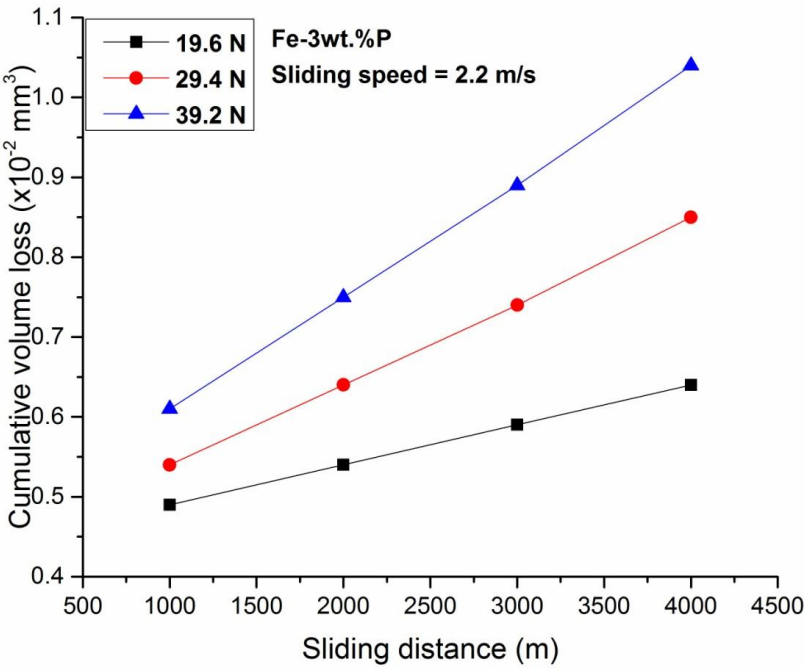

Figure 5.19: Variation of cumulative wear volume loss as a function of sliding distance at different loads for Fe-3wt.%P at 2.2 m/s.

The cumulative wear volume for Fe-3wt.%P alloy is found to be much lower as compared to iron, Fe-0.35wt.%P, Fe-0.65wt.%P, Fe-1.3wt.%P and Fe-2wt.%P at all the normal loads. The wear resistance increases with increasing P content of the alloy.

The wear rate (volume loss per unit sliding distance) at a given load was calculated from the slope of the lines in Figure 5.14 to 5.19 by linear least-squares fit at different loads. The wear rate increases more or less linearly at loads between 19.6 to 39.2 N. This is also in accordance with Archard Wear Equation (Eqn.5.3). This equation states that as the hardness of the samples increases wear rate decreases for a given load. In the present work, it has been found that the wear rate decreases with increasing phosphorus content of the alloy. This is due to an increase in the hardness of the sample. Fe-P alloys prepared by conventional powder metallurgy process (pressing and sintering) and casting route to show higher wear rates (Tomlinson and Dennison 1989; Zhang et al.1993; Fedorchenko et al. 1969) than the corresponding values obtained in the present work. This may be because of high density and uniform distribution of phosphides achieved in the present work by powder forging.

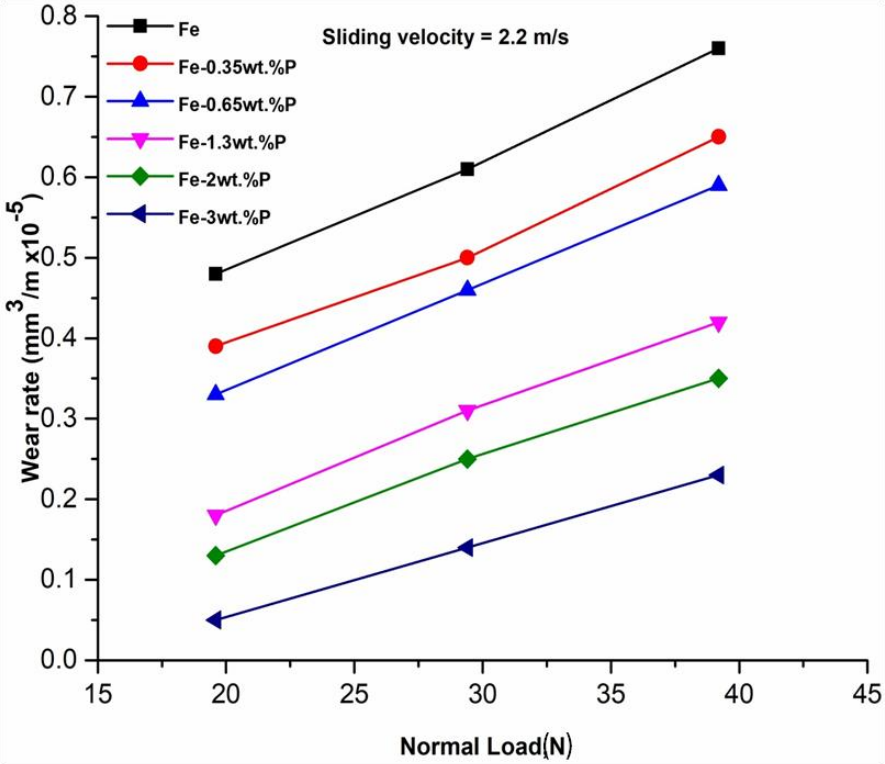

Figure 5.20: Variation of wear rate with normal load for pure iron, Fe-0.35wt.%P, Fe-0.65wt. %P, Fe-1.3wt.%P, Fe-2wt.%P and Fe-3wt.%P containing 0, 7, 10, 21, 25 and 34 % phosphide respectively at 2.2 m/s.

Figure 5.20 shows variation of wear rate with normal load. The wear rate increases with increasing load. The variation of wear rate with phosphide volume % at the normal loads of 19.6, 29.4 and 39.2N is shown in Figure 5.21. The wear rate decreases as the volume fraction of phosphide increases in the iron. Also, the decrease in wear rate with phosphide volume fraction is relatively more at a higher load of 39.2 N as compared to the lower load of 19.6 N. For all the loads, wear rate is maximum for the pure iron sample. This higher wear rate is attributed to the absence of iron phosphide in the pure iron. Iron phosphide is the load bearing phase in the alloy. Phosphorus addition to iron has also been reported (Moyer 1998; Chaurasia et al. 2012) to improve density in P/M Fe based alloys. This has also been observed in the present work. Apart from that phosphorus also goes into iron and causes solid solution strengthening of ferrite matrix.

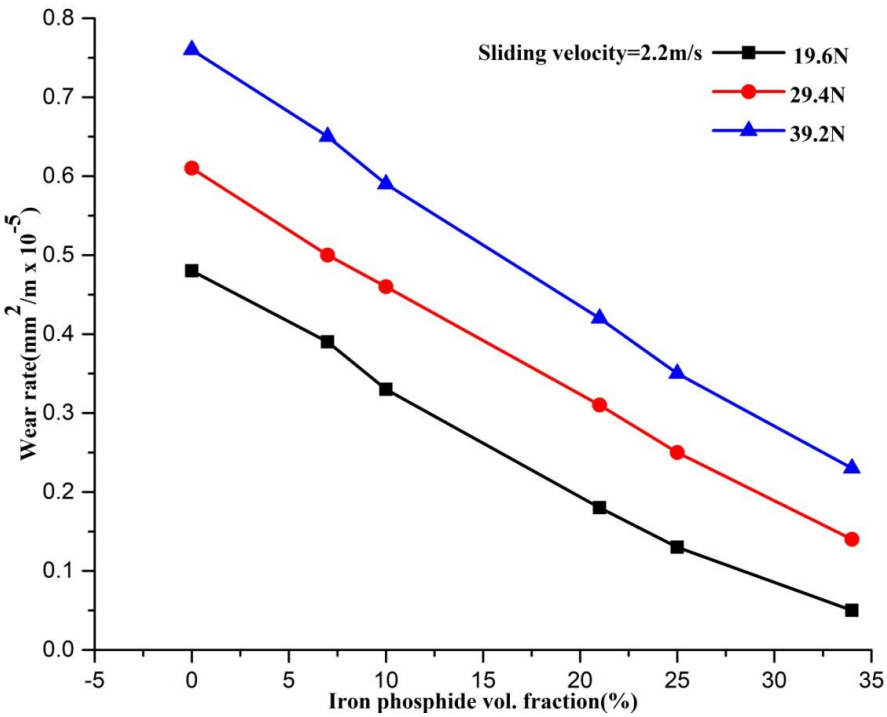

Figure 5.21: Variation of wear rate against phosphide volume fraction at the normal loads of 19.6, 29.4 and 39.2N at 2.2 m/s.

Hardness significantly affects wear characteristics. According to the Archard Wear Equation 1(b), as the hardness of the sample increases, the wear rate decreases for a given load. The wear coefficient was calculated from the slope of wear rate against load, and by multiplying it with the hardness of the corresponding pin sample. The wear coefficients for the alloys studied are given in Table 5.3.

Table 5.3: Wear rate and Wear coefficient of F-P alloys for sliding velocity 2.2m/s

Sample	**Wear rate (mm^3/m) x 10^{-5}**			**Wear coefficient**
	Normal load (N)			
	19.6	**29.4**	**39.2**	
Fe	0.48	0.61	0.76	$0.25x10^{-6}$
Fe-0.35wt.%P	0.39	0.50	0.65	$0.15x10^{-6}$
Fe-0.65wt.%P	0.33	0.46	0.59	$0.14x10^{-6}$
Fe-1.3wt.%P	0.18	0.31	0.42	$0.11x10^{-6}$
Fe-2wt.%P	0.13	0.25	0.35	$0.10x10^{-6}$
Fe-3wt.%P	0.05	0.14	0.23	$0.07x10^{-6}$

5.3.1.2 Dry sliding friction

Figure 5.22 shows the variation of coefficient of friction (COF) with normal load and phosphorus content. It is observed that the average COF decreases linearly with load. It also decreases with increasing phosphorus content.

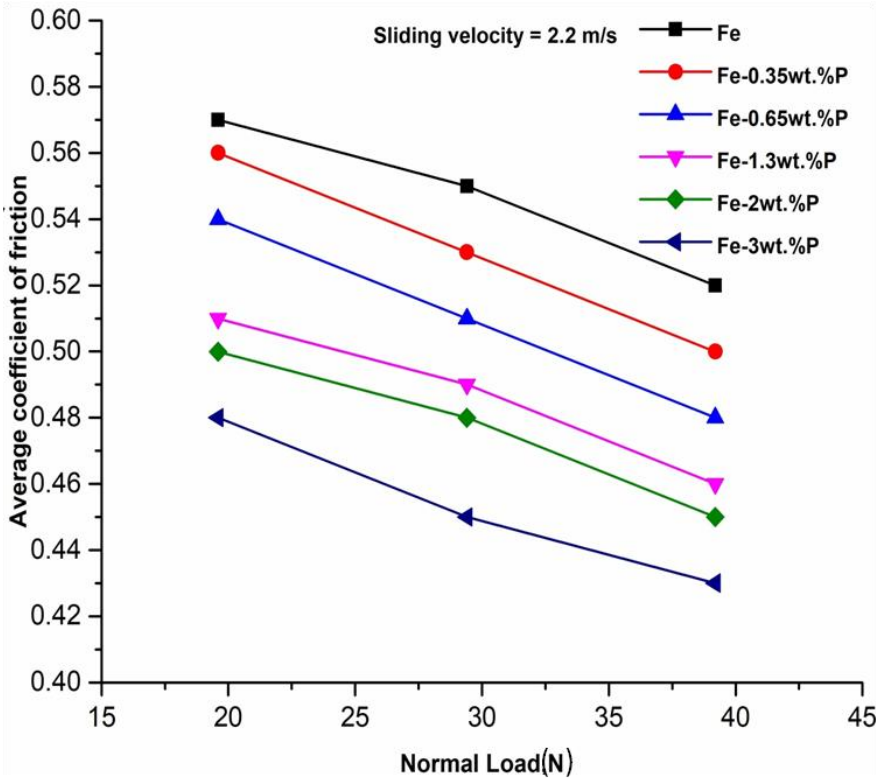

Figure 5.22: Variation of average coefficient of friction as a function of normal load for pure iron, Fe-0.35wt.%P, Fe-0.65wt.%P, Fe-1.3wt.%P, Fe-2wt.%P and Fe-3wt.%P containing 0, 7, 10, 21, 25 and 34 % phosphide respectively at 2.2 m/s.

The variation in the average coefficient of friction with iron-phosphide volume fraction is shown in Figure 5.23. The average COF is observed to decrease more or less linearly with increase in volume fraction. The average value varies from about 0.57 to 0.43. As phosphorus content increases in the alloy, the coefficient of friction decreases for a given load (Eyre and Williams 1973). This is attributed to the increase in the volume fraction of hard iron phosphide phase. This can be explained on the basis of more spread of compacted layer between the specimen and the disc and thereby reducing the real area of contact between the pin sample and disc.

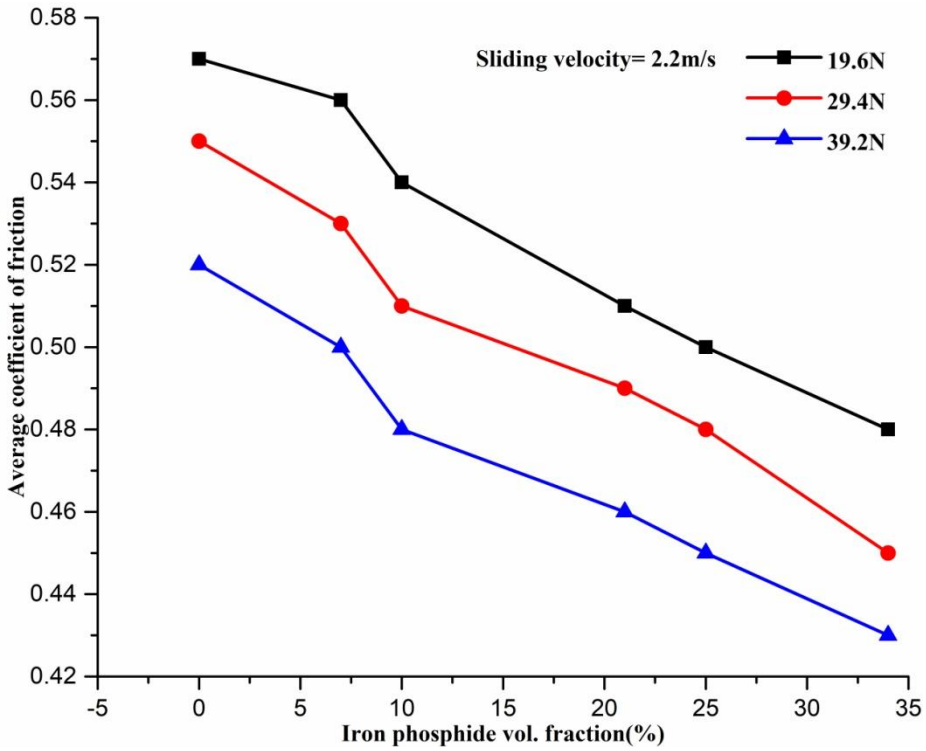

Figure 5.23: Variation of average coefficient of friction as a function of phosphide volume fraction at the normal loads of 19.6, 29.4 and 39.2N at 2.2 m/s.

The compacted layers consist of iron oxide and iron-phosphide as the presence of oxygen and phosphorus is detected on the worn surface of the specimen by SEM-EDS (Figure 5.25). Under the dry sliding wear, an oxide layer is formed due to the frictional heating over the sliding surface. The oxides are detached by repeated contacts and the wear debris of oxide particles is generated. The wear debris gets fascinated between the sliding surfaces and formed layers. The presence of iron oxide and phosphide layer suggests that the oxidation of iron and phosphorus takes place due to severe plastic deformation (Eyre and Williams 1973; Tomlinson and Dennison 1989) of wear debris in the presence of atmospheric oxygen. Further, it can be observed that COF also decreases with increase in load for given phosphorus content in the alloy (Figure 5.21).

This may be due to the improved rate of oxidation and better compaction of the oxides caused by the enhanced frictional heating at higher loads. The junctions formed due to oxide-oxide contact requires relatively less energy to shear during sliding as compared to that required for metallic micro welds due to higher hardness of iron oxide as compared to metallic iron. The average COF is higher for all the loads for pure iron. This is attributed to easier metal-metal micro weld formation as compared to iron phosphorus alloys as iron-phosphorus

alloy has higher hardness as compared to pure iron. The larger extent of the compacted layer formed can also account for the decrease in friction at higher load.

5.3.1.3 Worn surface analysis and wear mechanism

SEM images of worn surfaces are shown in Figure 5.24. Wear tracks and compacted layer can be observed on the worn surfaces. These wear tracks and compacted layers have been indicated by arrows in the figures. The worn surfaces are characterized by the presence of fine wear tracks parallel to sliding direction. During the sliding wear, frictional forces cause deformation of the metal surface which in turn plastically shears the surface in the sliding direction. As the ductility of the 0wt.% P alloy is relatively high due to soft ferritic matrix of single phase, continuous sliding causes the accumulation of plastically sheared surface. This results in nucleation of cracks that grows with sliding by shearing-fracture and finally delaminate the surface layer in the form of flakes like debris. Apart from delaminations, the worn surfaces also exhibit parallel lines in the direction of sliding that were formed due to abrasion (Gurumoorthy et al. 2007) by the wear debris which increases the wear rate. The delamination and abrasion in Fe result in higher volume loss.

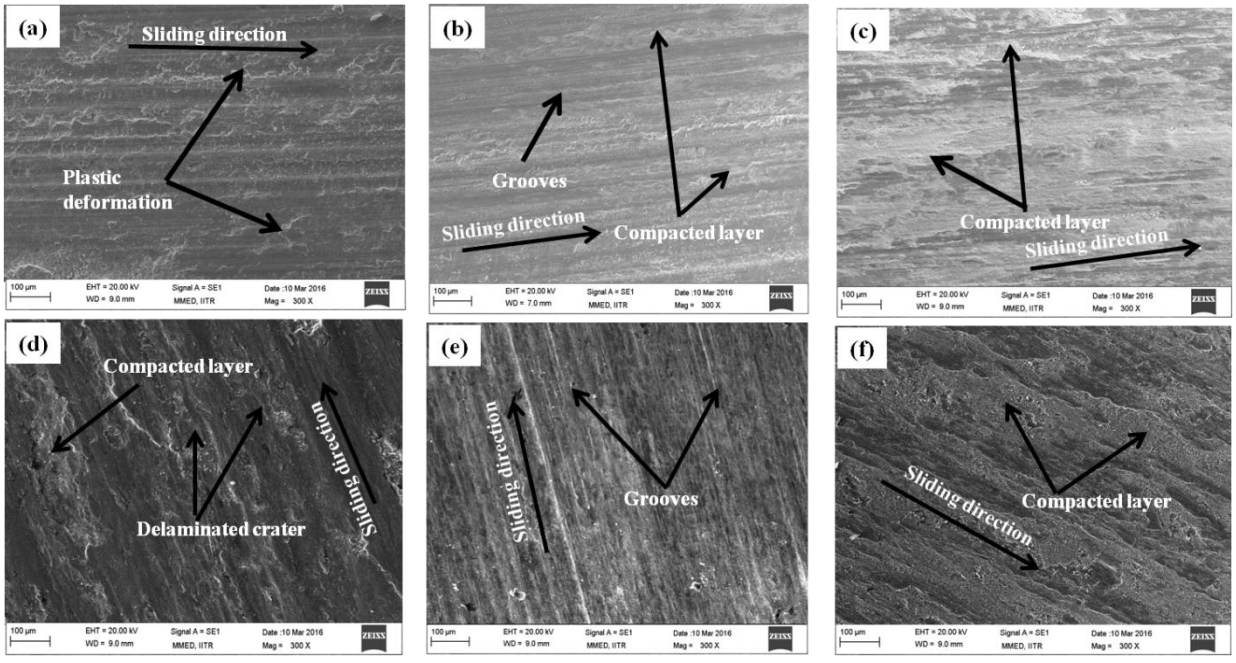

Figure 5.24: SEM images of worn surfaces of (a) pure iron (Fe), (b) Fe-0.35wt. %P, (c) Fe-0.65wt.%P, (d) Fe-1.3wt. %P, (e) Fe-2wt. %P and (f) Fe-3wt. %P alloys at 29.4 N after sliding for 30 min at a sliding speed of 2.2 m/s.

Fe-0.35wt.%P and Fe-0.65wt.%P alloys were found to be subjected to low wear loss compared to the pure iron (0wt.%P), as the presence of phosphide precipitates supports its wear

resistance behavior. The surface layer got detached at certain locations in few patches intermittently as generation and failure of a crack due to strain accumulation occurred with the progress of sliding as discussed earlier. A comparison of Figure 5.24(a) and Figures 5.24(b-f), clearly shows that the extent of cover is provided by the transfer layer in Fe-P alloys when it begins to form by compacting the wear debris entrapped between the sliding surfaces. This transfer layer of the compacted debris provides the protection to underlying metal and as a result the wear rate decreases (Figure 5.24 (f)).

From the SEM images of the Fe-0.35wt.%P and Fe-0.65wt.%P alloys (Figure 5.24), the compact layer appearance is clearly evident on the worn surfaces of these alloys. These compacted layers consist of iron oxide and iron phosphide as the presence of oxygen and phosphorus is detected on the worn surface of the specimen by SEM-EDS (Figure 5.25).

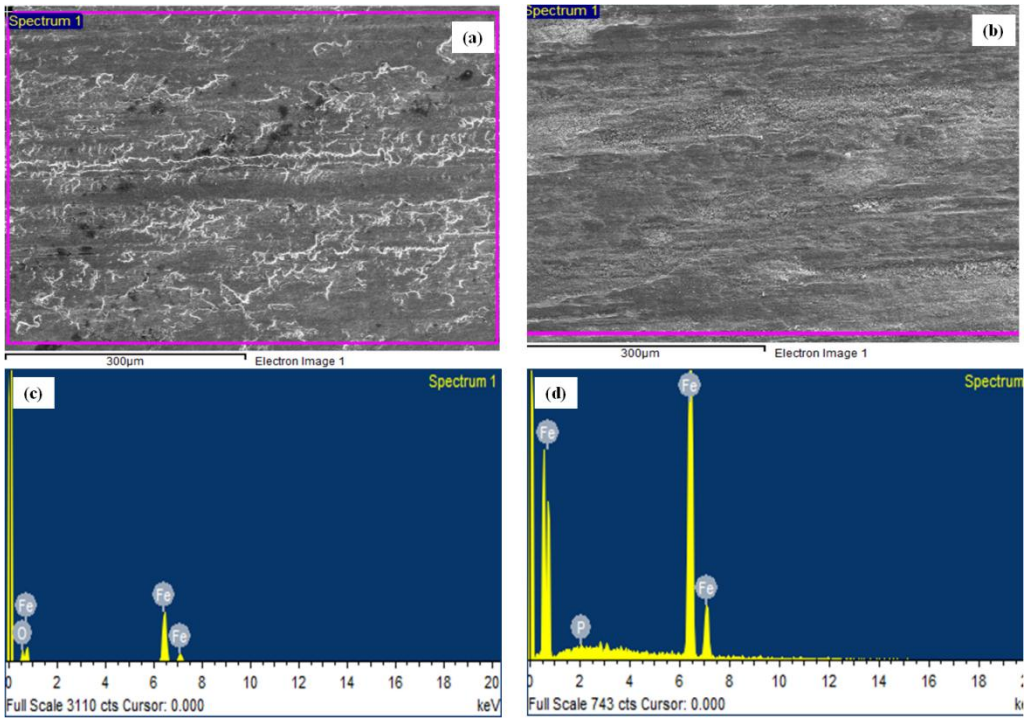

Figure 5.25: (a) SEM micrograph of worn surfaces of Fe (b) SEM micrograph of worn surfaces of Fe-0.35wt. %P. (c) Elemental analysis of Fe (d) Elemental analysis of Fe-0.35wt. %P.

In the presence of atmospheric oxygen, the oxidation of iron and phosphorus takes place due to severe plastic deformation of wear debris and form iron oxide and phosphide layer on the sliding surface. The presence of iron oxide and phosphide layer suggests that the oxidation of iron and phosphorus takes place due to severe plastic deformation of wear debris in the presence of atmospheric oxygen. The presence of oxide layer in images indicates oxidative wear mechanism. However, the presence of some wears debris and detachment of oxide layer

also manifested abrasion, as well as delaminations. Wear tracks can be observed on the worn surface (Figure 5.24). Wear tracks are deeper and wider in the pure iron sample as compared to Fe-0.35wt.%P and Fe-0.65wt.%P suggesting more wear volume loss. A continuous surface oxides layer which could be iron oxide is mechanically stable and delineates oxidative wear as a dominating wear mechanism in higher P content alloys. Formation of stable oxide layer supports decreased wear volume and coefficient of friction. Further, due to hard and homogeneous phosphide phase, 3wt.% P specimen exhibited highest wear resistance.

5.3.2 Dry Sliding Wear and Friction Behaviour at 3m/s Sliding Velocity

5.3.2.1 Wear characteristics

The cumulative wear volume loss varied with a sliding distance under different normal loads (19.6, 29.4 and 39.2N) and at a sliding velocity of 3 m/s are shown in Figures 5.26 to 5.31 respectively. It is observed in these figures that cumulative wear volume loss increases with increasing sliding distance. It is further noted that for a given sliding distance cumulative wear volume loss increases with increasing load. These two observations are in line with Archard Wear Equation (Equ. 5.2). It is also noted that cumulative wear volume loss decreases with increasing phosphorus content for a given sliding distance and load.

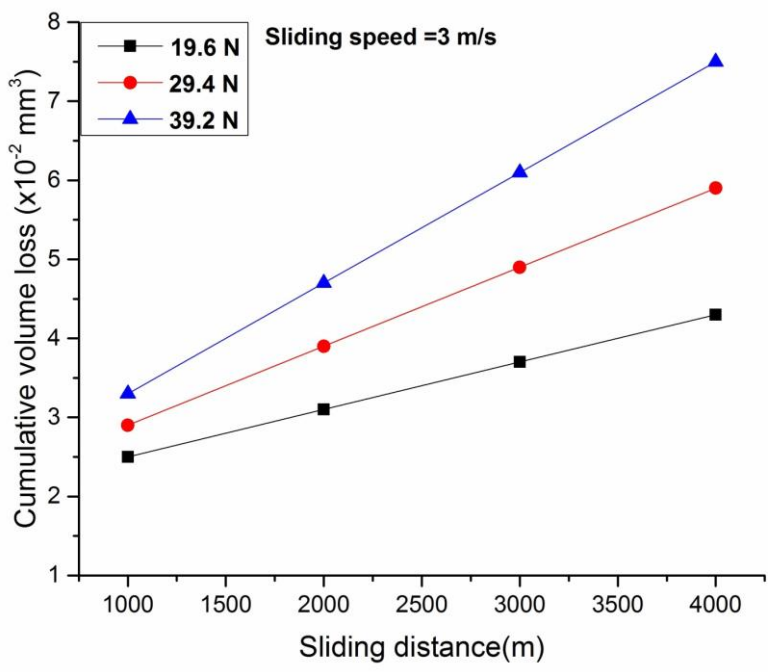

Figure 5.26: Variation of cumulative wear volume loss as a function of sliding distance at different loads for pure iron at 3 m/s.

Figures 5.26 shows variation of cumulative wear volume loss with sliding distance at different loads of 19.6, 29.4 and 39.2N for pure iron. The cumulative wear volume is found to increase with sliding distance at a particular load say 19.6N

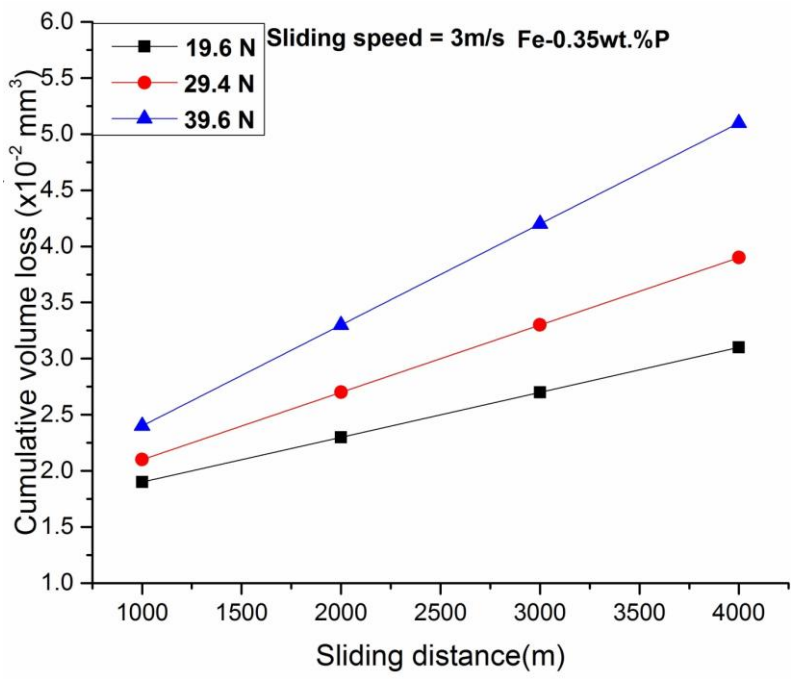

Figure 5.27: Variation of cumulative wear volume loss as a function of sliding distance at different loads for Fe-0.35wt.% P at 3 m/s.

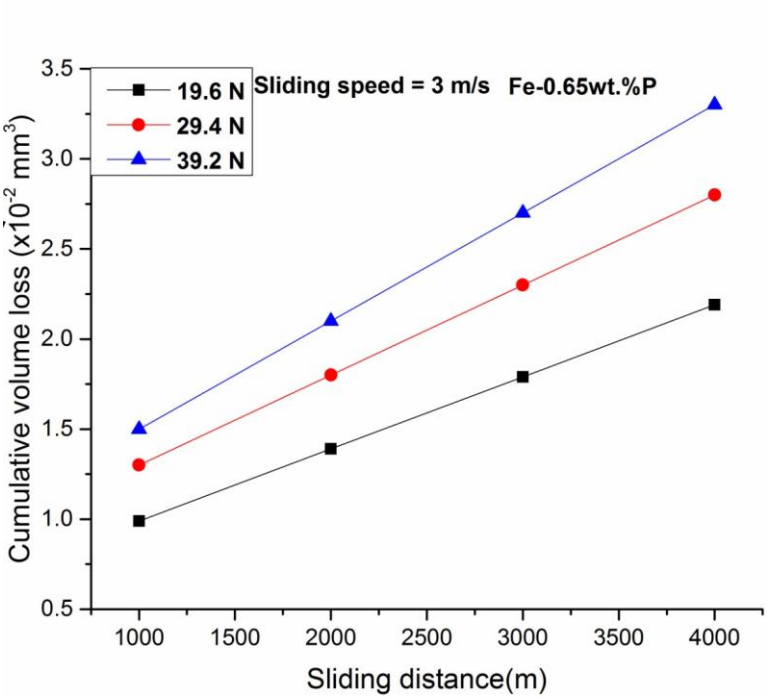

Figure 5.28: Variation of cumulative wear volume loss as a function of sliding distance at different loads for Fe-0.65wt.% P at 3 m/s.

A similar trend of variation of cumulative wear volume with sliding distance is also observed for other normal loads i.e., 29.4 and 39.2N. The cumulative wear volume is also observed to increase with the increase in normal load.

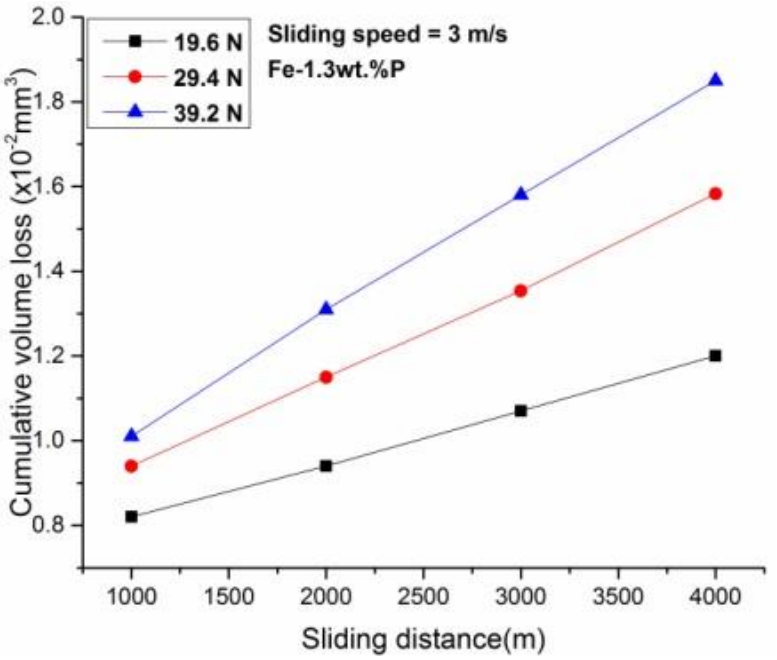

Figure 5.29: Variation of cumulative wear volume loss as a function of sliding distance at different loads for Fe-1.3wt.% P at 3 m/s.

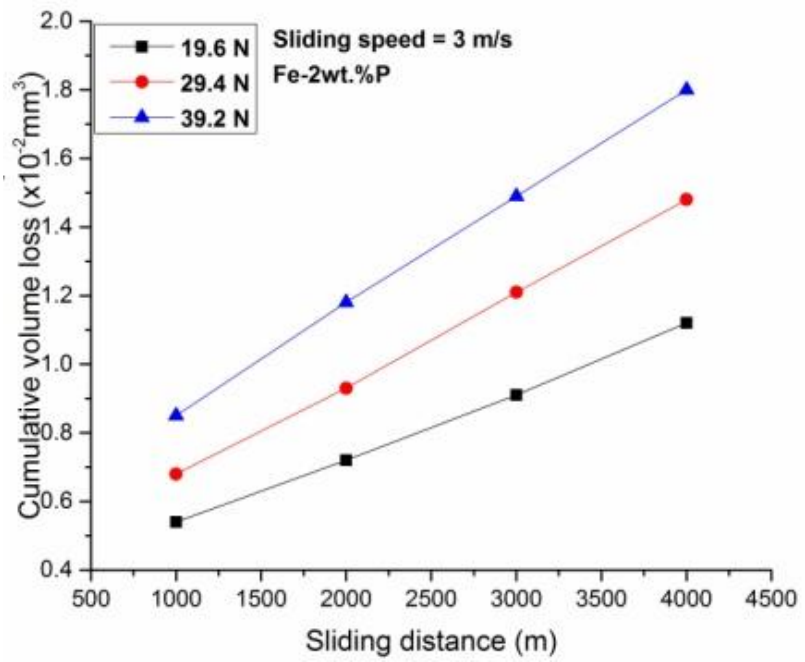

Figure 5.30: Variation of cumulative wear volume loss as a function of sliding distance at different loads for Fe-2wt.% P at 3 m/s.

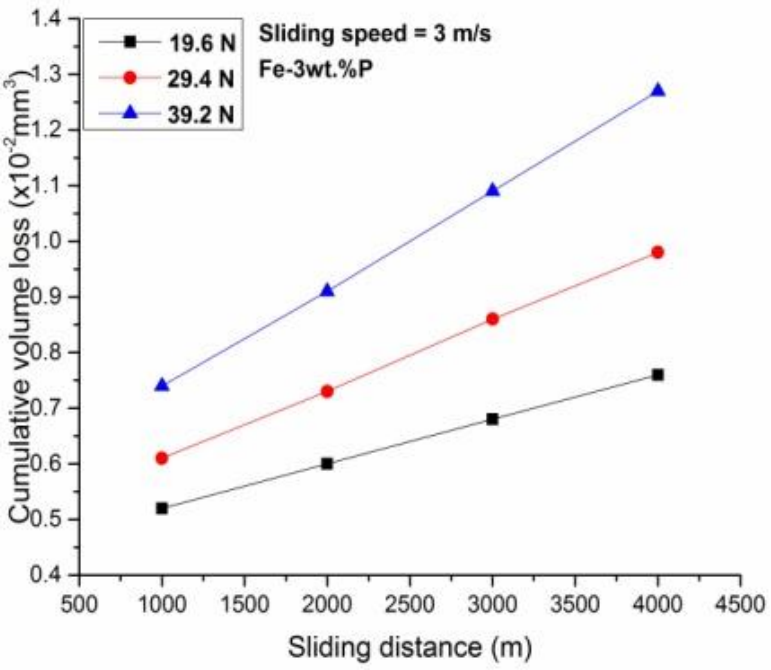

Figure 5.31: Variation of cumulative wear volume loss as a function of sliding distance at different loads for Fe-3wt.%P at 3 m/s.

The cumulative wear volume for Fe-3wt.%P alloy is found to be much lower as compared to iron, Fe-0.35wt.%P, Fe-0.65wt.%P, Fe-1.3wt.%P and Fe-2wt.%P at all the normal loads with wear loss decreasing with increasing P content of the alloy.

The variation of the wear rate vs normal load is shown in Fig. 5.32. The wear rate (volume loss/sliding distance) at a given load was determined from the slope of the lines in Figs. 5.26 to 5.31 by linear least-squares fit at different loads. The wear rate increases linearly with increasing loads, from 19.6 to 39.2N. The similar trends have been observed by (Mohan and Srivastava 2006) in their study conducted to see the effect of applied load on wear rate irrespective of sliding velocity on as-cast Al–Fe inter-metallic composites. For any given load wear rate is maximum for Fe among all the alloys. It is further observed that the wear rate is minimum at all loads for Fe-3wt. %P alloy.

Fe-P alloys developed by conventional (pressing and sintering) and casting route to show higher wear rates (Tomlinson and Dennison 1989; Zhang et al.1993; Fedorchenko et al. 1969). This may be because of high density and uniform phosphide distribution achieved in the present work by hot powder forging.

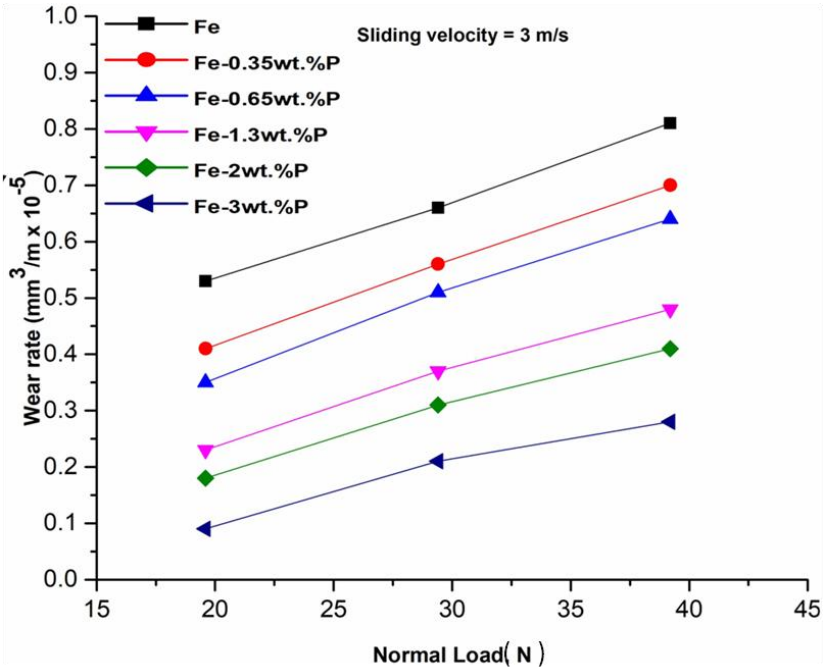

Figure 5.32: Variation of wear rate with a normal load for pure iron, Fe-0.35wt. %P, Fe-0.65wt. %P, Fe-1.3wt. %P, Fe-2wt. %P and Fe-3wt. %P containing 0, 7, 10, 21, 25 and 34 % phosphide respectively at 3 m/s.

The variation of wear rate with phosphide volume fraction at the normal loads of 19.6, 29.4 and 39.2N is shown in Figure 5.33. It shows that as phosphorus content increases in the iron, wear rate decreases. Other researchers have also found the same trend (Zhang et al.1993; Fedorchenko et al. 1969). In another study the wear rate and coefficient of friction reduced by the introduction of reinforced particles in an aluminum matrix (Roy 1992). Wear rate is maximum at 39.2N and minimum at 19.6N for Fe. This higher wear rate is attributed to the soft ferrite matrix phase. Since Iron phosphide is the load bearing phase in the alloy. Phosphorus addition to iron results in the formation of phosphide phase which produces a denser structure with higher hardness. Apart from that phosphorus also goes into iron up to the solubility limit and causes solid solution strengthening of ferrite matrix. In the present investigation, the average micro-hardness of iron-phosphide is 480VHN.

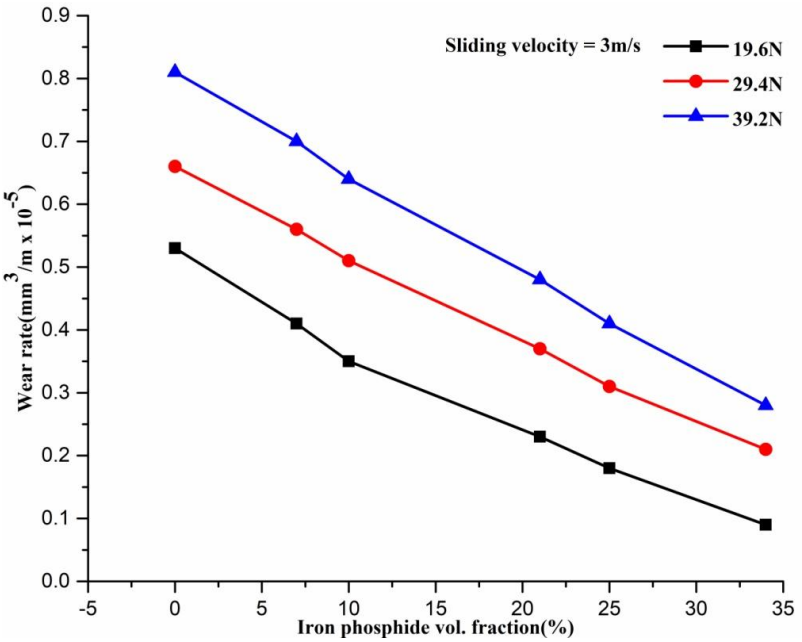

Figure 5.33: Variation of wear rate as a function of phosphide volume fraction at the normal loads of 19.6, 29.4 and 39.2N at 3 m/s.

The wear coefficient was calculated from the slope of wear rate with load, by multiplying it with the hardness of the corresponding pin sample. The wear coefficients for alloys studied are given in Table 5.4.

Table 5.4: Wear rate and Wear coefficient of Fe-P alloys for sliding velocity of 3m/s

Sample	**Wear rate ($mm^3/mx10^{-5}$)**			**Wear coefficient**
	Normal load (N)			
	19.6	**29.4**	**39.2**	
Fe	0.53	0.66	0.81	$0.31x10^{-6}$
Fe-0.35wt.%P	0.41	0.56	0.70	$0.20x10^{-6}$
Fe-0.65wt.%P	0.35	0.51	0.64	$0.18x10^{-6}$
Fe-1.3wt.%P	0.23	0.37	0.48	$0.13x10^{-6}$
Fe-2wt.%P	0.18	0.31	0.41	$0.11x10^{-6}$
Fe-3wt.%P	0.09	0.21	0.28	$0.09x10^{-6}$

5.3.2.2 Dry sliding friction

Figure 5.34 shows the variation of coefficient of friction (COF) with normal load and phosphorus content. The average COF decreases linearly with increase in the load, for all the alloys. It also decreases with increasing phosphorus content.

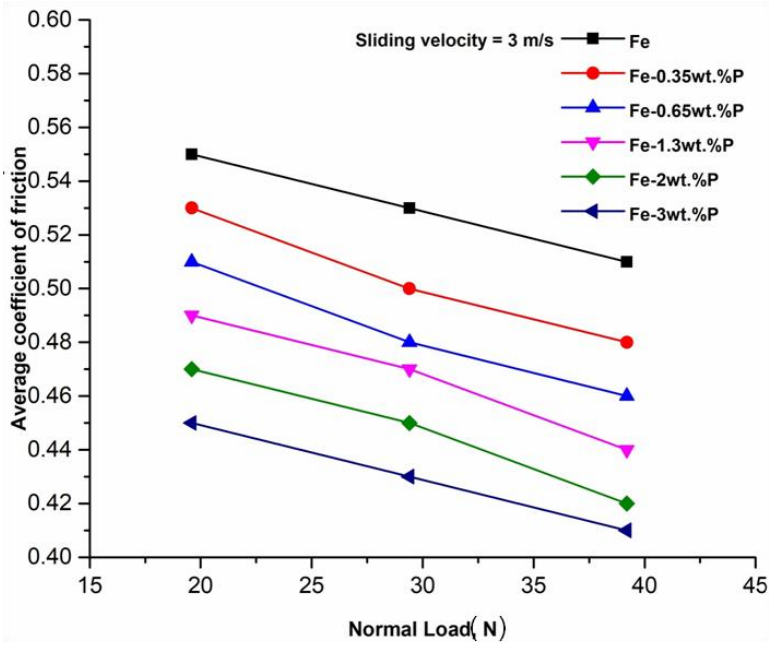

Figure 5.34: Variation of average coefficient of friction as a function of normal load for pure iron, Fe-0.35wt.%P, Fe-0.65wt.%P, Fe-1.3wt.%P, Fe-2wt.%P and Fe-3wt. %P containing 0, 7, 10, 21, 25 and 34 % phosphide respectively at 3 m/s.

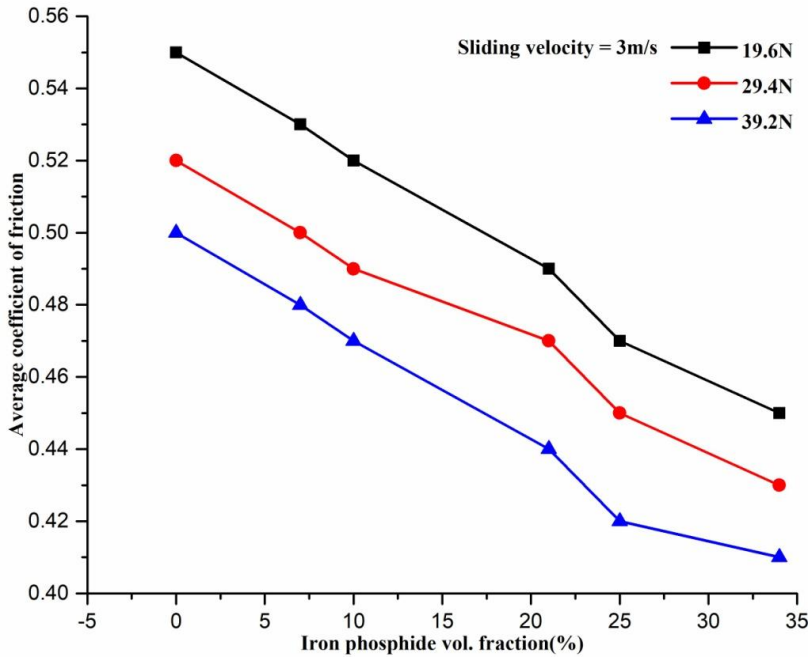

Figure 5.35: Variation of average coefficient of friction as a function of phosphide volume fraction at the normal loads of 19.6, 29.4 and 39.2N at 3 m/s.

Figure 5.35 shows the variation in the average coefficient of friction with iron phosphide volume fraction at given loads. The average value of changing frictional force was recorded at a regular interval of time for calculating the coefficient of friction. The average

coefficient of friction decreases more or less linearly with increase in volume fraction of iron-phosphide. Similar observations have been reported by Roy 1992. He reported that when hard particles are introduced into the matrix, the coefficient of friction values decreases for all sliding distances. The average value varies from about 0.55 to 0.41 at 3m/s. Further, it can be observed that the coefficient of friction also decreases with increase in load for a given phosphorus content in the alloy (Figure 5.35). Kchaou et al. 2013 have also studied that when the applied load is increased, the values of the coefficient of friction decreases for all sliding distances. This can be explained on the basis of the presence of compacted layer between the specimen and the disc. These compacted layers consist of iron oxide and iron phosphide as the presence of oxygen and phosphorus is detected on the worn surface of the specimen by SEM-EDS (Figure 5.36).

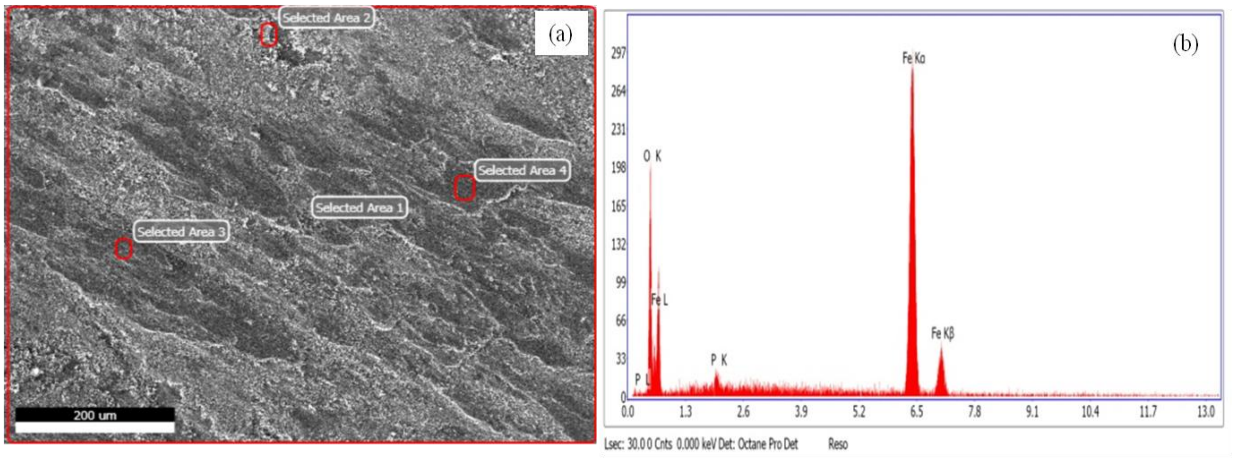

Figure 5.36: (a) Worn surface of Fe-3wt.%P under SEM (b) Elemental analysis of worn surface using energy dispersive analysis of X-rays. It shows the compacted layer of phosphorus at the worn surface.

Due to severe plastic deformation of wear debris, the oxidation of iron and phosphorus takes place in the presence of atmospheric oxygen. The scanning electron micrographs of worn surfaces of pure iron (Fe), Fe-0.35wt.%P, Fe-0.65wt.%P,Fe-1.3wt.%P, Fe-2wt.%P and Fe-3wt. %P is shown in Fig. 5.37. Wear tracks can be observed on the worn surface. Figures 5.37 clearly show that the deformed layers are along the direction of sliding which experienced a significant amount of plastic deformation during wear. It has been reported in the literature that the coefficient of friction decreases with P content for a given load (Lindskog et al.1977). During dry sliding wear at sliding speed 3m/s and load 39.2N, strains were accumulated on sliding surfaces by repeating contact of the counter surface.

5.3.2.3 Worn surface analysis and wear mechanism

Figure 5.37 shows the worn surface morphologies of Fe-P alloys. The morphologies show plastic deformation, wear tracks, delaminations, ploughing, and oxidation which have been indicated by arrows in the figures. Under a normal load of 39.2 N, the worn surface of the Fe-0.35wt.%P alloy (Figure 5.37 (b)) depicts ploughing. The worn surface of the Fe-0.65wt.%P alloy (Figure 5.37(c)) exhibits delaminations. Oxidative wear can be found on the worn surface of Fe-1.3wt.%P. For Fe-2wt.%P with 25vol% phosphide, abrasion seems to play a role in wear mechanism. The more delaminated layers can be observed on the worn surfaces of Fe-3wt.%P (Figure 5.37 (f)). The worn surface of a fully ferritic alloy shows wider wear track and plastic deformation because the fully ferritic alloy has a weaker matrix (Figure 5.37(a)).

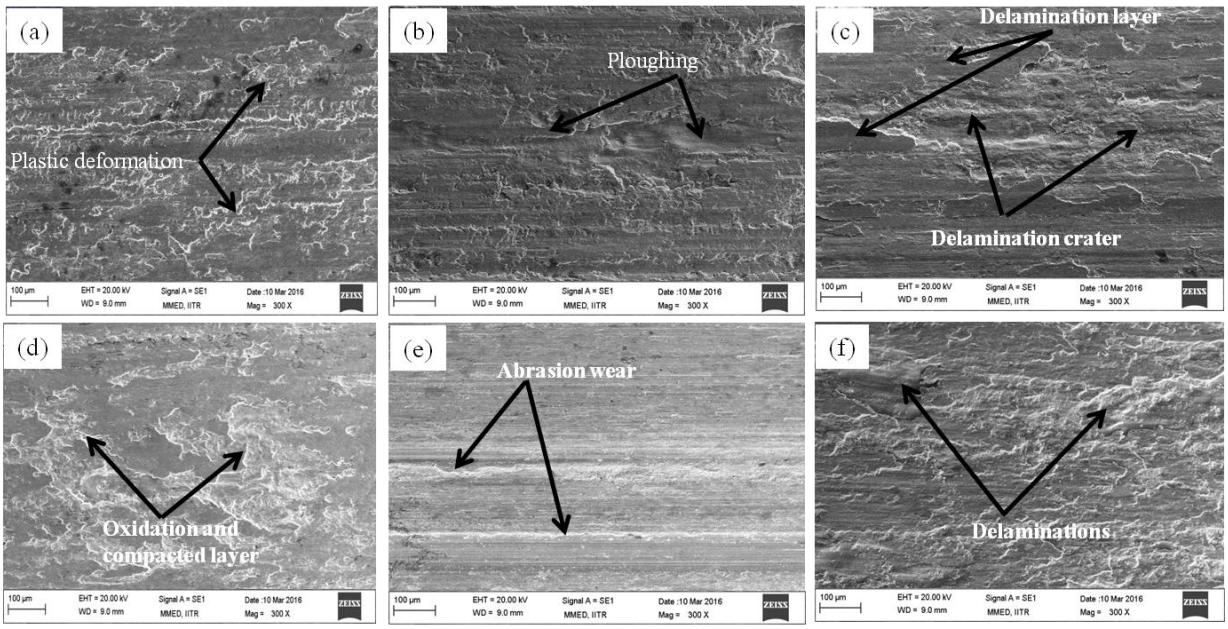

Figure 5.37: SEM images of worn surfaces of (a) pure iron, Fe (b) Fe-0.35wt.%P, (c) Fe-0.65wt.%P, (d) Fe-1.3wt.%P, (e) Fe-2wt.%P and (f) Fe-3wt.%P alloys at 39.2 N after sliding for 30 min at a speed of 3 m/s.

Due to the soft ferritic matrix of single phase, continuous sliding causes the accumulation of plastically sheared surface. Obviously, under normal loads the Fe-3wt.%P alloy with 34vol % phosphide shows better resistance to wear and plastic deformation. The delaminated layer can be seen on the worn surface of Fe-3wt.% P alloy because this alloy shows the higher hardness as well as more phosphide among six Fe-P alloys as shown in Figure 5.37. These properties are required for reducing the wear and resisting the initiation and propagation of the cracks.

In the presence of atmospheric air, the iron and phosphorus form layers of iron oxide and phosphide at the sliding surface suggesting that the oxidation of iron and phosphorus takes place due to severe plastic deformation of wear debris. However, the presence of some wear debris and detachment of oxide layer also manifested abrasion as well as delamination wear (especially in P content alloys) as dominating wear mechanism. Wear tracks can be observed on the worn surface. In high P content alloys, a continuous oxides layer would be formed on the surface which is mechanically stable and delineates. It shows that the dominating mechanism of wear is oxidative wear. Further, due to the hard phosphide phase, 3wt.% P specimen exhibited highest wear resistance. Further, the presence of phosphide precipitates supports its wear resistance behavior. The surface layer got detached at certain locations in few patches intermittently as generation and failure of a crack due to strain accumulation occurred with the progress of sliding as discussed earlier. A comparison of Figure 5.37(a) and Figure 5.37(b-f), clearly shows that the extent of cover provided by the transfer layer in Fe-P alloys when it begins to form by compacting the wear debris trapped between the sliding surfaces. This transfer layer of the compacted debris provides the protection to underlying metal and thus the wear rate decreases (Figure 5.37(f)). Jiang et al. 1998 have studied the role of triboparticulates in dry sliding wear. They have seen that very fine particles are accumulated on the worn surface which forms a load bearing compacted layer resulting in oxide-to-oxide contact between the rubbing surfaces.

5.3.2.4 Wear debris analysis

The debris particles were collected from iron (Fe), Fe-0.35wt.%P, Fe-0.65wt.%P, Fe-1.3wt.%P, Fe-2wt.%P and Fe-3wt.%P alloys surfaces and subjected to SEM-EDS analysis. Typical SEM image of the debris particles from the iron (Fe), Fe-0.35wt.%P, Fe-0.65wt.%P, Fe-1.3wt.%P, Fe-2wt.%P and Fe-3wt.%P alloys at 39.2 N are shown in Fig. 5.38. Debris generated from pure iron is typically large in size and irregular in shape. The presence of oxygen in the EDS analysis of the debris essentially suggests the formation of iron-oxide during sliding (Figure 5.38 (a)). Figure 5.38(a) shows that the wear mechanism involved is primarily mild oxidative wear. With increasing phosphorus content in iron, debris became blunt and soften compacted layers.

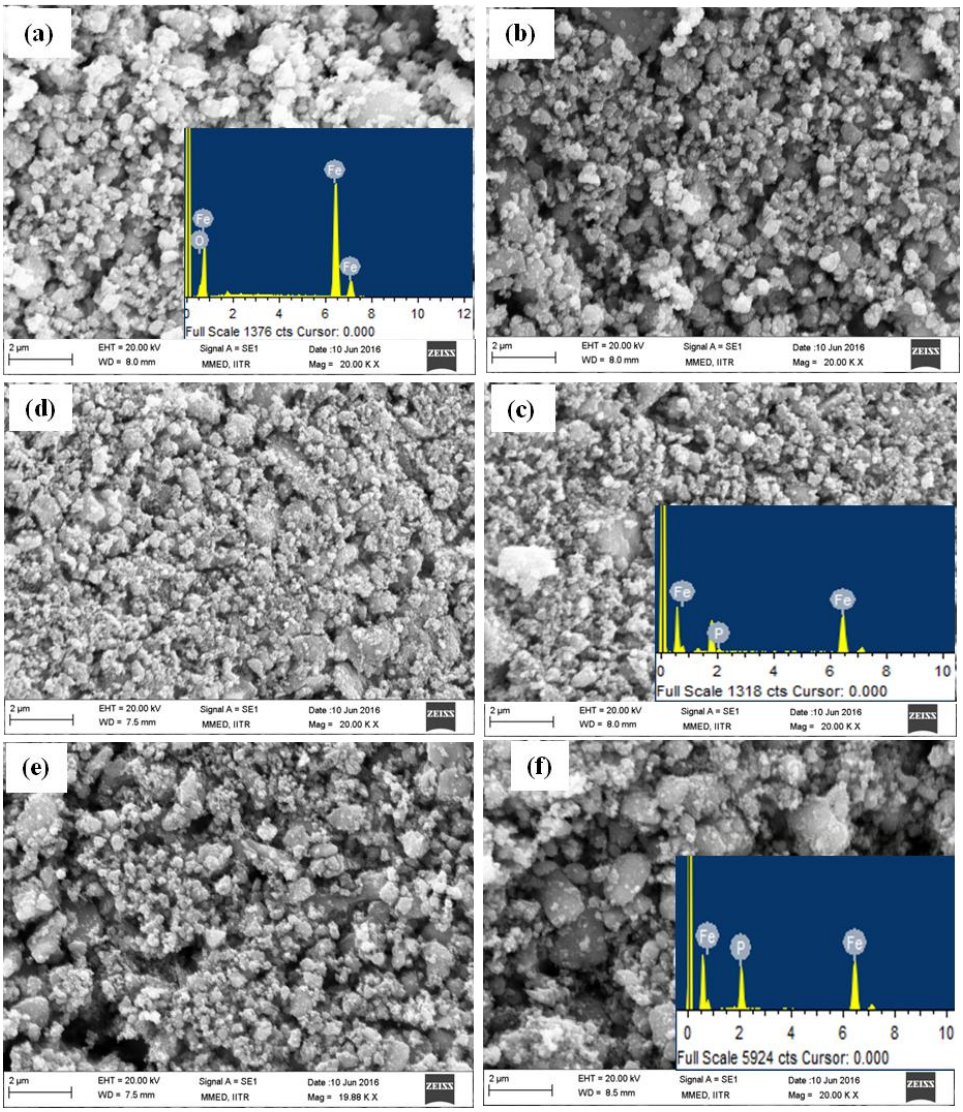

Figure 5.38: SEM images of debris collected after sliding at 29.4 N normal load for (a) pure iron, Fe (b) Fe-0.35wt. %P, (c) Fe-0.65wt.%P, (d) Fe-1.3wt.%P, (e) Fe-2wt.%P and (f) Fe-3wt.%P alloys. Insets in (a), (c) and (d) are EDS of debris collected from the worn surfaces.

The presence of phosphorus in the EDS analysis indicates the formation of a compacted layer of phosphide during sliding as seen in Figures 5.38 (b-f). The morphologies of debris belonging to different phosphorus content alloys are shown in Figures. 5.38 (b-f). Debris corresponding to 0.35wt.% P, 0.65wt.%P, 1.3wt.%P and 2wt.%P are similar and are compacted agglomerates of fine particles (Figures.5.38 (b-e)). Debris in Fe-3wt.% P are large and rounded as well as agglomerates of fine particles (Figure 5.38 (f)). However, in reference to worn surface analysis, the formation of an oxide or phosphide layer was favored in the investigated sliding conditions. Therefore, it is possible that the sliding of Fe-P alloys causes fracture and removal of phosphide.

5.4 EFFECT OF CARBON ON MICROSTRUCTURE AND MECHANICAL PROPERTIES OF Fe-0.65wt.% P ALLOY

This section deals with the strength, hardness, ductility and toughness of alloy Fe-0.65wt.%P-0.20wt.%C. The influence of addition of carbon (graphite) on these properties is discussed. All above mechanical properties were correlated with the observed microstructure.

5.4.1 Microstructure

The microstructures of Fe-0.65wt.%P-0.20wt.%C alloy developed through hot powder forging route have been examined under an optical and scanning electron microscope to find the amount and the distribution of phases in the microstructure.

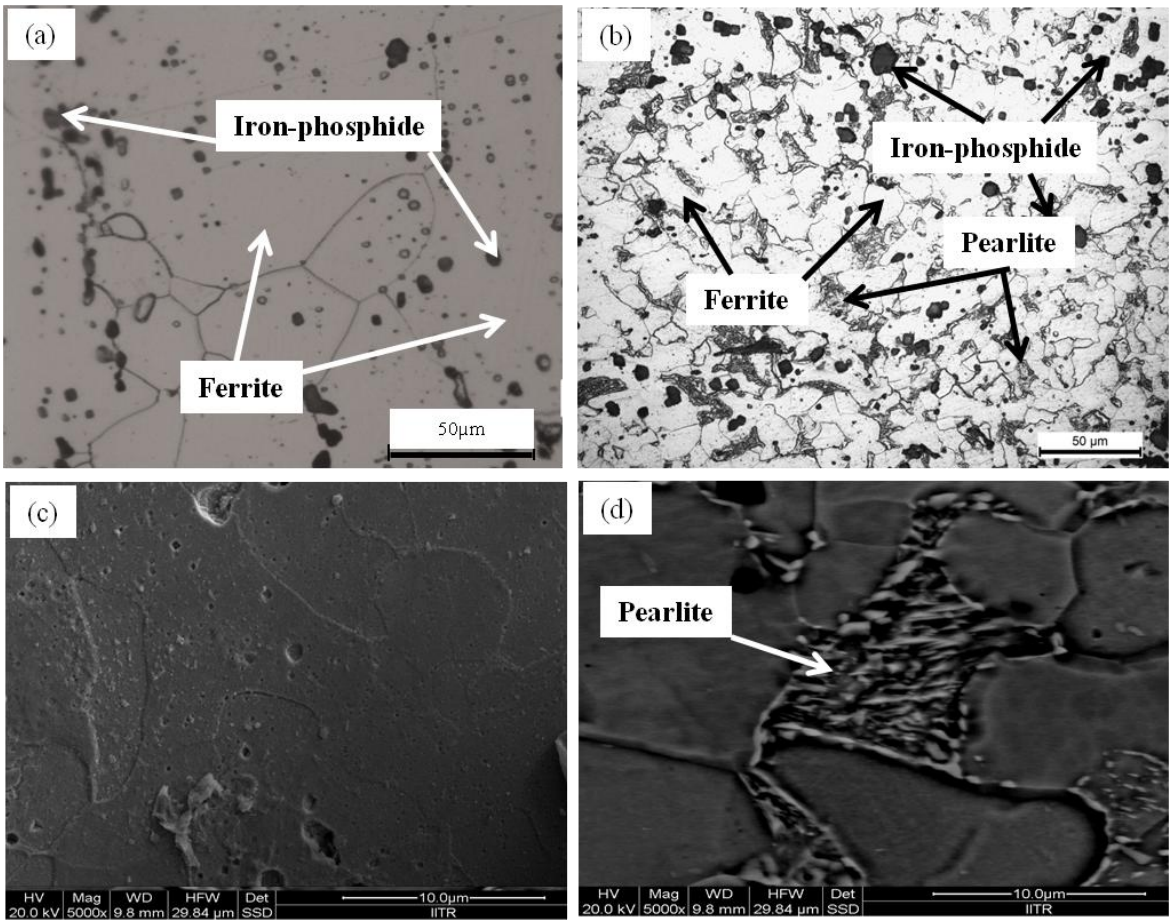

Figure 5.39: (a) and (b): Optical microstructure for Fe-0.65 wt.%P and Fe-0.65 wt.%P-0.20wt. % C, respectively; (c) and (d): SEM microstructure for Fe-0.65 wt.%P and Fe-0.65 wt. %P-0.20wt. % C, respectively

Representative optical microstructure of the samples in stress relieved condition (at 873K for 1hr and cooled in the furnace) is shown in Fig.5.39 and 5.45. The forged alloys exhibit iron phosphide (Fe_3P) and pearlite in a ferrite matrix **(**Figure 5.39). The Figure 5.39(a)

exhibits iron phosphide (Fe_3P) precipitate (as shown by the arrow) in a ferrite matrix**.** Similarly, carbon containing alloy show presence of pearlite along with phosphide **(**Figure 5.39(b)). Presence of pearlite has been highlighted by the arrow. Forged Iron-phosphorus P/M alloys do not exhibit segregation of phosphorus along the grain boundaries.

The carbon helps in a number of ways; (i) acts as a solid state reducing agent during processing, (ii) combines with oxygen and makes a protective reducing environment of CO (Lejcek 2010), (iii) drives phosphorus into ferrite matrix as a solute and depresses it to precipitate as phosphide along grain boundaries (Balasubramaniam 2000).

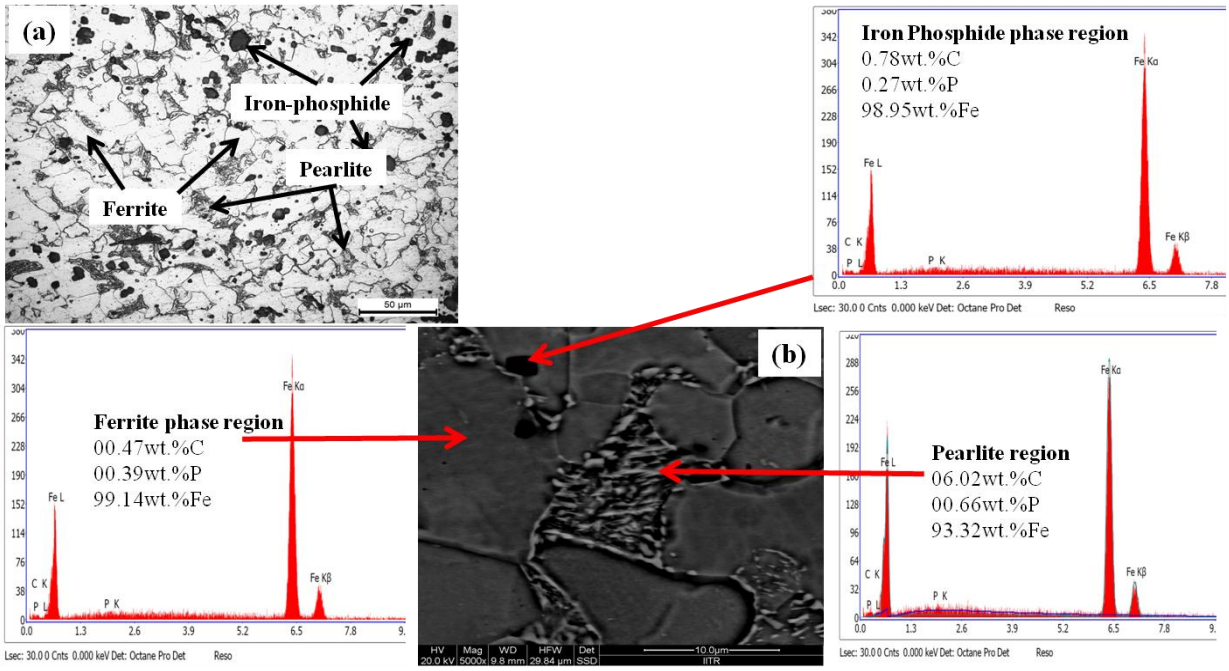

Figure 5.40: SEM and EDS analysis from the matrix, iron phosphide and pearlitic region of Fe-0.65wt.%P-0.20wt.%C alloy showing the presence of phosphorus.

The Figure 5.40 shows the SEM and EDS analysis from the matrix, iron phosphide and pearlitic region of Fe-0.65wt.%P-0.20wt.%C alloy. The EDS analysis of the different region has been shown by the arrow. It shows that the carbon present in the ferrite matrix as well as in iron phosphide and pearlite.

5.4.2 Mechanical Properties

The Vickers hardness for Fe-0.65wt.%P-0.20wt.%C alloy has been found to be 200HV (Table 5.5). A small amount of carbon addition (0.2wt %) in the Fe-P based alloy improved the hardness to approximately double as reported for corresponding alloy without carbon. The

hardness of the alloy without carbon content is 111HV. This may be because of high density achieved in the present work by powder forging. Alloy developed by the conventional route of powder metallurgy having 1wt%P is 99HV (Eyre and Walker 1976).

The yield and tensile strength for Fe-0.65wt.%P-0.20wt.%C alloy are shown in Table 5.5. The yield strength (YS) and ultimate tensile strength (UTS) of the Fe-P based alloy increases with the addition of C. The yield strength of the alloy was influenced by the strengthening of ferrite matrix. It was indirectly strengthened by the presence of C in the Fe-P based alloy. The ferrite matrix is strengthened by the solid solution of phosphorus in iron (Hansel and Grabke 1986). Tensile properties are significantly influenced by the addition of phosphorus and carbon in iron. The tensile strength is improved by the addition of carbon in Fe-P based alloy without compromising the ductility. The measured strength and ductility of the alloy are superior to those described in the literature (Hopkins and Tipler 1958; Straffelini et al. 1993; Suzuki et al.1985) for Fe-P alloys with carbon content. The powder forging process provides high density to alloys among the powder metallurgy processes. Further, forging may also lead to improved chemical and structural homogeneity (James et al. 1998). In the casting route, the last molten liquid to solidify is enriched with phosphorus during the solidification which is segregated along the grain boundaries (Lindskog 1973). The segregation of P may lead to deterioration of mechanical properties due to the brittleness of grain boundary (Hansel and Grabke 1986). In the present investigation the yield strength (YS), ultimate tensile strength (UTS), % elongation and hardness have been obtained 465MPa, 552MPa, 13%, and 200HV respectively with the addition of 0.20wt.%C in the Fe-0.65wt.%P alloy.

Table 5.5: Mechanical properties of alloys.

Sample	**Yield Strength (MPa)**	**Ultimate Tensile Strength (MPa)**	**Total elongation (%)**	**Hardness (Hv/5kgf)**	**Impact energy (J/mm^2)**
Fe-0.65wt.%P	260±6	365±7	12±0.50	111±7	7.84
Fe-0.65wt.%P-0.20wt.%C	465±9	552±8	13±0.30	200±8	5.40

The liquid phase sintering relies on the formation of P-rich liquid at particle interfaces which may lead to phosphorus enrichment at these sites. In the present investigation, the enhancement in ductility (absence of embrittlement) may be associated with the absence of liquid phase during (solid state powder) processing. It is expected that the main cause of embrittlement in the conventional steels is the occupation of the phosphorus-enriched liquid layer along the

grain boundaries. The SEM micrographs of fracture surfaces of tensile and Charpy impact specimens are shown in Figure 5.41. Fracture morphologies depict dimples indicating that the fracture was ductile in nature.

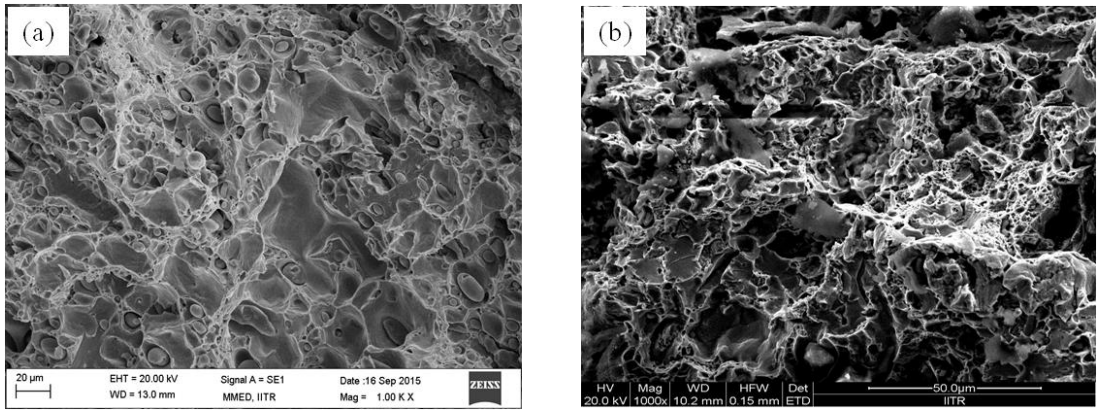

Figure 5.41: Tensile fracture surfaces of powder forged specimens by SEM of (a) Fe-0.65 wt. %P and (b) Fe-0.65 wt. %P-0.20wt. %C showing ductile dimple failure.

The fracture surfaces of Fe-0.65 wt. %P and Fe-0.65 wt. %P-0.20wt. %C specimens shown above are related to a certain microstructural constituent. Ferrite and pearlite showed ductile fracture which is found in the carbon-containing alloy. The microstructure of Fe-0.65 wt. %P-0.20wt.%C the alloy is composed of ferrite and pearlite mainly. The fracture behavior of Fe-0.65 wt.%P alloy (ferrite) can be attributed to the high content of P in ferrite as shown in the microstructure.

Charpy impact results are shown in Table 5.5. The impact energy decreased with the addition of carbon in Fe-0.65wt.% P alloy. The Charpy impact fracture surfaces of alloys exhibit ductile dimple failure (Figure 5.42).

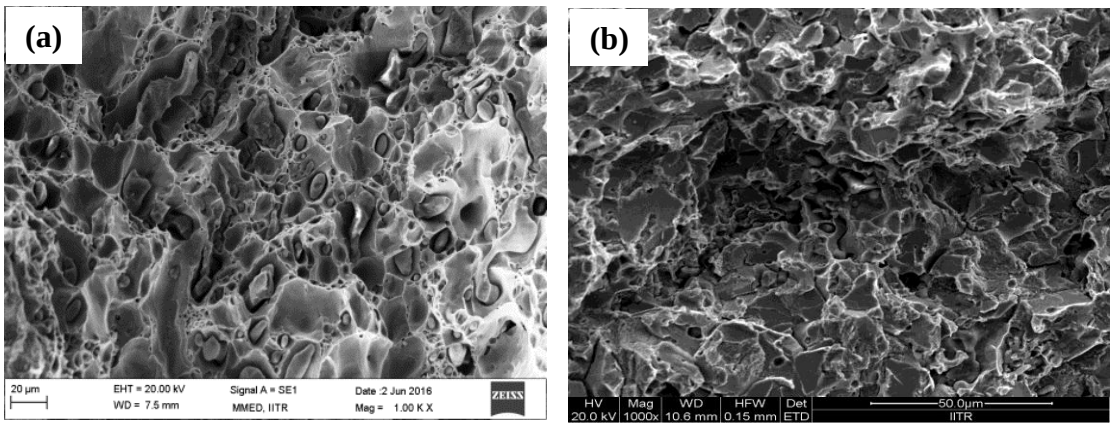

Figure 5.42: SEM images of Charpy fracture surfaces of powder forged specimens for (a) Fe-0.65 wt. %P, and (b) Fe-0.65wt. %P-0.20wt.% C. The alloys exhibit ductile dimple failure.

This suggests a greater cohesion, less porosity, and more efficient bonding than that reported (Moyer 1998) during sintering. The use of hydrogen atmosphere during heating of powders may reduce surface oxides and improve inter particle bonding and cleanliness of the P/M part. Further, the coated iron particle surface ($Fe_3 (PO_4)_2$) will be transformed into iron-phosphide (Fe_3P) during heating. The alloy with carbon content shows more ductile dimples due to reduced non-segregation of P at the grain boundary.

Summary

1. Addition of carbon in Fe-0.65wt.%P alloy considerably improved the hardness as well as strength. A small amount of carbon addition in the Fe-0.65wt.%P alloy improved the hardness to approximately double compared to that without carbon.
2. Microstructural and SEM studies at different locations show the carbon present in the ferrite and pearlite phase.
3. The alloy Fe-0.65wt.%P exhibited iron phosphide (Fe_3P) precipitate in a ferrite matrix whereas carbon containing (Fe-0.65wt.%P-0.20wt.%C) alloy show presence of pearlite along with phosphide in the ferrite matrix.

5.5 EFFECT OF CARBON ON TRIBOLOGICAL PROPERTIES OF Fe-0.65 wt.% P ALLOY

Dry sliding wear behavior of Fe-P-C alloy has been investigated in terms of friction and dry sliding wear on the counterface of steel disc. The main aim of this study is to understand the role of carbon addition in Fe-P, normal load and sliding speed on the wear and friction characteristics of an alloy having different microstructures.

5.5.1 Wear Characteristics

The variation of cumulative wear volume with sliding distance for a sliding speed of 2.2 m/s is shown in Fig. 5.43 for Fe-0.65wt.% P-0.20wt.% C alloy. The cumulative wear volume loss increases with increasing sliding distance at a particular load. Also, for a given sliding distance cumulative wear volume loss increases with increase in load. These two observations are in line with Archard Wear Equation 5.2.

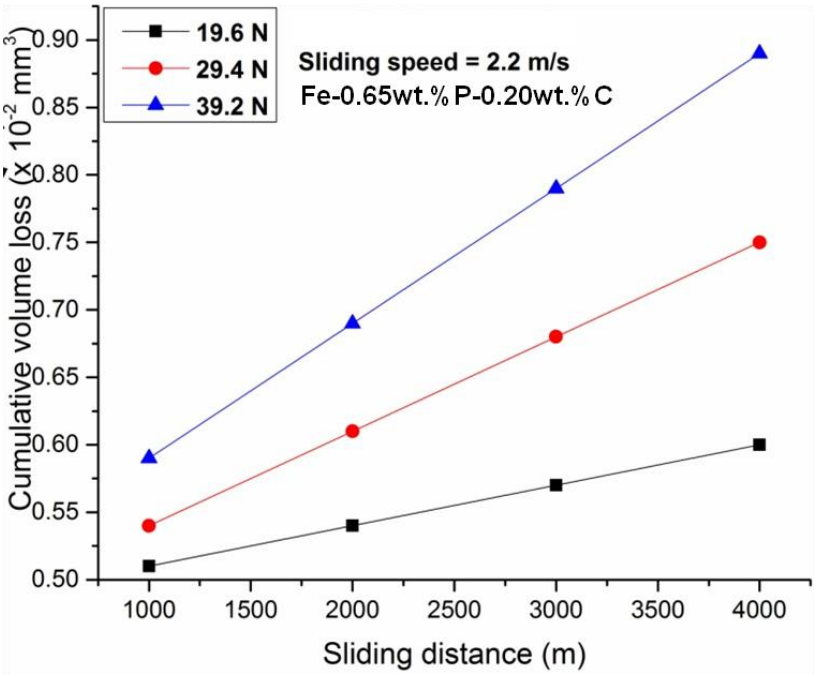

Figure 5.43: Cumulative wear volume loss vs sliding distance at different normal loads for Fe-0.65wt.% P-0.20wt.% C at 2.2 m/s.

The wear rate (volume loss per unit sliding distance) at given load was calculated from the slope of the lines in Figure 5.43 by linear least-squares fit at different loads. The wear rate increases more or less linearly with normal load (Figure 5.44). For a given load wear rate decreases with the addition of carbon in Fe-P alloy. The decrease in wear rate can be attributed to the combination of phosphide and pearlite phase present in the Fe-0.65wt.% P-0.20wt.% C alloy. In this alloy, pearlite was determined by phase analyzer and found to be 24vol. % while phosphide was 10vol. %. This leads to increase in hardness (200HV) of the alloy due to the formation of pearlite. The hardness observed is greater than that reported for the alloy (Fe-0.60wt.% P-0.20wt.% C) developed by compaction and sintering which is 150HV (Igharo and Wood 1988). This may be attributed to higher density obtained in powder forged alloy.

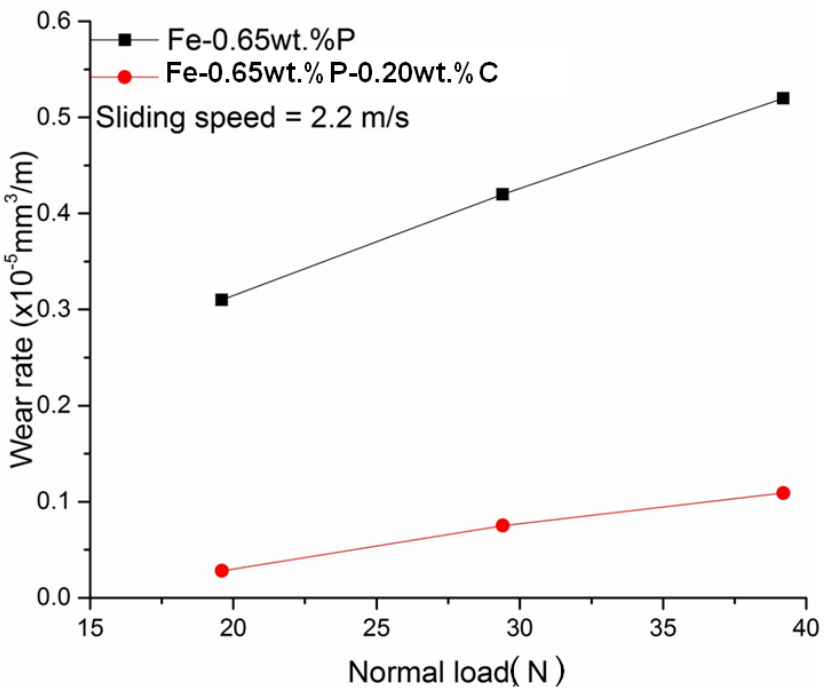

Figure 5.44: Variation of wear rate vs normal load for Fe-0.65wt.% P and Fe-0.65wt.% P-0.20wt.% C containing 10 % phosphide and 23 % pearlite at 2.2 m/s.

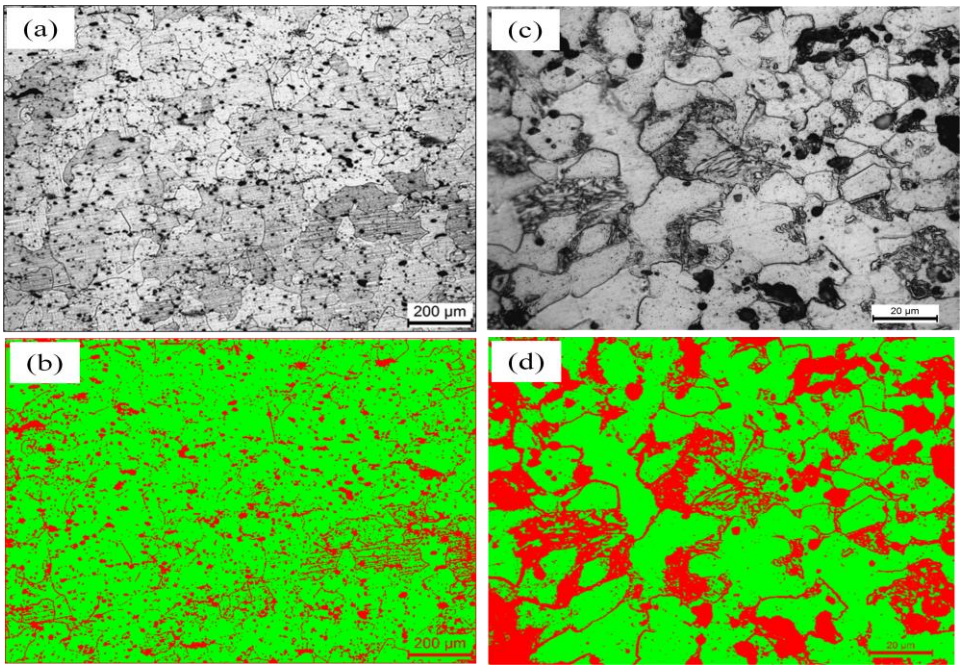

Figure 5.45: (a) and (c): Optical microstructure for Fe-0.65 wt.%P and Fe-0.65 wt.%P-0.20wt. % C, respectively; (b) and (d): Red color indicates the presence of phosphide and pearlite phase for Fe-0.65 wt. %P and Fe-0.65 wt. %P-0.20wt. % C, respectively.

The wear coefficient was calculated from the slope of wear rate with normal load, and by multiplying it with the hardness of the alloy sample. The wear coefficient for Fe-0.65wt. %P-0.20wt.%C is 0.51 $x10^{-7}$.

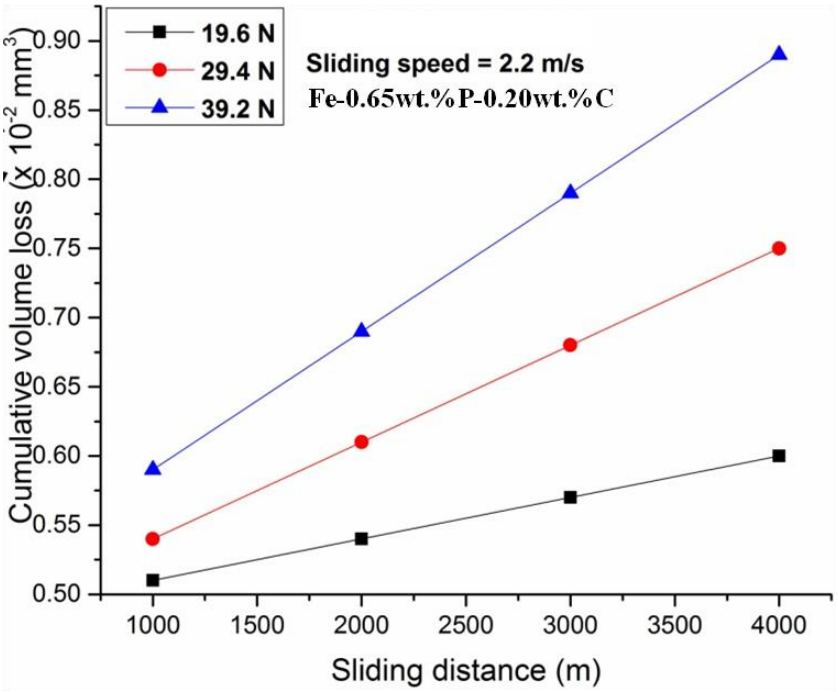

Figure 5.46: Variation of cumulative wear volume loss vs sliding distance at different loads for Fe-0.65wt.%P-0.20wt.%C.

The variation of cumulative wear volume vs sliding distance for Fe-0.65wt.%P-0.20wt.%C alloy at normal loads on a sliding speed of 3 m/s is shown in Figure 5.46. It is observed that cumulative wear volume loss increases with increase in sliding distance. It is further noted that for a given sliding distance cumulative wear volume loss increases with increase in the load. These observations are in line with Archard Wear Equation 5.2. The cumulative wear volume is found to increase with sliding distance at a particular load. The wear rate (volume loss per unit sliding distance) at a given load was calculated from the slope of the lines in Fig. 5.47 by linear least-squares fit at different loads. The wear rate increases more or less linearly under the range of normal load between 19.6 to 39.2 N for Fe-0.65wt.%P and Fe-0.65wt.%P-0.20wt.%C as shown in Fig. 5.47.

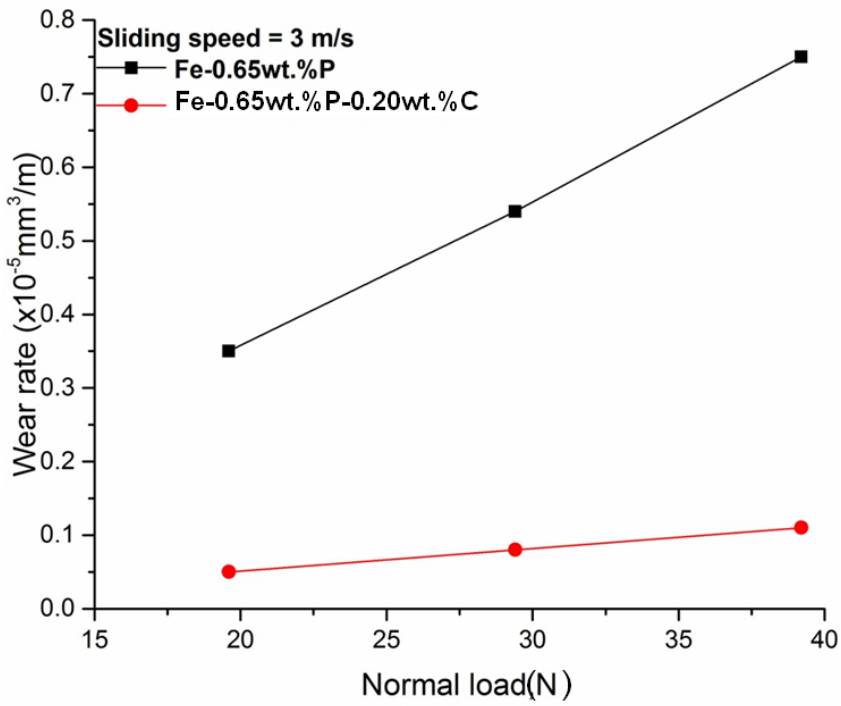

Figure 5.47: Variation of wear rate vs normal load for Fe-0.65wt.%P and Fe-0.65wt.%P0.20wt.%C containing 10 % phosphide and 23 % pearlite at 3 m/s.

For a given load wear rate decreases with the addition of carbon in Fe-P alloy. The decrease in wear rate can also be attributed to the combination of phosphide and pearlite phase present in the Fe-0.65wt.%P-0.20wt.%C alloy. This is also in accordance with Archard Wear Equation 5.2. It is further observed that alloy with carbon has much lower wear rate as compared to alloy without carbon (Figure 5.47). The wear coefficient was calculated from the slope of wear rate against normal load, and by multiplying it with the hardness of the alloy sample. The wear coefficient for Fe-0.65wt.%P-0.20wt.%C is 0.60 $x10^{-7}$.

5.5.2 Dry Sliding Friction

Figure 5.48 shows the variation of coefficient of friction (COF) for alloys Fe-0.65wt.%P and Fe-0.65wt.%P-0.20wt.%C with three normal loads (19.6, 29.4, 39.2 N) and at a sliding speed of 2.2 m/s. It is observed that the average coefficient of friction decreases more or less linearly as the load increases in both the alloys.

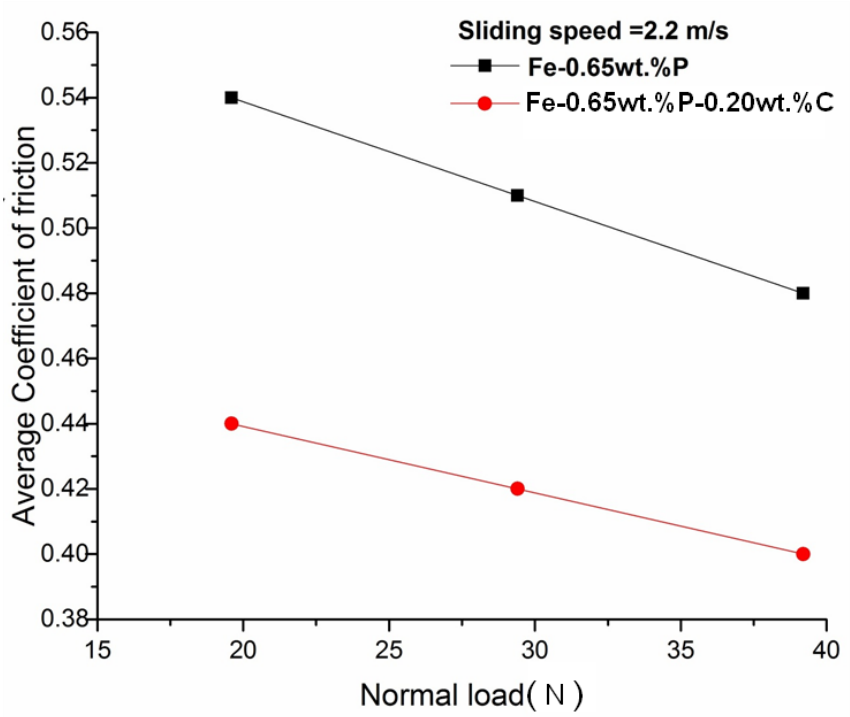

Figure 5.48: Variation of average coefficient of friction vs normal load in Fe-0.65wt.%P and Fe-0.65wt.%P-0.20wt.%C containing 10 % phosphide and 23 % pearlite at 2.2 m/s.

It is further noted that at given normal load average coefficient of friction is less for Fe-0.65wt.%P-0.20wt.%C alloy, as compared to Fe-0.65wt.%P alloy for all the three loads. The average COF value varies from 0.54 to 0.48 in Fe-0.65wt.%P.The average COF decreases by the addition of carbon in the alloy and its value varies from 0.44 to 0.40. This may be attributed to the presence of pearlite in the alloy which may reduce the friction between the rubbing surfaces.

Figure 5.49 shows the variation of coefficient of friction (COF) for alloys Fe-0.65wt.% P and Fe-0.65wt.%P-0.20wt.%C with three normal loads and sliding speed of 3m/s. It is observed that the average coefficient of friction decreases more or less linearly vs load. It is further noted that at a given load average coefficient of friction is less for alloy Fe-0.65wt.%P-0.20wt.%C as compared to alloy Fe-0.65wt.%P at normal loads.

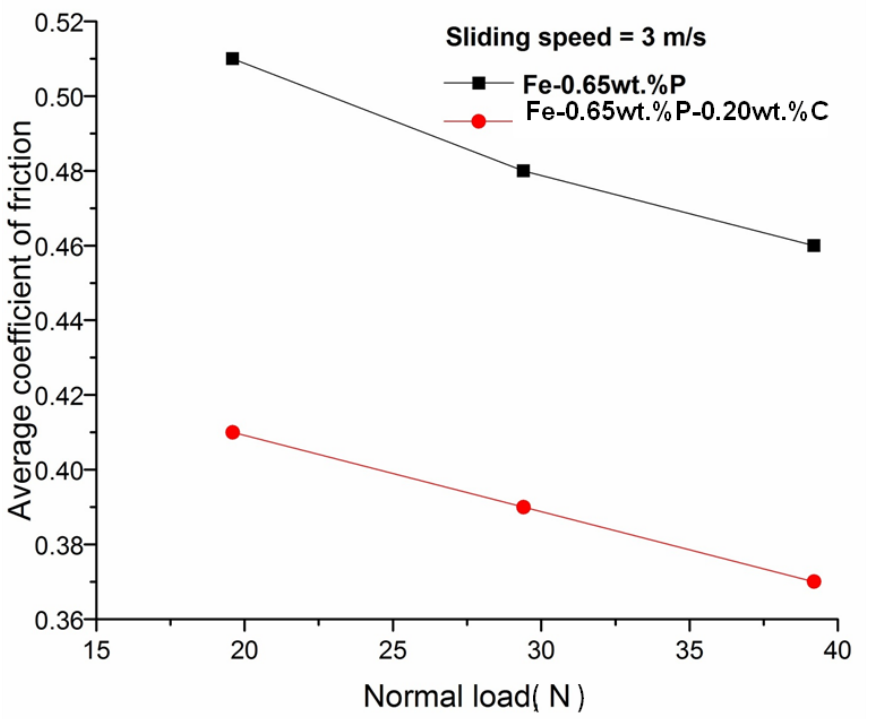

Figure 5.49: Variation of average coefficient of friction with normal load for Fe-0.65wt.% P and Fe-0.65wt.%P-0.20wt.%C containing 10 % phosphide and 23 %. pearlite.

The average COF value varies from 0.51 to 0.46 for Fe-0.65wt.%P. The average COF varies from 0.41 to 0.37 in Fe-0.65wt.%P-0.20wt.%C at the normal loads of 19.6, 29.4 and 39.2 N. The coefficient of friction observed here in Fe-0.65wt.%P-0.20wt.%C is less than the values attained in case of the Fe-0.65wt.%P. This may be attributed to the presence of pearlite in the alloy which may reduce the friction between the rubbing surfaces.

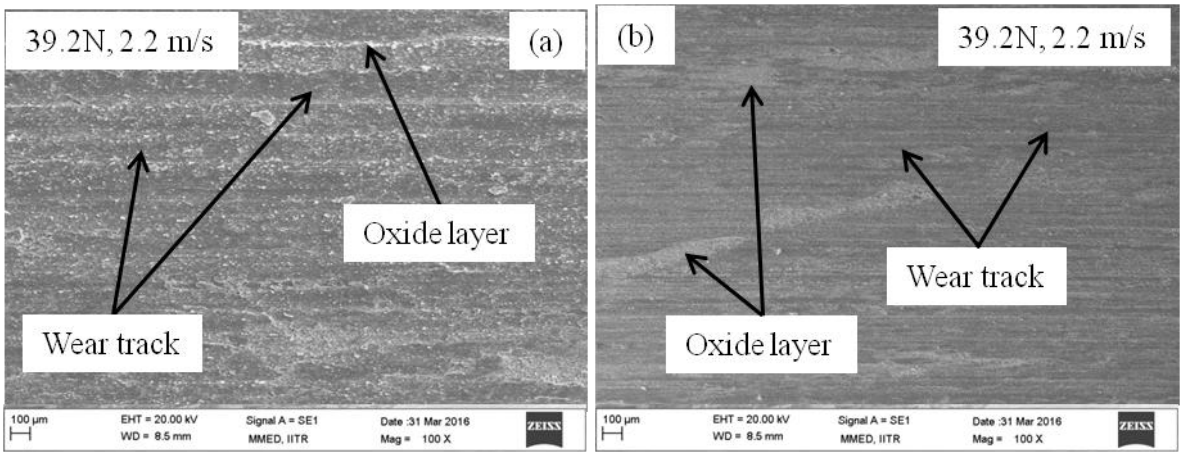

Figure 5.50: SEM images showing the worn surface of (a) Fe-0.65wt.%P and (b) Fe-0.65wt.%P-0.20wt.%C after sliding for 30 min at a sliding speed of 2.2 m/s.

The SEM images of the worn surface of Fe-0.65wt.%P and Fe-0.65wt.%P-0.20wt.%C alloy are shown in the Figure 5.50(a & b). Wear tracks (shown by arrows) in the direction of sliding wear were observed on the worn surfaces of Fe-0.65%P and Fe-0.65%P-0.20%C alloys. However, wear tracks are deeper in Fe-0.65wt.%P alloy (Figure 5.50(a)) as compared to alloy Fe-0.65wt.%P-0.20wt.%C (Fig. 5.50(b)). Further compacted layers of oxides and phosphides (shown by arrows) are also visible on the worn surfaces of both the specimens. The worn surface showed oxidative wear mechanism in both alloys.

CHAPTER 6

CONCLUSIONS

The important contributions of the present work include the hot powder forging route to obtain improved ductility in Fe-P alloys and investigating their tribological properties. Also, the effect of carbon addition on the selected Fe-P alloy was studied. The important conclusions obtained from these studies are listed below:

1. The hot powder forging technique employed in the present study does not require any binder and/ or lubricant, compaction of powders at high pressure, sintering at high temperature and extended sintering time. It allows processing of high phosphorus content up to 3wt.% without the shrinkage and segregation as is observed with the conventional compaction and sintering route.

2. Higher density Fe-P alloys with varying amount of phosphorus were successfully developed using the hot powder forging technique. Such high densities are essential to obtain superior mechanical properties, including good ductility/toughness.

3. In general, the yield strength, tensile strength, and hardness increased with the addition of phosphorus in the iron. This is accompanied by a loss in ductility, particularly in compositions with more than 1wt.%P.

4. Strength and ductility values obtained are considerably higher as compared to studies reported in the literature. The good combinations of strength and ductility can be achieved by using hot powder forging technique in these alloys. The hot powder forging leads to higher density of the alloys. The strength values increased gradually with P addition and its values ranged from 302MPa in 0 wt.%P (Pure iron) to 495MPa in 2wt. %P content alloys. The percentage elongation for iron was found to be highest having values of 20 % whereas it is found to be lowest for 3wt.% P with a value of only 2 %. The ductile alloys are more suitable for the engineering application which gives the prior information before the failure of the component.

5. Addition of 0.20wt.% C in Fe-0.65wt.% P alloy leads to an 80% increase in hardness. The carbon spreaded out the phosphorus from grain boundary throughout which favours in the densification of the alloy. Also, the yield strength (YS) and ultimate tensile

strength (UTS) of the Fe-P based alloy increases with the addition of carbon without compromising the ductility.

6. The alloys containing less than 1wt.% P exhibited a ductile dimple failure during tensile testing as observed in the Fe, Fe-0.35wt.%P and Fe-0.65wt.%P samples. However, alloys containing 1.3wt.%P and 2wt.% P showed a mixed mode of failure whereas the alloy containing 3wt.%P underwent a brittle mode of failure.

7. The Charpy impact energy of Fe-P alloys decreases with increase in phosphorus content. The Charpy impact fracture surfaces of alloys with <1%P exhibit ductile dimple failure. For the alloys with higher phosphorus content (>1 wt.%), the fracture mode is a mix of ductile and cleavage. Its values decrease from 53.46 x 10^{-2} J/mm^2 to 4.10 x 10^{-2} J/mm^2 on addition of P (0wt% to 3wt %). The loss in impact energy was observed due to increase in the phosphide phase as increases the phosphorus content in the alloys

8. The wear and friction behavior of Fe was influenced by the addition of P. For a given load wear rate decreased with increasing phosphorus content in iron which leads increase in the hardness. A lowest wear rate of 0.05 x10^{-5} mm^3 /m for Fe-3wt. %P with normal load 19.6N and highest wear rate of 0.76x$10^{-5}$$mm^3$/m for a pure iron sample with normal load 39.2N at 2.2m/s sliding speed were observed whereas the wear rate ranged from 0.09 x10^{-5} mm^3 /m to 0.81x$10^{-5}$$mm^3$/m respectively for a similar load at 3m/s sliding speed. However, Archard wear coefficient has been found to decrease from 0.25 x 10^{-6} to 0.07 x 10^{-6} with increasing amount of phosphorus from 0% to 3wt% in the alloys at 2.2 m/s sliding speed. At sliding speed 3m/s, the wear coefficient decreased from 0.31 x 10^{-6} for pure iron to 0.09 x 10^{-6} for 3wt.%P.

9. The wear rate was observed to decrease with the addition of 0.20wt.%C in the Fe-0.65wt.%P. It was found to be 0.03 x10^{-5} mm^3/m for Fe-0.65wt. %P-0.20wt. %C alloy with normal load 19.2N at 2.2m/s sliding speed. It's value was 0.05 x10^{-5} mm^3/m for a similar load at 3m/s sliding speed. However, Archard wear coefficient was found to be 0.05 x 10^{-6} at 2.2 m/s sliding speed and 0.06 x 10^{-6} at 3m/s sliding speed for Fe-0.65wt. %P-0.20wt. %C alloy.

10. The average coefficient of friction (COF) decreases with increasing normal load for all the alloys containing 0, 0.35, 0.65, 1.3, 2 and 3wt.%P. It's average value varies from 0.57 to 0.43 at 2.2 m/s sliding speed whereas the average value varies from 0.55 to 0.41

at 3m/s sliding speed. In spite of that, the average COF is observed to decrease more or less linearly with increase in volume fraction of iron phosphide for pure iron (0 vol. % phosphide) to Fe-3wt. %P (34 vol. % phosphide) for all the three normal loads of 19.6, 29.4 and 39.2 N.

11. The coefficient of friction (COF) decreased with the addition of carbon (0.20wt.%) in Fe-0.65wt.%P at all normal loads and sliding speeds. This may be attributed to the presence of pearlite in the alloy which may reduce the friction between the rubbing surfaces. It's value decreased from 0.54 for Fe-0.65wt.%P to 0.44 for Fe-0.65wt.%P-0.20wt.%C with normal load 19.6N at 2.2m/s sliding speed. The coefficient of friction decreased with increase in the speed at all normal loads for Fe-0.65wt. %P-0.20wt. %C alloy. The average coefficient of friction (COF) of 0.4 was obtained on normal load 39.2N at 2.2 m/s sliding speed and 0.37 on similar load at 3m/s sliding speed for Fe-0.65wt. %P-0.20wt. %C alloy.

12. The mechanism of wear is primarily oxidative for all the alloys. However, delamination caused by subsurface cracking could also be observed in some alloys and at a few places, particularly at higher loads. The presence of oxygen in the EDS analysis of the debris essentially suggests the formation of iron-oxide during sliding and oxidative wear mechanism.

13. For a given load, the cumulative wear volume loss increases linearly with increasing sliding distance. On the other hand for a given sliding distance, cumulative wear volume loss increases with increasing load. It is also noted that cumulative wear volume loss decreases with increasing phosphorus content for a given sliding distance and load.

CHAPTER 7

SUGGESTIONS FOR THE FUTURE WORK

The present investigation has focused on the development and wear studies of Fe-P and Fe-P-C alloys. Some of the points that emerged during investigation can be further investigated in details. These are as follows:

1. The present study has shown that in Fe-P alloys there is a strong tendency of phosphide formation. Appropriate alloy design incorporating higher carbon content and heat treatments and restricting phosphorus up to 0.65wt.% need to be carried out in order to further enhance mechanical and tribological characteristics to a level higher than those obtained in convention route of powder metallurgy.
2. Investigations of the effect of carbon and heat treatments on mechanical properties of Fe-2wt.%P alloy developed by hot powder forging route.
3. Fatigue properties can be investigated in order to make these alloys applicable for dynamic loading and high-stress conditions like in automotive applications.
4. Wear and friction behavior of these alloys can be further investigated at different wear conditions/parameters to elaborate insight of wear mechanism and characteristic of these alloys.

REFERENCES

1. Abbaschian R., and Robert E. Reed-Hill., Physical metallurgy principles, Cengage Learning, 2008.
2. Abbasi H. R., Bazdar M., and Halvaee A., Effect of phosphorus as an alloying element on microstructure and mechanical properties of pearlitic gray cast iron, Materials Science and Engineering: A 444, No. 1-2, pp. 314-317, 2007.
3. Abiko, K., Suzuki S., and Kimura H., Effect of carbon on the toughness and fracture mode of Fe–P alloys, Transactions of the Japan Institute of Metals, 23, No. 2, pp. 43-52,1982.
4. Abouei, V., Saghafian H., and Sh Kheirandish., Effect of microstructure on the oxidative wear behavior of plain carbon steel, Wear, 262, No. 9-10, pp. 1225-1231, 2007.
5. Adkins, N. J. E., and P. Tsakiropoulos., Design of powder metallurgy aluminium alloys for applications at elevated temperatures Part 2 Tensile properties of extruded and Conformed gas atomised powders, Materials Science and Technology,7, No. 5, pp. 419-426, 1991.
6. Anne Gajanan, M. R. Ramesh, H. Shivananda Nayaka, Shashi Bhushan Arya, and Sandeep Sahu., Microstructure Evolution and Mechanical and Corrosion Behavior of Accumulative Roll Bonded Mg-2% Zn/Al-7075 Multilayered Composite, Journal of Materials Engineering and Performance, 26, No. 4, pp. 1726-1734, 2017.
7. Anne Gajanan, M. R. Ramesh, H. Shivananda Nayaka, and Shashi Bhushan Arya., Microstructure, mechanical and corrosion properties of accumulative roll bonded Mg-2% Zn/anodized Al-7075 composite, In International Conference on Emerging Trends in Materials and Manufacturing Engineering, organized by department of Metallurgical and Materials Engineering, NIT Thiruchirapalli, Tamil Nadu, pp. 10-12, 2017.
8. Archard, J. F., and Hirst W., An examination of a mild wear process, Proc. R. Soc. Lond. A, 238, No. 1215, pp. 515-528, 1957.
9. Archard J. F., and Hirst W., The wear of metals under unlubricated conditions, Proc. R. Soc. Lond. A, 236, No. 1206, pp. 397-410, 1956.
10. Argon A. S., Mechanical properties of near-surface material in friction and wear, Fundamentals of tribology, pp.103-117, 1978.
11. Arora, H. S., H. Singh, and B. K. Dhindaw., Wear behaviour of a Mg alloy subjected to friction stir processing, Wear, 303, No. 1-2, pp. 65-77, 2013.

12. Atkinson M., Strain hardening behavior of polycrystalline iron and low-carbon steels—A statistical analysis, Metallurgical and Materials Transactions A, 15, No. 6, pp. 1185-1192, 1984.
13. Balasubramaniam R., Alloy design of ductile phosphoric iron: ideas from archaeometallurgy, Bulletin of Materials Science, 26, No. 5, pp. 483-491, 2003.
14. Balasubramaniam R., On the corrosion resistance of the Delhi iron pillar, Corrosion Science, 42, No. 12, pp. 2103-2129, 2000.
15. Balasubramaniam R., Studies on the corrosion resistance of the Delhi iron pillar, NML Technical J., 1995.
16. Balasubramaniam R., The decorative bell capital of the Delhi iron pillar, JOM, 50, No. 3, pp. 40-47, 1998.
17. Balasubramaniam R., Story of the Delhi iron pillar, Foundation Books, 2005.
18. Balasubramaniam R., Some aspects of presence of lead in the Delhi iron pillar, Current Science, pp. 681-686, 1999.
19. Barber J. R., Thermoelastic instabilities in the sliding of conforming solids, Proc. R. Soc. Lond. A, 312, No. 1510, pp.381-394, 1969.
20. Batienkov R.V., Dorofeev V.Y., Eremeeva Z.V., and Artemov V.V., Preparation of wear-resistant powder materials based on iron by hot stamping in the presence of a liquid phase, Metallurgist, 55, pp. 289, 2011.
21. Bhattacharyya S., Wear and friction in steel, aluminum and magnesium alloys I. Pearlitic and spheroidized steels, Wear, 61, No. 1, pp. 133-141,1980.
22. Bhushan B., Introduction to tribology, 2nd ed.Wiley, New York, 2013.
23. Bleck, Wolfgang, Spyros Papaefthymiou, and Andreas Frehn., Microstructure and tensile properties in dual phase and trip steels, Steel research international, 75, No. 11, pp. 704-710, 2004.
24. Bleck, Wolfgang, and Kriangyut Phiu-on., Grain refinement and mechanical properties in advanced high strength sheet steels, The Joint International Conference of HSLA Steels 2005 and ISUGS 2005, pp.50, 2005.
25. Bowden F. P., and Tabor D., Mechanism of Friction and Lubrication in Metalworking, Journal Institute of Petroleum, 40, pp. 243-253, 1954.
26. Bowden Frank P., and Tabor D., The friction and lubrication of solids, Clarendon Press, 1950.

27. Byun Thak S., and Kim In S., Tensile properties and inhomogeneous deformation of ferrite-martensite dual-phase steels, Journal of Materials Science, 28, No. 11, pp. 2923-2932, 1993.
28. Capus J., The mechanism of temper brittleness In Temper Embrittlement in Steel, ASTM International, 1968.
29. Chaurasia S. K., Prakash U., Misra P. S., and Chandra K., Development of P/M Fe–P soft magnetic materials, Bulletin of Materials Science, 35, No. 2, pp. 191-196, 2012.
30. Chaurasia S.K., Prakash U., Chandra K., and Misra P. S., Comparisons of Sintered Technology with Powder Forging for Fe-P Soft Magnetic Alloys, Mater. Sci. Forum, 710, pp. 297, 2012.
31. Chawla N., and Deng X., Microstructure and mechanical behavior of porous sintered steels, Materials Science and Engineering: A, 390, No. 1-2, pp. 98-112, 2005.
32. Clayton P., The relations between wear behaviour and basic material properties for pearlitic steels, Wear, 60, No. 1, pp. 75-93, 1980.
33. Conway J. J., and Rizzo F. J., Hot isostatic pressing of metal powders, ASM Handbook, 7, pp. 605-620, 1998.
34. Correa E. O., Costa S. C., and Santos J. N., Studies on weldability of iron-based powder metal alloys using pulsed gas tungsten arc welding process, journal of materials processing technology, 209, No. 8, pp. 3937-3942, 2009.
35. Correa E. O., Costa S. C., and Santos J. N., Weldability of iron-based powder metal materials using pulsed plasma arc welding process, journal of materials processing technology, 198, No. 1-3, pp. 323-329, 2008.
36. Coyle J. P., and Tsang P. H. S., Microstructural changes of cast iron rotor surfaces and their effects on brake performance and wear resistance, No. 830534. SAE Technical Paper, 1983.
37. Danninger H., and Gierl Ch., New alloying systems for ferrous powder metallurgy precision parts, Science of Sintering, 40, No. 1, pp. 33-46, 2008.
38. Das.J., Chandra K., Mishra P.S.,Sarma.B., Novel Powder Metallurgy Technique for Development of Fe-P based Soft magnetic materials, Journal of Magnetism and Magnetic Materials, 320, pp. 906, 2008.
39. Deacon, R. M., J. N. DuPont, C. J. Kiely, A. R. Marder, and P. F. Tortorelli., Evaluation of the Corrosion Resistance of Fe–Al–Cr Alloys in Simulated Low NO x Environments, Oxidation of metals, 72, No. 1-2, pp. 87-107, 2009.
40. Dieter G.E., Mechanical Metallurgy, Mc Graw-Hill New York, pp. 564, 1986.

41. Dlapka M., Danninger H., Gierl C., and Lindqvist B., Defining the pores in PM components, Metal Powder Report, 65, No. 2, pp. 30-33, 2010.
42. Dumoulin Ph., Guttmann M., Foucault M., Palmier M., Wayman M., and Biscondi M., Role of molybdenum in phosphorus-induced temper embrittlement, Metal Science, 14, No. 1, pp. 1-15, 1980.
43. Eisen, W. B., B. L. Ferguson, R. M. German, R. Iacocca, P. W. Lee, D. Madan, Kenneth Moyer, H. Sanderow, and Y. Trudel., Powder metal technologies and applications, 1998.
44. Engstrom U., Lindberg C., and Tengzelius J., Powders and processes for high performance PM steels, Powder metallurgy, 35, No. 1, pp. 67-73, 1992.
45. Everhart John L., Copper and copper alloy powder metallurgy: Properties and applications, Metal Powder Industries Federation, 1975.
46. Exner Hans E., and Mueller C., Particle Rearrangement and Pore Space Coarsening During Solid-State Sintering, Journal of the American Ceramic Society, 92, No. 7, pp. 1384-1390, 2009.
47. Eyre T. S., and Walker R. K., Wear of sintered metals, Powder metallurgy, 19, No. 1, pp. 22-30, 1976.
48. Eyre T. S., and Williams P., Effect of phosphorus on the friction and wear characteristics of grey cast iron, Wear, 24, No. 3, pp. 337-349, 1973.
49. Fedorchenko I. M., Derkacheva G. M., and Panaioti I. I., Effect of phosphorus on the friction properties of a material based on alloyed iron, Powder Metall. and Metal Cera., 8, pp. 945-947,1969.
50. German Randall M., Introduction to Liquid Phase Sintering In Liquid Phase Sintering, Springer, Boston, MA, pp. 1-11., 1985.
51. German R. M., Powder Metallurgy of Iron and Steel, Wiley-Interscience, 1998.
52. Ghosh M. K., The Delhi iron pillar and its iron, NML Technical Journal, 5, No. 1, pp. 31-45, 1963.
53. Gladman Terence., Medium/High Carbon Steels for Rails, Rods, Bars and Forgings, Materials Science and Technology, 2006.
54. Glascott J., Stott F. H., and Wood G. C., The effectiveness of oxides in reducing sliding wear of alloys, Oxidation of metals, 24, No. 3-4, pp. 99-114, 1985.
55. Goodway M., and Fisher Robert M., Phosphorus in low carbon iron: Its beneficial properties, Hist. Metall., 22, No. 1, pp. 21-23, 1988.

56. Gordon Robert B., RF Tylecote, The Prehistory of Metallurgy in the British Isles (Book Review), Technology and Culture, 29, No. 1, pp.133,1988.
57. Grewal, Harpreet S., Harpreet Singh, Anupam Agrawal, and Harpreet S. Arora., Friction stir processing of mild steel to enhance its surface hardness, Advanced Materials Research, 620, pp. 117-121, 2013.
58. Guillou R., Guttmann M., and Dumoulin Ph., Role of molybdenum in phosphorus-induced temper embrittlement of 12% Cr martensitic stainless steel, Metal Science, 15, No. 2, pp. 63-72, 1981.
59. Gurumoorthy, K., M. Kamaraj, K. Prasad Rao, and S. Venugopal., Development and use of combined wear testing equipment for evaluating galling and high stress sliding wear behaviour., Materials & design, 28, No. 3, pp. 987-992, 2007.
60. Gutsfeld Ch., and Thummler F., Mechanically alloyed sintered steels with a high hard phase content, Metal Powder Report, 45, No. 11, pp. 769-771, 1990.
61. Hanejko Francis., High density via single pressing/single sintering, Powder Metallurgy Technology, 1, pp. 016, 2010.
62. Hanejko F. G., Howard G. R., Christopher G. O., Effects of processing and materials on soft magnetic performance of powder metallurgy parts, Advances in Powder Metallurgy & Particulate Materials 6, pp. 375-403, 1992.
63. Hanejko Francis G., Rutz Howard G., and Oliver Christopher G., Effects of processing and materials on Soft magnetic performance of powder metallurgy parts, Hoeganaes Corporation Riverton, NJ 08011,Presented at the 1992 powder metallurgy world Congress san Francisco, CA,www.hoeganaes.com/ - 9k, 1992.
64. Hansel H., Grabke H.J., Grain boundary segregation of phosphorus and carbon in ferritic iron, Scripta metal., 20, pp. 1641-1644, 1986.
65. Hansen Max., Anderko K., and Salzberg H. W., Constitution of binary alloys, Journal of the Electrochemical Society, 105, No. 12, pp. 260-261, 1958.
66. Hirschhorn Joel S., Introduction to powder metallurgy, American powder metallurgy Institute, NJ, pp. 96, 1976.
67. Hoganas Handbook for Sintered Components-3.Design and Mechanical Properties. Hoganas AB, 2004.
68. Hopkins B. E., and Tipler H. R., The effect of phosphorus on the tensile and notch-impact properties of high-purity iron and iron-carbon alloys, Journal of the iron and steel institute, pp. 218-237, 1958.

69. Huppmann W. J., and Hirschvogel M., Powder forging, International Metals Reviews, 23, No. 1, pp. 209-239, 1978.
70. Hudson, J. C., The Delhi Pillar, Nature, 172, No. 4376, pp. 499, 1953.
71. Hu Hsun., Effect of Carbon Content on Annealing Texture, Plastic Anisotropy, and Mechanical Properties of 0.07% Phosphorus Sheet Steels, Texture, Stress, and Microstructure, 3, No. 4, pp. 215-230, 1979.
72. Huppmann W. J. and Hirschvogel. M., Powder forging, International Metals Reviews, 23, No. 1, pp. 209-239, 1978.
73. Hutchings Ian., and Shipway P., Tribology: friction and wear of engineering materials, Butterworth-Heinemann, 2017.
74. Igharo M., and Wood J. V., Sintering of Mixed High Speed Steel and Iron-Phosphorus Powders, Powder metall., 31, pp. 184-188, 1988
75. Islam M. A., Sato N., and Tomota Y., Tensile and plane bending fatigue properties of pure iron and iron-phosphorus alloys at room temperature in the air, Transactions of the Indian Institute of Metals, 64, No. 3, pp.315-320, 2011.
76. James W. Brian., Powder forging, Rev. Part. Mater., 2, pp.173-213, 1994.
77. James W. B., McDermott M. J., Powell A. Robert., Powder Forging, ASM Hand Book on Forming and forging, 14, pp. 188,1998.
78. Jandeska W. F., Strength and ductility enhancement of low temperature sintered iron powder structures, SAE Technical Paper No. 820231, 1982.
79. Jiang, Jiaren, F. H. Stott, and M. M. Stack., The role of triboparticulates in dry sliding wear, Tribology International, 31, No. 5, pp. 245-256, 1998.
80. Jiang J., Stott F. H., and Stack M. M., The role of triboparticulates in dry sliding wear, Tribology International, 31, No. 5, 245-256, 1998.
81. Jonsén Par., Haggblad Hans A., Troive L., Furuberg J., Allroth S., and Skoglund P., Green body behaviour of high velocity pressed metal powder, Materials Science Forum, 534, pp. 289-292, 2007.
82. Kalpakjian Serope., and Schmid Steven R., Manufacturing Processes for Engineering materials, Pearson Education (Singapore) Pte.Ltd, Branch, Delhi, pp. 260, 2003.
83. Kang, Jee-Hyun, Shanghong Duan, Sung-Joon Kim, and Wolfgang Bleck., Grain boundary strengthening in high Mn austenitic steels, Metallurgical and Materials Transactions A, 47, No. 5, pp.1918-1921, 2016.

84. Kato H., Effects of supply of fine oxide particles onto rubbing steel surfaces on severe mild wear transition and oxide film formation, Tribology International, 41, No. 8, pp. 735-742, 2008.
85. Kchaou, Mohamed, Amira Sellami, Riadh Elleuch, and Harpreet Singh., Friction characteristics of a brake friction material under different braking conditions, Materials & Design, 52, pp. 533-540, 2013.
86. Khorsand H., Habibi S. M., Yoozbashizadea H., Janghorban K., Reihani S. M. S., Seraji H. R., and Ashtari M., The role of heat treatment on wear behavior of powder metallurgy low alloy steels, Materials & design, 23, No. 7, pp. 667-670, 2002.
87. Kirchheim R., Grain coarsening inhibited by solute segregation, Acta Materialia, 50, pp. 413-9, 2002.
88. Klar E., Svilar M., Berry D.F., Infiltrated powder metal part having improved impact strength tensile strength and dimensional control and method for making same, United States patent US 4,861, pp. 373, 1989.
89. Krahe, P. R., and Guttman M., On the segregation of manganese and antimony to the grain boundaries of temper embrittled steel, Scripta Metallurgica, 7, No. 4, pp. 387-393, 1973.
90. Krecar D., Vassileva V., Danninger H., Hutter H., Analy. Bioanaly. Chem., 379, pp. 610–618, 2004.
91. Kubaschewski Ortrud., Iron-Binary phase diagrams, Springer Science & Business Media, 2013.
92. Kumar V., and Balasubramaniam R., On The Origin of High Phosphorus Contents in Ancient Indian Iron, Metal Mater. And Processes, 14, No. 1, pp. 1-14, 2002.
93. Kubota M., Hamabe T., Nakazono Y., Fukuda M., and Doi K., Development of a lightweight brake disc rotor: a design approach for achieving an optimum thermal, vibration and weight balance, JSAE review, 21, No. 3, pp. 349-355, 2000.
94. Lejcek P., Grain boundary segregation in metals, Springer Science & Business Media, 136, 2010.
95. Lim S. C., Ashby M. F., Overview no. 55 wear-mechanism maps, Acta metallurgica, 35, No. 1, pp. 1-24, 1987
96. Lim S. C., Ashby M. F., Brunton J. H., Wear-rate transitions and their relationship to wear mechanisms, Acta metallurgica, 35, No. 6, pp. 1343-1348, 1987.
97. Lindskog P., Svensson L., Steel powder containing phosphorus, U.S. Patent 3,836,355, issued September 17, 1974.

98. Lindskog P., Tengzelius J., Kvist S., Phosphorus as an alloying element in Ferrous P/M, Modern Developments in Powder Metallurgy, 10, 1977.
99. Lindskog P., The effect of phosphorus additions on the tensile, fatigue, and impact strength of sintered steels based on sponge iron powder and high-purity atomized iron powder, Powder Metallurgy, 16, No. 32, pp. 374-386, 1973.
100. Liu, Cheng, and Rana Radhakanta., Low density high strength steel and method for producing said steel, U.S. Patent Application 14/241,644, filed December 11, 2014.
101. Loberto A., Lopes H., I. Fernando, S. Lucio, PM Trends for the Automotive Industry, SAE International, pp 4, 2010.
102. Madakson Peter B., The frictional behaviour of materials, Wear, 87, No. 2, pp.191-206, 1983.
103. Marucci Michael L., Rawlings Arthur J., Full Density Properties of Low Alloy Steels, In International Conference on Powder Metallurgy and Particulate Materials. 2004.
104. McDonnell G., Iron and its alloys in the fifth to eleventh centuries AD in England, World Archaeology, 20, No. 3, pp. 373-382, 1989
105. Menyhard M., Phosphorus on the non-brittle grain boundaries of iron, Scripta metallurgica et materialia, 26, No. 11, pp.1695-1700, 1992.
106. Mediratta S. R., Ramaswamy V., Singh V., Ramarao P., Dependence of strain hardening exponent on the volume fraction and carbon content of martensite in dual phase steels during multistage work hardening, Journal of Materials Science Letters, 9, No. 2, 205-206, 1990.
107. Mohan, S., and S. Srivastava., Surface behaviour of as-Cast Al–Fe intermetallic composites, Tribology Letters, 22, No. 1, 45-51, 2006.
108. Mohan, S., Ved Prakash, and J. P. Pathak., Wear characteristics of HSLA steel, Wear, 252, No. 1-2, pp. 16-25, 2002.
109. Moyer K.H., Magnetic materials and properties for part applications, ASM Hand Book on powder metallurgy and application, 7, pp. 1006-1019, 1998.
110. Muchnik S.V., Phosphorus-containing sintered alloys (review), Inst. of Mater. Sci. translated from poroshkovaya Metallurgiya, 12(264), pp. 20-27, 1984.
111. Narasimhan K. S.,Sintering of powder mixtures and the growth of ferrous powder metallurgy, Materials Chemistry and Physics, 67, No. 1-3, 56-65, 2001.
112. None, PM94 World Congress, Powder Metallurgy, 37:3, pp. 168-191, DOI: 10.1179/pom. 37.3.168, 1994.

113. Norman A. F and P. Tsakiropoulos, Strengthening mechanisms in powder metallurgy AI-Li-Hf alloys, Materials Science and Technology, 9, pp 228-234, 1993.
114. Panasyuk O. A., Radomyselskii I. D., Effect of phosphorus additions upon the magnetic properties of parts from iron powder, Soviet Powder Metallurgy and Metal Ceramics, 12, No. 4, pp. 289-292, 1973.
115. Panetoa F.J., Pereiraa J.L., Limaa J.O., Jesusa E.J., Silvaa L.A., Limab E.Sousa., Cabrala R.F., Santos C., Effect of porosity on hardness of Al2O3–Y3Al5O12 ceramic composite, Int. Journal of Refractory Metals and hard Materials, 48, pp. 365-368, 2015.
116. Park Chul-Woo., Jong-Ok Park.,Young-Ho Kim., A Study on the Effect of Powder Forging for Cup-shaped Products, International Journal of the Korean Society of Precision Engineering , 3, No. 4, pp. 37, 2002.
117. Paruz H., Edmonds D. V., The strain hardening behaviour of dual-phase steel, Materials Science and Engineering: A 117, pp. 67-74, 1989.
118. Pathak, J. P., and S. Mohan. Wear behaviour of Ni–Cr–Mo–V steel under dry sliding, Zeitschrift für Metallkunde, 93, No. 11, pp. 1140-1145, 2002.
119. Pavlygo T. M., Sakhnenko A. V., Sakhnenko S. A., Serdyuk G. G., Development of powder material hot forging in the Ukraine, Powder Metall. Metal Cera., 39, pp. 183-197, 2000.
120. Production of Sintered Components in Höganäs Handbook 2, Höganäs AB, 2004.
121. Quinn T. F. J., Review of oxidational wear: Part I: The origins of oxidational wear, Tribology International, 16, No. 5, pp. 257-271, 1983.
122. Rabinowicz E., Friction and wear of materials, Willey, New York, 1965.
123. RaghavanV., Material science and Engineering, Prentice-hall of India Private Limited, New Delhi, pp. 372, 2000.
124. Raghavan V., C-Fe-P (carbon-iron-phosphorus), Journal of Phase Equilibria and Diffusion 25, No. 6, pp. 541, 2004.
125. Ramakrishnan P., Automotive applications of powder metallurgy, Advances in powder metallurgy, Woodhead publishing Limited, pp.493-585, 2013.
126. Rana R., Shiv Brat Singh, and Omkar Nath Mohanty., Effect of copper on annealing characteristics of interstitial free steels, Journal of materials science, 42, No. 17, pp.7508-7513, 2007.
127. Rana, R., S. B. Singh, and O. N. Mohanty., Thermoelectric power studies of copper precipitation in a new interstitial-free steel, Scripta materialia, 55, No. 12, pp.1107-1110, 2006.

128. Rao, SR Koteswara, G. Madhusudhan Reddy, K. Srinivasa Rao, P. Srinivasa Rao, M. Kamaraj, and K. Prasad Rao., Gas tungsten arc welded AA2219 alloy using scandium containing fillers–mechanical and corrosion behavior, Trans. Indian Inst. Met., 57, No. 5, pp. 451-459, 2004.
129. Richter D., Haour G., Richon D., Hot isostatic pressing (HIP),Materials & design, 6, No. 6, pp.303-305, 1985.
130. Rigney D. A., Sliding wear of metals, Annual Review of Materials Science, 18, No. 1, 141-163, 1988.
131. Rigney D. A., Hirth J. P., Plastic deformation and sliding friction of metals, Wear, 53, No. 2, pp. 345-370, 1979.
132. Rosskamp H., Ostgathe M., Thummler F., Engstrom U., Vannman E., Sintered steels with inert hard phase produced by mechanical alloying in ball mill, Powder metallurgy, 39, No. 1, pp. 37-43, 1996.
133. Roy, Manish., Use of wear mechanism map to engineer surfaces for enhanced wear resistance, Transactions of the Indian Institute of Metals, 62, No. 3, pp.197-208, 2009.
134. Roy, M., Ch V. Subha Rao, D. S. Rao, and G. Sundararajan., Abrasive wear behaviour of detonation sprayed WC–Co coatings on mild steel, Surface Engineering, 15, No. 2, pp. 129-136, 1999.
135. Roy, Manish, B. Venkataraman, V. Vetat Bhanuprasad, Y. R. Mahajan, and G. Sundararajan., The effect of participate reinforcement on the sliding wear behavior of aluminum matrix composites, Metallurgical Transactions A 23, No. 10, pp. 2833-2847, 1992.
136. Rutz H. G., and Hanejko F. G., High density processing of high performance ferrous materials, Adv. Powder Metall. Part. Mater., 5, pp. 117, 1994.
137. Rutz H. G., Hanejko F. G., High density processing of high performance ferrous materials, Advances in Powder Metallurgy and Particulate Materials, 5, pp. 117-117, 1994.
138. Sarkar, S., A. Mohan, C. K. Behera, and S. Mohan. Comparative study of sliding wear characteristics of Ni and N austenitic steels, Tribology-Materials, Surfaces & Interfaces , 3, No. 2, pp. 92-96, 2009.
139. Sherwood D. J., Hamilton C. H., A mechanism for deformation-enhanced grain growth in single phase materials, Scripta metallurgica et materialia, 25, No. 12, pp. 2873-2878, 1991.

140. Shirokov V. V., Arendar L. A., Slynko H. I., Volchok I. P., Influence of Phosphide Eutectics on the Wear Resistance of High-Strength Cast Irons, Materials Science 39, no. 2, pp. 295-298, 2003.
141. Shokrollahi H., Janghorban K., Soft magnetic composite materials (SMCs), Journal of Materials Processing Technology 189, No. 1-3, pp. 1-12, 2007.
142. Shyrokov V. V., Arendar L. A., Rytsar D. I., Tribological properties of gray cast irons alloyed with phosphorus, Materials Science 40, No. 4, pp. 512-517, 2004.
143. Shyrokov, V. V., L. A. Arendar, and D. I. Rytsar. Tribological properties of gray cast irons alloyed with phosphorus, Materials Science 40, No. 4, pp. 512-517, 2004.
144. Sin H., Saka N., Suh N. P., Abrasive wear mechanisms and the grit size effect, Wear, 55, No. 1, 163-190, 1979.
145. Skoglund P., High density PM parts by high velocity compaction, Powder metallurgy 44, No. 3, pp. 199, 2001.
146. Slynko G. I., Grabovyi V. M., Volchok I. P., Effect of phosphide eutectic on the properties of a cast iron alloy, Metal science and heat treatment 35, No. 3, pp. 155-159, 1993.
147. Smith, A. F., The unlubricated reciprocating sliding wear of a martensitic stainless steel in air and CO2 between 20 and 300° C, Wear, 123, No. 3, pp. 313-331, 1988.
148. Song X., Yuan Z., Jia J., Wang D., Li P., Deng Z., Effect of phosphorus grain boundaries segregation and precipitations on mechanical properties for Ti-IF steel after recrystallization annealing, Journal of Materials Science & Technology, 26(9), pp. 793-7, 2010.
149. Straffelini G., Fontanari V., Molinari A., Tesi. B., Tensile and fatigue behaviour of phosphorus alloyed sintered steels, Powder metallurgy, 36, No. 2, pp. 135-141, 1993.
150. Stack, M. M., and Mathew Mathew. Micro-abrasion transitions of metallic materials, Wear, 255, No. 1-6, pp.14-22, 2003.
151. Stewart J. W., Charles J. A., Wallach E. R., Iron–phosphorus–carbon system: Part 1–Mechanical properties of low carbon iron–phosphorus alloys, Materials science and technology 16, No. 3, pp. 275-282, 2000.
152. Stewart J. W., Charles J. A., Wallach E. R., Iron–phosphorus–carbon system: Part 3–Metallography of low carbon iron–phosphorus alloys, Materials science and technology 16, No. 3, pp. 291-303, 2000.
153. Stott F. H., and Wood G. C., The influence of oxides on the friction and wear of alloys, Tribology International 11, No. 4, pp. 211-218, 1978.

154. Straffelini G., Fontanari V., Molinari A., Tesi, B., Tensile and fatigue behavior of phosphorus alloyed sintered steels, Powder metal., 36, pp.135-141, 1993.
155. Suh Nam P., Sin H.C., The genesis of friction, Wear, 69, No. 1, pp. 91-114, 1981.
156. Suh, Nam P., An overview of the delamination theory of wear, Wear, 44, No. 1, pp. 1-16, 1977.
157. Suh Nam P., Tribophysics, Pretice-Hall, Englewood Cliffs, New Jersey 07632, USA, 1986.
158. Sundaram Maheswaran V., Processing Methods for Reaching Full Density Powder Metallurgical Materials, 2017.
159. Suzuki S., Obata M., Abiko K., Kimura H., Role of carbon in preventing the intergranular fracture in iron-phosphorus alloys, Transactions of the Iron and Steel Institute of Japan 25, No. 1, pp. 62-68, 1985.
160. Tanase T., Mayama O., Matsunaga H., Properties of sintered wear-resistant alloys having high volume fraction of carbides, Metal Powder Report 45, No. 3, pp. 198-201, 1990.
161. Tandon R., Johnson J., Liquid Phase Sintering, in ASM Handbook, Volume 7 - Powder Metal Technologies and Applications, Vol. 7, pp. 565–573, 1998.
162. Tengzelius J., Avoiding Brittleness in Iron--Phosphorus Alloys, Metal Powder Report(UK) 48, No. 1, pp. 36-39, 1993.
163. Terheci, M., Manory R. R., Hensler J. H., The friction and wear of automotive grey cast iron under dry sliding conditions Part 2. Friction and wear-particle generation mechanisms and their progress with time, Wear, 185, No. 1-2, pp. 119-124, 1995.
164. Tomlinson W. J., Vandrill G. J., Dry sliding wear of grey cast iron containing 0.2–1.0 wt.% P, Wear, 117, No. 3, pp. 375-379, 1987.
165. Tomlinson W.J., Dennison G., Effect of phosphide and matrix microstructures on the dry sliding wear of grey cast iron, Tri. International, pp. 259-264, 1989.
166. Tholander E., Experimental studies on early iron-making, pp. 0165-0165, 1989.
167. Vogel R., On the system iron-phosphorus-carbon, Arch Eisenhuttenwes 3, No. 5, pp. 369-371, 1929.
168. Welsh N. C., The dry wear of steels II. Interpretation and special features, Phil. Trans. R. Soc. Lond. A, 257, No. 1077, pp. 51-70, 1965.
169. Welsh N. C., The dry wear of steels I. The general pattern of behavior, Phil. Trans. R. Soc. Lond. A, 257, No. 1077, pp. 31-50, 1965.

170. Wettlaufer M., Kaspar R., Effect of phosphorus on the ductility of high strength spring steels, Steel research international, 71, pp. 357-61, 2000.
171. Whittaker D., PM structural parts move to higher density and performance, Powder Metallurgy, 50, No. 2, pp. 99-105, 2007.
172. Wranglén G., The "rustless" iron pillar at Delhi, Corrosion science 10, No. 10, pp. 761-770, 1970.
173. Yamamoto Y., Kiggans Jim O., Clark Michael B., Nunn Stephen D., Sabau Adrian S., Peter William H., Consolidation process in near net shape manufacturing of Armstrong CP-Ti/Ti-6Al-4V powders, In Key Engineering Materials, Trans Tech Publications, 436, pp. 103-111., 2010.
174. Zaitsev A. I., Dobrokhotova Zh V., Litvina A. D., Mogutnov B. M., Thermodynamic properties and phase equilibria in the Fe–P system, Journal of the Chemical Society, Faraday Transactions, 91, No. 4, pp. 703-712, 1995.
175. Zapf G., Gerard Hoffmann, and Klaus Dalal., Effect of additional alloying elements on the properties of sintered manganese steels, Powder Metallurgy, 18, No. 35, pp. 214-236, 1975.
176. Zhang Y. Z., Wu S. J., Liu W. M., Chen Y., Guan B. Shang,, Tie X. H., Ni. F., Metallurgical investigations of dry sliding surface layers in phosphorus iron/steel friction pairs, Wear, 252, pp. 269-275, 2002.
177. Zhang Y., Chen Y., He R., Shen B., Investigation of tribological properties of brake shoe materials-phosphorous cast irons with different graphite morphologies, Wear, 166, pp. 179-186, 1993.

Weblinks

1. None, Cast steel: Microstructure and grain size, 2000. (https://www.totalmateria.com/page.aspx?ID=CheckArticle&LN=EN&site=kts&NM=259).
2. None, Metal injection molding in Japan: Growth anticipated after a poor 2015, 30.06.2016.(http://www.pim-international.com/metal-injection-molding-japan-growth-anticipated-poor-2015/)
3. None, Iron pillar of Delhi, 2016.(https://en.wikipedia.org/wiki/Iron_pillar_of_Delhi)
4. Lumbley R N., Fundamentals of aluminium metallurgy, 2018. (https://books.google.co.in/books?isbn=0081020643)